Stony Brook University

Characterization of Intracranial Pulsatility in a Rat Model of Communicating Hydrocephalus: An MRI and Two-Photon Microscopy Study

A Dissertation Presented

by

Shams Rashid

to

The Graduate School

in Partial Fulfillment of the

Requirements

For the Degree of

Doctor of Philosophy

in

Biomedical Engineering

Stony Brook University

May 2012

Stony Brook University

The Graduate School

Shams Rashid

We, the dissertation committee for the above candidate for the

Doctor of Philosophy degree, hereby recommend

acceptance of this dissertation.

Mark E. Wagshul, Ph.D. – Dissertation Advisor
Associate Professor, Dept. of Radiology

Mary D. Frame, Ph.D. – Chairperson of Defense
Associate Professor and Vice-Chair, Dept. of Biomedical Engineering

Helene Benveniste, M.D., Ph.D.
Professor, Depts. Of Anesthesiology & Radiology
Vice Chair for Research, Department of Anesthesiology

James P. McAllister II, Ph.D.
Professor, Dept. of Neurosurgery
Primary Children's Medical Center, University of Utah

This dissertation is accepted by the Graduate School

Charles Taber
Interim Dean of the Graduate School

Abstract of the Dissertation

Characterization of Intracranial Pulsatility in a Rat Model of Communicating Hydrocephalus: An MRI and Two-Photon Microscopy Study

by

Shams Rashid

Doctor of Philosophy

in

Biomedical Engineering

Stony Brook University

2012

Introduction

Communicating hydrocephalus (CH) is a severe neurodegenerative disorder characterized by an increased volume of cerebrospinal fluid (CSF) within enlarged cerebral ventricles. Previous studies have found that pulsatile CSF flow in the human cerebral aqueduct is elevated in CH, and have suggested that the causes of CH may be related to this increased pulsatility, as opposed to the traditionally accepted view of CSF malabsorption at the arachnoid villi. However, this has yet to be proven. In this dissertation, our goal was to investigate the significance of elevated aqueductal pulsatility in CH. We hypothesized that pulsatile CSF flow is a significant non-invasive marker of clinical outcome in CH.

Methods

We explored our hypothesis by characterizing the course of CH development in a recently developed rat model of CH, by MRI measurement of the volume of the cerebral

ventricles and pulsatile CSF flow in the cerebral aqueduct and studying the relationship between ventricular dilation and aqueductal pulsatility. Aqueductal pulsatility may strongly be influenced by intracranial compliance, which is known to affect intracranial pressure pulsations. To understand how compliance affects aqueductal pulsatility, we studied the changes in aqueductal pulsatility produced by surgical modulation of compliance by shunting and craniectomy. Since increased blood flow pulsatility in the cerebral microvasculature has been suggested as a mechanism of increased CSF pulsatility in CH, we next explored a possible source of elevated aqueductal pulsatility by measuring capillary blood flow pulsatility in the CH rat neocortex with two photon microscopy. Finally, we investigated whether aqueductal pulsatility correlates with severity of CH in our animal model by characterizing behavioral deficits in our CH rats.

Results

At four weeks following hydrocephalus induction, the volume of the ventricles increased by a factor of 12 on average and aqueductal pulsatile flow of CSF increased by a factor of 101 compared to control rats. Aqueductal pulsatility was correlated to ventricular size, but this relationship varied significantly over the course of CH development, suggesting that both pulsatility and ventricular size may depend on another parameter, such as intracranial compliance. Aqueductal pulsatility had a strong dependence on compliance; increased compliance produced by shunting or craniectomy caused a drop in aqueductal pulsatility. Upon investigation of capillary blood flow pulsatility as a possible source of aqueductal pulsatility, we found that capillary pulsatility in our CH rat model depended on the anesthetic paradigm and was increased by 21% in CH under isoflurane anesthesia, but not under ketamine-xylazine. Finally, aqueductal pulsatility was not correlated to behavioral deficits in motor coordination, even though motor coordination (but not cognitive ability) is impaired in CH rats.

Conclusions

Our results show that aqueductal pulsatility is elevated in our rat model of CH, and is correlated to ventricular size. However, the relationship varies over time and may be related to changes in intracranial compliance. Decreased aqueductal pulsatility caused by increased compliance support the hypothesis that aqueductal pulsatility is influenced by intracranial compliance. Elevated capillary pulsatility supports the pulsation redistribution theory of hydrocephalus, suggesting that increased microvascular pulsations are an important component of the mechanism of CH. Using our model of communicating hydrocephalus, we have been able to demonstrate that there are clear changes in pulsatile dynamics in the hydrocephalic brain, both macroscopically as measured in the cerebral aqueduct and microscopically within the cerebral microvasculature. While our results have not established a clear link between these marked changes in pulsatility and clinical outcome, our work has laid the groundwork for future studies in experimental hydrocephalus and for future clinical trials looking into alternate mechanisms of communicating hydrocephalus.

Dedication

This dissertation is dedicated to the people who have helped me get where I am today: my Parents, my Grandparents, Boro Fuppi and Fuppa, my Wife Dhara, and all my Teachers.

Table of Contents

List of Figures

List of Tables

List of abbreviations

CH: communicating hydrocephalus

SV: stroke volume (defined in §4)

VV: ventricular volume (defined §4)

PI: capillary pulsatility index (defined §6)

RBC: red blood cell

ICP: intracranial pressure (defined in §5)

CSF: cerebrospinal fluid

MRI: magnetic resonance imaging

PC: phase contrast

ECG: electrocardiogram

BPM: beats per minute

PFA: paraformaldehyde

SBU: Stony Brook University

AECOM: Albert Einstein College of Medicine

Acknowledgements

This dissertation is result of the combined effort of a great many people, and I would like to acknowledge some of the key players.

First and foremost, I would like to thank my advisor, Dr. Mark Wagshul, who has been one of the greatest teachers in my life, and has helped me gain a true appreciation for scientific research. Mark has always had time for me and has always been there to help me and answer my every question. Mark taught me the value of scientific integrity, and I am certain that I will continue to find his lessons and examples invaluable throughout my professional career. I would also like to thank Dr. James (Pat) McAllister, who was a member of my dissertation committee and who, over the last few years, has acted as my co-advisor and has always been available to me as a source of advice and encouragement, especially at the times when I was faced with difficulty. I simply cannot thank Pat enough for flying all the way out to New York for the sole purpose of being there at my defense. I just do not have the words to express the gratitude and appreciation that I feel for Mark and Pat. I would also like to express my sincerest gratitude to Dr. McAllister and Dr. Jie Li for teaching me the specialized surgical techniques that we used throughout the dissertation, particularly the basal cistern induction technique, craniectomies, cranial window and cardiac perfusion, as well as many helpful tips in animal surgery and handling. I would like to thank Dr. Li also for induction of all the CH in rats in the studies of chapter 4 and the first part of chapter 6. I would also like to thank my dissertation committee members Dr. Helene Benveniste and Dr. Mary Frame, whose advice and guidance were key factors in the completion of this dissertation. Dr. Benveniste has helped us design many of the studies in this dissertation from their inception, and her advice and suggestions are evident in various places throughout this dissertation. I would also like to sincerely thank the Brain Child Foundation, STARS-kids and the Batterman Family Foundation for their financial support in the experiments in this dissertation. I would particularly like to thank Mr. Curt Stewart from the Brain Child Foundation for his support and encouragement in our studies throughout my tenure as a graduate student.

I would like to sincerely thank Dr. Craig Branch of Gruss MRRC, Albert Einstein College of Medicine, who graciously allowed to complete the last two years of my doctoral studies at the Gruss

MRRC Lab and gave me permitted me to use the resources of Gruss MRRC. I would also like to thank all the other members of Gruss MRRC for their constant support and encouragement during my time at Gruss MRRC. I would also like to thank Dr. Emilia Entcheva, Dept. of Biomedical Engineering, and the members of her lab, for helping us get started with dye preparation and for allowing us to use their lab facilities at the early stages of our experiments.

I would like to thank the following people, who have helped me throughout these studies in various capacities: Maura Chodkowski, Bridget O'Connor, Mei Yu, Dr. S. David Smith, Jean Rooney, Nicole Steinhauff, Dr. Thomas Zimmerman, Dr. Irene Solomon, Dr. Kelly Warren, Dr. Aija Birzgalis, Dr. G. Zhang, Dr. J. Chen, Dr. Guo-Wei Tian, Jeffery Wyckoff, David Entenberg, Dr. Yiting Yu, Dr. Mimi Kim, Dr. Daniel Theele, Ms. Maritza Arce, Ms. Diana Tirrado and Ms. Bianca Morales. I would like to thank Jeryes (Jerry) Freih and David Chan, who worked as undergraduate/post-graduate students in our lab at Stony Brook and directly contributed to the studies in Chapter 6. I would also like to sincerely thank all my former lab colleagues: Dr. Hui Jing Yu, Dr. Mayuresh Korgaonkar, Dr. Laura Fanea, Dr. Erin McCormack-Kelly and Dr. Sachin Jambawalikar, for their constant support, encouragement and suggestions. I would also like to thank my friends, Hui Jing Yu, Muhammad Adeel Parvaz, Jawaad Sheriff and Jeremy Kim, who have helped me in more ways than I can count throughout my time as a graduate student at Stony Brook.

I would like to thank my family: my parents, my uncles and aunts (Boro Fuppi & Fuppa, Choto Fuppi & Fuppa), who have always supported me, and helped me in every way possible, and encouraged me to keep going ahead and not falter. I would like to thank Boro Fuppa for being the role model that I can always aspire to. And finally, I would like to thank my wife, Dhara, whose amazing love, support, patience, and constant and unwavering help and confidence has truly made the greatest difference in my life. Without having her at my side, this dissertation may never have been completed. I would like to thank all of my teachers from childhood, school, high school, college and grad school. The things they taught me have shaped me into the person I am, and they are therefore responsible for the production of this dissertation.

Publications

The following are a selection of peer-reviewed publications and conference abstracts that were produced as a result of the work in this dissertation:

- S. Rashid, J. P. McAllister, Y. Yu, M. E. Wagshul, “Neocortical Capillary Pulsatility is not elevated in experimental communicating hydrocephalus”, *J Cereb Blood Flow Metab,* 2011 (epub).

- G. Nagra, M. E. Wagshul, S. Rashid, J. Li, J. P. McAllister, M. Johnston, “Elevated CSF outflow resistance associated with impaired lymphatic CSF absorption in a rat model of kaolin-induced communicating hydrocephalus,” *CSF Research* 2010, 7:4.

- M.E. Wagshul, J.P. McAllister, S. Rashid, J. Li, M.R. Egnor, M.L. Walker, M. Yu, S.D. Smith, G. Zhang, J.J. Chen, and H. Benveniste, “Ventricular dilation and elevated aqueductal pulsations in a new experimental model of communicating hydrocephalus,” *Exp Neurol* 2009, 218:1.

- S. Rashid, J. P. McAllister II, M. Schuhmann, M. E. Wagshul, "Reduction in CSF Pulsatility with Altered Intracranial Compliance by Craniectomy in Communicating Hydrocephalus”, *19th Annual Meeting of the ISMRM*, 2011, Montreal, QC, Canada.

- M. E. Wagshul, S. Rashid, J. P. McAllister II, “Prediction of Behavioral Deficits using Diffusion Tensor Imaging in Experimental Hydrocephalus”, *19th Annual Meeting of the ISMRM*, 2011, Montreal, QC, Canada.

- S. Rashid, J. Li, J. P. McAllister, G.-W. Tian, M. E. Wagshul, “Microvascular pulsatility in the hydrocephalic rat neocortex by two-photon microscopy”, *39th Annual Conference of the Society of Neuroscience,* 2009, Chicago, IL

- S. Rashid, J. Li, J. P. McAllister, M. Walker, M. E. Wagshul, “Two-Photon Microscopy of Neocortical Microvascular Pulsatility in Communicating Hydrocephalus”, *Annual Meeting of the International Society of Hydrocephalus and CSF Disorders*, 2009, Baltimore, MD

- S. Rashid, H. Benveniste, M. R. Egnor, J. Li, J. P. McAllister, M. Yu, and M. E. Wagshul, “Temporal Course of Hyperdynamic Pulsatility and Ventricular Dilation in a New Rat Model of Communicating Hydrocephalus”, *16th Annual Meeting of the ISMRM*, 2008, Toronto, ON, Canada.

Chapter 1

---

1. Introduction

Hydrocephalus is a severely debilitating disease that afflicts over 1 in 500 people in the US alone. It is often accompanied by headache, nausea, seizures, gait disturbances, incontinence, dementia and personality changes [1]. In infants, it can cause rapidly increasing head size and can lead to loss of developmental progress [2]. Its most common feature is dilation of the cerebral ventricles, the CSF filled spaces in the brain. There is, as yet, no cure for hydrocephalus, and the only treatment options for it are palliative and require neurosurgery. The treatments frequently require surgical revisions and are known to fail often [1, 3-5]. If left untreated, hydrocephalus can lead to coma and eventually death.

The etiology of communicating hydrocephalus (CH), one of the major types of hydrocephalus, is poorly understood. CH has traditionally been explained in terms of the "bulk flow theory" of CSF circulation. However, this view has been unable to account for several observations, such as dilation of the cerebral ventricles instead of subarachnoid spaces (SASs) and absence of a transmantle pressure gradient [6-8]. Recently, based on growing evidence that the pulsatile flow of CSF may play an important role in

intracranial dynamics and the pathophysiology of CH, a pulsatility theory of CH has been proposed as a possible mechanism for the development of CH. This theory suggests that CH is a consequence of redistribution of arterial-driven pulsations in the cranium, which gives rise to elevated CSF pulsatility in the cerebral aqueduct as seen in CH patients. This theory accounts for many old and new unexplained observations regarding CH [6, 8], but it has not been experimentally verified.

The primary purpose of this dissertation was to investigate this pulsatility theory by quantifying two components of intracranial pulsatility: aqueductal CSF pulsatility and cerebral microvascular pulsatility. A careful study of intracranial pulsatility changes can be effectively carried out in an animal model. Animal models of communicating hydrocephalus had been lacking until the recent development of a rat model of CH, which closely mimics the clinical presentation of CH [9]. This animal model will be used to explore the pulsatility redistribution theory of CH.

In this dissertation, our goal was to investigate the significance of elevated aqueductal pulsatility in CH. We hypothesized that pulsatile CSF flow is a significant non-invasive marker of clinical outcome in CH

The main objective of this dissertation was to investigate the significance of elevated aqueductal pulsatility in CH. Our central hypothesis is that pulsatile CSF flow is a significant non-invasive marker of clinical outcome in CH. The following four specific aims will be explored:

- **Characterization of aqueductal CSF pulsatility flow and ventricular dilation in the CH rat.**

  Hypotheses:

- Pulsatile CSF flow in the aqueduct of normal and CH rats can be measured using phase contrast MRI.
- Aqueductal CSF pulsatility will be elevated in CH rats and will be as high as a factor of 10 above normal.
- Aqueductal CSF pulsatility will not be significantly correlated to the ventricular volume of CH rats.

Rationale:

Aqueductal CSF pulsatility is routinely measured in clinical MRI, but it has not been quantified in the rat. Thus, it is necessary to first develop the techniques for measuring and calculating aqueductal pulsatility in a rat using MRI. Aqueductal pulsatility can be as high as a factor of about 10 compared to normal, in CH patients, so it is hypothesized that aqueductal pulsatility in the CH rat will also be 10 times higher than normal. Several studies have shown that ventricular volume in CH is a poor prognostic marker for disease severity and for guiding shunt surgery, but the CSF pulsatility may potentially be of value in both. Thus, it is hypothesized that there will be no functional relationship between aqueductal pulsatility and ventricular size.

- **Characterization of aqueductal pulsatility alterations under compliance modulation by craniectomy and shunting**

Hypotheses:

- Increase in intracranial compliance will cause a decrease in aqueductal CSF pulsatility

- Intracranial compliance can be modulated by craniectomy and shunting, both of which will produce an increase in compliance

Rationale:

Intracranial compliance is a parameter that is known to have a significant effect on intracranial pressure pulsations, but the effect of compliance on aqueductal pulsatility has not been studied. By quantifying changes in aqueductal pulsatility, produced by surgically altering compliance, it will be possible to study the effects of compliance on aqueductal pulsatility. Intracranial compliance can be altered by surgical procedures such as craniectomy and CSF diversion by shunting; these are the techniques that will be used.

- **Characterization of neocortical capillary pulsatility in CH rats**

Hypotheses:

- Blood flow and pulsatility in capillaries can be measured in the rat neocortex down to a depth of 600 μm using two photon microscopy.
- Pulsatility of neocortical capillaries will be elevated in CH rats immediately following kaolin induction and will persist into the long-term stages of the disease
- Elevated capillary pulsatility will be correlated with aqueductal CSF pulsatility in CH rats.

Rationale:

The pulsatility redistribution theory suggests that elevated aqueductal pulsatility in CH is a result of redistribution of systolic arterial-driven pulsations in the cranium. A consequence of this redistribution is elevated microvascular pulsatility in the capillary beds of the brain, which may produce elevated aqueductal pulsatility. This view can be explored by measuring capillary pulsations in the cortex of CH rats. Capillary pulsatility has not been studied deep in the rat brain, and it is hypothesized that pulsatility as deep as 600 μm in the brain can be measured with two-photon microscopy. Because elevated pulsatility results in elevated aqueductal pulsatility, it was hypothesized that capillary pulsatility will be correlated to aqueductal pulsatility in the CH animal model.

- **Characterization of behavioral deficits in CH rats.**

Hypotheses:

- CH rats will exhibit behavioral deficits in memory, cognitive ability and motor coordination, compared to normal rats.
- Behavioral deficit in CH rats will be correlated with aqueductal CSF pulsatility.

Rationale:

Severity in clinical CH is best gauged by behavioral deficits, as they provide a measure of functional impairment. Since aqueductal pulsatility may be a prognostic marker for CH treatment, it may also be measure of severity. This can be determined by characterizing cognitive and motor impairments in the CH rat model, and correlating these parameters with aqueductal pulsatility.

Chapter 2

---

2. Background

2.1 Anatomy and Physiology of CSF and CSF Spaces

Communicating hydrocephalus is a disorder of cerebrospinal fluid circulation, and is closely tied to the anatomy and physiology of the cerebrospinal fluid spaces. A brief review of the CSF spaces, CSF formation, absorption and physiology is presented below, to introduce the context in which communicating hydrocephalus is discussed in this dissertation.

2.1.1 Cerebral Ventricles

The cerebral ventricles are sac-like cavities present within all mammalian brains and contain the clear, water-like fluid known as cerebrospinal fluid (CSF). In most mammals, the ventricles can be categorized as the left and right lateral ventricles (LV), the third ventricle and the fourth ventricle. Images of the ventricles in the human brain are depicted in Fig. 2.1. The lateral ventricles are connected to the third ventricle via the

left and right foramina of Monroe. The third ventricle connects to the fourth ventricle by a long narrow channel called the aqueduct of sylvius or cerebral aqueduct. The fourth ventricle narrows at its caudal end and eventually forms the central canal of the spinal cord. The ventricles and the aqueduct are collectively referred to as the “ventricular system”.

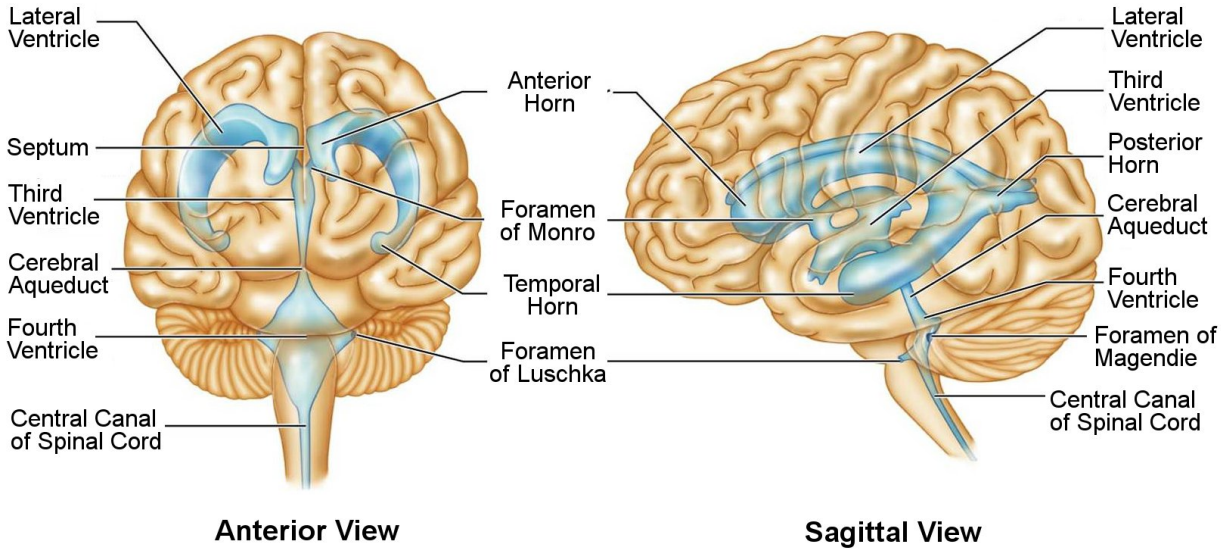

Figure 2.1: The cerebral ventricles in the human brain.
The ventricles are the spaces inside the brain that contain CSF. There are 4 ventricles, as shown here: the 2 lateral ventricles, which are the largest, the donut-shaped third ventricle, which lie inferior to the lateral ventricles and is connected to the lateral ventricles via the inter-ventricular foramen or foramen of Monro, and the fourth ventricle, which lies anterior to the cerebellum and is connected to the third ventricle via the cerebral aqueduct. Modified from [10].

2.1.2 Subarachnoid Spaces and Cisterns

The subarachnoid spaces (SAS) lie within the meninges, which are contiguous layers of tissue which surround and cover the brain and spinal cord (Fig. 2.2). The innermost meningeal layer is the pia mater, a thin layer of connective tissue lying very close to the brain surface, and separated from the brain by a basement membrane and

a layer of astrocytes (glia limitans). The middle layer is the arachnoid mater, a thin transparent membrane of fibrous tissue, which gets its name from its spider-like appearance. The outermost layer of the meninges is the dura mater, a thick and inelastic membrane of dense fibrous tissue that serves as a protective layer around the brain and spinal cord. The arachnoid membrane is attached to the dura, and the SAS is the region lying between the arachnoid and the pia (Fig. 2.2). Since the arachnoid does not follow the foldings of the brain, the SAS widens at the brain sulci.

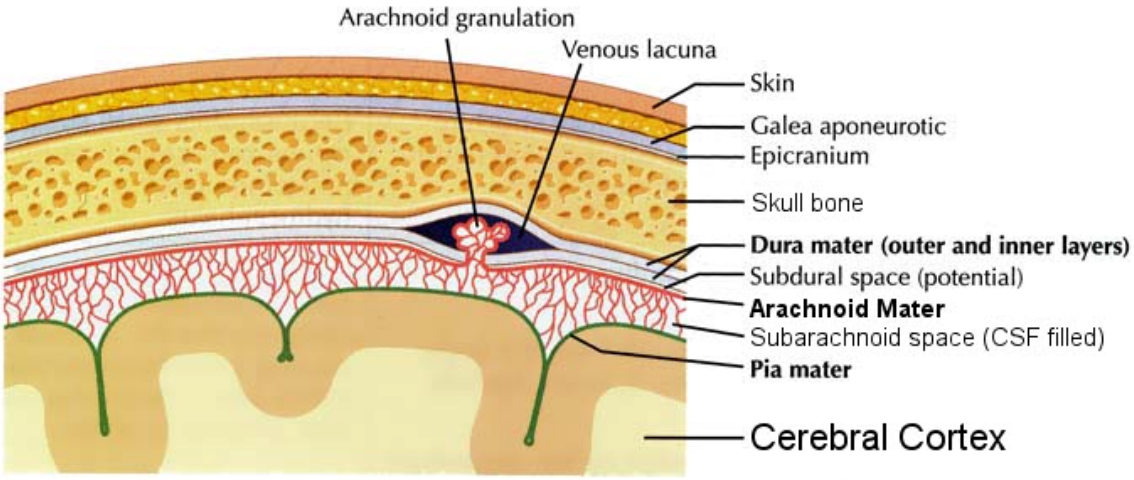

Figure 2.2: The meningeal layers surrounding the brain.
The outermost membrane is the dura mater, a thick, tough layer of fibrous tissue that protects the brain and spinal cord from physical injury. The middle layer is the arachnoid mater, which gets its name from its spidery appearance. The innermost layer is the pia mater, which lies next to the brain surface. The space between the arachnoid and pia is the subarachnoid space, which contains CSF. Arachnoid granulations, which are thought to be involved in CSF reabsorption, are projections of the arachnoid membrane into dural sinuses or venous lacunae, as shown here. Modified from [11]

CSF can flow out from the ventricular system into the SAS through the foramen of Magendie (medial aperture) and the left and right foramina of Luschka (lateral apertures). All three apertures lie near the distal end of the fourth ventricle. The foramen

of Magendie opens into the cisterna magna, which lies between the ventral side of the cerebellum and the brainstem (Fig. 2.3). The foramina of Luschka open into the subarachnoid space surrounding the brainstem, adjacent to the cisterna magna.

The SAS contains vasculature and is filled with CSF. It contiguously surrounds the cerebrum, cerebellum, brainstem and extends down into the spinal canal, surrounding the spinal cord. Because it surrounds the entire brain on all sides, it causes the brain to “float” in CSF, effectively reducing the weight of the brain [8] and acting as a cushion against shocks. At certain places, the subarachnoid space widens to form CSF-filled recesses or cisterns. Some of these cisterns are the cisterna magna (cerebellomedullary cistern), described above, the prepontine cistern, lying along the ventral surface of the pons, and the interpenduncular cistern, ventral to the midbrain. The prepontine and interpenduncular cisterns are collectively known as the basal cisterns.

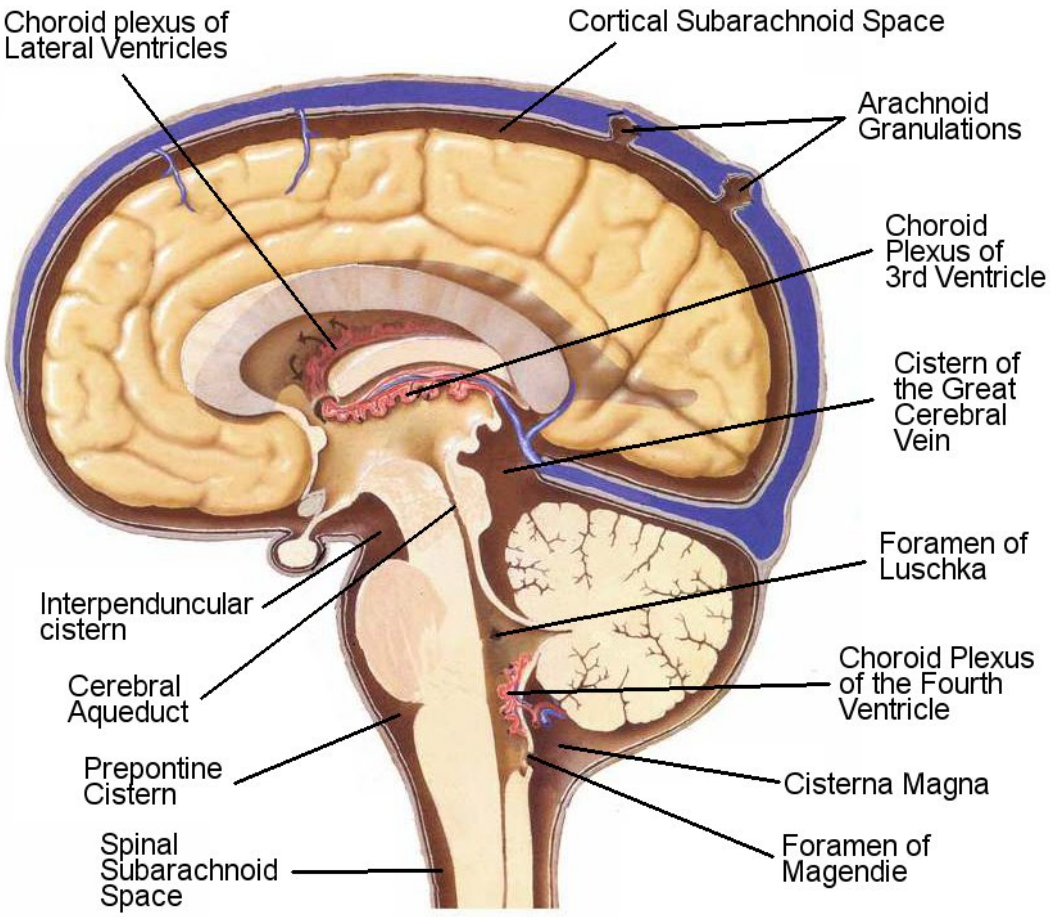

Figure 2.3: The subarachnoid spaces and cisterns in the human cranium. The subarachnoid space is the layer surrounding the brain and spinal cord that contains CSF. At the base of the skull, the subarachnoid space widens to form cisterns. The cerebellomedullary cistern or cisterna magna lies inferior to the cerebellum and posterior to the brainstem; the prepontine cistern and interpenduncular cistern lie anterior to the brainstem and are collectively called the basal cisterns. Modified from [11]

2.1.3 Ependyma, Choroid Plexus and Arachnoid Villi and Granulations

The surface of the entire ventricular system is covered by an epithelial layer known as the ependyma, which consists of special glial cells that form gap junctions with each other. These gap junctions are not tight, and permit water, ions and macromolecules to easily diffuse through, allowing intermixing of CSF with brain

parenchymal interstitial fluid. For this reason, CSF and brain interstitial fluid have similar chemical compositions [12].

At certain regions of the ventricular system, the ependyma becomes fenestrated with invaginations of the pia mater, which give rise to densely packed capillaries covered by ependymal cells, forming the choroid plexus. The inner layers of most of the lateral, third and fourth ventricles are covered by choroid plexus. The choroid plexus is thought to be the major site of CSF production.

Arachnoid villi and arachnoid granulations are CSF-filled projections of the arachnoid mater that protrude into the venous sinuses in the dura at the convexity of the brain (Fig. 2.2, 2.3). The villi are microscopic while the granulations are visible by eye. Arachnoid projections also exist in the spine. CSF has traditionally been thought to be reabsorbed back into blood through the arachnoid projections.

2.1.4 CSF Physiology, Formation and Absorption

Cerebrospinal fluid (CSF) is a clear, water-like fluid present within specific spaces/ventricles and subarachnoid spaces in all mammalian brains. CSF is present within the cerebral ventricles, the cranial and spinal subarachnoid spaces, the spinal thecal sac and the central canal of the spinal cord. CSF has several important physical and physiological functions in the brain. A major mechanical function of CSF is to act as a cushion to protect the brain from the inner surface of the skull during head motion and minor trauma. CSF increases the buoyancy of the brain and prevents lower surfaces of the brain from coming in contact with the skull [13]. In addition, CSF circulation provides peptides and micro-nutrients to neural networks and removes waste produced by brain

metabolism [14], and is also involved in transport of proteins and hormones [15]. It has been hypothesized that severe disruptions in CSF circulation contributes to dementia in the elderly [14, 16].

The total volume of CSF within the human cranium is approximately 165 ml, while average volume of the cerebral ventricles range from 15 to 32 ml [17-19]. Tanna et al. reported that the total intracranial CSF volume in an MRI study of a group of 15 healthy elderly subjects varied from 62.2 to 267.0 ml, and the ventricular volume range was from 7.49 to 70.5 ml [18]. CSF formation rate in the human brain varies from 0.3-0.6 ml/min, depending on the measurement technique [14, 17, 20, 21]. CSF formation rate has a circadian variation and is higher at night than during the day [22]. The volume of CSF produced in adult humans is 500-600 ml per day [14].

CSF is produced predominantly at the choroid plexi of the lateral, third and fourth ventricles. CSF was once thought to be produced by ultrafiltration of blood at the choroid plexi, but later studies showed that CSF formation is an active process and mediated by a number of ion transporters and aquaporin channels at the choroidal membranes [14]. CSF is also formed at the ependyma by secretion or diffusion of extracellular fluid from brain parenchyma into ventricles [23, 24], through gap junctions in the ependyma [12, 14]; some investigators consider the secretion at the ependyma to account as much as 50% or more of CSF formation [17], although most authorities agree that the choroid plexi produces 70-80% of CSF [25].

CSF has traditionally been thought to be absorbed back into the blood supply at the arachnoid granulations and villi in the cranial and spinal dura [26]. The exact mechanism of CSF transfer is unclear, and thought to be by pinocytosis, phagocytosis,

through vacuoles or channels or through gaps between cells [27]. However, there are a number of observations that raise questions as to whether the arachnoid projections are the *only* site of CSF absorption. For instance, arachnoid granulations are not present in humans before birth, although presence of choroid plexus and CSF formation in fetal stages has been demonstrated [28]. Thus, CSF absorption must take place at an alternate site at these stages. In animals, it has been shown that a major portion of CSF is absorbed into the lymphatic system from the subarachnoid spaces adjacent to the olfactory nerves, which pass out of the cranial vault into the nasal submucosa through the cribriform plate [27, 29]. CSF is absorbed into cervical lymphatics from the olfactory nerves. This effect has been demonstrated experimentally in rats [30-32] and sheep [33, 34], and post-mortem morphological studies suggest that this absorption pathway may also exist in humans and primates [35, 36]. In rats, CSF absorption into lymphatics via spinal nerves has also been demonstrated [37].

2.1.5 Summary

The preceding descriptions of the ventricles, subarachnoid spaces and CSF are important to understand the context of CH in the following studies and discussions. Communicating hydrocephalus is characterized by enlarged ventricles and elevated pulsatile flow of CSF, as will be discussed below. The basal cisterns are important in the context of the animal model of CH used in these studies. As will be seen, a clear understanding of the anatomy and physiology are essential to gain insight into various aspects of the complex disorder of communicating hydrocephalus.

2.2 Background on hydrocephalus

2.2.1 Definition and types

Hydrocephalus is a poorly understood, severe neurological disorder characterized by excessive accumulation of CSF in the brain ventricles. It can be congenital or acquired at birth or later in life. It is one of the most common birth defects and is present at birth in 1 in 500 children [38]. Due to a lack of national registries or databases, the exact number of adult patients is unknown, but about 75,000 patients diagnosed with hydrocephalus are released from US hospitals each year [39]. It is estimated that there are a total of 38,200-39,900 hospital admissions involving pediatric hydrocephalus [40]. Hydrocephalus can be fatal if left untreated.

There are two major types of hydrocephalus: obstructive and communicating. Obstructive hydrocephalus is characterized by a blockage to CSF flow somewhere within the ventricular system. It can be caused by many factors, such as aqueductal stenosis, head trauma, intraventricular hemorrhage and tumors. Communicating hydrocephalus, the object of the proposed study, is not characterized by any obstruction within the ventricular system. Obstructions may be present within the subarachnoid spaces, but sometimes remain unidentified. Communicating hydrocephalus can occur secondary to subarachnoid hemorrhage, meningitis, spina bifida and syringomyelia. A subtype of communicating hydrocephalus is normal pressure hydrocephalus (NPH). This is usually found in elderly patients. It is characterized by ventricular dilation, but intracranial pressure is either normal or only slightly elevated, in contrast to other instances of communicating hydrocephalus where intracranial pressure is significantly elevated. NPH is usually classified as idiopathic, and its most common symptoms are

urinary incontinence, gait apraxia and dementia. Because of the gait and dementia components, the diagnosis of NPH can sometimes be confused with Alzheimer's or Parkinson's diseases [41-44].

2.2.2 Symptoms

The most common characteristic of hydrocephalus is dilation or widening of the CSF filled cerebral ventricles. In infants, this can cause a bulging "soft spot" or rapid enlargement of the head. In adults, dilated ventricles are detected by a radiological exam (MRI, CT or ultrasound) or other tests, such as a lumbar tap, which reveal elevated intracranial pressure, another frequent feature of hydrocephalus. The symptoms of hydrocephalus can vary, but commonly include headache, vomiting, nausea, seizures, walking and gait disturbances, urinary incontinence, blurred or double vision, sunsetting of the eyes, as well as forms of dementia including memory loss and changes in personality [2, 38].

2.2.3 Treatment: Shunting

There is, as yet, no cure for hydrocephalus, and the only treatment options for it are palliative and involve invasive neurosurgery. The most frequently used treatment for obstructive and communicating hydrocephalus (including NPH) is shunting, whereby the excess CSF is drained out of the ventricles into another part of the body. A shunt consists of two catheters and a mechanical valve, as shown in Fig. 2.4. The valve controls the drainage flow of CSF from the ventricles. Control of drainage is important,

because overdrainage can lead to collapse of the lateral ventricles, giving rise to a complication known as slit-ventricle syndrome [1]. The proximal end of the shunt is inserted into one lateral ventricle through a small craniectomy and the distal end is inserted into the peritoneum (in some cases, it may be placed elsewhere in the body, as described below). The catheters are tunneled under the skin and connected to each other via the valve. A shunt which drains CSF into the peritoneum is known as a ventriculoperitoneal shunt. In some cases, the distal end of the shunt is placed in the atrium (ventriculoatrial shunt).

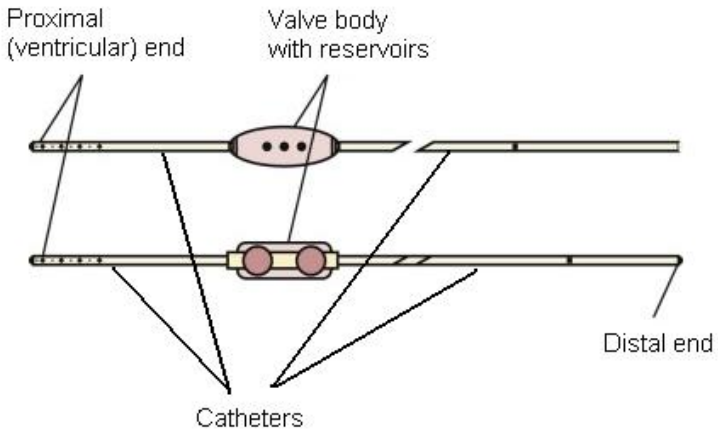

Figure 2.4: Schematics of typical shunts.
The shunt consists of a proximal and a distal catheter and a valve in between. The valve generally controls the drainage of CSF and often contains a reservoir for CSF. The proximal catheter is placed in the lateral ventricle and the distal end is usually placed in the peritoneum. The entire shunt is tunneled under the skin, with the valve generally placed at the back of the head under the scalp. Modified from [1].

Shunt malfunction is a frequent problem, and shunts can often become obstructed or infected. Within one year after shunting, up to 40% of shunts are known to fail [3] and 10% become infected [4]. Two-thirds of new shunts fail within two years [3, 5]. The shunt has to be used throughout the patient's life, and therefore upon failure, it

needs surgical revision. Nevertheless, shunting is often successful as a treatment, and many patients are able to lead mostly normal lives after shunting.

Shunt surgeries for hydrocephalus, including initial shunt placement, revisions and removal, constitute one of the most common neurosurgical procedures in adults, and the most frequent neurosurgical procedure in children. Shunt surgery represents a significant medical problem, and the total cost for shunt-related procedures have been estimated at $1.1 billion per year in the US, as of the year 2000 [45]. Similar costs per population were also found in a study focusing on patients in Canada [46]. A more recent study estimated that pediatric hydrocephalus-related hospital charges totals to $1.4-2 billion per year in the US, using data from the years 1997, 2000 and 2003 [40].

2.3 Conventional bulk flow theory of CH.

Since communicating hydrocephalus is primarily a CSF flow disorder, a discussion of CSF circulation is necessary. Traditionally, CSF circulation has been explained in terms of the “bulk flow theory” [47]. According to this view, CSF is produced primarily at the choroid plexus (CP) in the cerebral ventricles, flows unidirectionally and is absorbed into dural venous sinuses through arachnoid villi and granulations in the dorsal subarachnoid spaces (SAS). CSF thus flows out of the ventricles through the foramina of Luschka and Magendie in the fourth ventricle, circulates in the cranial and spinal SAS, moving with a unidirectional “bulk” flow, before finally being absorbed into the blood at the arachnoid villi and granulations. This unidirectional flow has been assumed to be driven by a transmantle pressure difference in CSF between its site of

formation and its site of absorption, and this pressure gradient has also been thought to be responsible for the intracranial pressure [6, 8].

These views were initially suggested by the work of Faivre, who hypothesized that CSF may be produced in the CP [48], and Key and Retzius, who proposed that CSF may be absorbed at the arachnoid granulations [49]. Evidence of this view was presented by Dandy, who showed that blocking the cerebral aqueduct in dogs caused CSF to build up in the lateral and third ventricles, forcing them to dilate [50]. This indicated that the choroid plexus in the lateral and third ventricles is a source of CSF. In addition, experiments by Welch and Friedman indicated that arachnoid granulations may act as mechanical valves for CSF, which supported the view that they are responsible for CSF resorption into the venous sinuses [51].

The nature of the flow of CSF was also under considerable debate, with some groups maintaining that CSF flow was simply a passive diffusion process, while others supported the view of an active circulation, until finally Di Chiro proved the latter view [52]. Using radionuclide cisternography, Di Chiro showed that the spread of radionuclide tracer in CSF was too rapid and hence must involve some form of active circulation as opposed to mere diffusion. This was interpreted to imply the existence of a bulk CSF flow. In addition, Di Chiro observed a maximum concentration buildup of isotope near arachnoid granulations in the convexity, which was interpreted as evidence that CSF is indeed reabsorbed through the arachnoid granulations. These findings appeared to bring an end to all the controversies that had surrounded the theories of the formation and absorption of CSF [7].

In light of these views, communicating hydrocephalus has traditionally been explained as the consequence of an imbalance between the formation and absorption of CSF [6-8]. Obstruction to CSF flow in the subarachnoid spaces (SASs) leads to reduced absorption of CSF across the arachnoid granulations, giving rise to a buildup of CSF and an increase in intracranial pressure, which causes dilation of the ventricles, the most characteristic feature of CH [6]. Meningitis and subarachnoid hemorrhage have been implicated as frequent causes of subarachnoid CSF blockage and giving rise to CH [53-55].

2.4 Observations inconsistent with the bulk flow theory

As stated earlier, the unidirectional bulk flow of CSF inherently assumes the existence of a transmantle pressure gradient between the ventricles and the SASs that causes CSF to flow from the source at the CP to the sink at the arachnoid granulations [6, 8]. This assumed pressure gradient is the first challenge to the bulk flow theory when applied to CH: CSF malabsorption at the arachnoid granulations should cause the assumed transmantle pressure gradient to increase, and this should cause the SAS to dilate, not the ventricles. SAS dilation is in fact observed in a different disease state known as external hydrocephalus, which incidentally is also thought to be caused by reduced CSF absorption at the arachnoid granulations [56]. Why the ventricles dilate as opposed to the SAS is one of the questions raised in a recent position paper that identified different areas of communicating hydrocephalus that requires further study [57].

This dilemma of CH, i.e. ventricles dilate at the expense of the SAS, had first been pointed out by Dandy [50] (even though his research had been used to support the bulk flow theory) and has been emphasized by other investigators [6-8]. Scientists also maintain that the subarachnoid spaces always remain narrow in CH [6, 8, 50, 58, 59]. Experiments that have attempted to quantify the transmantle pressure gradient using invasive pressure monitoring have yielded contradictory results. Conner et al. showed an elevated transmantle pressure gradient of 3.4 ± 3.9 cm saline in a cat CH model [60], but other investigators have been unable to show a significantly increased transmantle pressure gradient in animal models of CH as well as clinical hydrocephalus [61-63]

In addition, numerous studies have shown that CSF reabsorption takes place not only at the arachnoid granulations, but also via nasal and spinal lymphatics [27, 29-34, 64, 65]. While these pathways have been characterized mainly in sheep and rats [31, 65], post-mortem studies indicate that these pathways also exist in humans and primates [35, 36]. The existence of these alternate pathways are emphasized by the observation that arachnoid granulations and villi do not develop until birth, and do not exist in the fetal stage even when CSF formation is evident [28]; this indicates the existence of alternate pathways. Moreover, the mechanical valve action of the arachnoid granulations (as described by Welch and Friedman [51]) has not been anatomically demonstrated, and no quantitative data has been provided to support this form of CSF reabsorption [8]. This has prompted a few investigators to suggest outright that no CSF reabsorption takes place at the arachnoid granulations [8]. Greitz argues that 80-90% of isotope in radionuclide cisternography studies is absorbed in the spinal

canal, and maintains that CSF is absorbed by the cerebral capillaries, and that this process occurs throughout the brain; he uses this view to argue against the traditional bulk flow model of CH, and suggests that CSF circulation is driven primarily by pulsatile flow. It should be noted that recent in-vitro and ex-vivo studies utilizing human arachnoid tissue have demonstrated unidirectional flow of CSF across arachnoid granulations under normal intracranial pressure levels, with decreased hydraulic conductivity when the direction of flow is reversed [66-68]. These models were hypothesized to resemble the in-vivo CSF outflow across the arachnoid membrane in humans.

These observations raise questions regarding the traditional view of the etiology of communicating hydrocephalus: why would malabsorption of CSF at the arachnoid granulations give rise to CH? If absorption at the arachnoid granulations is compromised, it is likely that the lymphatic absorption sites should be able to compensate [32]. Then how do conditions such as meningeal infection or subarachnoid hemorrhage, which are thought to disrupt absorption at the arachnoid projections, give rise to CH? It is evident that the bulk flow view of communicating hydrocephalus is an inadequate description of a highly complex disorder.

2.5 CSF Pressure Pulsatility in CH

CSF flow in the ventricles has been known to have a pulsatile component for many years, ever since Magendie first described that CSF moves by “ebb and flow” [69, 70]. The driving force behind these pulsations was disputed, until O’Connell noted that the pulsations were synchronous with the heart rate and could be altered by changes in

venous pressure in 1943 [71]. He also hypothesized that elevated CSF pulse pressure (pressure amplitude) in the ventricles may give rise to CH, even if the mean pressure remains unchanged. Based on spinal blockage studies, Antoni has suggested in 1946 that the CSF pulse wave originates from the large arteries at the base of the brain, since CSF pulsations in the lumbar SAS were shown to disappear below a spinal block [72].

These theories were partially verified by Bering, who in 1962 postulated that CSF pulsatility originated from cardiac-induced arterial pulsations in the choroid plexus [73, 74]. Bering's postulates thus differed from O'Connell's hypothesis that CSF pulsatility originated from the arteries in the basal cisterns, and from the systolic expansion of the brain itself. Bering also suspected that arterial pulsations in the choroid plexus (CP) of the lateral ventricles may play a role in hydrocephalus. He conducted experiments in dogs where he removed the CP from one lateral ventricle (plexectomy), while leaving the CP in the other lateral ventricle intact, taking care to ensure the foramina of Monro were open [74]. He then induced CH by kaolin injection into the cisterna magna, and found that dilation took place only in the ventricle with the intact choroid plexus (Fig. 2.5). He thus showed that ventricular dilation was not due to increased intraventricular pressure due to accumulated CSF, since the lateral ventricles were communicating and would experience the same fluid pressure. Bering also showed that the CSF pulse pressure in the normal (dilated) ventricle was elevated compared to the pulse pressure in the plexectomized ventricle (Fig. 2.6). Therefore, Bering concluded that ventricular dilation was due to choroid plexus pulsations [74].

There was considerable skepticism to Bering's findings in the scientific community. For instance, Dunbar et al. showed that CSF pulse wave in the ventricles,

cisterna magna and lumbar SAS were almost identical, and that the lumbar CSF pulse wave persists even after a complete cervical block, which prevents communication of cranial and spinal CSF [75]. They use this data to critique Bering's theory that the pulse wave originates in the choroid plexus of the ventricles, and conclude that "arteries supplying the spinal cord make a major contribution to the formation of the CSF pulse wave" [75].

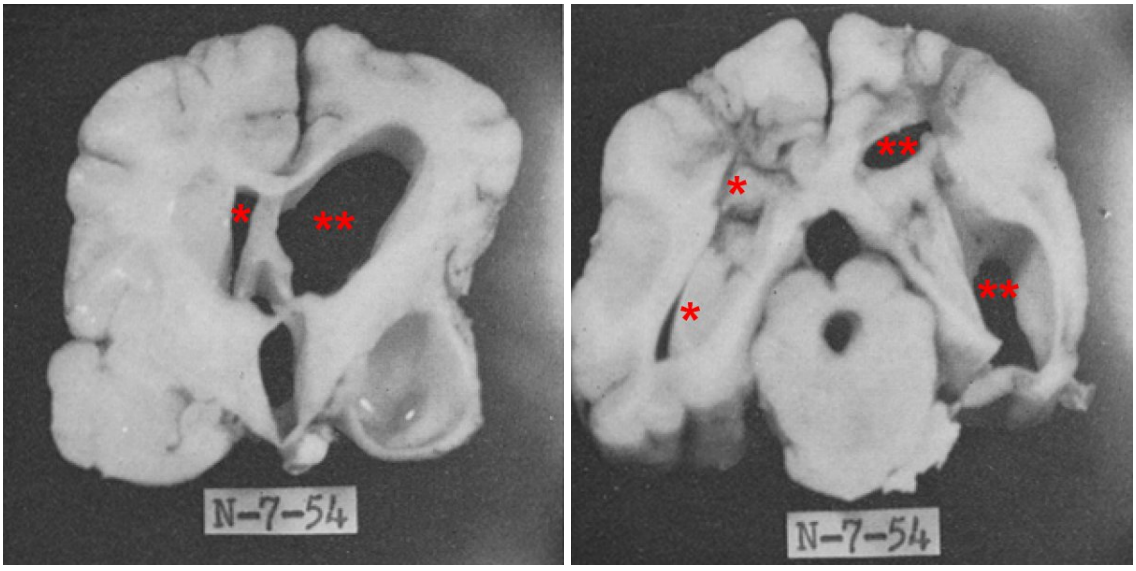

(A) (B)

Figure 2.5: Unilateral ventricular dilation in a dog from Bering's study.
These coronal sections show the anterior horns (A) and posterior horns (B) of the lateral ventricles of a dog brain from Bering's experiments. The choroid plexus from the left ventricle was surgically removed, following which hydrocephalus was induced by cisternal kaolin injection. At 9 weeks post induction, only the right ventricle (marked with **), with the intact choroid plexus, had dilated, while the left ventricle (marked with *) did not expand, even though both foramina of Monro were open. Based on this and other results, Bering suggested that ventricular dilation is caused by increased pulsations of the choroidal arteries. Modified from [74].

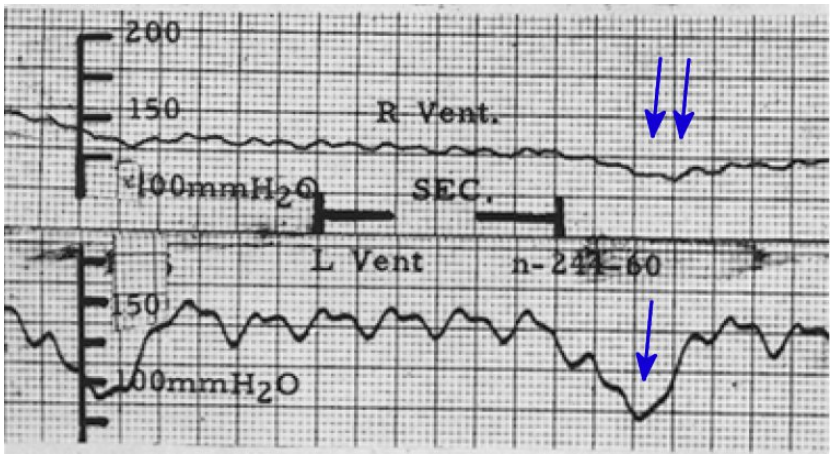

Figure 2.6: CSF pressure pulse waves ventricles of a dog from Bering's study. In Bering's experiments, the choroid plexus from the right ventricle of a dog was surgically removed, while that in the left ventricle was left intact. Consequently, the intraventricular pressure pulse waveform was markedly lower in the right ventricle (double arrow, upper waveform) than in the left ventricle (single arrow, lower waveform), even though both foramina of Monro were open. Modified from [74].

Bering's results were further substantiated by the work of Wilson and Bertan [76] who also induced CH in dogs cisternally, but using lampblack instead of kaolin. They occluded an artery leading to the choroid plexus in one lateral ventricle, leaving the other intact, and obtained results similar to Bering's: dilated ventricle and elevated CSF pulse pressure in the ventricle with the functioning choroidal artery, but not in the other.

The strongest evidence of the importance of intracranial pulsations in CH was provided by Di Rocco and colleagues, who induced hydrocephalus in sheep by introducing a catheter with a small pulsating balloon at the tip into a lateral ventricle. [77-79]. This balloon was made to expand and contract simultaneously with the animal's heartbeat. The animals developed CH which was pathologically indistinguishable from CH in animal models based on SAS obstruction. Thus, these investigators demonstrated that abnormal intraventricular pulsations alone can produce CH,

indicating that intracranial pulsations may play an important role in the development of CH.

2.6 Aqueductal CSF Pulsatility in Communicating Hydrocephalus

Pulsatile CSF *flow* was first experimentally demonstrated by Du Boulay in 1966, using pneumoencephalography [80], but it was not considered significant in clinical hydrocephalus until the advent of in vivo imaging using MRI. Later, several investigators noticed a signal loss in the aqueduct in MR spin echo scans, and determined that this was due to MR signal dephasing from pulsatile CSF flow [81, 82]. This signal loss or "flow void" was more pronounced in CH and NPH patients, and this suggested that pulsatile flow in the aqueduct is elevated in hydrocephalus. [83].

This led investigators to consider whether elevated aqueductal flow may constitute a new parameter of disease severity, and whether this should be considered in the decision to shunt a hydrocephalic patient or not [84]. Shunting was known to produce no improvement in NPH patients in as many as 50% of cases [85], and so there was a great demand to find a way of predicting shunt surgery outcome [84, 86-89]. A retrospective analysis of NPH patient data, in which the extent of the aqueductal flow void was qualitatively scored to determine the level of aqueductal velocity, suggested that the increased flow void in the presence of other clinical symptoms (gait disturbance, incontinence and dementia) may indicate a greater likelihood of improvement with shunting [84].

With the introduction of phase contrast MRI, it became possible to quantitatively measure the amplitude of pulsatile flow in the aqueduct [81, 82, 90]. This was met with

great interest by many investigators, because now it was possible to accurately determine if aqueductal flow could be considered a parameter for improvement with shunting. By analyzing the aqueductal “stroke volume” (the volume of CSF flowing cranially in systole or caudally in diastole in the aqueduct) in eighteen NPH patients, Bradley et al. established that patients with an aqueductal stroke volume greater than 42 µl have a greater likelihood of improving with shunt surgery [91]. Aqueductal stroke volume in normal subjects is approximately 31 µl [92].

Another study by Dixon et al. showed, however, that there may be no correlation between elevated aqueductal flow and improvement with shunt surgery [93]. This study differed from Bradley’s investigation because it measured aqueductal “flow”, and not “stroke volume”. A more recent study by Kahlon et al. [94], showed that there is no significant relationship between improvement after shunt surgery and aqueductal stroke volume. In this study, 24 patients were selected from a larger group of 32 for shunt surgery based on lumbar infusion or CSF tap tests. Aqueductal stroke volumes were measured but kept blinded. Twenty of the patients selected for surgery improved. There was no significant difference in stroke volume between patients who did not undergo surgery and operated patients. This study questions whether aqueductal pulsatility could be a useful parameter in determining shunt outcome. Thus, it is very important to investigate aqueductal pulsatility and determine its role in CH. Evidence indicates that pulsatility is a key indicator of CH severity (as established from tests of gait, memory and reflex) [91, 95], but there may be conditions under which it is not as useful. This was one of the primary motivations behind the studies in this dissertation.

Chapter 3

---

3. The Basal Cistern Model of Communicating Hydrocephalus

3.1 Introduction & Background

Hydrocephalus has been studied using animal models frequently and extensively. A need for animal models exists because various factors in the pathophysiology of hydrocephalus are poorly understood. These are better studied in an animal model of acquired hydrocephalus instead of human patients for three primary reasons: 1) an animal model allows the study of pure hydrocephalus without the effect of co-morbidities (e.g. meningeal infection, subarachnoid hemorrhage, atrophy, trauma, etc.), which are often present in human hydrocephalus, 2) an animal model allows the use of surgical manipulations and other interventions which may not be safe or ethical in human patients, and 3) an animal model allows investigation of the disorder throughout its course of development, i.e. from start to late stages, which is not always possible or

feasible in human patients. As there is still no cure for hydrocephalus, and the only treatment option, shunting, is often met with complications and require revisions, further studies are essential.

3.1.1 Brief Descriptions of Animal Models of Hydrocephalus.

Experimental models of hydrocephalus have been produced in a variety of animals, including dogs, cats, rabbits, sheep, monkeys, mice and rats. The majority of these models involved obstruction of CSF both in the ventricular system and in subarachnoid spaces using materials such as kaolin [9, 74, 96-101], lampblack [76, 102, 103], silicone oil [104-107], blood [108, 109], teratogenic agents [110-113] and other materials [110, 114, 115], as well as inflatable rubber balloons [116-121]. Congenital models [122-129] as well as models produced using bacterial inoculation [130] and viral infection [131-133] also exist. Some of the more commonly used animal models of hydrocephalus are reviewed below.

Dog. Dogs served as the first subjects in experimental hydrocephalus, nearly a century ago, in which hydrocephalus was induced by plugging the aqueduct with cotton pledgets [115]. These studies led to the important finding that CSF is produced by the choroid plexus, and that an obstruction to intraventricular CSF flow can give rise to obstructive hydrocephalus. Later studies of hydrocephalus involved injection of kaolin suspension [73, 74] or lampblack [76, 102, 103] into the cisterna magna in dogs, where obstruction of the 4th ventricle outlets gave rise to ventricular dilation. Hydrocephalus has also been induced by Schurr et al. by injecting Pantopaque, a CT contrast agent,

into the cisterna magna of dogs [114]. Success of this technique was attributed to an inflammatory reaction of the subarachnoid spaces, where Pantopaque was injected. However, injections of kaolin into the basal cisterns by the same group produced little or no ventricular dilation. Comparisons of dog hydrocephalus was made with hydrocephalus in cats and Rhesus monkeys. This study yielded several key findings, among which are: CSF circulation can vary among different species, and so the results obtained from animal studies should only be applied in humans with caution, and that arachnoid villi play an important role in CSF reabsorption in dogs but not in cats or Rhesus monkeys [114].

Rabbit. Hydrocephalus has been induced in rabbits by injecting silicone oil into the cisterna magna or the spinal thecal sac [104]. Both techniques produced ventricular dilation, although the injection into the spinal subarachnoid space was noted to produce better results, and extent of hydrocephalus was dependent on time after induction, as opposed to the volume of oil infused. The authors could not discern the mode of hydrocephalus production, and thought that it was due to blockage of CSF flow in the posterior fossa [104]. This study demonstrated a novel technique for induction of communicating hydrocephalus, which was not characterized by inflammatory reactions of meninges or ependyma often seen in other models. A later investigator noted extensive ventricular dilation by the cisternal silicone injection in young rabbits as early as 3 days post induction; this study revealed new findings of decreased capillary density in white matter and reduced cerebral blood flow, both of which could be reversed by shunting at the early stages of the disease [105]. Acute hydrocephalus was also

produced in young rabbits by injection of kaolin into the cisterna magna, giving rise to ventricular dilation as early as two days after surgery. This study established a time-course of ventricular enlargement in rabbits, and showed that the ependyma remains intact during the early stages of the disease [134].

Cat. Severe hydrocephalus has been produced by intracisternal kaolin injection in adult cats [135]. Hydrocephalus has been studied in this model with the calvarium and dura removed [101], as well as in intact animals [136-138]. Removal of the calvarium and dura produced hydrocephalus with greater extent of ventricular enlargement than that in animals with an intact skull, presumably due to increased compliance produced by absence of the rigid skull and inelastic dura. These were some of the first studies to explore the role of compliance in hydrocephalus, and showed that increased compliance induced by removal of the skull exacerbates ventricular dilation. In addition, extensive studies of cerebral blood flow in hydrocephalus and reversibility of ventricular dilation and restoration of the cortical mantle upon shunting were made using this animal model [137, 139-142].

Rat. Rats are currently one of the most commonly used animal models of hydrocephalus. Early models of rat hydrocephalus involved induction of congenital hydrocephalus by in-utero procedures on rat fetuses [110]. Later studies produced used injection of kaolin into the cisterna magna [100, 143-145], producing ventricular dilation by obstructing CSF outflow from the 4^{th} ventricle. These were some of the earliest studies of rat hydrocephalus and showed that hydrocephalus in this species could alter

growth, damage the ependyma and produce changes in while matter morphology. One group attempted to produce communicating hydrocephalus by kaolin into the cortical subarachnoid space. This produced hydrocephalus with mild to moderate ventricular dilation, but this technique was not ideal since it had a great potential for severe damage to the cortex [97, 98]. A successful and frequently used congenital rat model is the H-Tx rat, in which hydrocephalus develops due to aqueductal stenosis within a few days of birth. Ventricular dilation is severe and rapid. H-Tx rats generally do not survive beyond 3-4 weeks of age unless they are treated with shunting. H-Tx rats have been often used in studies of intracranial pressure, outflow resistance and shunting. [146-148].

3.1.2 Need for a True Communicating Model of Hydrocephalus

Hydrocephalus is produced in most animal models to date by obstructing CSF flow in the cisterna magna, generally by partially obstructing CSF outflow out of the 4th ventricles. Many investigators describe this as a “communicating” model of HC [6, 74], since by traditional definition, communicating hydrocephalus is caused by obstruction to CSF flow *outside* the ventricular system. However, cisternal obstruction can partially block CSF flow out of the ventricles, rendering these models as effectively obstructive [9, 100, 101]. Few investigators have attempted induction of truly communicating models, such as Schurr et al, where they injected kaolin into the basal cisterns of dogs [114], and Cosan et al, who injected kaolin into the subarachnoid spaces of the cranial convexity of neonatal rats [97, 98], as well as others [9, 149, 150]. However, Schurr’s procedure produced little or no hydrocephalus, while Cosan’s technique employed blind

injection through the fontanel into the very narrow cortical subarachnoid space, and very likely produced significant damage to the cortex by the needle. Thus, there is a need for models of the truly communicating hydrocephalus, since most models effectively study obstructive forms of hydrocephalus, and leaves the other major subtype largely unexplored. In particular, it is not possible to study CSF flow pulsatility as an indication of intracranial pulsatility without the availability of a communicating model of hydrocephalus, since in an non-communicating model, obstruction to CSF flow will reduce or altogether eliminate CSF flow pulsatility (although it may be possible to study pressure pulsatility in obstructive models).

Recently, a novel model was proposed by Li et al [9]. This model is similar to the technique attempted by Schurr et al. [114], except that the basilar subarachnoid spaces are accessed through the C1-clivus interval, and does not require a craniectomy, as in Schurr's model. Moreover, this model has been shown to produce severe and extensive ventricular dilation, and the animals can survive more than 30 days (one group of animals survived as long as 105 days, until euthanasia (§4)). This is the model described here and used in the studies included in this thesis. Inductions used in §4, §5 (SBU animals) and parts of §6 were done Dr. Jie Li (then at Wayne State University, MI and the University of Utah, UT, currently at the University of Syracuse, NY), while the remaining inductions (§3, §5 (AECOM animals) and §7) were done by the author.

3.2 Methods

All animal handling and surgical techniques were approved by the Institute of Animal Care and Use Committees (IACUC) of Stony Brook University and Albert

Einstein College of Medicine. All experimental procedures were carried out in accordance with the NIH Guide for Care and Use of Laboratory Animals. All efforts were taken to minimize any suffering of the animals and the number of animals used in experiments.

The surgical technique described here was used to produce communicating hydrocephalus in the rat, by an injection of kaolin into the subarachnoid spaces of the basal cisterns. These techniques were originally developed by Dr. James P. McAllister and Dr. Jie Li and published [9]. This technique has been adopted and refined by the author, as described below.

3.2.1 Animal Preparation

Animals were anesthetized with 5% isoflurane, and maintained on 2.5% isoflurane mixed with medical grade air (initial surgeries used an isoflurane-O_2 mixture). Animals were intubated with a 16G catheter and allowed to breathe freely. In initial experiments, animals were ventilated with a small animal respirator at 70 breaths per minute and tidal volume of 1.5 ml. The developer of the surgical technique, Dr. Jie Li, had noted that animals that were not intubated and ventilated did not survive the surgery. However, the author found that mechanical ventilation was not needed, so long as animals were intubated. The intubation tube is required to support the trachea and ensure that the trachea does not collapse and respiration is not restricted during the surgical procedure. As will be seen below, the surgical technique involves pushing the trachea aside for a brief period of time, and animals that are not intubated are unable to breathe during this maneuver.

3.2.2 Surgical Technique

The ventral side of the neck was shaved and cleaned with Betadine and 70% alcohol. Animals were placed supine over a heating pad, and the forepaws spread laterally and attached to the surgical table. Under a surgical microscope, using aseptic techniques, a 4 cm incision was made on the neck along the ventral midline. The underlying adipose tissue and glands were blunt-dissected along the midline and retracted, exposing the sternohyoid muscle (covering the trachea). Blunt dissection was done at the junction formed by the sternohyoid, sternomastoid and caudal digastric muscles (see Fig. 3.1), revealing the carotid bundle. The connective tissue between the sternohyoid muscle and the carotid bundle was then carefully dissected and the trachea and sternohyoid muscle were retracted to reveal the two muscles that lie beneath the trachea. These were separated along the midline to expose the base of the skull and C1-clivus interval, where the dura is visible in a small depression between the skull-base and the C1 vertebra (Fig. 3.2).

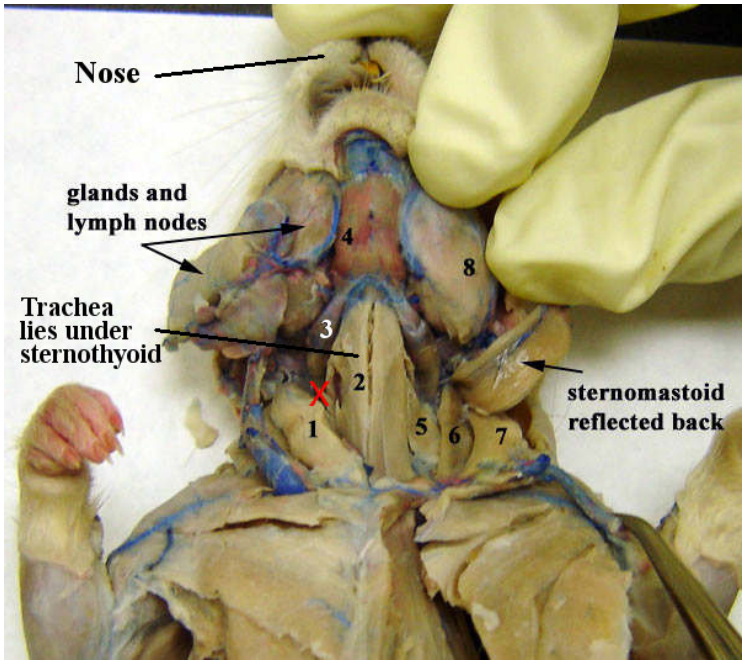

Figure 3.1: Musculature of the ventral neck in a rat cadaver.
The junction formed by the sternohyoid, sternomastoid and caudal digastric muscles are marked with a red "x", indicating the site of blunt dissection. Muscle legend: 1: sternomastoid, 2: sternohyoid, 3: caudal digastricus, 4: cranial digastricus. Modified from [151].

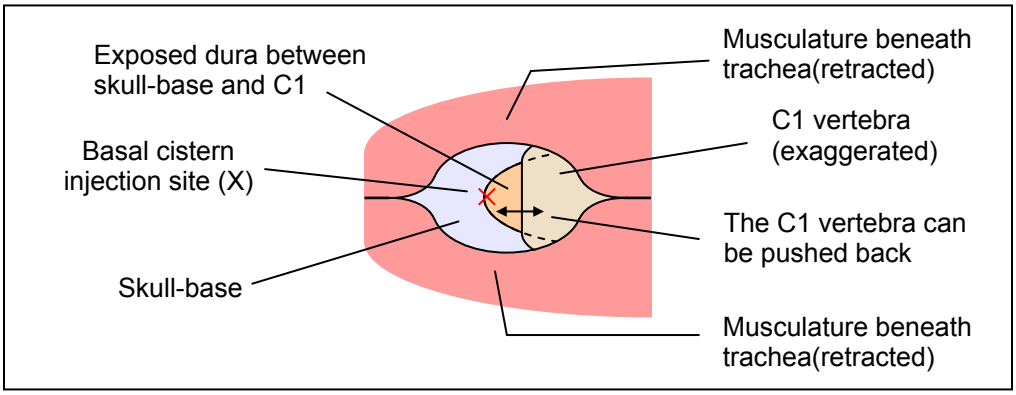

Figure 3.2: Schematic of the basal cistern injection site.
The basal cistern injection site in the rat is a small, narrow space that requires a surgical microscope for visualization. The area in the center lies under the sternohyoid muscle and trachea, which had to be pushed to a side (not shown). The dura is perforated at the location marked with a red "x", with the needle directed towards the left in this diagram (towards the animal's head).

A sharp, custom bent 30 gauge needle (1-2 mm of the tip bent at a 30° angle) was used to perforate the dura along the edge of the skull-base (Fig. 3.3). Care was taken to avoid damage to the underlying brainstem and basilar artery. Correct perforation was visually verified by leakage of a small amount of clear CSF. A second 30G needle, bent in the same manner, but with its tip blunted, was inserted into the perforation and a 30-50 µl volume of a sterile suspension of 25% kaolin (Sigma, St. Louis, MO) in saline was injected slowly over 5-6 seconds. Successful kaolin injection was verified by observing a subtle change of color of the skull-base and the dura to off-white. Following injection, the needle was gradually and carefully removed, to ensure that the kaolin does not flow back out. In recent experiments (last 8 animals used in §5 (AECOM studies), last 10 animals used in §6 and all animals in §7), the needle was held in place for 40-60 seconds before being carefully removed, to further reduce backflow of kaolin.

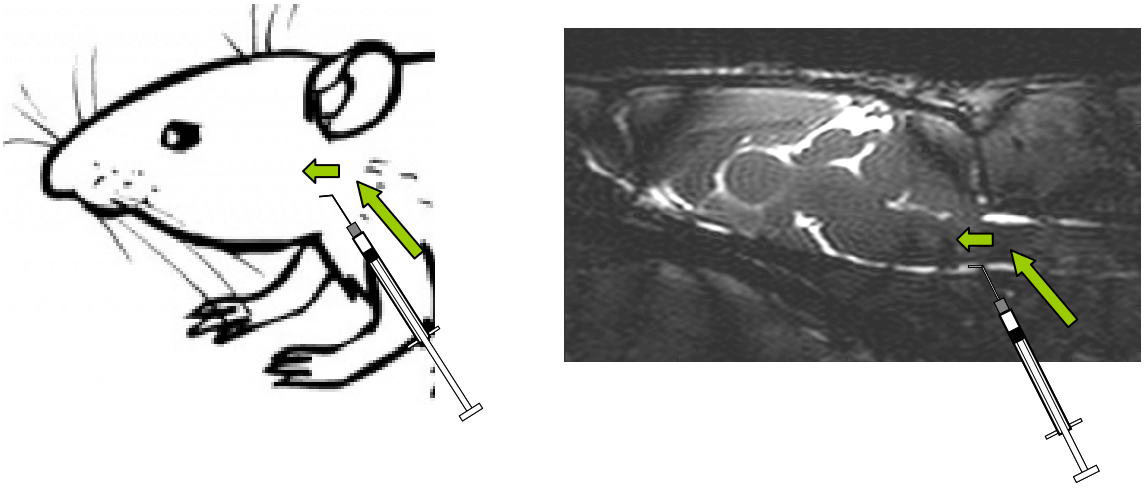

(A) (B)

Figure 3.3: Depictions of the anatomic location of the basal cistern injection site. The basal cistern injection site is approached from the ventral side of the neck (A). The bent tip of the needle is inserted into the CSF at the basal cistern SAS (B), and the tip is advanced toward the anterior. Great care needs to be taken in this procedure, as the basal cistern SAS is very narrow and lies adjacent to the brainstem.

In the original technique, kaolin injection was done using a sharp needle instead of a blunted one. However, in the author's experience, use of a sharp needle for injection often results in severe bleeding, probably caused by damage to the basilar artery, which runs ventral to the injection site. Use of a blunted needle minimizes the occurrence of this bleeding. Care has to be taken while making the initial perforation with the sharp needle; generally, a very small perforation was made carefully with the sharp needle, which was then gently widened with the blunt needle to provide access to the basal cistern for kaolin injection.

Following injection, the incision was sutured and the animal was extubated and allowed to recover. Animals were monitored closely for 3-4 days post-operatively, and received twice daily subcutaneous injections of ketorolac (2-5 mg/kg) as analgesia, the antibiotic Baytril (10 mg/kg) (Bayer HealthCare, Pittsburg, PA) and 5-15 ml of lactated Ringer's solution and 5% dextrose, for 3 days post operatively to counter weight loss. Animals' diets were supplemented with nuts, dried fruit and candy pieces with which we found less severe weight loss (ideally given to animals 1-2 days prior to surgery to acclimate them to the new food and increase their weight). This dramatically helped to counter the weight loss often encountered in initial experiments.

3.2.3 Surgical Control Animals

Surgical CH control animals were used to verify that hydrocephalus induction was due to the use of kaolin and not a result of the surgery, perforation of the dura or the injection itself. Surgical controls underwent the same surgery as the kaolin animals,

but received 30-50 µl of sterile saline, instead of kaolin suspension. Following surgery, these animals received similar post-operative care (ketorolac, antibiotic and lactated Ringer's solution) as needed.

3.2.4 Experimental Design

To determine the efficacy of the basal cistern CH induction technique, an initial group of 21 adult Sprague-Dawley rats were used for CH induction with kaolin (Cohort 1 – note that these experiments were carried out for the author's hydrocephalus inductions. Earlier inductions done by Dr. Li had been validated independently). The animals were sacrificed approximately 2 weeks after induction by cardiac perfusion with saline followed by 4% paraformaldehyde (PFA) in phosphate buffered saline. The brains of the animals were extracted and post-fixed in 4% PFA. The brains were then cut with a scalpel to produce coronal sections at the anterior horns of the lateral ventricle (LV) (1 mm anterior to bregma), foramen of Monro (1 mm posterior to bregma), posterior horns of the LV (4 mm posterior to bregma) and the widest portion of the cerebral aqueduct (8.3 mm posterior to bregma). Digital photographs of the brain slices were acquired, and the ventricles were examined qualitatively to determine the extent of hydrocephalus.

Later groups of animals were also induced, totaling 78 female adult Sprague-Dawley rats of weight 250-300 g. These animals were used in later parts of this dissertation (§5, 6 and 7). Ventricular dilation was characterized in these animals by measuring the ventricular volume, using MRI techniques described in §4. The extent and variability of ventricular dilation, as well as success-to-failure ratios, were assessed.

3.3 Results

3.3.1 Post-operative Animal Condition

Kaolin injected animals typically lost weight over 2-3 days following surgery, up to a maximum of ~20% of body weight or ~50g in the most severe cases. Most animals started to regain weight after 3 days. Many animals exhibited lethargy and adopted a hunched posture during this period. Some animals also exhibited porphyrin secretions at the nose and eyes, and sometimes faint porphyrin stains in the fur behind the neck; these are all signs of distress, most likely due to the acutely elevated intracranial pressure. A few animals exhibited paresis of the hindpaws, resulting in weakened or disuse of the hindpaws, although neurological reflexes to noxious stimuli (paw pinch) were normal. These cases may have resulted from accidental damage to the brainstem during induction.

3.3.2 Hydrocephalus Outcome

Of the 21 animals used, 3 animals were sacrificed following surgery, because there was severe bleeding from the basal cisterns (likely caused by damage to the basilar artery by the injection needle), 2 animals died after surgery, one of which had severe bleeding from the basal cisterns (again possibly caused by damage to the basilar artery) while the other did not recover spontaneous respiration possibly due to damage to the brainstem during injection, and one animal died two days following surgery possibly due to damage to the trachea from intubation. Of the remaining 16 animals, 8 animals developed mild to severe hydrocephalus (qualitative enlargement of

ventricles compared to control), determined from qualitative examination of the ventricles, while the remaining 8 animals did not have any form of ventricular dilation. Photographs of the fixed brains slices of some of the hydrocephalic animals are shown in Fig. 3.4. A success rate of 68% was established in the inductions of the 78 animals used in later in later parts of this dissertation (§5, 6 and 7).

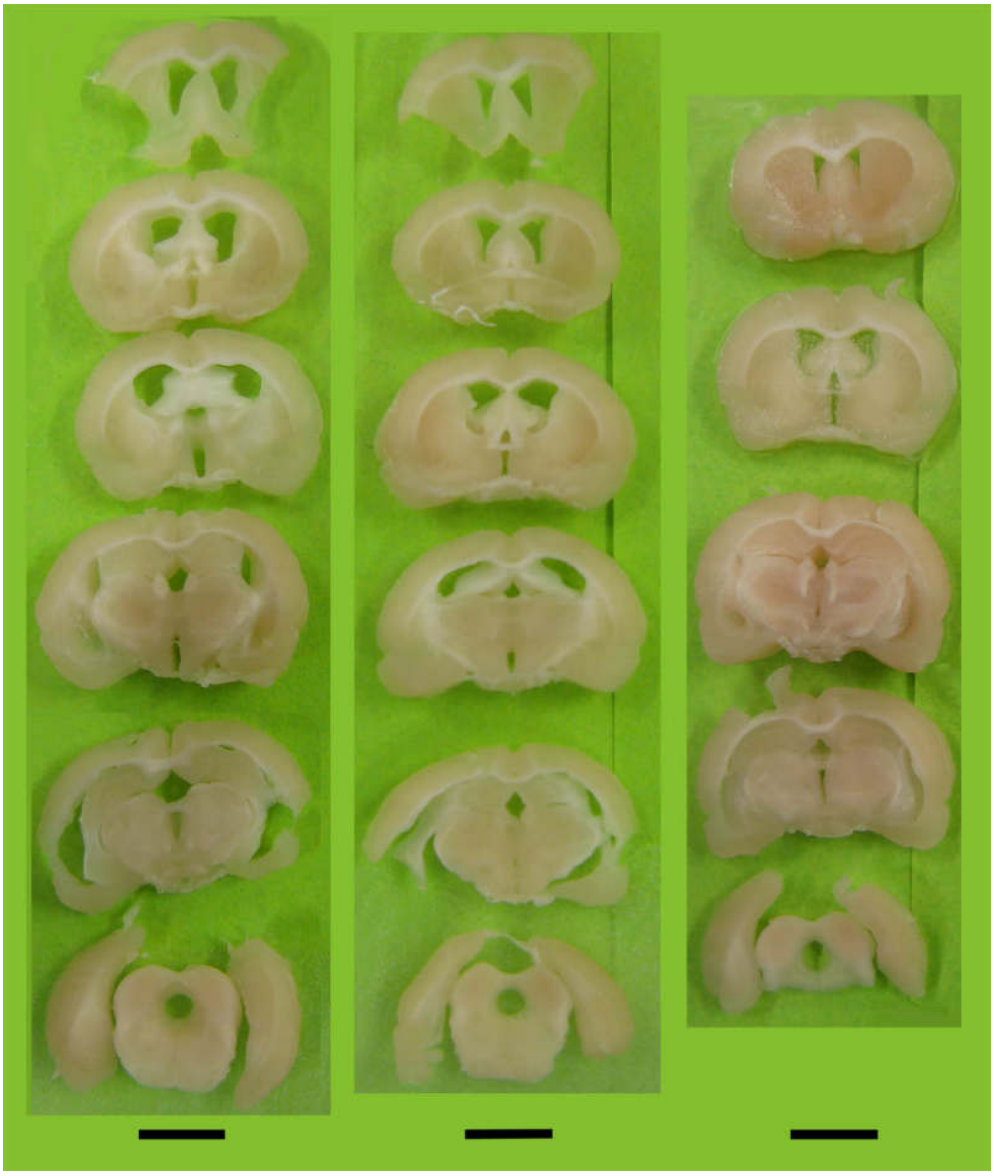

Figure 3.4: Coronal slices of perfused brains from three hydrocephalic animals. Animals from the first cohort developed mild to moderate ventricular dilation (determined by qualitative examination), as shown in this figure. The animals were perfused with PFA, brains were post-fixed and sectioned. The bar represents 5 mm.

3.3.3 Kaolin Deposits

Upon extraction of the fixed brain, a deposit of kaolin was found stuck to the base of the skull in most animals that failed to develop hydrocephalus (Fig. 3.5). No kaolin deposit was found in animals that developed moderate or severe ventricular dilation (Fig. 3.5). In one animal with mild ventricular dilation, a small deposit of kaolin was observed.

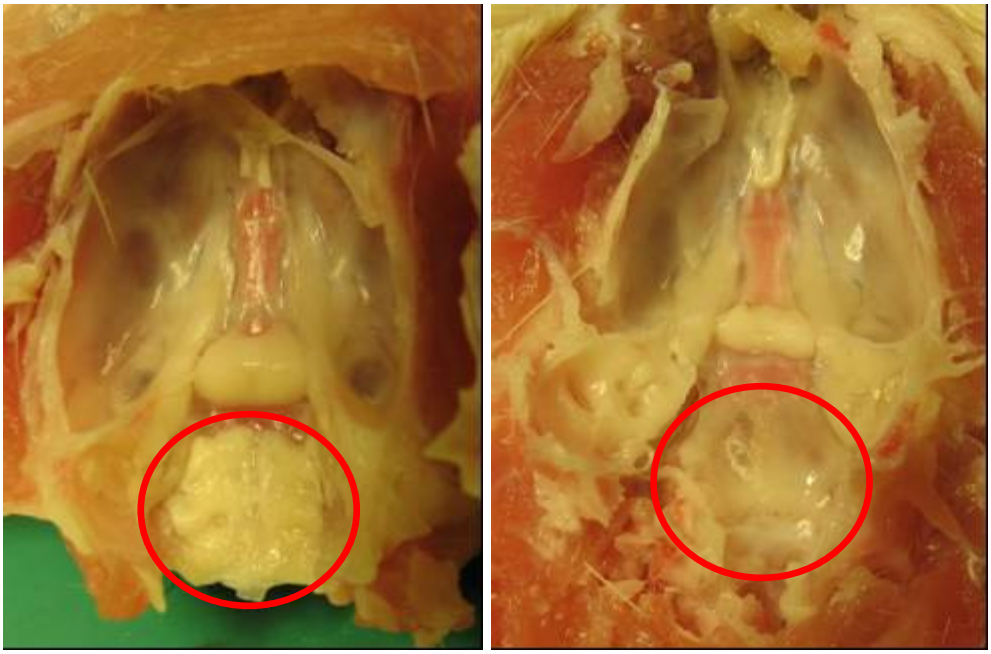

Figure 3.5: Differences in kaolin deposit in basal cisterns in a CH and non-CH rat. A kaolin deposit at the base of the skull underlying the brainstem is frequently found in non-CH rats (right, circled). CH rats usually have no such kaolin deposit (left, circled).

3.4 Discussion

3.4.1 Clinical Significance of the Basal Cistern Model

The basal cistern model is clinically very relevant, because it produces hydrocephalus by obstruction of CSF flow at the basal cisterns, which is similar to the etiology often observed in cases of communicating hydrocephalus in children [9, 25].

Moreover, many cases of communicating hydrocephalus are secondary to subarachnoid hemorrhage, which is often associated with the large arteries at or near the circle of Willis. These vessels are present in the basal interpenduncular and prepontine cisterns. Thus, hemorrhage at these sites may produce obstruction of CSF flow at the basal cisterns.

3.4.2 Advantages and Limitations

The main advantage of the basal cistern model is the fact that this is a “true” communicating model, in that it does not produce hydrocephalus by obstruction of the 4^{th} ventricle outlets as in most existing rat models. Histological studies (as well as MRI evidence shown in §4) have shown that the 4^{th} ventricle outlets remain patent [9, 152]. Hydrocephalus develops rapidly and extensively, and animals can survive indefinitely. In fact, all preliminary studies revealed that animals can continue to survive with hydrocephalus beyond 30 days. One group of animals (§4, Cohort 1) survived beyond 105 days, until they were euthanized.

One limitation of this model is the relatively “blind” injection; once the needle tip is inserted into the subarachnoid space, it is not possible to ascertain its exact location. Indeed, we hypothesize that in animals that fail to develop hydrocephalus, the kaolin is injected into an epidural space and that this causes the kaolin deposits frequently seen at the skull-base of failed hydrocephalic animals (Fig. 3.5). However, failed inductions were more frequent in the early stages of inductions (50%, as demonstrated in this chapter). With practice, inductions became more successful, and the fraction of failed inductions decreased. The overall success rate of inductions was 68%.

Since the working space in the rat basal cisterns is extremely narrow, great care needs to be taken in performing the surgical technique. While the proportion of animals that died following surgery was low, the smallest slips can cause damage to the brainstem or perforation of the basilar artery. Imperfect perforation with the sharp needle can easily damage the basilar artery and/or brainstem, both of which lie immediately ventral to the kaolin injection site. This can cause death or additional neurological symptoms unrelated to hydrocephalus. Indeed, a number of animals suffered from severe bleeding from the basilar artery at early surgeries. While most of these animals survive, none were found to develop hydrocephalus, possibly because all the blood exited the basal cisterns during surgery. Animals with damaged brainstems typically do not survive after surgery, or suffer and need to be sacrificed. During the initial phase of surgeries, one animal was encountered which had complete paresis of hindpaws and respiratory distress, and post-mortem histopathology revealed that the brainstem in this animal had been severed (this is extremely rare and was only observed on this one occasion).

3.4.3 Kaolin Neuroinflammation and Fibrosis

Even though kaolin (aluminum silicate) is an inert compound, it is known to cause neuroinflammation and fibrosis of the arachnoid and pial membranes, and can give rise to scar formation [9, 136, 153-157]. Kaolin is thought to produce a global inflammatory reaction causing obliteration of the entire subarachnoid spaces, and causing obstruction of the 4th ventricle outlets, rather than physical blockage by kaolin itself [60, 158]. However, this is quite unlikely, because neuroinflammation caused by kaolin is likely a

largely localized effect and no study has demonstrated a global inflammatory response of the brain or the cranial system to kaolin injections. Localized inflammation caused by kaolin may be causing obstruction of 4th ventricle outlets in cisterna magna injection models, but this is not the case in the basal cistern model because kaolin deposition occur at the basal cisterns, which are far from the 4th ventricle outlets and the amount of kaolin used in basal cistern injections are 3-fold smaller than those employed in intracisternal induction models (~100 µl of 25% kaolin suspension). The kaolin volume used in basal cistern injections (30-50 µl of 25% kaolin suspension) was chosen to ensure that the kaolin deposition does not exceed the size of the basal cisterns [9]. Finally, histological studies as well as MRI followed by intraventricular gadolinium injections into CSF have shown that the foramina of Luschka remain patent in the basal cistern model [9].

It is possible, however, that the neuroinflammation produced by kaolin is a confounding factor in experimental hydrocephalus. Reactive gliosis, one component of neuroinflammation, as well as glial scar formation, are consistent findings in human hydrocephalus patients [23, 159-163] as well as animal subjects of experimental hydrocephalus, in both mechanical and non-mechanical induction models [164-169]. In an effort to circumvent any possible neuroinflammation, Slobodian et al. attempted to induce hydrocephalus in rats by intracisternal injections of several different materials such as Matrigel, rat tail collagen, fibrin glue, n-butyl-cyanoacrylate, and ethylene vinyl alcohol copolymer, and compared the results with kaolin hydrocephalus [153]. They found that some of these tested materials produced other forms of inflammation, while other materials were inadequate for rat hydrocephalus induction for various reasons.

They concluded that despite kaolin's neuroinflammatory and fibrotic effects, it is still the most reliable agent for mechanical hydrocephalus induction in rats [153]. In addition, as noted above, by limiting the volume of kaolin we have limited the potential extent of any neuroinflammation to the basal cisterns themselves. Even if neuroinflammation does occur within the basal cisterns, this would merely compound the blockage effect of the kaolin, producing the communicating hydrocephalus which we were aiming to achieve in the first place.

3.4.4 Variability of Hydrocephalus Severity

One of the characteristics of the basal cistern model is the large degree of variability in ventricular dilation. Even though the kaolin volume and the injection technique is identical across animals, there is pronounced variability in the severity of hydrocephalus. Variability in ventricular dilation may occur when only a part of the injected kaolin enters the subarachnoid space, while the rest enters a epidural space; this is also possible since the size of the kaolin deposit at the skull-base often varies. Another scenario that is likely in some animals is the possibility that all of the kaolin does not remain at the basal cisterns upon injection. In basal cistern inductions, kaolin particles have been found at the 4^{th} ventricle outlets in a few animals, even though the 4^{th} ventricle foramina were patent [9]. In addition, gliosis and scarring, which are known to occur with kaolin injections, can differ across animals, especially if there is slight damage to the brainstem by the needle during some injections (which can exacerbate neuroinflammation), and these may contribute to the overall variability in ventricular dilation. Small amounts of bleeding caused by slight damage to blood vessels during

injection can also add to the variability, and this may not be apparent to the surgeon. Further histological study is required to evaluate these various factors.

Chapter 4

---

4. Characterization of Ventricular Size and Aqueductal Pulsatility in the Rat using MRI

4.1 Introduction

Communicating hydrocephalus (CH) is a severe neurodegenerative disorder characterized by dilated cerebral ventricles. Its main treatment is drainage of the excess cerebrospinal fluid (CSF) by shunting, but shunting is not a cure; it is only palliative, and is not a perfect solution: 50% of patients do not improve following shunting, 78% of shunted patients continue to have residual deficits, and 40-50% of patients require shunt revision within 1 year [3-5]. One of the difficulties with this treatment is that it is difficult to predict whether a given patient will improve with shunting or not. The degree of ventricular enlargement is a poor prognostic marker for hydrocephalus, and

neurosurgeons utilize a variety of parameters for prognosis, including clinical symptoms [86, 170, 171], outflow resistance in CSF infusion tests [172, 173], lumbar puncture [174], computerized tomography [175] and cerebral blood flow measurements [176, 177]. There is, as yet, no single prognostic marker that may be used to guide shunt surgery [178, 179].

A recent review discussing various parameters for preoperative assessment of NPH listed the aqueductal CSF stroke volume as the only non-invasive marker that may have prognostic value in predicting shunt success [179]. Aqueductal stroke volume is often dramatically elevated in NPH [70, 91, 93, 180, 181], and several studies have suggested that a high stroke volume may be indicative of good outcome after shunting [83, 84, 91, 182]. However, this technique is known to produce variable results [93, 94, 183], and so further study is required to elucidate its utility in the management of hydrocephalus [179]. Moreover, the pathophysiological basis for and relevance of elevated stroke volume in CH is still unknown.

To further evaluate the usefulness of the aqueductal stroke volume as a prognostic marker of CH, an extensive study of the dynamics of CSF pulsatility and its relationship to disease severity is needed. Such a study can be rigorously done with the novel rat model of CH recently developed in Dr. James P. McAllister's laboratory [9], as discussed above (§3). Hydrocephalus is induced in this model by injecting kaolin into the basal cisterns, ensuring that CSF obstruction occurs in the subarachnoid spaces far from the fourth ventricle outlets, as discussed above (§3). These animals have been shown to develop moderate to severe levels of ventriculomegaly.

The objective of this study was to quantify aqueductal stroke volume in CH rats using MRI and explore the temporal course of evolution of the stroke volume with the development of CH. A further objective was to investigate whether any relationship exists between elevated stroke volume and increased ventricular size in CH rats. Even though pulsatile CSF flow is routinely measured by MRI clinically, CSF pulsatility has not been measured in the rat using MR; therefore, as a first step, techniques for MRI measurement of CSF flow were established. The following hypotheses were tested:

- Pulsatile CSF flow in the aqueduct of normal and CH rats can be measured using phase contrast MRI.
- Aqueductal CSF pulsatility will be elevated in CH rats. Elevated pulsatility will vary and, based on findings in clinical CH, will be as high as a factor of 10 above normal.
- Aqueductal CSF pulsatility will not be significantly correlated to the ventricular volume of CH rats.

Clinical studies have shown that CSF pulsatility displays a great deal of variability in both healthy subjects as well as CH patients, and so it is expected that pulsatility in rats will have the same characteristic. Mean aqueductal stroke volume in normal humans is about 30 µl, while the stroke volumes as high as 400 µl has been recorded in CH patients. Based on these numbers, we hypothesized that aqueductal stroke volume in the CH rat will also be up to 10 times higher than normal. Additionally, numerous studies have shown that ventricular size is a poor prognostic marker for disease severity

and for guiding shunt surgery, but the CSF stroke volume may potentially be of value in both. Thus, it is hypothesized that there will be no functional relationship between stroke volume and ventricular size.

4.2 Methods

All animal handling and surgical techniques were approved by the Institute of Animal Care and Use Committees (IACUC) of Stony Brook University and Albert Einstein College of Medicine. All experimental procedures were carried out in accordance with the NIH Guide for Care and Use of Laboratory Animals. All efforts were taken to minimize any suffering of the animals and the number of animals used in experiments.

4.2.1 CH Induction

Communicating hydrocephalus (CH) was induced in adult rats by injection of 30 µl of 25% kaolin suspension in saline into the basal cistern of the rat, as described above (§3). Surgical controls were induced by injecting saline instead of kaolin, and intact controls received no surgical intervention.

4.2.2 Experimental Design & Imaging Timeline

Twenty six adult female Sprague-Dawley rats (~250g weight) were included in the study, to investigate the evolution of ventricular size and aqueductal pulsatility over the course of development of the disorder. CH was induced in 16 animals (kaolin animals), while 4 animals were used as surgical controls (saline animals) and an

additional 4 animals were used as intact controls. The CH animals were studied in two separate cohorts of 8 animals each.

Since one of the objectives of the study was to follow the temporal course of ventricular dilation and changes in aqueductal CSF pulsatility, MRI scans were performed on the CH and surgical control animals at the following time-points post induction: day 0-1, day 2, day 7-8 (week 1), day 15-16 (week 2), and day 29-31 (week 4). Most of these time-points are a range of 2-3 days because the animals in the two cohorts could not be imaged on the same day due to scheduling constraints. Animals in the first cohort (all kaolin, n = 8) were also imaged at days 51 and 102. Intact control animals were imaged at a single time-point, since they received no surgery and their ventricular size and CSF pulsatility was not expected to change over time. Two of the saline control animals were also studied at the same time-points as the second cohort. The remaining two saline controls were studied only at two-weeks post induction.

To study the relationship between aqueductal pulsatility and ventricular size, we included kaolin induced CH animals from other experiments in this dissertation to improve the power of the statistical analysis. These animals were divided into three cohorts according to when they were imaged after kaolin induction:

- Cohort 3 (n = 15): imaged approximately 1 week after induction (5-8 days)
- Cohort 4 (n = 9): imaged approximately 2 weeks after induction (12-17 days)
- Cohort 5 (n = 18): imaged approximately 4 weeks after induction (23-28 days)

The data from these cohorts were used in combination with Cohort 1 and 2 data at the appropriate time-points when comparing aqueductal pulsatility and ventricular size, as described below (§4.3.6).

4.2.3 MRI

All animals were imaged in a 9.4T Bruker Biospec MR scanner (Bruker Biospin Corp., Billerica, MA), equipped with 400-2000 mT/m/ms gradient coils, a 10 cm diameter radiofrequency (RF) birdcage coil (for RF transmit) and a 3 cm diameter RF surface coil. Animals were initially anesthetized with methohexital sodium (50 mg/kg). Animals were placed supine on a custom-made acrylic animal holder, which slid into the bore of the magnet. The animal's head was placed on the surface coil, with the aqueduct approximately over the center of the coil. Anesthesia was switched to 0.5-2% isoflurane with a 2:1 mixture of oxygen:air, which was delivered to the animal via a loosely fitted nose cone. Respiration, heart rate and core temperature were monitored with MR-compatible physiological monitoring equipment from SAII (Small Animal Instruments, Inc., Stony Brook, NY). Core temperature was maintained at about 37°C by blowing warm air over the animal. Heart rate was monitored by collecting the peripheral pulse waveform from a pulse oxymeter attached to the hindpaw, and respiration was monitored using a respiratory pillow under the upper abdomen.

4.2.4 CSF Volume Measurements and Distribution

4.2.4.1 MR Pulse Sequences

Two MR scans were used to image CSF:

- 3D TrueFISP: this sequence is ideal for CSF volumetric measurements, as it images CSF with a very high contrast compared to brain tissue. Images acquired were true 3D on a 128x128x100 matrix, with voxel dimensions of 0.23 x 0.23 x

0.32 mm^3 (coronal slice orientation). The following parameters were used: FOV = 3 cm, TR/TE = 4/2 ms, NEX = 4.

- T_2-weighted fast spin echo (FSE): this sequence provides high contrast images of various brain structures, including the CSF-filled ventricles. The contrast for CSF is not as high as TrueFISP, and CSF is sometimes difficult to distinguish from edema. Reasonable volumetric measurements of CSF are still possible. Images from these scans were used for visualization and display, and as a backup if the corresponding TrueFISP images were corrupted by banding artifacts. Images acquired were 2D multislice on a 256 x 256 matrix and 40 slices, with a slice thickness of 0.6 mm interleaved by gaps of 0.1 mm. The following parameters were used: FOV = 3 cm, TR/TE = 3074/36 ms, ETL = 8, NEX = 4.

4.2.4.2 Ventricular Volume Analysis

Ventricular volumes (VV) used throughout this study consisted of the volume of the two lateral ventricles, the 3rd ventricle and the aqueduct, including the widest section of the aqueductal recess. Volumes were computed from the TrueFISP images by thresholding CSF and other high intensity pixels in each coronal slice and manually removing the non-ventricular regions (such as subarachnoid spaces, blood vessels, etc., see Fig. 4.1). In images where artifacts distort parts of the image (such as banding artifacts due to B_0 inhomogeneity), ROIs are drawn manually to select CSF regions, using the FSE images as a guide when needed. In rare cases where TrueFISP images were too poor for volumetrics, the FSE images were used instead. A specially designed

graphical user interface program in Matlab (The Mathworks, Natick, MA), which allows the user to scroll through the slices of TrueFISP or FSE images in coronal, axial or sagittal orientations, was used for volumetrics (Fig. 4.1A).

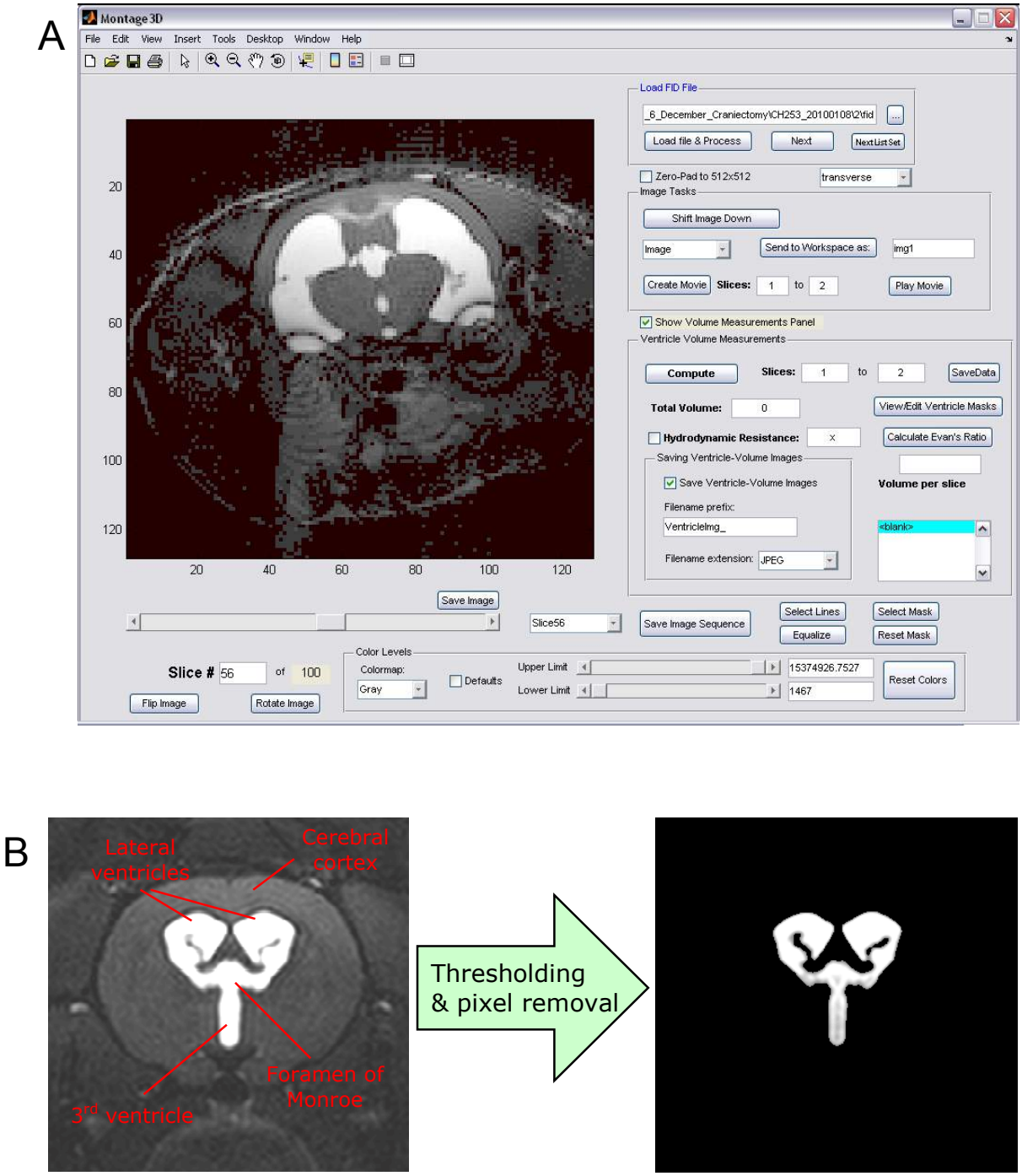

Figure 4.1: Ventricular volume measurement program and technique.
A Matlab GUI was designed to compute ventricular volumes from FSE and TrueFISP MRI images (A), where ventricles were selected based on a threshold chosen from image pixels at the edge of a ventricle (B). Any spurious regions not part of the ventricle (such as SAS – not shown here) were manually removed. This measurement technique produced reliable and reproducible ventricular volumes from the MRI images.

Evan's ratio was computed for all animals at all time-points as the ratio of the maximum lateral width of the ventricles to the maximum lateral width of the cortex at the level of the foramen of Monro on coronal slices, to compare ventricular dilation in the CH animals with human hydrocephalus.

4.2.4.3 Subarachnoid CSF Distribution Analysis

Because kaolin could not be directly visualized in the MR images, due to its very short T_2*, CSF distribution in the basilar subarachnoid spaces was estimated by a qualitative scoring system to indirectly determine the extent of CSF obstruction by kaolin. CSF distribution was scored in the anterior-ventral, basal and spinal subarachnoid spaces (Fig. 4.9 A & B) in all animals using sagittal TrueFISP images. Scores were on a scale of 0-3, with 0 indicating no CSF presence, and 3 indicating maximum CSF presence (with score steps of 0.25).

4.2.5 Pulsatile CSF Flow Measurement

4.2.5.1 MR Pulse Sequence & Hardware

A cine phase contrast gradient echo sequence was used to measure pulsatile CSF flow at the aqueduct. The sequence was retrospectively gated on the peripheral pulse, with 16-22 frames acquired per cardiac cycle. Images were acquired as a single slice positioned perpendicular to the aqueduct on a 128 x 128 matrix with a slice thickness of 1 mm. The following parameters were used: FOV = 3 cm, TR/TE = 10/6 ms, FA = 5°, NEX = 10. Velocity encoding was 1 cm/s, for control and mildly

hydrocephalic rats, and 2 cm/s for severely hydrocephalic rats. For retrospective reconstruction of images, TR gating signals from the MR scanner and peripheral pulse waveforms from the physiological monitoring equipment were captured using a NIDAQ 6042 data acquisition board (National Instruments, Austin, TX) into a personal computer with data acquisition programs designed in Matlab. A second cine phase contrast image was also acquired, in which all parameters were kept the same, but the velocity encoding gradients were reversed, producing “negative” velocity encoding. The initial “positive” encoding image was then subtracted from the “negative” encoded image, to eliminate phase errors that arise due to field inhomogeneity or radiofrequency penetration effects [184].

4.2.5.2 Flow and Pulsatility Analysis

The CSF flow images were retrospectively reordered, using the TR gating signal and the peripheral pulse waveforms, and reconstructed offline using programs written in Matlab (Fig. 4.2). The result was a sequence of complex 2D images over time, each depicting flow through the aqueduct at equally spaced intervals over the cardiac cycle. Aqueductal CSF velocity was given by the phase of the complex image at the aqueduct pixels. The aqueduct region-of-interest (ROI) was chosen using a Fourier-transform based thresholding scheme [92], which selected pixels that have a pulsatile velocity signal over time (Fig. 4.2). In animals with low CSF pulsatility, the aqueduct ROI was selected based on the phase intensity and location of the aqueduct from the magnitude image. Flow was calculated from the velocity waveform as the integral of the net flow over time for all flow in one direction (i.e. flow above the mean). Aqueductal pulsatility

was quantified as the aqueductal stroke volume (SV), defined as the volume of CSF flowing in a single direction in one cardiac cycle. A typical pulsatile aqueductal flow waveform for a hydrocephalic animal is illustrated in Fig. 4.3.

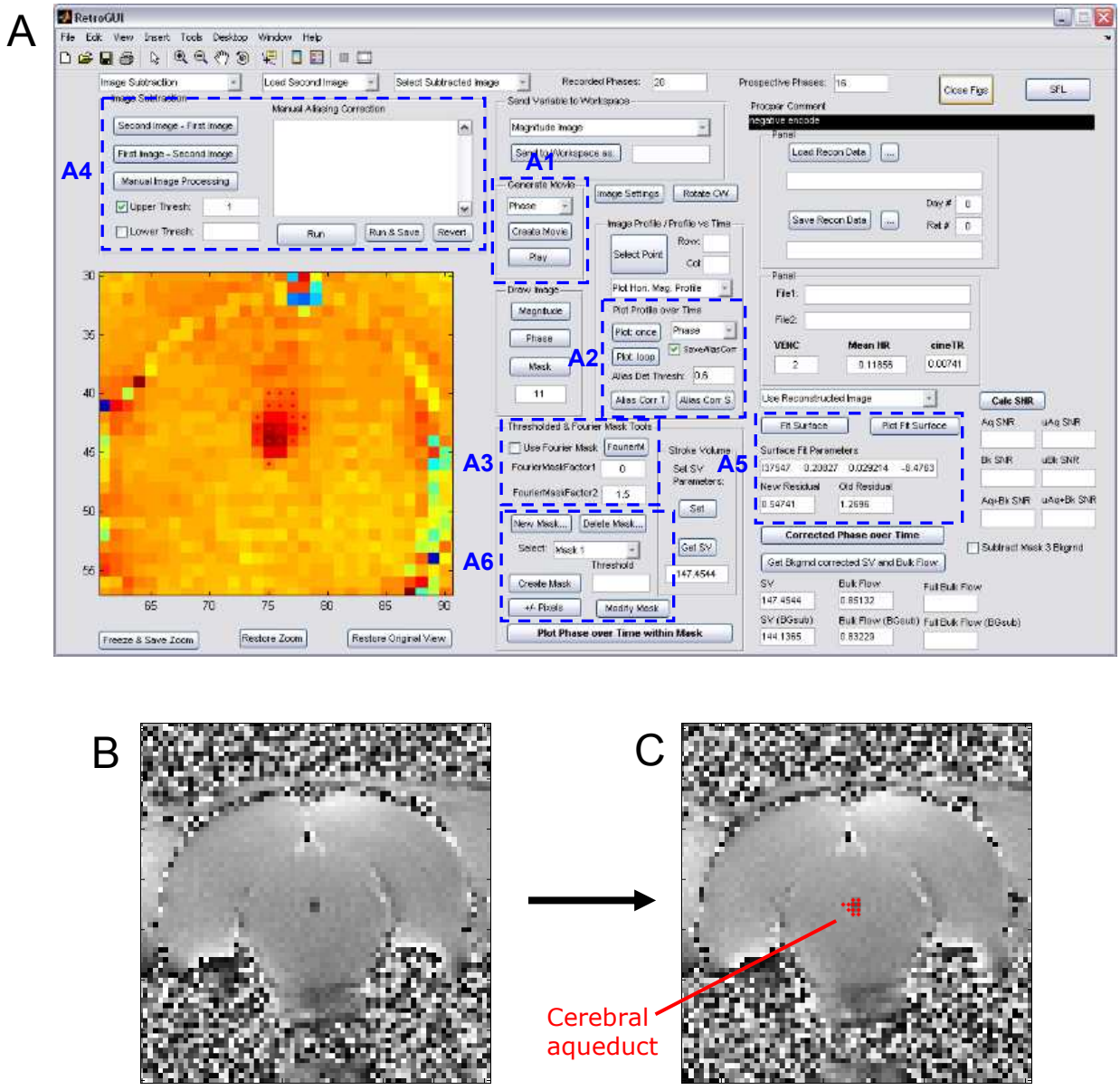

Figure 4.2: Aqueductal pulsatility calculation program and technique.
A Matlab GUI was designed for viewing aqueductal flow images and calculating aqueductal pulsatility (A). Notable features of this program include playback of cine flow movies (A1), flow viewing in individual pixels (A2), automatic (A3) and manual (A4) correction of flow aliasing, background subtraction in flow calculation (A5) and automatic and manual selection of aqueductal pixels (A6). CSF velocity corresponds to intensity of the pixels in the aqueduct (B). The aqueductal flow pixels are selected using a Fourier-based thresholding technique, which chooses pixels based on a pulsatile pattern at the region of the aqueduct (C). Manual adjustment to select or deselect pixels are made as needed (A6).

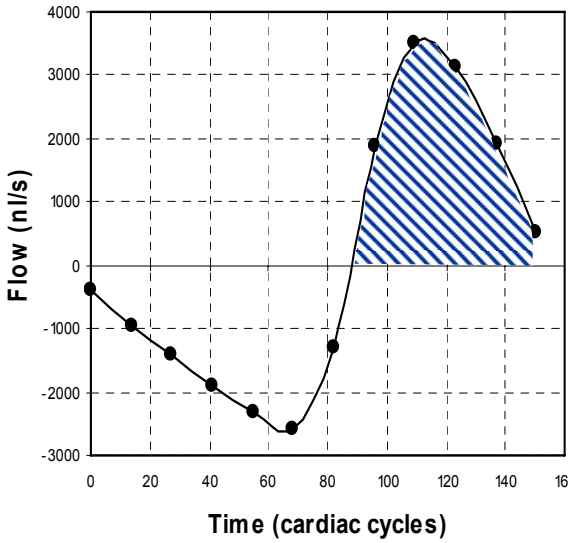

Figure 4.3: Stroke volume calculation from flow waveform.
The total flow through the aqueduct over cardiac cycle was clearly pulsatile in CH rats. Stroke volume was calculated from the shaded area, which represented CSF flow in a single direction during one cardiac cycle.

4.2.6 Data Analysis and Statistics

All results of VV, SV, Evan's ratios and CSF distribution scores are reported as mean ± standard deviation. Comparisons between kaolin animals and control animals were done using a one-way ANOVA; differences were considered significant at $p < 0.05$. In cases where significant differences were found, post hoc tests were used to determine the specific group contributing to the difference. A qualitative comparison was made between the intact control animals and two of the saline control animals at 2 weeks post induction, to rule out possible effects of the surgical technique independent of kaolin (these are the two saline controls that were studied at different time-points, while the other saline controls were studied at a single time-point each).

Further examination of the data for the kaolin animals revealed three distinct temporal dynamics for the stroke volumes: one where the stroke volume remained

elevated, one where stroke volume was elevated transiently before returning to control levels, and one where there was no change in stroke volume at any time-point. Based on these criteria, animals were divided into three post-hoc groups. Differences in stroke volume between these groups were analyzed at one week post induction and two weeks post induction using a one-way ANOVA (followed by a post hoc test if a significant difference was found). Comparison between early and late stroke volumes within individual groups was done using a paired t-test.

Regression analysis was carried out between SV and VV by calculating Pearson correlation coefficients, to explore any relationship between these two parameters. Data from CH animals in cohorts 3, 4 and 5 were added to data from cohorts 1 and 2 to increase the statistical power of the analysis. Only animals that developed hydrocephalus in Cohorts 1 and 2 were included in the regression analysis. SV-VV relationships were also studied using analysis of covariance (ANCOVA) to determine whether SV-VV correlations varied over the development of CH, as discussed later (see addendum §4.5). The ANCOVA test was used since it is the ideal test when comparing the regression between different datasets.

Regression analysis was also used to study the relationship between *changes* in SV and *changes* in VV, to further explore the relationship between elevated aqueductal pulsatility and ventricular dilation and investigate whether there is a relationship between the increments/decrements of SV and VV rather than the total SV and VV. Pearson correlation coefficients were calculated for changes in SV and VV between all adjacent time-points, as well as changes from the early or acute stage (average of day 2 and week 1) to late or chronic stage (average of weeks 2 and 4).

4.3 Results

4.3.1 CH Induction

Two animals died immediately after surgery for unknown reasons. All the remaining animals recovered well from surgery. The animals exhibited the usual post-induction symptoms within one day after surgery, including lethargy and porphyrin secretions from the eyes and nose, which lasted no more than five days. Two additional animals died during induction of anesthesia at imaging (one kaolin and one saline animal). The remaining animals survived until euthanasia at the end of the study.

4.3.2 Summary of Control Volumetrics and Aqueductal Flow

As described in the Methods, 4 intact controls were imaged at a single time-point. These animals were not followed over a period of time as with kaolin animals because in our experience with intact controls, there has never been a change in VV or SV over time. In addition, 3 saline animals were studied, one of which was followed throughout the whole time-course with cohort 2 animals, while the other two were imaged at two weeks post induction.

There was no significant difference in ventricular volume (VV) between the intact controls and three of the saline controls at two-weeks post induction (15.5 ± 2.0 µl vs. 18.7 ± 4.4 µl, $p = 0.25$) (the fourth saline control died due to anesthesia overdose during imaging). Ventricular volume for the saline animal that was studied at multiple time-points was 14.7 ± 3.3 µl. The Evan's ratio for the intact and saline controls were 0.28 ± 0.02 and 0.31 ± 0.02 respectively.

There was no difference in aqueductal stroke volume (SV) between the intact controls (0.72 ± 0.13 nl) and the saline control (1.3 ± 0.1 nl) (average of 1 and 2 weeks post induction). The aqueductal velocity for the intact and saline controls was not pulsatile; i.e. the aqueductal velocities were below the noise level. This would indicate that the control stroke volumes listed above are an upper bound rather than an actual representation of aqueductal flow in normal rats.

4.3.3 Summary of CH Volumetrics and Aqueductal Flow in Kaolin Animals

Hydrocephalus developed and progressed rapidly in many of the kaolin animals. After one week, there was a stark difference between size of the ventricles of the more severely hydrocephalic animals and controls. Ventricular dilation was the most rapid during the first week, after which enlargement became slower, and stabilized in most animals after two weeks (two animals showed a gradual increase). The highest volume recorded in one animal was 380 µl, a factor of 25 higher than controls. Fig. 4.4 illustrates the dramatic difference in ventricular sizes between a hydrocephalic and a control animal.

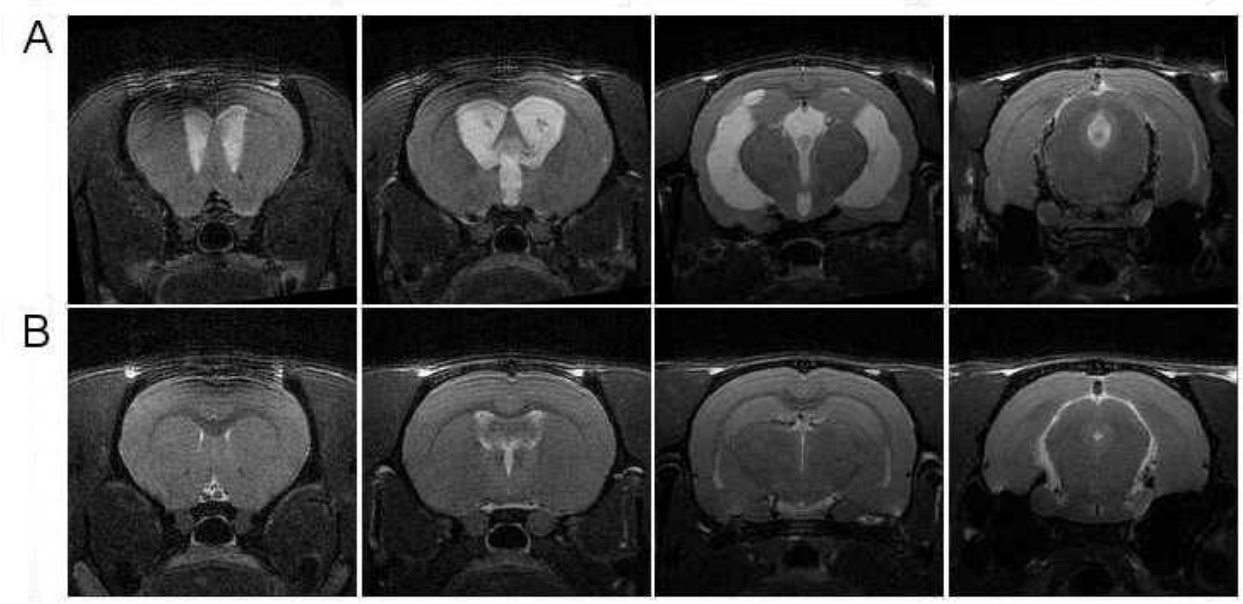

Figure 4.4: Coronal MRI sections of ventricles in a CH animal and a control. Coronal slices of the brains of a CH animal (A, top row) and a control (B, bottom row) from T_2-weighted FSE images demonstrate the severe dilation within all regions of the ventricular system in the CH rat. Severe dilation of the lateral ventricles, third ventricle and aqueduct is evident in the CH animal, whereas the ventricles in the control are very small. Parts of the ventricles in control animals are often difficult to detect on T_2-weighted FSE images.

4.3.3.1 Ventricular Dilation

Ventricular volume for all the kaolin animals was 80.7 ± 82.3 µl (average of volumes at the 2 and 4 week time-points), significantly higher than that of intact controls ($p = 0.0099$). The Evan's index for the kaolin animals was 0.44 ± 0.11. A number of the kaolin animals failed to have any qualitatively noticeable ventricular dilation; their ventricles remained comparable in size to that of controls, and hydrocephalus induction was assumed to have failed in these animals. This gave rise to the large variability in the mean ventricular size of the kaolin animals. The kaolin animals were separated into two groups: CH (successful induction, n = 8) and non-CH (presumed failed induction, n = 7), based on whether the ventricular volume became larger than the cutoff criteria of

31 µl, which is a factor of two above the intact control ventricular volume. Ventricular volume for the non-CH animals was 19.7 ± 2.0 µl, which was slightly higher than that of the intact controls (p = 0.041). On the other hand, the ventricles of the CH animals had a dramatically larger volume of 130.2 ± 83.2 µl, which was significantly higher than that of both non-CH and intact control animals (p = 0.021 and 0.018 respectively). Note that by excluding the non-CH animals from the CH volume measurement, the percent standard deviation has been reduced from 100% to 64% Fig. 4.5 shows the course of ventricular volumes for the CH and non-CH animals over 4-week and 7-week periods, which shows the large variability in ventricular volumes of the CH animals.

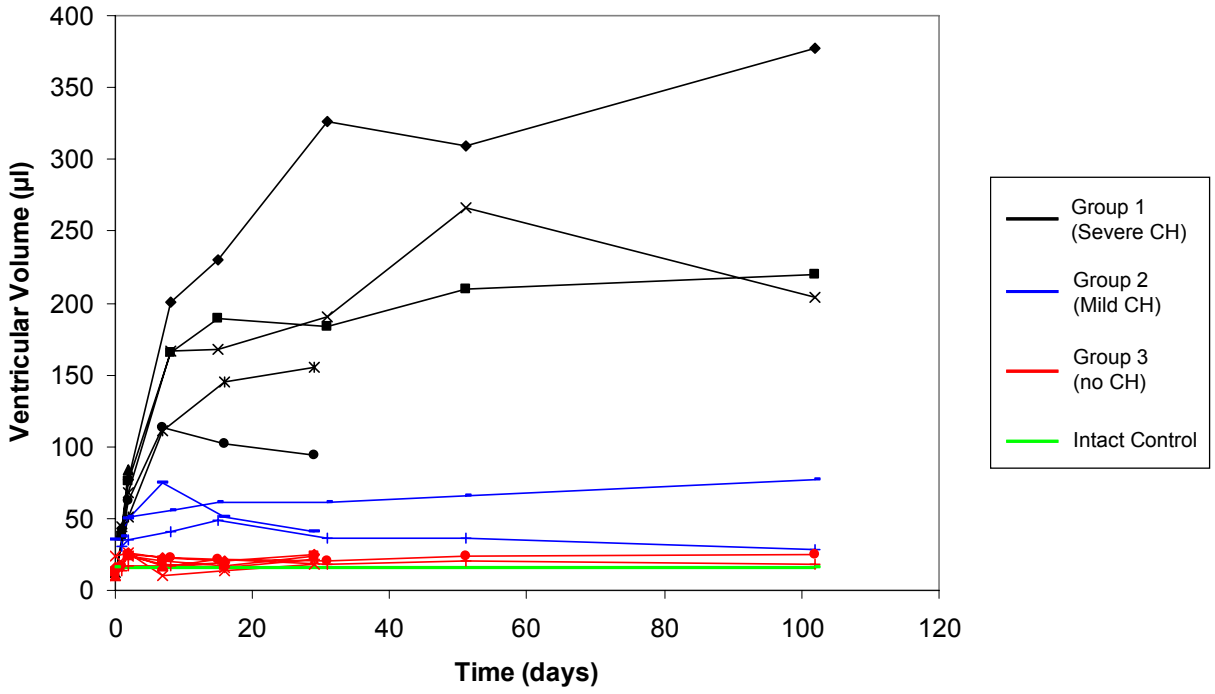

Figure 4.5: Temporal evolution of ventricular volume in kaolin animals.
The ventricular volume for the Group 1 animals (black line) increased rapidly and remained significantly elevated, while the Group 2 animals had mild ventricular dilation (blue lines). The non-CH animals (red lines) did not have any appreciable ventricular dilation, with ventricular volumes that remained near control levels (green line).

4.3.3.2 Aqueductal Pulsatility

Aqueductal SV was dramatically elevated in the CH animals. Unlike the controls, CSF flow was clearly pulsatile for the CH animals (Fig. 4.6). In non-CH animals, CSF flow was similar to that observed for the controls. SV of the CH animals (114.5 ± 106.3 nl, average of 2-week and 4-week) was increased compared to that of the non-CH animals (1.17 ± 0.44 nl) ($p = 0.058$), as well the intact controls (0.72 ± 0.13 nl) ($p = 0.056$).

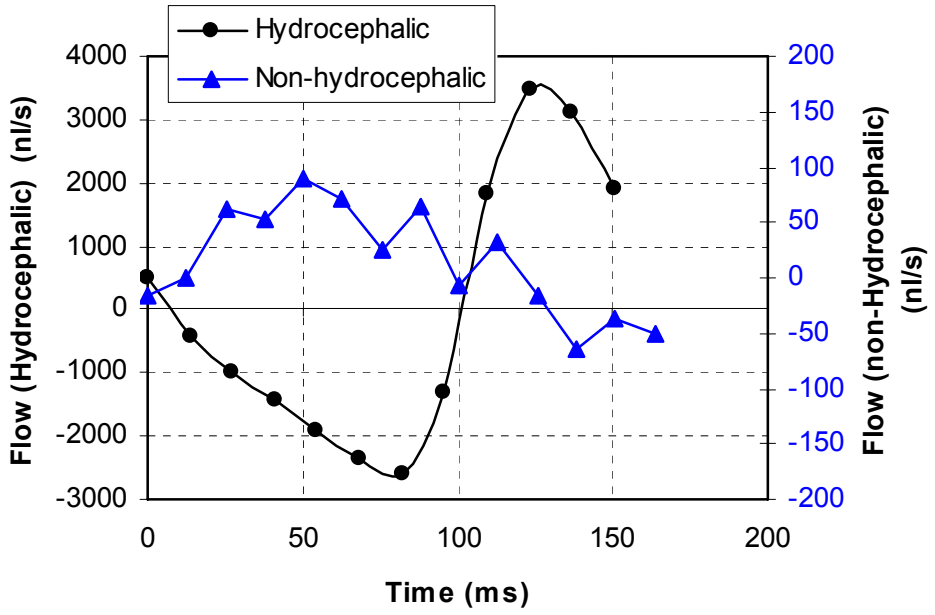

Figure 4.6: CSF flow differences in normal and CH rat aqueduct.
CSF flow waveforms through the aqueduct for a hydrocephalic animal (black) and a non-hydrocephalic animal (blue). Note the 20 fold difference in axes for the two waveforms. Hydrocephalic animals had clearly pulsatile flow, while flow in the non-hydrocephalic animals was buried in noise.

CSF flow starts to increase within 1-2 days after induction, taking on a distinctly pulsatile shape. In the CH animals, SV reached a maximum between one and two weeks post induction, after which, the flow decreased slightly in all animals, but

remained markedly elevated over controls values. Fig. 4.7 illustrates the stroke volumes for the CH and non-CH animals.

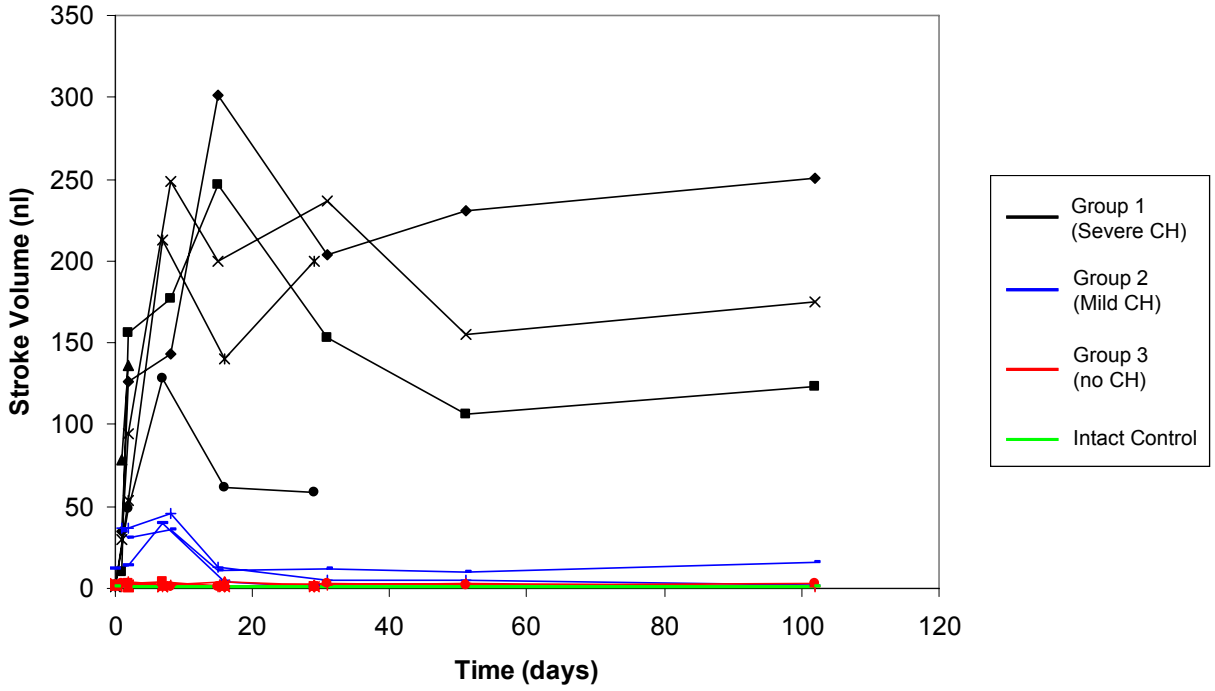

Figure 4.7: Temporal evolution of stroke volume in kaolin animals.
The stroke volume (SV) for the Group 1 animals (black lines) increased sharply and rapidly, reaching maximal values within two weeks post induction, after which the SV dropped slightly but remained persistently elevated. In contrast, Group 2 animals (blue lines) had a mild increase in SV at about 1 week after induction, but the SV dropped back to control levels after two weeks post induction. The non-CH animals (red lines) did not have any SV higher than that seen in controls (green line).

4.3.4 Post-Hoc Grouping of CH Animals by Flow Dynamics

VV and SV of the CH animals exhibited very large variability, as stated earlier. A close examination of the course of development of the stroke volumes in Fig. 4.7 revealed that there were three distinct groups of kaolin animals in this dataset: one group (n = 5, black lines in Fig. 4.7) in which stroke volume was dramatically and persistently elevated, a second group (n = 3, red lines in Fig. 4.7) in which stroke volume was moderately elevated at one week post induction, but dropped to near-

normal levels after two weeks post induction, and a third group in which stroke volumes did not rise significantly over control levels (n = 7, red lines in Fig. 4.7); this third group had been previously identified as the non-CH group (based on ventricular size criteria). These groups will be referred to as Groups 1, 2 and 3 respectively, and can be clearly distinguished by studying their stroke volumes at one week and two weeks post induction (Fig. 4.8). At one week post induction the SV between the three groups were significantly different from each other ($p < 0.02$). At two weeks post induction, that the SV of Group 1 animals were significantly higher than SV of Group 2 and 3 ($p < 0.05$ for each), but SV of Group 2 became similar that of Group 3 ($p > 0.3$).

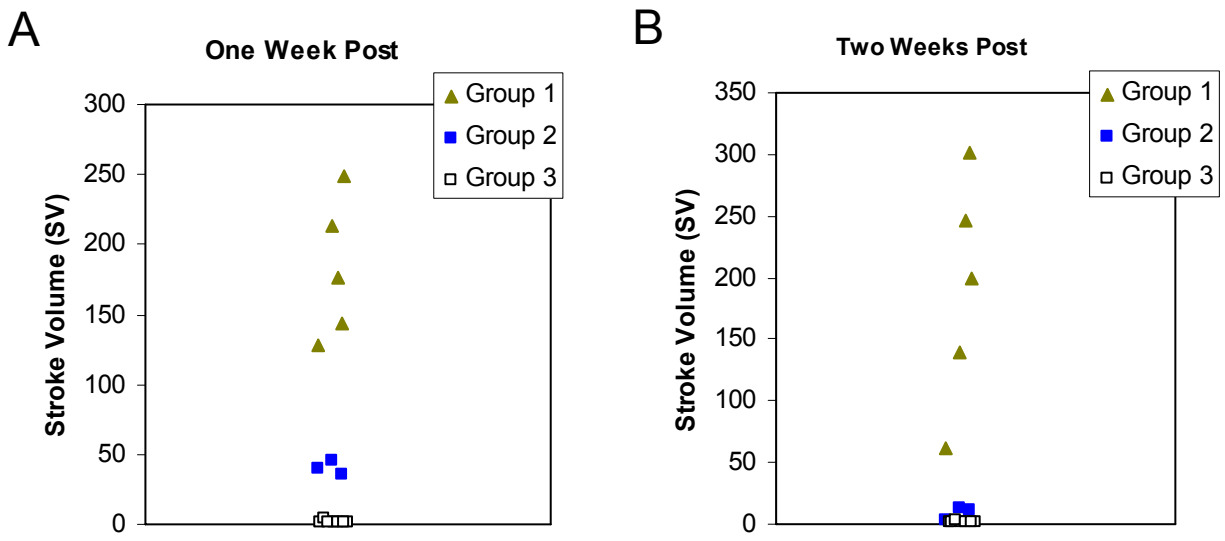

Figure 4.8: SV changes from one-week-post induction to two-weeks-post. Scatterplots of SV of all kaolin animals at 1 week post induction (A) and two weeks post induction (B), clearly showing the separation of group 2 animals at 1 week post. SV of group 2 animals became similar to that of group 3 animals at two weeks post induction ($p > 0.3$).

4.3.4.1 Ventricular Dilation

VV for the three post-hoc groups were 178.4 ± 66.4 µl for Group 1, 49.8 ± 10.6 µl for Group 2 and 19.8 ± 2.9 µl for Group 3 (average of 2- and 4-week post induction values). VV of Group 1 was significantly larger than both Groups 2 and 3 ($p = 0.032$ and 0.017 respectively). There was no significant difference in VV between Group 2 and 3 ($p = 0.10$). It was assumed that the lack of significance was primarily due to the large variability and small number of animals in Group 2 ($n = 3$) (even though the ventricles in Group 2 animals appeared visibly enlarged compared to control size, and the mean VV was above the cut-off threshold used above to identify non-CH animals).

Of the two Group 2 animals studied at 14-weeks post induction, VV of one animal remained elevated throughout the entire time, starting at 50 µl (2-days post induction) and ending at 77 µl (14-weeks post induction), while the volume of the other animal gradually decreased from 48 µl (2 weeks post induction) and reached 29 µl (14-weeks post induction), which was similar to that of the two Group 3 animals studied at 14-weeks post induction (18 and 25 µl) (Fig. 4.5).

4.3.4.2 Aqueductal Pulsatility

As expected, because the post-hoc groups were separated based on SV dynamics, SV also differed significantly among the three post-hoc groups. SV at the early developmental stage of CH (average of 2 day and 1 week post induction values) were 138.6 ± 60.7 nl for Group 1, 33.6 ± 10.8 nl for Group 2 and 2.3 ± 1.0 nl for Group 3. SV at the late developmental stage of CH (average of 2 week and 4 week post induction values) were 180.3 ± 78.0 nl, 7.4 ± 4.7 nl and 1.6 ± 0.8 nl for Groups 1, 2 and

3 respectively. As described above, SV for each Group was significantly different from the other groups at the early stage ($p < 0.01$ for all). At the late stage, stroke volume of Group 1 was significantly higher than both Groups 2 and 3 ($p < 0.01$ for both), but stroke volumes of Groups 2 and 3 were not different ($p = 0.08$).

The SV of Group 2 animals decreased significantly from the early stage (33.6 ± 10.8 nl) to the late stage (7.4 ± 4.7 nl) ($p = 0.01$). There was no such variation between early and late pulsatility for either Group 1 (138.6 ± 60.8 nl to 180.1 ± 78.0 nl, $p = 0.14$) or Group 3 animals (2.2 ± 1.0 nl to 1.6 ± 0.8 nl, $p = 0.17$).

4.3.5 Subarachnoid CSF Distributions

CSF distributions in the anterior, basal and spinal subarachnoid spaces (SAS) were quantified from TrueFISP images, as an indirect measure of kaolin distribution, to determine whether kaolin distribution had any correlation with development of CH. The locations of these three regions are illustrated in a control and a CH animal (Fig. 4.9 A & B). In general, CH animals (Groups 1 & 2) had a distinct lack of CSF in the SAS compared to controls and non-CH (Group 3) animals.

Distributions were measured qualitatively by scoring on a scale of 0 to 3, 0 being no CSF present and 3 being full CSF coverage. There was no difference in CSF distributions between intact and saline control animals for all three regions ($p > 0.05$). CSF scores for CH animals were significantly lower than that of controls animals in all three regions ($p < 0.001$ for all). Non-CH animals had similar CSF distribution to controls in the anterior SAS, but CSF scores in the basal and spinal SAS was smaller than control ($p > 0.05$) and larger than CH animals ($p < 0.05$ for basal and $p < 0.005$ for

spinal). Among the CH animals, basal CSF scores for Group 1 and 2 were similar (0.25 ± 0.15 vs. 0.17 ± 0.14, p = 0.48), as were spinal CSF scores (0.15 ± 0.33 vs. 0.17 ± 0.14, p = 0.94), but ventral CSF score was lower for Group 1 than Group 2 (0.15 ± 0.06 vs. 0.75 ± 0.33, p < 0.01) (Fig. 4.9C).

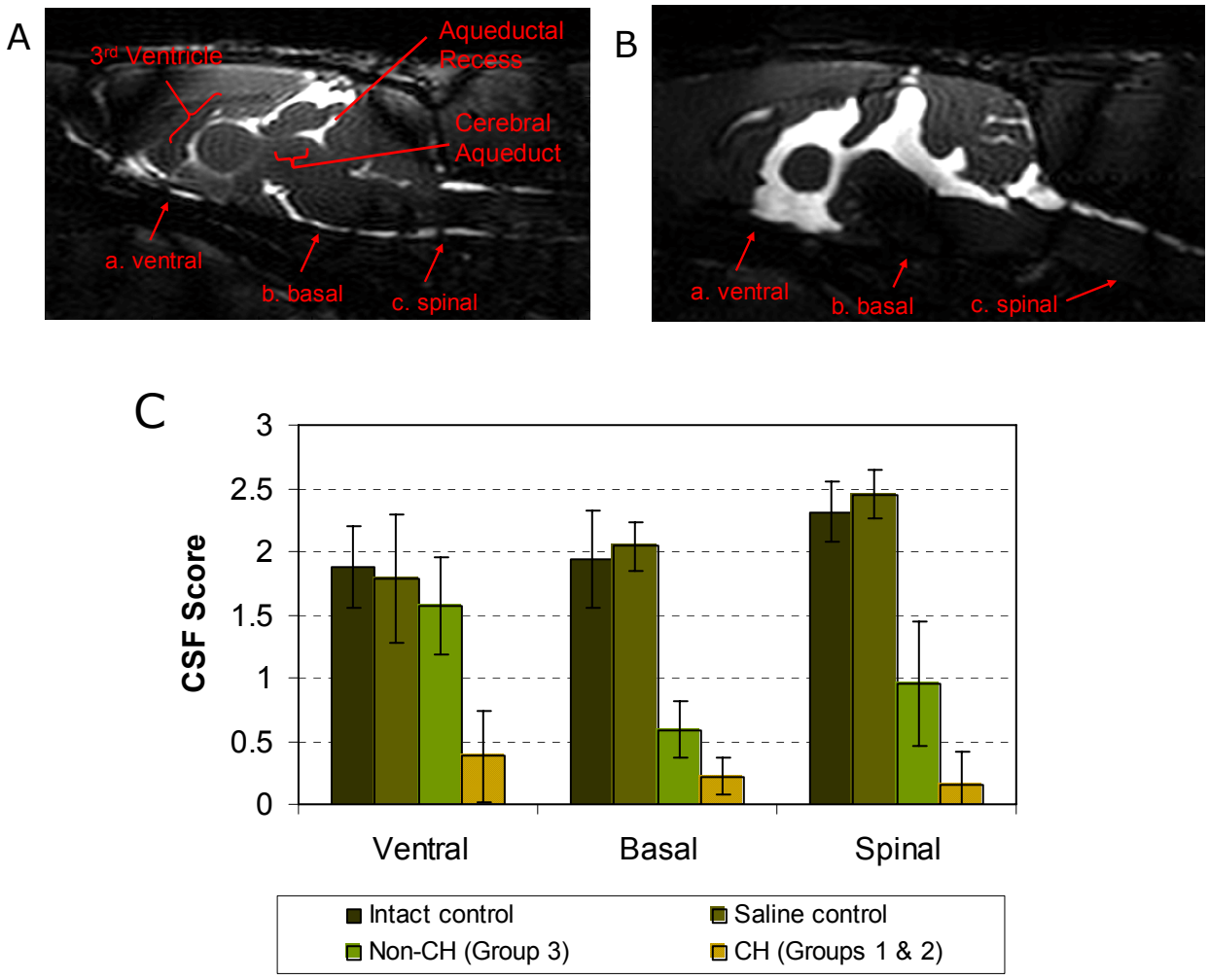

Figure 4.9: Subarachnoid CSF distributions and scores.
CSF distribution scores were measured in the following regions of the subarachnoid spaces: the anterior (ventral) space, the basal space and the spinal space (A & B). Control animals have high CSF deposition, clearly visible in this TrueFISP midline sagittal image (A), while CH animals have very low CSF (B). CSF distribution was computed from the midline sagittal and adjacent slices. Distribution scores show that the largest difference in CSF distribution between CH and non-CH animals was in the ventral space.

4.3.6 Correlations between Stroke Volumes and Ventricular Volumes

Regression analysis was carried out between SV and VV at various time-points to investigate associations between SV and VV (Fig. 4.10 A-D). Correlations were computed for Groups 1 and 2 at 2-day (Fig. 4.10 A), Groups 1 and 2 and Cohort 3 at one week post induction (Fig. 4.10 B), Groups 1 and 2 and Cohort 4 at two weeks post induction (Fig. 4.10 C), and Groups 1 and 2 and Cohort 5 at 4 weeks post induction (Fig. 4.10 D). The regression results of R^2, p-value, and slope of the linear least-squares-line fitted to the data, are given below. The correlations were significant at all time-points, with $p < 0.05$:

- Day 2 – Groups 1 & 2 (n = 9)
  - $R^2 = 0.77$, $p < 0.002$
  - Slope of fit-line: 2816 nl/ml
- Week 1 – Groups 1 & 2 + Cohort 3 (n = 23)
  - $R^2 = 0.26$, $p = 0.014$
  - Slope of fit-line: 887 nl/ml
- Week 2 – Groups 1 & 2 + Cohort 4 (n = 17)
  - $R^2 = 0.67$, $p < 0.001$
  - Slope of fit-line: 1449 nl/ml
- Week 4 – Groups 1 & 2 + Cohort 5 (n = 26)
  - $R^2 = 0.44$, $p < 0.001$
  - Slope of fit-line: 491 nl/ml

While significant correlations existed for the hydrocephalic animals studied at each time-point, the slope of the regression fit-line changed over the time course. This is illustrated in Fig. 4.11, where all four datasets with their individual regression fit-lines are plotted on the same axes. This indicates that even though ventricular volume and stroke volume were statistically correlated at all times, the actual association between these parameters varied over the course of CH development.

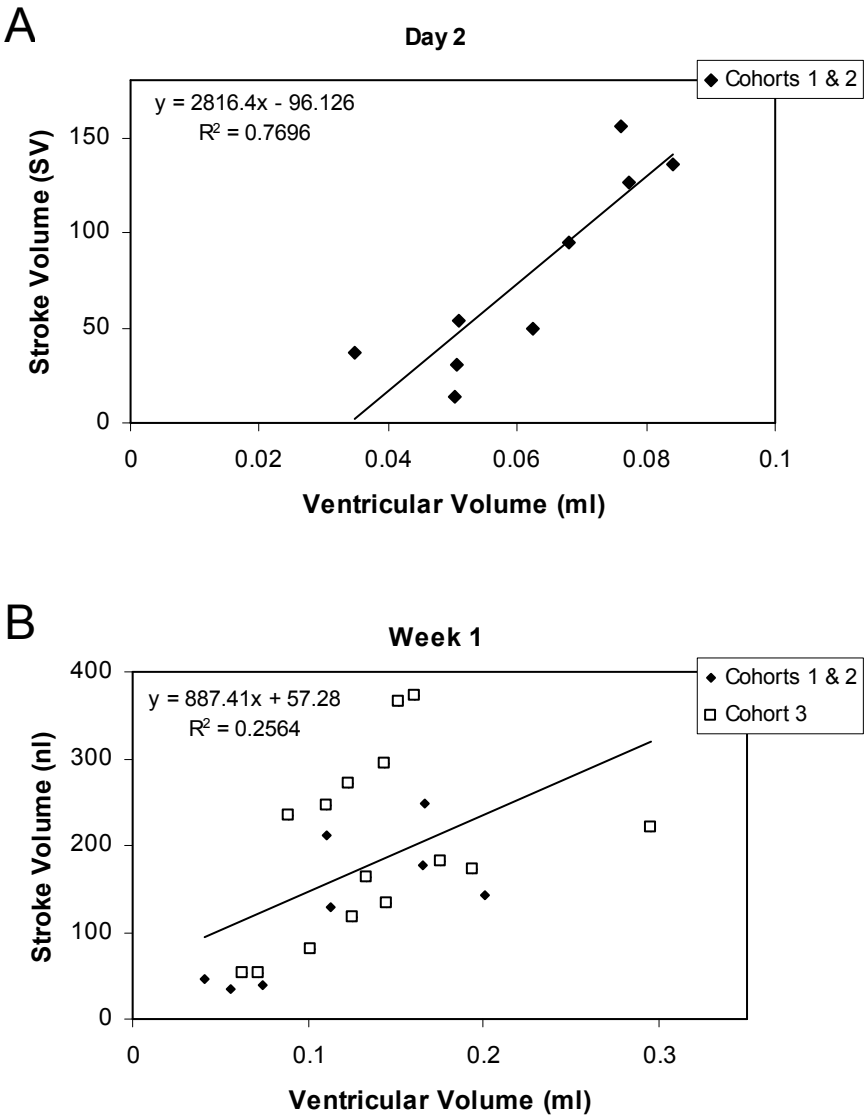

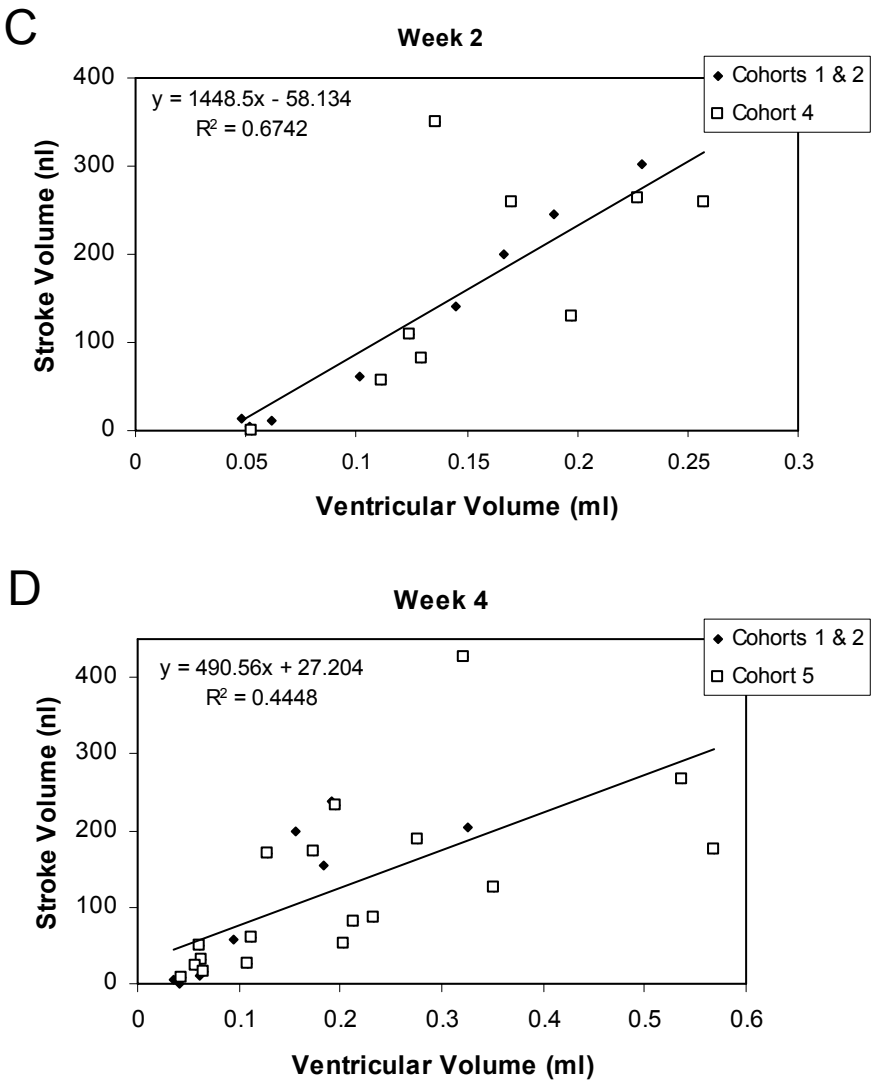

Figure 4.10: Correlations between SV and VV at individual time-points.
The correlations were computed at day 2 (A), week 1 (B), week 2 (C) and week 4 (D). Correlations were significant at all time-points ($p < 0.02$), but the correlation coefficient and the slope of the regression fit line varied across time-points, indicating that both SV and VV may be influenced by another parameter, such as intracranial compliance.

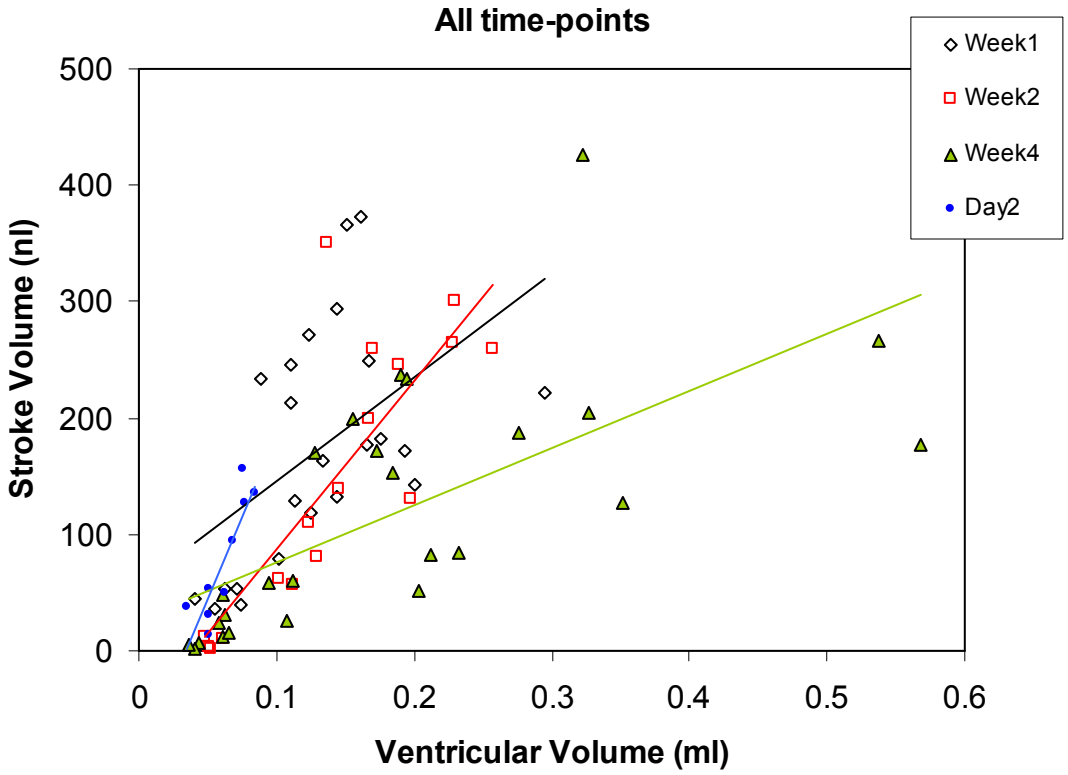

Figure 4.11: Correlation between SV and VV over all time-points.
The slope of the regression fit line varied from one time-point to another, as seen in this figure where all correlation data were overlayed in the same axis. Correlation between SV and VV over all time-points was also significant ($R^2 = 0.31$, $p < 0.001$).

The relationships between *changes* in stroke volume and *changes* in ventricular volume were also studied, to further investigate the relationship between aqueductal pulsations and ventricular size. There was no correlation between changes in SV and changes in VV when changes between all adjacent time-points over the entire course were considered ($R^2 = 0.02$, $p = 0.5$, Fig. 4.12A). A significant correlation was found when the changes were considered during the transition from the acute stage (day 2 & week 1) to the chronic stage (week 2-4) ($R^2 = 0.95$, $p < 0.001$, Fig. 4.12B).

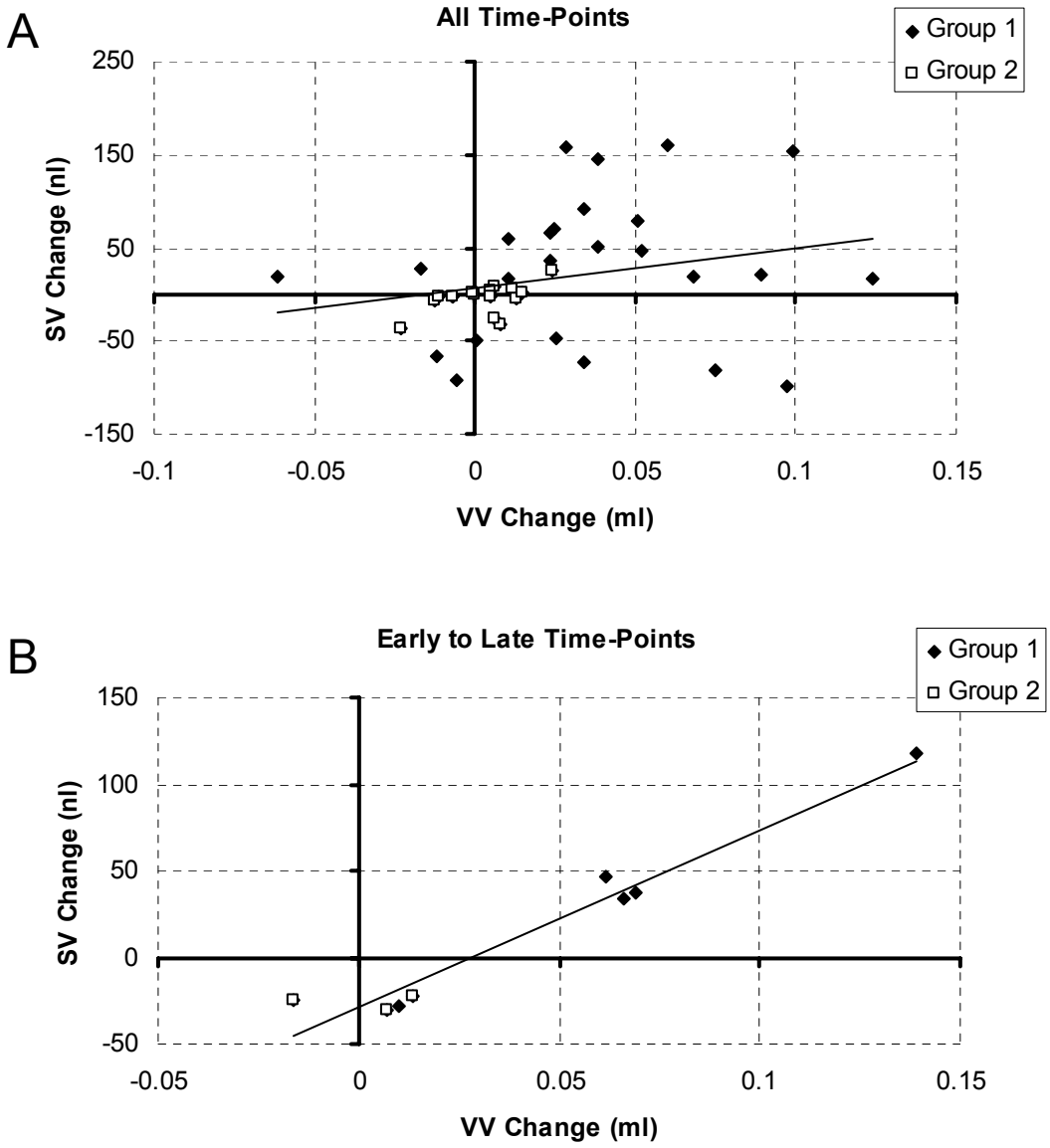

Figure 4.12: Correlations between changes in SV and changes in VV.
In the regression analysis between changes in SV and changes in VV, no correlation was found for changes over all adjacent time-points when SV and VV were measured (A). A significant correlation was observed during the transition from the acute phase (average of day 2 and week 1) to the chronic phase (average of week 2 and 4) (R^2 = 0.95, $p < 001$, B). It should be noted that the negative SV change values are mainly from the Group 2 animals, for which SV dropped between the two time-points.

4.4 Discussion

The present study was designed to investigate three specific hypotheses, that 1) pulsatile CSF flow in the aqueduct of normal and CH rats can be measured using phase contrast MRI, 2) aqueductal CSF pulsatility will be elevated in CH rats and will be as high as a factor of 10 above control values, and 3) aqueductal CSF pulsatility will not be significantly correlated to the ventricular volume of CH rats. We have successfully measured pulsatile CSF flow in the CH rat aqueduct using phase contrast MRI; in fact, this study was the first demonstration of pulsatile CSF flow measurement in the rat. However, we found that aqueductal CSF flow in normal rats was so small that it could not be distinguished from noise using our technique at 9.4T magnet strength. Our results of stroke volume in control rats represent an upper bound for normal rat aqueductal pulsatility, rather than the true value. It is possible that a stronger magnet and/or an MR pulse sequence more optimized for measuring CSF flow (such as a phase contrast balanced SSFP sequence, which has been used in human MRI [19, 92, 185]) could discern true aqueductal pulsatility in control rats.

We also demonstrated that aqueductal pulsatility is indeed significantly elevated in CH rats, as compared to normal animals, but we found that this increase in pulsatility was much greater than what we had predicted. A 10-fold increase was estimated based on the increase in pulsatility in human CH. In rat CH, we found that the lower bound on the pulsatility increase is by a factor of 150 on average, with a maximum factor of over 400 in the most severe animals (since our control SV is an upper bound, these numbers represent lower bounds and may actually be higher). It is interesting to note that the SV increase with hydrocephalus is so much larger in rats than in humans. Human

intracranial compliance is approximately a factor of 50 higher than normal rat intracranial compliance; PVI values of normal human brains are in the order of 50 ml [186], while that in rats is in the order of 1 ml [187]. It is very likely that the this lower compliance gives rise to the proportionately higher increase in pulsatility with the development of CH in rats.

4.4.1 Failed Inductions and non-CH animals

Injection of kaolin into the basal cisterns does not always produce hydrocephalus, as seen by the fact that nearly half of the animals in this study (Group 3, the non-CH animals) did not develop any appreciable form of hydrocephalus. Presumably, this was due to a failed induction because either the kaolin was injected into an extra-dural space and not the subarachnoid spaces (discussed above in §3 as a limitation of the “blind” injection technique) or because the kaolin did not remain in the basal cisterns (BC) after injection (either leaked out after injection or was carried away by CSF flow). Moreover, it is possible that ventricular dilation is highly dependent on the distribution of kaolin within the BC. For instance, if there is a slight opening, this may allow enough CSF flow to prevent ventriculomegaly. Indeed, the CSF distribution data indicate that there was a significant drop in CSF score of the non-CH kaolin animals in the BC, but not in the ventral space (Fig. 4.9). This would indicate the injection was successful in blocking the basal cistern (although somewhat less of a blockage), but was not successful in blocking the more distal anterior SAS and perhaps it is this distal blockage which is more critical for the development of ventricular dilation.

4.4.2 Severity of Hydrocephalus and Post-Hoc Grouping

One of the most interesting findings in this study is the distinct post-hoc grouping of the hydrocephalic animals based on severity and temporal dynamics of CSF pulsatility: Group 1 animals, which demonstrate severely dilated ventricles and persistently elevated aqueductal pulsatility, and Group 2 animals, which have mildly dilated ventricles, and whose aqueductal pulsatility is elevated only temporarily. Since these animal groups were not created intentionally, it is difficult to pinpoint the actual cause(s) of these differences; however, one comment can be made as to a possible cause. It was noted that both the Group 1 and Group 2 animals had similar CSF distribution scores for the basal and spinal subarachnoid spaces. However, Group 1 had a lower score for CSF presence in the anterior-ventral subarachnoid space, as compared to Group 2 animals (Fig. 4.9). This indicates that the development of ventricular dilation may be related to CSF access to the anterior-ventral subarachnoid spaces, as opposed to only CSF blockage itself within the basal cistern. While there have been no direct studies of hydrocephalus involving obstruction of CSF in the anterior-ventral subarachnoid spaces, recent studies show that ventricular dilation may be linked to deficiencies in CSF transport into the nasal lymphatic system through the cribriform plate, which is situated near the anterior-ventral subarachnoid space [32, 64].

Since the exact cause of the difference between the post-hoc groups is unknown, it is difficult to make clinical inferences from the results of the Group 2 animals. However, it is clear that a diagnosis of hydrocephalus for these animals based on aqueductal pulsatility would require knowledge of pulsatility at various points in the course of development of hydrocephalus. If pulsatility was measured in these animals at

only a chronic stage, i.e. after two weeks post induction, the transient increase in pulsatility would have been missed. This leads one to speculate whether similar situations exist in human hydrocephalus. Most patients are imaged at a single time-point, as a result of which information on temporal dynamics is lost. A recent study has shown that in NPH patients, SV increases with the development of hydrocephalus, reaches a plateau and then falls within a period of a few months [188]. Thus, the temporal dynamics of SV may be an important factor which was not considered in studies that show that patients with low aqueductal pulsatility are as likely to improve from shunting as patients with high pulsatility [93, 94, 183].

4.4.3 Relationship between Aqueductal Pulsatility and Ventricular Size

One of the objectives of this study was to investigate the relationship between SV and VV. We had hypothesized that there would be no correlation between these parameters, since clinically, there is often no functional relationship between ventricular size and symptoms, and we anticipate that aqueductal pulsatility will have such a functional relationship. However, regression analysis between SV and VV showed significant correlations between aqueductal pulsatility and ventricular size at all time-points, particularly at the day 2, week 2 and week 4 post induction time-points (Fig. 4.10). Based on these results, it is tempting to suggest that there is indeed a functional relationship between ventricular size and pulsatility. However, care should be taken in making this assessment. There is large variation across the time-points in both the correlation coefficient and the slope of the regression line fitted to the data at each time-point (Fig. 4.11). This indicates that the association between stroke volume and

ventricular volume changes over the course. Finally, comparison between changes in SV and changes in VV shows a strong correlation only at the transition from acute to chronic stage, but show no correlation when all time-points are considered (Fig. 4.12). These suggest an alternate hypothesis: that while there may be some functional relationship between stroke volume and ventricular volume, these parameters are likely driven by some other pathophysiological factor, such as intracranial compliance. Intracranial compliance is known to be decreased in the hydrocephalic brain [189-191]; this may be a consequence of neuroinflammatory reactions such as gliosis [167, 169]. Changes in compliance and gliosis has not been studied over the course of hydrocephalus development, so it is as yet unknown how these parameters may influence SV and VV.

4.4.4 Limitations

One possible limitation of this study was the small number of animals that were followed over the course of hydrocephalus development, especially since nearly half of these animals did not develop any form of hydrocephalus. A consequence of the surgical technique is that we are unable to predict how many animals in any group will ultimately develop hydrocephalus. However, our results were sufficient to demonstrate statistically significant effects, in terms of elevated pulsatility, relationship between stroke volume and ventricular dilation, and post-hoc grouping of the two hydrocephalus subtypes. Moreover, data from other experiments using this model (included in this study as Cohorts 3-5) demonstrated the same trends, i.e. severe ventricular dilation was

generally accompanied by highly elevated aqueductal pulsatility, and mild ventricular dilation was accompanied by pulsatility similar to or slightly greater than control.

One other possible limitation of this study is the use of ventricular dilation as a marker for disease severity, and comparing the efficacy of aqueductal pulsatility against this measure. Ventricular size is generally considered a poor indicator of disease severity, and that there is often no correlation between ventriculomegaly and disease severity [99, 192] until the cortex is severely compressed [193, 194] (although it should be noted that most studies addressing this issue use ventricular widths as a measure of ventriculomegaly, as opposed to a true ventricular volume that we have used [165]). However, ventricular dilation is often used as a measure of hydrocephalus severity in animal studies [104, 110, 114, 119, 195] and may be related to behavioral outcome [193, 196]. Even so, the gold standard for hydrocephalus severity lies with behavioral outcome. This issue has been addressed in this animal model in a later part of this thesis using different groups of animals where behavioral deficits were quantified and compared against both ventriculomegaly and aqueductal pulsatility.

4.5 Addendum: Statistical Analysis of SV-VV Relationships with ANCOVA

Significant correlations between SV and VV was observed at different time-points over the course of CH development (§4.3.6, §4.4.3). This relationship was found to vary over time, based on the slope of the regression line (Fig. 4.10, 4.11). A one-way analysis of covariance (ANCOVA) was carried out to determine whether the changes in the correlations were significant.

ANCOVA is a combination of analysis of variance (ANOVA) and linear correlation and regression techniques. It is used to compare the correlation between two variables (e.g. X and Y) under two or more different conditions, e.g. time, i.e. it answers the question whether the correlation between two variables X and Y changes significantly from one time-point to another. The condition variable is termed as the covariate. In other words, ANCOVA can be used to determine whether the slopes of two or more regression lines are significantly different under different conditions or covariates. Thus, ANCOVA is ideal to determine whether the change in the relationship between SV and VV over time is significant.

Comparison	DF	Contrast SS	Mean Square	F Value	Pr > F
2-day vs. 1-wk.	1	3790.5	3790.5	0.65	0.4235
2-day vs. 2-wk.	1	11241.3	11241.3	1.92	0.1701
2-day vs. 4-wk.	1	7542.2	7542.2	1.29	0.2600
1-wk vs. 2-wk.	1	56256.6	56256.6	9.63	0.0028
1-wk vs. 4-wk.	1	11064.3	11064.3	1.89	0.1734
2-wk vs. 4-wk.	1	9814.8	9814.8	1.68	0.1994

Table 4.1: Post-hoc results of ANCOVA between SV and VV
A one-way ANCOVA was carried out between SV and VV using time after induction as the covariate. This test was done to determine whether the difference in the association between SV and VV over time was significant. Results of the ANCOVA show that the difference is significant ($p = 0.01$). Results of post-hoc tests, shown in this table, indicate that the significance is primarily driven by the 1-week vs. 2-week difference.

ANCOVA was carried out in our SV-VV dataset at two-days, one-week, two-weeks and four-weeks post induction, using the time after induction as the covariate. The results of the test showed that the slopes of the regression lines, as shown in Fig.

4.11, are indeed significantly different ($p = 0.01$). A post-hoc test showed that the significance is due to the difference between the correlations at one-week and two-week post induction ($p < 0.01$) (Table 4.1).

These results indicate that the relationship between SV and VV does vary significantly over the course of CH progression. We hypothesized earlier that this may be because both SV and VV are driven by changes in another parameter, such as intracranial compliance. In this case, our results indicate that compliance decreases from 1-week to 2-weeks post induction (compliance at each time-point can be approximated by 1/slope of the regression line, since compliance = Δvolume/Δpressure (§6.1) and SV is related to a change in intracranial pressure through its relationship with pulse pressure). This result is in agreement with the well known finding of decreased compliance hydrocephalus [189-191, 197]. Although there was no significant difference between correlations at week 4 and other time-points, it is interesting to note that the slope of the regression-line decreases from week 2 to week 4, indicating an increase in compliance. This may be due to a decrease in ICP from week 2 to week 4 (compliance is inversely related to ICP, as discussed later in §6.1). Although we did not measure ICP in our animals, anecdotal evidence from later experiments suggest that ICP is elevated early after induction, but is back to normal at chronic stages (upon craniectomy, brain herniation is severe at acute stages of CH, but is similar to control animals at chronic stages of CH).

Chapter 5

---

5. Alterations of Aqueductal Pulsatility by Compliance Modulation

5.1 Introduction

5.1.1 Variability in Communicating Hydrocephalus

In the previous chapter, we had observed that the correlation between stroke volume and ventricular volume varies significantly over the course of hydrocephalus development, especially between the one-week and two-week time-points. The changes in this relationship indicated that stroke volume and ventricular volume are possibly related to another parameter, and alterations in this parameter give rise to the variations in stroke volume and ventricular volume observed. We had hypothesized that the most likely parameter that can explain these changes is the intracranial compliance. Intracranial compliance has been shown to be decreased in hydrocephalus [189-191,

197-199], possibly as a consequence of subarachnoid CSF obstruction (caused by kaolin in our model) as well as gliosis in the gray and white matter [168, 200]. As our next step, we decided to extend our studies of aqueductal pulsatility by investigating the relationship between stroke volume and intracranial compliance.

As discussed below, intracranial pressure pulsations are related to compliance, but the effect of compliance on stroke volume and their interrelationships have not been studied. Our objective in this study was to examine the effects of altering compliance on aqueductal stroke volume in order to attempt to gain a clearer picture or the role of CSF pulsatility in communicating hydrocephalus (CH), understand the variability seen in the pulsatility and ventricular dilation in our animal model and elucidate the functional relationship between pulsatility and ventriculomegaly. We hypothesize that stroke volume will drop with an increase in compliance. Compliance will be manipulated in two distinct manners: with craniectomy and with shunting, both of which will give rise to an increase in compliance.

5.1.2 Intracranial Compliance

Intracranial compliance is defined as the compliance of the cranial contents, including the brain, the cerebral vasculature and the cerebrospinal fluid (CSF) spaces of the cerebrum and spine as a whole. Because cranial CSF is in free communication with the CSF of the spinal subarachnoid spaces and the spinal thecal sac, it is useful to consider intracranial compliance as the compliance of the craniospinal system as a whole.

Compliance is a physical property of any closed container. The compliance of such a container is a measure of its distensibility, i.e. the degree to which it resists a change in volume when a volume of fluid is added or removed. Compliance is defined as the ratio of the change in volume to the change in pressure. A highly compliant container will experience only a small change in pressure when a large volume of fluid is added or removed, while a low-compliance container will undergo a large change in pressure when even a small volume of fluid is added or removed. The major determinant in the compliance of the intracranial cavity is the skull, which is rigid and prevents expansion. Brain parenchyma itself is fluid-based and incompressible. The ingress and egress of blood through arteries and veins, and CSF through the foramen magnum (and the spinal canal, to a small extent) allow volume exchange between the brain and the rest of the body. Arteries themselves are stiff-walled and relatively non-compliant compared to veins. Thus, the main sources of compliance in the craniospinal system are the veins and the spinal thecal sac.

5.1.3 Intracranial Pressure-Volume Relationships

Intracranial compliance can be measured by the CSF infusion experiment, where boluses of known volumes of CSF (or other physiological fluid) are injected into the ventricles or CSF-filled subarachnoid spaces (cranial or spinal), and the corresponding peak rise in fluid pressure is measured. When a volume of fluid is inserted into the CSF compartment, the pressure rises abruptly and then returns to equilibrium, due to CSF absorption [201]. Compliance is measured by calculating the ratio of the volume increase to pressure increase, i.e. dV/dP. A variation of the technique employs constant

infusion of fluid at known rates. The first experiments to measure changes in CSF pressure upon fluid infusion showed that the relationship between volume and pressure was not linear; Ryder et al. described it as hyperbolic [202]. The intracranial volume pressure relationship was more thoroughly characterized by Marmarou et al., who showed that there is an exponential relationship between pressure and volume of the CSF compartment [201, 203, 204] (Fig. 5.1).

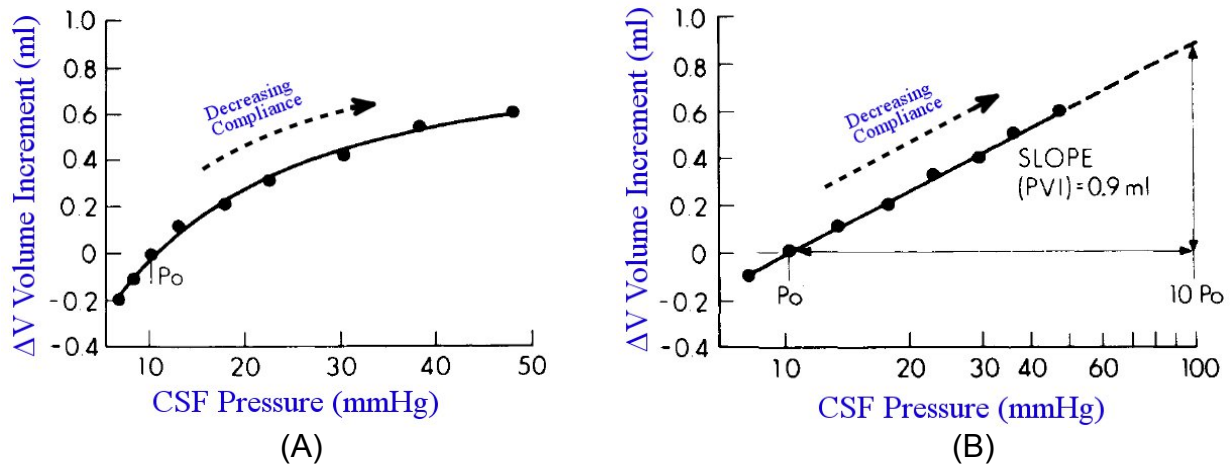

Figure 5.1: The pressure-volume relationship.
The pressure-volume curve of an intracranial system is exponential in nature, which is evident when volume and pressure are plotted on a linear axis (A); consequently, the relationship becomes linear when plotted on a semi-log pressure axis (B). Compliance is calculated from the slope of the curve; compliance can be seen to decrease with increasing mean pressure (A). The slope of the straight line in the semi-log axis (B) is defined as the pressure-volume-index (PVI). Modified from [203].

The exponential nature of the relationship between volume and pressure of the craniospinal system has some interesting consequences. Since compliance is given by the slope of the volume-pressure curve (Fig. 5.1A), this implies that compliance decreases as intracranial pressure increases, i.e. intracranial compliance is not constant if the intracranial pressure varies. Because of the dependence of compliance on mean

pressure, one method for characterizing the intracranial system taking this into account is to calculate the pressure-volume-index (PVI), which is defined as the slope of the resultant curve when the change in volume is plotted against the logarithm of the change in pressure; because the volume-pressure relationship is exponential, this curve is a straight line. The PVI is thus equal to the fluid volume required to produce a ten-fold increase in the initial pressure, and describes the entire pressure-volume curve independent of mean pressure [187, 201].

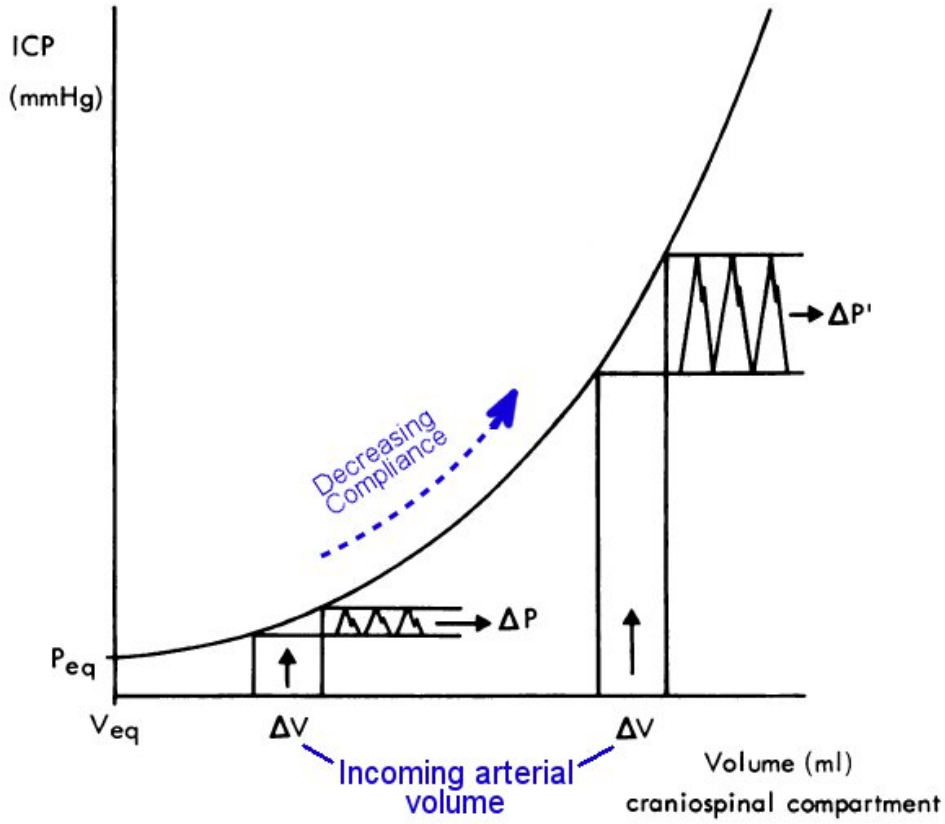

Figure 5.2: Intracranial pulsatility alterations with changing (ICP) or compliance. This shows how systolic arterial pulsations give rise to intracranial pressure pulsations. Because of the exponential nature of the relationship between pressure and volume, the pressure change induced by the systolic influx of blood produces a higher pressure pulse at a higher ICP level or lower compliance level. Modified from [205].

Another important consequence of the exponential nature of the volume-pressure relationship is that cardiac-induced intracranial (and CSF) pressure pulsatility increases as intracranial pressure increases (or compliance decreases). Cardiac induced pulsations occur when a volume of blood enters the cranium through the arteries during systole. This temporary volume increase, ΔV in Fig. 5.2, corresponds to a temporary pressure increase, ΔP that is felt throughout the brain and cranial CSF as the pressure pulse. At elevated intracranial pressures, the same systolic volume ΔV produces a larger pressure pulse, on account of the exponential volume-pressure relationship, as shown in Fig. 5.2. Such elevated pressure pulsations have been experimentally observed in CSF infusion tests [refs].

5.1.4 Compliance changes in Hydrocephalus

Several studies, using CSF infusion tests and CSF and venous flow quantification by MRI, have established that intracranial compliance is diminished in hydrocephalus, both in clinical studies and animal experiments [189-191, 197-199]. Decreased compliance has been considered a factor behind elevated aqueductal stroke volume [6, 8]. However, a recent report suggested that brain compliance may in fact be *increased* in normal pressure hydrocephalus [206]. The investigators in this study used a novel MR technique, magnetic resonance elastography (MRE), which measures viscoelastic properties of the brain *in vivo*, and showed that brain compliance was increased in the periventricular tissue as well as in deep white and cortical grey matter. It should be noted, however, that these results are in sharp contrast with the well-established findings of decreased compliance in hydrocephalus described above. These

disparities might be explained by considering that the MRE is a measure of “local” tissue compliance, while CSF infusion measures the “global” compliance of the entire cranial CSF system, and thus may reflect different aspects of compliance changes in the brain.

5.2 Methods

All animal handling and surgical techniques were approved by the Institute of Animal Care and Use Committees (IACUC) of Stony Brook University and Albert Einstein College of Medicine. All experimental procedures were carried out in accordance with the NIH Guide for Care and Use of Laboratory Animals. All efforts were taken to minimize any suffering of the animals and the number of animals used in experiments. For both craniectomy and shunting studies, communicating hydrocephalus (CH) was induced in adult female Sprague-Dawley rats (weight = 200-250g) using the techniques described in §3.

5.2.1 Craniectomies

CH was induced in twenty-one rats; the craniectomy experiment was performed two weeks after induction. Animals were anesthetized using 5% isoflurane; anesthesia was maintained using 1-2% isoflurane and oxygen. A set of MRI scans were done prior to craniectomies to characterize CH by measuring ventricular volume (VV) and aqueductal CSF stroke volume (SV), using the techniques described in §4 (VV and SV

were defined in §4). Animals that failed to develop hydrocephalus were excluded, since they do not demonstrate measurable aqueductal stroke volume.

Bilateral craniectomies were performed immediately after the MRI scans (without allowing the animal to awaken); the craniectomy technique was similar to that described in §5. The animal was removed from the magnet and secured on a stereotaxic head-holder in the prone position. The isoflurane level was increased to 2-2.5%. The head was shaved, and a 2.5 cm midline incision was made on the top of the head, extending from between the eyes to the back of the head. The underlying tissue was removed, and bleeding was stopped by cauterizing and using gauze. Craniectomies were made using a high-speed Dremel-style drill equipped a 0.75 mm burr. Each craniectomy was approximately 9 x 4 mm in size and centered over the left or right parietal bone. Each craniectomy was positioned at least 1 mm away from the midline suture, to prevent damage to the superior sagittal sinus. The craniectomies were made by drilling along the periphery until the groove became very thin, and then carefully removing the resulting bone flap with forceps. The dura was left intact in all animals, although small tears were present in a few cases.

Following bilateral craniectomies, the head incision was sutured. The animal was removed from the head-holder and returned to the MRI (without being allowed to awaken). MRI scans were repeated to measure ventricular size and pulsatile CSF flow in the aqueduct. The isoflurane level was maintained at the same 1-2% level during the second set of scans. Animals were euthanized following the second set of MR scans.

5.2.2 Shunting

CH was induced in a total of 8 animals for the shunting experiments. CH was characterized in the animals by MRI, obtaining measurements of ventricular size and pulsatile CSF flow in the aqueduct (as described in §4), prior to shunt surgery. Animals that failed to develop hydrocephalus were excluded. Shunt surgery was done in 4 animals.

The shunt consisted of a flexible polyethylene tube (outer/inner diameter = 1/0.6 mm) with a 30 mm piece of stiff tubing at the proximal end. The last 5 mm of the proximal end was bent at 90° to facilitate insertion into the ventricle and securing of the shunt to the skull. The full length of each shunt was approximately 30 cm.

The position for shunt insertion was determined from the pre-shunt MRIs. Shunts were to be inserted into the right anterior horn of the lateral ventricles at the level of the foramen of Monro. From the MRI scans, it was determined that the shunt tip needed to be inserted to a depth of 4 mm. So to facilitate shunt insertion and securing of the shunt to the skull, the proximal tip of the shunt was cut so that only 4 mm of tubing extended from the bend. This way, the shunt could be inserted all the way to the bend, and the shunt tubing could then be secured to the bone easily. The stereotaxic coordinates of the shunt location on the skull surface were 1 mm posterior and 1.4 mm right from bregma.

Shunt surgeries were done under aseptic conditions. Each animal was secured on a stereotaxic head-holder in the prone position. The head, neck and back of the animal was shaved and cleaned with povidone solution and 70% alcohol. A 2 cm midline incision was made on the top of the head, and the underlying tissue was

removed to expose the parietal bone. A 1-2 mm diameter craniectomy was drilled at the predetermined shunt site and the dura was exposed. The proximal end of the shunt was inserted vertically downwards until the bend was flush against the skull. When clear CSF was seen in the catheter, the craniectomy was sealed with cyanoacrylate gel, which was also used to attach the shunt to the skull. The shunt was held in place until the glue hardened sufficiently. The distal end of the shunt was tunneled under the skin down to the animal's abdomen. A small skin incision was made on the side of the animal's upper abdomen, 1 cm lateral from the spine and below the liver, to view the insertion of the distal end of the shunt. Another small incision was made in the peritoneum, through which the distal end of the shunt was inserted. The peritoneal incision was closed with absorbable suture, ensuring that the distal end of the shunt was secured against the peritoneum. Both head and abdominal skin incisions were also closed.

Following successful shunting, a second set of MRI scans were acquired to measure ventricular size and pulsatile CSF flow in the aqueduct. These scans were also used to verify that the shunt was properly inserted. Animals were then allowed to recover. Animals received ketorolac as analgesic and Baytril as an antibiotic. Another set of MRI scans were acquired one week after shunting, also to measure ventricular size and pulsatile CSF flow in the aqueduct. These scans were also used to verify that the shunt remained at its proper position in each animal after one week.

The shunt surgeries described here were carried out by Dr. James McAllister.

5.2.3 Data Analysis and Statistics

Ventricular volumes from each anatomical MR image were computed as the volume of the lateral ventricles, third ventricle and aqueduct (up to the aqueductal recess). Details for the measurement technique are described in §4. Aqueductal CSF pulsatility was calculated as the stroke volume of CSF from the phase contrast images; the technique is described in §4. Statistical comparisons of pre- and post-craniectomy SV and VV were carried out using paired t-tests. Regression analysis was carried out between change in SV and initial VV by calculating Pearson correlation coefficients. Statistical comparisons were not done for the shunting experiments because of the small animal number. All data is presented as mean ± standard deviation.

5.3 Results

5.3.1 Craniectomies

Six animals failed to develop hydrocephalus and were excluded (VV < 30 µl) (§4). One animal was sacrificed due to significant weight loss (> 30%) due to severe progression of CH. Three animals died during the craniectomy experiments, due to problems encountered during the craniectomy surgery. The remaining 11 animals developed mild to severe ventricular dilation, with a ventricular volume of 178.8 ± 69.8 µl (range: 65.8 – 322.1 µl). Pre-craniectomy SV in these animals was 139.4 ± 114.1 nl (range: 15.0 – 426.5 nl).

Following craniectomy, the aqueductal pulsatility decreased significantly, with a new stroke volume of 72.2 ± 31.4 nl ($p < 0.05$). Even though the average stroke volume

decreased by about 50% across all animals, individual differences varied greatly, with the largest decrease as high as 75% in one animal, while stroke volume increased in one animal by 13% post-craniectomy (Fig. 5.3). Reduced pulsatility was distinguishable in some animals from diminished flow voids in the T_2-weighted FSE images (Fig. 5.4). There was no significant change in ventricular volumes following craniectomies ($p = 0.28$).

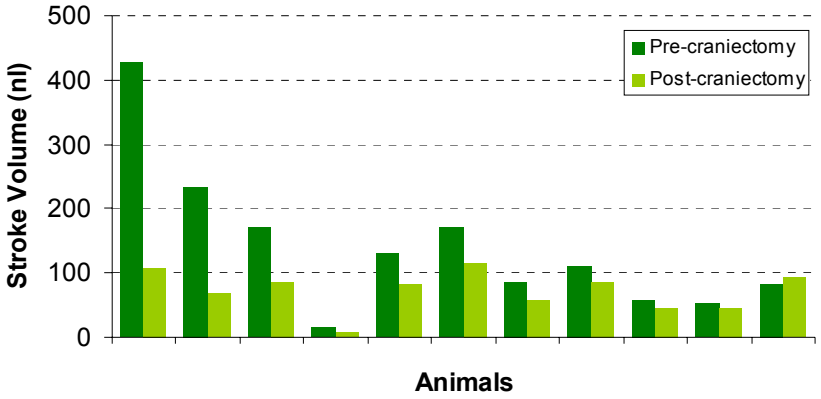

Figure 5.3: Change in stroke volume after bilateral craniectomy.
Aqueductal CSF pulsatility was measured by stroke volume (SV), which decreased in all but one animal following bilateral craniectomy. The drop in SV varied across the animals.

To investigate whether the decrease in stroke volume was related to the animals' ventricular sizes, correlations were computed between decrease in stroke volume and ventricular volume (Fig. 5.5). A weak correlation was found between these two parameters ($R = 0.64$, $p = 0.04$), but this was most likely driven by the animal with the highest ventricular volume; exclusion of this point from the regression computation results in no correlation ($R = 0.13$, $p = 0.72$).

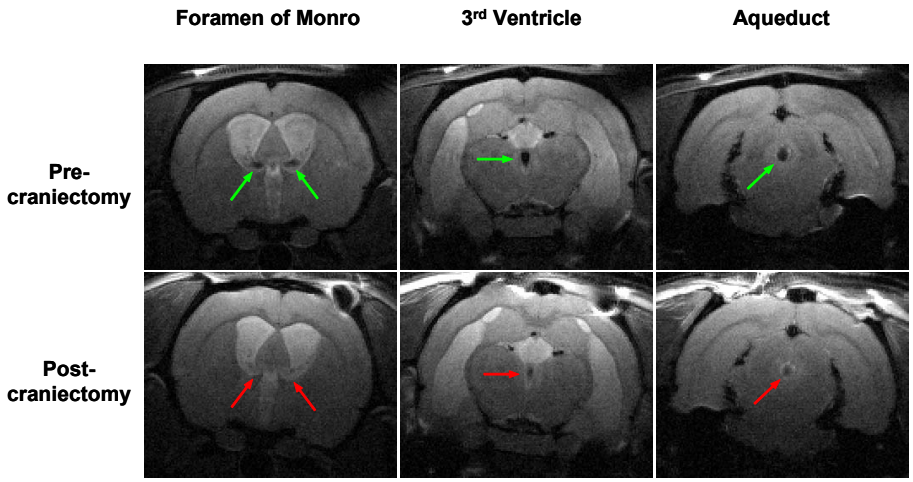

Figure 5.4: Coronal MRI images before and after craniectomy.
T_2-weighted FSE images of the craniectomy animals showing lateral ventricles before and after craniectomy. Reduced pulsatility was evident from diminished flow voids in T_2-weighted FSE images. Prominent flow voids were present in this animal before craniectomy (upper images, green arrows) at the aqueduct (right), parts of the 3rd ventricle (middle) and at the foramen of Monro (left). Flow voids decreased at all 3 locations (red arrows) in the same animal immediately after craniectomy.

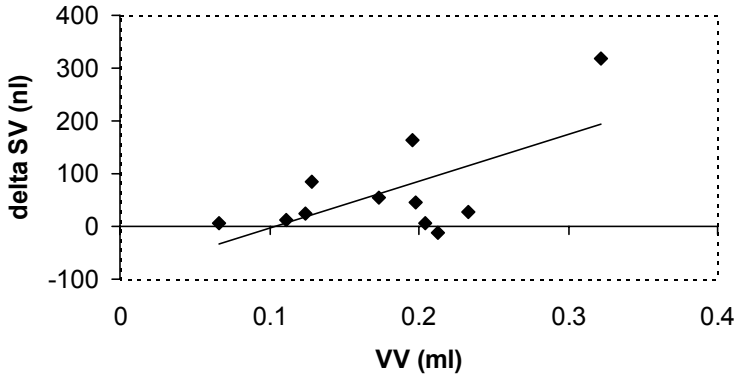

Figure 5.5: Correlation between change in stroke volume and ventricular volume.
Regression analysis between change in stroke volume and ventricular volume was carried out to investigate whether there the drop in stroke volume was associated with ventricular volume. Since bilateral craniectomies were expected to produce the same increase in compliance in all animals, variation in stroke volume change indicated that the initial compliance in each animal was different, and may depend on ventricular size. A weak correlation was found ($R = 0.64$, $p < 0.05$), but this seemed primarily driven by the right-most data point, removal of which gives rise to no significant correlation ($R = 0.13$, $p > 0.1$). This suggests that the initial compliance was not related to ventricular size in the CH animals.

5.3.2 Shunting

Mild to severe levels of hydrocephalus developed in 5 of the 8 animals induced for shunting; the remaining 3 animals in which hydrocephalus failed to develop (ventricular volume < 20 µl) were excluded. One animal was sacrificed because it was sick due to severe hydrocephalus, and was deemed unlikely to survive the shunt surgery. One animal died during shunt surgery.

Shunt surgery was done successfully in 3 animals. In 2 animals, after shunt insertion, some blood appeared in the shunt, followed by clear CSF. CSF with no blood appeared on shunt insertion in the third animal. MRI images immediately following shunting (Fig. 5.6) showed that the shunts had been inserted at the correct position. Hyperintensity within the shunt indicated presence of CSF.

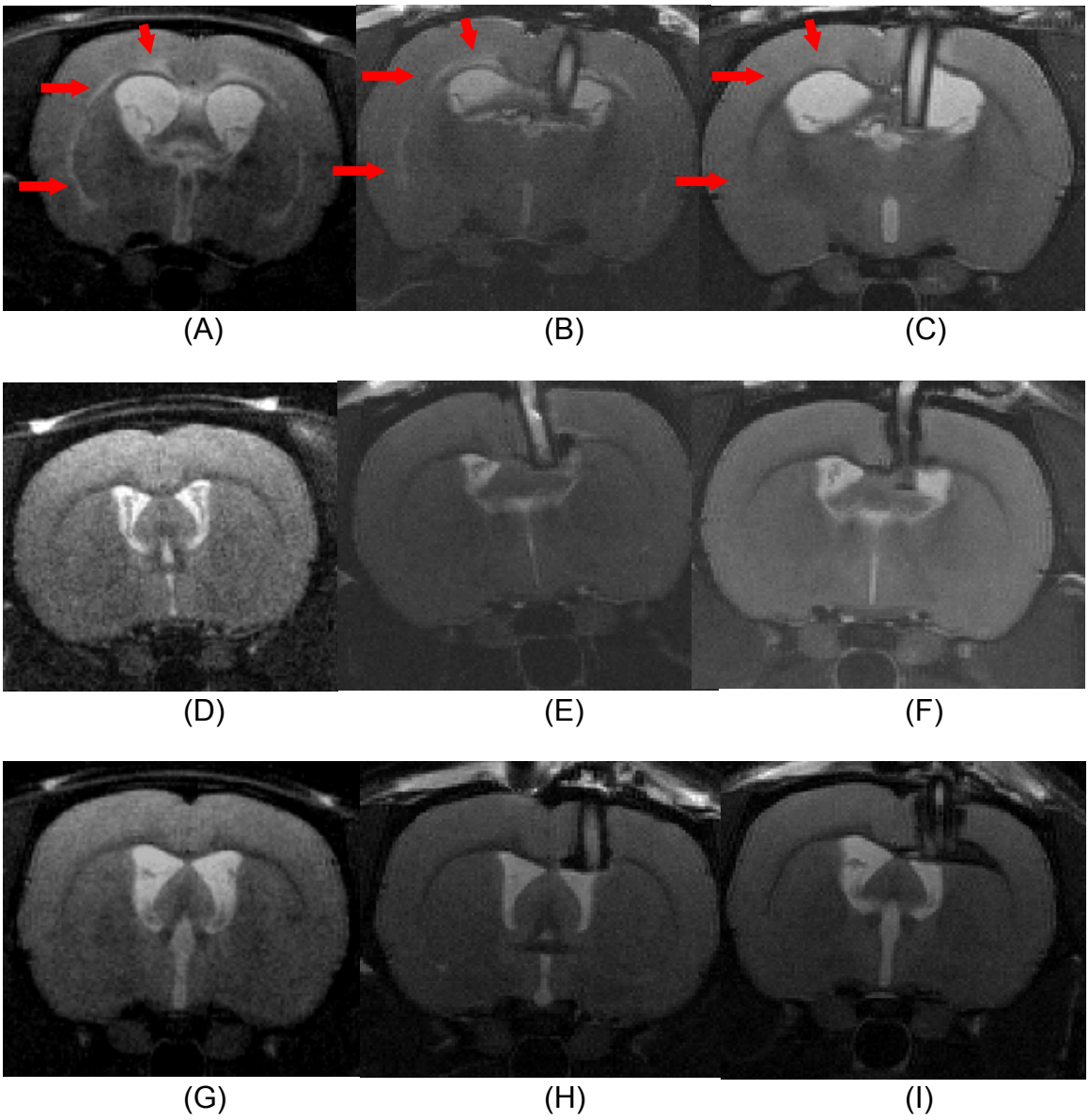

Figure 5.6: Coronal T_2-weighted FSE images before and after shunting.
Changes in ventricular size with the placement of a shunt are evident in these are T_2-weighted FSE images of the three shunted animals at the level of the foramen of Monro at different points in time. The left column represents images of the animals immediately before shunting (A, D, G); the center column represents the same images immediately after shunting (B, E, H) and the right column represents images 1 week after shunting (C, F, I). The proximal end of each shunt entered the ventricle, and hyperintensity in the shunt indicates presence of CSF. The shunt in the third animal appears to be obstructed at 1 week post shunting (I). In one animal, periventricular edema (red arrows) was prominent before shunting (A), but decreased immediately after shunting (B) and was further diminished 1 week after shunting (C).

Following shunting, there were immediate changes in both aqueductal pulsatility and ventricular size in all animals. Ventricular volume dropped from 63.9 ± 34.9 µl to 43.5 ± 19.7 µl, with the largest drop of 46% in one animal. Aqueductal stroke volumes also dropped from 27.8 ± 20.4 nl to 10.6 ± 2.7 nl, with the largest drop of 70% in one animal (stroke volume data immediately after shunting was available in only two animals). In addition, in one animal there was a significant decrease in periventricular edema immediately following shunting (edema typically is present only in animals with severe ventricular dilation, and thus was not present at any point in the other two animals).

MR images one week after shunting showed that aqueductal stroke volume remained lower than the pre-shunt stroke volumes, and comparable to the values obtained immediately after shunting. Ventricular volumes one week after shunting remained unchanged in one animal; however, in the other two animals, ventricular volumes increased back to the pre-shunt values. Periventricular edema in one animal decreased immediately after shunting and was not evident one week after shunting (Fig. 5.6 A-C) (the other two animals did not exhibit edema (Fig. 5.6 D-I)).

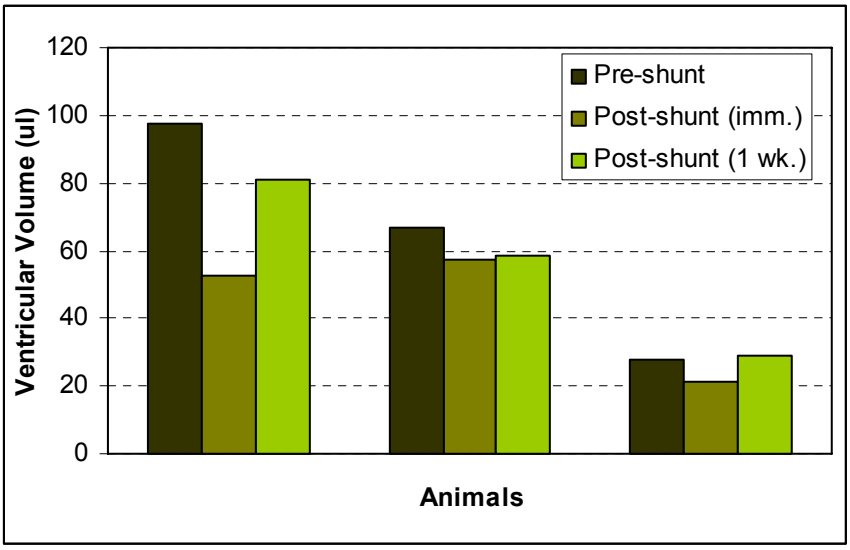

Figure 5.7: Changes in ventricular volume with shunting.
Ventricular volume in the animal with the largest ventricles dropped sharply immediately after shunting, but returned close to initial value after one week. Changes in ventricular size in the other two animals were smaller.

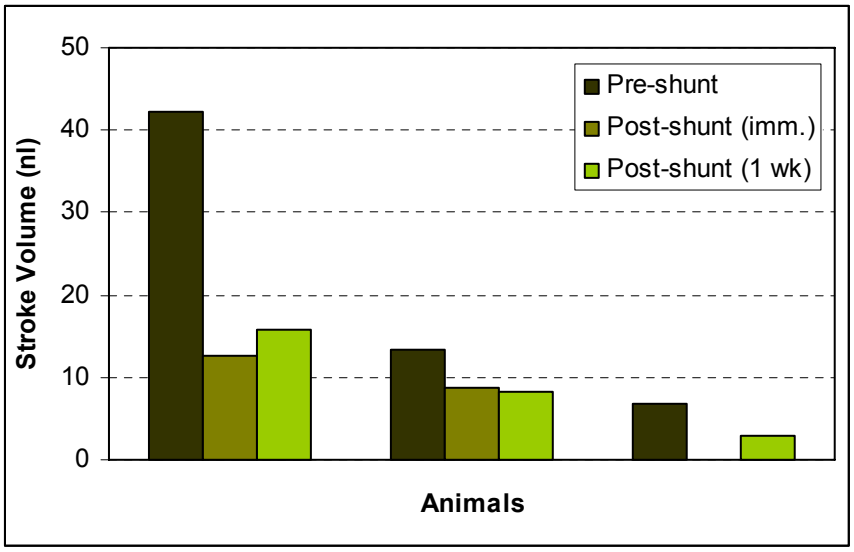

Figure 5.8: Changes in stroke volume in the shunted animals.
Stroke volume (SV) dropped sharply in the animal with the largest ventricles and highest SV; SV dropped less in the others. SV remained decreased after one week (pulsatility data immediately after shunting was unavailable in the third animal).

5.4 Discussion

This study was undertaken to explore the effects of altering compliance on aqueductal stroke volume in order to gain a clearer picture of the role of CSF pulsatility in communicating hydrocephalus (CH), understand the variability seen in the pulsatility and ventricular dilation in our animal model and elucidate the functional relationship between pulsatility and ventriculomegaly. We used two techniques for modulating compliance: bilateral craniectomy and shunting. PVI measurements in animal models show that compliance increases with craniectomy [100, 207]. This is because the main limit on intracranial compliance is placed by the rigid skull, which restricts the volume expansion of the brain's CSF or vascular spaces. Increase in volume of one of these fluid compartments causes decrease of volume in another compartment, and this fluid expulsion takes place through the relatively narrow foramen magnum or venous outlets. Removal of the calvarium removes this restriction, and thus increases intracranial compliance.

One of the main results of this study is that there was a significant decrease in aqueductal pulsatility (measured as the stroke volume) with increased compliance. It was expected that intracranial pressure pulsations would decrease when the compliance increases [201, 203]. Our results show that this is indeed the case. However, the link between stroke volume and intracranial pressure pulsatility has not been fully explored, although it is thought that the two quantities are related [208]. If we assume that the relative compliance change in all animals was the same, because the size of the craniectomy was kept constant, then the net compliance change after craniectomy should depend on the initial compliance. It is also reasonable to assume

that the initial compliance depends on the ventricular size, so one may expect the change in SV to be correlated with VV. However, we did not find such a correlation, which indicates that the initial compliance does not depend on the extent of ventricular dilation. It is possible that compliance changes in hydrocephalus may be a consequence of fibrotic scarring and kaolin distribution in the subarachnoid space, both of which obstructs CSF flow in the subarachnoid space, as well as gliosis of the cortical gray matter and periventricular white matter [168, 200]. If this is the case, the stroke volume may be considered to be indicative of the extent of neuroinflammatory reactions in the hydrocephalic brain and thus provide valuable information regarding the pathophysiology of hydrocephalus. Further study of correlations between the stroke volume and histopathological results of neuroinflammation are needed to explore this hypothesis.

Shunting drains CSF from the ventricles, causing a reduction in ventricular volume. In terms of the volume-pressure relationship, this implies that the animal's intracranial state moves down along the pressure-volume curve (see Fig. 5.2), giving rise to increased compliance. This would be expected to give rise to a decrease in aqueductal stroke volume. Our results show that stroke volume does decrease immediately after shunting (see Fig. 5.7). This effect is particularly prominent in the animal with the largest initial ventricular size. A rapid decrease in stroke volume is expected after shunting due to increased compliance. Over time after shunting, the compliance may increase further if the shunting reverses neuroinflammatory reactions that take place with the development of hydrocephalus [200]. Neuroinflammation has been shown to occur following ventricular dilation [167, 200], and it is known that it can

reverse partially with shunting [23, 209]. This is further supported by the change in periventricular edema in the animal with the largest ventricles (Fig 5.3.4 A-C). Neuroinflammation may also contribute to reduced compliance [168, 200]. Thus, reduction in neuroinflammation may cause a further increase in compliance, which may cause a further decrease in stroke volume. It is also possible that the shunt serves to keep the stroke volume reduced, by providing an alternate pathway for CSF flow. A clinical study which follows NPH patients over time after shunting shows that stroke volume does decrease progressively after shunting [210].

One of the main limitations of this study is that pressure measurements were not available in our animal model of communicating hydrocephalus. Compliance, as defined by Marmarou, is the ratio of volume change to pressure change when a small volume of fluid is input into the craniospinal system [201, 204]. As described earlier, removal of the calvarium alters the compliance. It was thought that a model could be designed using pressure-volume index (PVI) values from the literature and an estimation of how much it may decrease following craniectomy or shunting, and fit out data to this model to elucidate the relationship between stroke volume and ventricular size. However, one difficulty in doing this is that PVI data on rats is limited. The only data available in the literature involves H-Tx rats [146, 148, 187, 211]. This is not ideally applicable in our communicating hydrocephalus model because the congenital H-Tx rat represents a model of obstructive hydrocephalus produced by aqueductal stenosis. Moreover, the H-Tx rat represents a pediatric model of hydrocephalus, because H-Tx rats with hydrocephalus survive no more than a few weeks after birth. Finally, the PVI data available on H-Tx rats varies widely from one study to another. One study reports PVI

values of 0.05 in hydrocephalic animals, while other studies report values 10-fold higher [187, 211]. Therefore, modeling of the effect of compliance changes was deemed unreasonable until reliable pressure-volume data can be obtained in our animal model.

Other factors which may affect the degree of ventricular dilation and aqueductal stroke volume in these animals are variations in kaolin distribution in the basal cisterns and the extent of neuroinflammation, which we have not measured. Kaolin distribution in these animals is unknown. We attempt to inject kaolin into the subarachnoid spaces of the basal cistern, but the injection is blind, and we cannot directly confirm the final site of kaolin deposit. We know that hydrocephalus induction often fails if kaolin is injected into a compartment other than the subarachnoid spaces (see §4). We also do not know the degree of neuroinflammation and fibrotic scarring caused by kaolin in these animals. Some investigators suggest that kaolin causes extensive neuroinflammation and obliterates the entire subarachnoid spaces. We argue that this is not the case, since we use a relatively small volume of kaolin, and the fourth ventricle outlets are found to be open [9, 152]. However, we have not done a systematic study of the distribution of kaolin in the basal cistern and the degree of neuroinflammation and fibrotic scarring it produces. Such a study would be extremely valuable and may provide significant insight into the issue of variability in the relationship between ventricular size and stroke volume.

We have recently found that the aqueductal stroke volume can vary significantly with physiological parameters such as the rate of respiration. This is could be a potential source of variability in stroke volume. The rate of respiration is related to blood gas levels, particularly the partial pressure of carbon dioxide, P_{CO2}. Numerous studies have

shown that in hypercapnia, increased levels of P_{CO2} can cause vasodilation of the microvasculature. Dilated arterioles and capillaries can give rise to an increase in intracranial CSF pulse pressure, which may cause the aqueductal stroke volume to rise. Indeed, Portnoy et al. have shown the CSF pulse pressure to be elevated in rats under hypercapnic conditions [212, 213]. However, they did not make any measurements of CSF flow, so it is not possible to determine from their study whether CSF stroke volume is affected. On the other hand, low respiration rates can give rise to hypoxia, which may decrease the systemic blood pressure. Reduced blood pressure could give rise to a lower CSF pulse pressure and decrease the stroke volume. Since we have neither blood gas measurements nor data on intracranial pressure, we cannot do more than speculate on the actual physiological state of our animals and what effect this has on stroke volume. Needless to say, it is very important to carry out studies measuring the effect of varying physiological parameters on stroke volume, including blood pressure, heart rate, respiration rate and blood gas levels, as well as different levels of hypercapnia and hypoxia. Such a study may also provide a wealth of information that could explain the variability seen in aqueductal stroke volume in our animals. In fact, data recently obtained in five CH rats showed a dramatic increase in stroke volume with decreased respiration rate.

In the craniectomy experiments, we did not observe any changes in ventricular size. This is not unexpected, since it is likely that alterations in ventricular size will take more than the few hours that we allowed these animals to survive after craniectomy. However, a better experiment to test the effect of compliance on both stroke volume and ventricular volume would be to allow the animals to survive with the craniectomies

for several days and measure any change in both ventricular volume and stroke volume. If decreased compliance is tied to the level of ventricular dilation, then increased compliance may well cause a decrease in ventricular volume over a period of days. These potential changes in ventricular volume will be very interesting to observe, particularly in relation to changes in stroke volume, which we know decreases immediately after craniectomy.

A more intriguing question is: what is the effect of compliance on hydrocephalus development, e.g. when hydrocephalus is induced *after* craniectomy? In such an experiment, a bilateral craniectomy, identical to the ones we produced in this study, would be followed by induction of hydrocephalus with kaolin, and the development of hydrocephalus would be monitored. We in fact conducted this experiment on 3 rats. None of the animals developed any appreciable level of hydrocephalus, in terms of ventricular dilation or aqueductal pulsatility. While this could be an indication that the increased compliance produced by the craniectomy causes the ventricles to not dilate, the small number of animals precludes statistical comparison and prevents us from drawing any solid conclusion. However, we did see an effect in one of the animals that may be significant. This animal had mild ventricular dilation, but it had quite severe periventricular edema normally seen only in animals with severe hydrocephalus. This may be an indication that increased compliance caused by the craniectomy does not affect the neuroinflammatory reactions that are associated with hydrocephalus following ventriculomegaly, even though this increased compliance is halting ventricular dilation and preventing elevated CSF pulsatility. Again, this is another area that needs to be

investigated more thoroughly, as it might provide great insight into the various processes involved in CH and their interrelationships.

Chapter 6

---

6. Capillary Pulsatility in Communicating Hydrocephalus

6.1 Introduction

The etiology of elevated aqueductal CSF pulsations in CH is unknown, as discussed above (§2 & §4). One of the theories posited to explain this phenomenon is that obstructions to subarachnoid CSF flow prevents adequate dissipation of arterial-driven pulsations, which are instead redistributed into ventricular CSF via the cerebral microvasculature [6, 8]. Consequently, this would give rise to elevated microvascular pulsations. While this theory has been touched upon in the literature, no one has yet attempted to provide experimental evidence to support this theory. The present study

was designed to investigate this theory in a rat model of CH. The following three hypotheses will be tested:

- Blood flow and pulsatility in capillaries can be measured in the rat neocortex down to a depth of 600 μm using two-photon microscopy.
- Pulsatility of neocortical capillaries will be elevated in CH rats following kaolin induction and will persist into the long-term stages of the disease
- Elevated capillary pulsatility will be correlated with aqueductal CSF pulsatility in CH rats.

6.1.1 Intracranial Dynamics in the Normal Brain

The rationale behind these hypotheses are best understood by first considering intracranial dynamics in the normal brain (as summarized in Fig. 6.1A). With each heartbeat, a large volume of blood enters the brain, causing a systolic expansion of brain arteries and arterioles, which is a consequence of the windkessel mechanism whereby systolic arterial expansions give rise to steady flow. This causes the brain to expand as a whole in systole, and contract back in diastole, i.e. the brain “pulsates” with each heartbeat, a fact which is well documented in the MRI literature [7, 8, 214, 215] and known from neurosurgical experience. When the brain expands in systole, it compresses the CSF filled subarachnoid spaces (SAS), causing CSF to flow out of the SAS through the craniocervical junction (CCJ) into the spinal thecal sac. The flow reverses in diastole. This gives rise to pulsatile CSF flow in the CCJ, which has been measured in humans [70, 92, 216, 217]. In this way, arterial pulsations entering the brain are normally dampened via the windkessel mechanism [218] and coupled into

subarachnoid CSF. This also gives rise to extracerebral venous pulsatility, since the dural sinuses and extracerebral veins can also be compressed during systolic brain expansion.

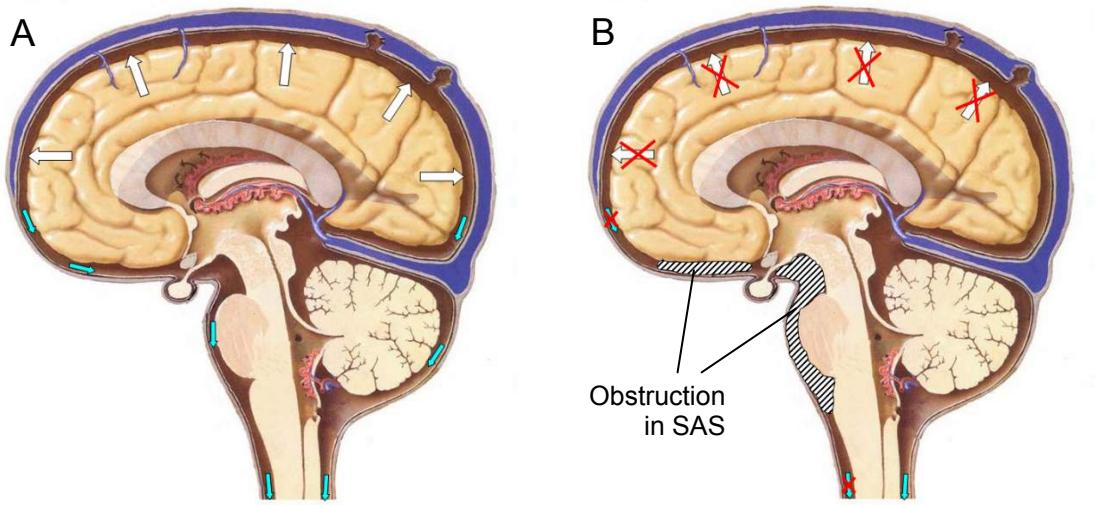

Figure 6.1: Pulsatile dynamics in the normal and CH brain.
With each heartbeat, the normal brain "pulsates" (A); this is due to systolic expansion of cerebral arteries and arterioles, which causes the brain to expand as a whole during systole (white arrows). This compresses the subarachnoid spaces (SAS), causing CSF to flow out of the cortical spaces into the spinal thecal sac through the foramen Magnum (blue arrows). In CH, obstruction in the SAS impedes CSF flow through the SAS, which in turn impedes systolic brain expansion (B). Brain images modified from [11].

It has been hypothesized that the systolic pulse in the normal brain are dissipated by the internal carotid and basilar arteries into subarachnoid CSF when these vessels pass through the prepontine/basal cisterns of the subarachnoid spaces [6, 71, 72]. While it is certainly possible that some part of the arterial pulse is dissipated in the basal cisterns, it is very unlikely that the majority of the pulse is dissipated here, because that would require approximately 25% expansion of the arteries, which is certainly not seen in clinical MRI. On the other hand, it is more likely that in the normal

brain, the arterial pulse causes the brain to expand as a whole in systole, as discussed above. If the brain expands outwards by as little as 20 μm, this would be sufficient to displace approximately 600 μl of CSF and blood via the CCJ (when modeling the brain as a half-sphere with diameter 14 cm), which falls within the range of the stroke volume of CSF across the CCJ in normal humans [70, 92].

6.1.2 Elevated Intracranial Pulsations in CH and Pulsatility Redistribution

In CH, obstruction of the SAS increases resistance to CSF flow in the SAS. This very likely counteracts the systolic whole brain expansion, which reduces the ability of arteries and arterioles to expand in systole, diminishing the transfer of arterial pulsations into subarachnoid CSF and veins and producing a decrease in CSF pulsatility at the foramen magnum [7] (Fig. 6.1B). With the removal of this major pulsatility dissipation pathway, arterial pulsations can propagate undampened into the cerebral microvasculature and can cause increased brain pulsatility, which acting on the walls of the lateral ventricles would produce increased ventricular CSF. So, this pulsatility redistribution theory, first proposed by Greitz [8], predicts that undampened arterial pulsations will be transmitted into the microvasculature, and should be detectable as increased flow pulsation in cerebral capillaries.

6.1.3 Goals and Objectives

The primary purpose of this study was to test the theory that microvascular pulsations are indeed elevated in CH, and that these are associated with elevated

aqueductal flow pulsations. To understand the connection between ventricular CSF pulsations and pulsatility at the capillary level, it is important to appreciate that almost all pulsatility in the brain is cardiac in nature and originates from arterial vasculature. However, the route of pulsations from the arteries into the ventricles is still debated [6, 8, 74, 80]. Since no studies have demonstrated increased *arterial* pulsations in CH (in fact, studies have shown decreased intracranial arterial pulsations [219]), increased ventricular CSF pulsations in CH most likely arise from changes in the transfer and dissipation of arterial-driven pulsations within the cranium.

In this study, we used two-photon laser-scanning microscopy [220, 221] to quantify microvascular flow pulsations *in vivo* and to probe their changes with the development of hydrocephalus. Using our at model of CH, discussed in §3 and §4, we studied capillary pulsatility at both the acute and chronic phases. Our main objectives were to determine the normal levels of capillary pulsatility in the rat neocortex, whether this pulsatility is elevated in communicating hydrocephalus, and to what extent pulsatility is related to aqueductal CSF pulsations and the degree of ventriculomegaly.

6.2 Background: Two Photon Microscopy

Two-photon microscopy, the most commonly used type of multiphoton microscopy [222], is a novel, specialized fluorescence-based imaging technique that uses multiphoton excitation to generate optical images. It has many similarities to, as well as advantages over, confocal microscopy, and is becoming more and more prevalent across laboratories and research institutes.

Multiphoton excitation is based on a concept first postulated by the physicist Maria Goeppert-Mayer, who developed the theory of two-photon quantum transitions in atoms in her doctoral thesis in 1931 [223]. Two-photon excitation fluorescence was first observed in 1961 following the development of the laser. From then, multiphoton excitation was considered to be an exotic phenomenon that was mainly used in physical chemistry and optical spectroscopy, and was of little practical use until the development of the first two-photon microscope in 1990 by Winfried Denk, James Strickler and Watt Webb [220].

To understand why two-photon microscopy represents such a significant breakthrough, it is important first to briefly describe the advantages of confocal microscopy over widefield (conventional light) microscopy, and then to describe the disadvantages of confocal microscopy. Widefield microscopy, which includes fluorescence microscopy as well as other forms of light microscopy (such as phase contrast and polarization microscopy) produces images of specimens by illuminating the entire specimen and using its optical system to bring the light from the specimen into focus at the eyepiece. Widefield microscopy is ideally suited to specimens which consist either of thin sections (such as those produced by a microtome), cells or tissue prepared on a glass slide or in-vitro cells/tissue cultured on a plate.

However, when three-dimensional whole structures needs to be imaged, or in-vivo tissue are imaged, widefield microscopy is at a disadvantage. Widefield microscopy does not attempt to restrict light from out-of-focus planes within the specimen. This is not needed when imaging thin slices, but represents a problem when imaging whose tissues or in-vivo structures. Light from out-of-focus planes within the specimen will also

enter the specimen and tend to blur the image significantly. Only structures at or close to the surface, within a depth of 10-20 μm, can be clearly visualized. Deeper structures will be difficult to visualize. Issues with blurring and out-of-focus illumination can be somewhat overcome using computational techniques such as deconvolution microscopy, but these applications are limited.

6.2.1 Confocal Microscopy

Confocal microscopy overcomes these difficulties by using a pinhole aperture to restrict light entering the objective to a single focal plane. The term “confocal” was coined to bring across this concept. By eliminating light from out-of-focus regions of the specimen, confocal microscopy is able to generate high resolution images with high contrast and great clarity. An example is shown in Fig. 6.2. In addition, it can produce images down to maximal depths of 100 μm in the specimen, giving rise to in-vivo optical sectioning of images [224]. As is evident from the figure, however, confocal imaging can only interrogate one “point” at a time. Thus, a technique is required for “scanning” the focal plane to produce an image. A few different methods exist, such as the Nipkow-Yokogawa spinning disk, where a spinning disk containing numerous precisely-positioned pinholes is used to scan the sample, and laser scanning microscopy, which is also the technique used in two-photon microscopy (described below).

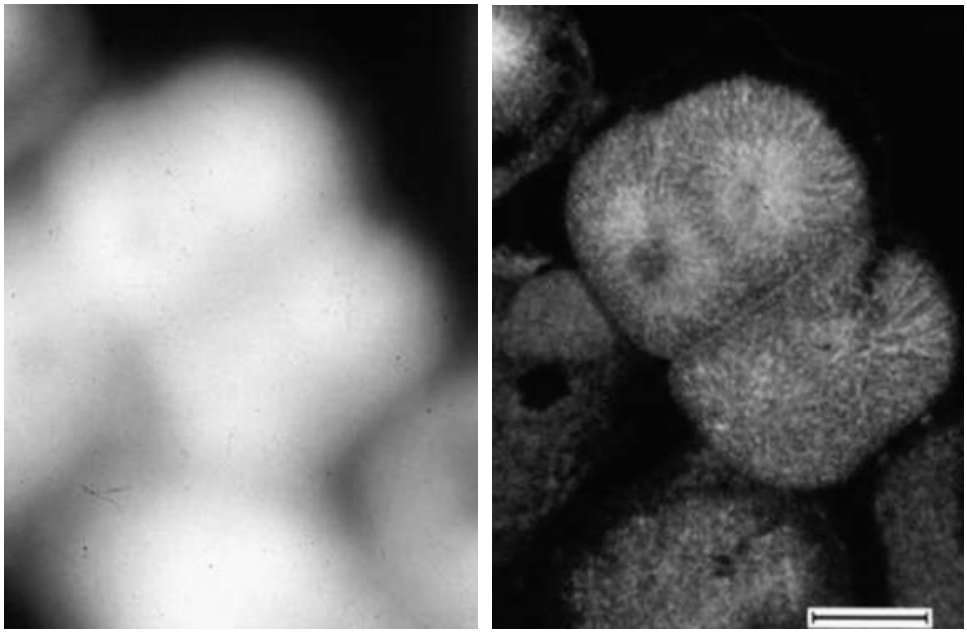

(A) (B)

Figure 6.2: Improvement in images from widefield to confocal microscopy. The same specimen is shown as viewed through a normal light (widefield) microscope (A) and through a confocal microscope (B). Out-of-focus light rejection significantly improves resolution and makes small structures visible. Modified from [225].

The main disadvantage of confocal microscopy is that a large segment of the specimen is illuminated, but light from only a small segment is used to generate the image. In fact, in specimens a few hundred microns thick, more than 99% of the emitted fluorescence light is wasted, giving rise to considerable but unavoidable photobleaching and photodamage [226].

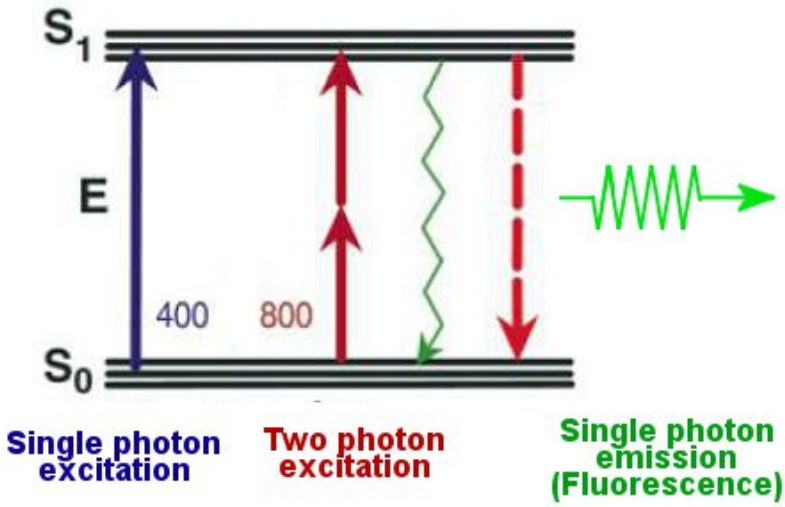

Figure 6.3: Jablonski diagram showing single and multiphoton excitation. Single photon excitation occurs when the fluorophore absorbs one photon, whereas multiphoton excitation occurs when the fluorophore is excited by multiple photons simultaneously. Modified from [227].

6.2.3 Two Photon Laser Scanning Microscopy

Two photon microscopy is based on the two photon excitation process. In one photon excitation (the process used in fluorescence and confocal imaging), each fluorophore is excited to a higher energy level by a single photon of a specific wavelength (or wavelength range). When the fluorophore returns to its ground state, it releases a photon, which is detected as the fluorescence emission in a sample. In two photon excitation, fluorophores are excited by the simultaneous absorption of two photons, each with half the energy or twice the wavelength required for single photon excitation of that fluorophore (Fig. 6.3). This implies that most commonly used fluorophores would be excited by infrared light instead of visible light. Once the fluorophore returns to its ground state, it emits a photon of the same wavelength as in

single photon excitation. However, the probability of two photon excitation is extremely low; “simultaneous” absorption of two photons requires an interval of less than 10^{-18} s for the two photons to reach the fluorophore [222]. Under normal arc-light conditions, the likelihood of such an interaction is practically zero. Two photon excitation requires a photon flux of 10^{20}-10^{30} photons/cm^2-s, and this is currently achieved in a focal volume with the use of pulsed femtosecond lasers, which generate high-intensity, ultrashort pulses of light [222]. The main advantages of two photon microscopy over confocal and widefield microscopy stem from the two photon excitation process:

- Localized excitation. Since two photon excitation requires such large photon flux, it only takes place at a small focal volume in the sample; the imaging process is inherently confocal and there is no out-of-focus excitation (Fig. 6.4).
- Increased depth penetration. Infrared light, owing to its longer wavelength, is scattered less in tissue than visible light, and consequently this makes deep tissue imaging possible (Fig. 6.5). The theoretical maximum depth in two photon microscopy is about 1 mm [228].
- Reduced photodamage and photobleaching: Since the only excitation/emission takes place at the focal volume, there is far less photobleaching. Moreover, because of the use of infrared light, there is far reduced photodamage in the light cone (Fig. 6.6).

The main drawback of two-photon microscopy is that the pulsed femtosecond laser sources remain very expensive.

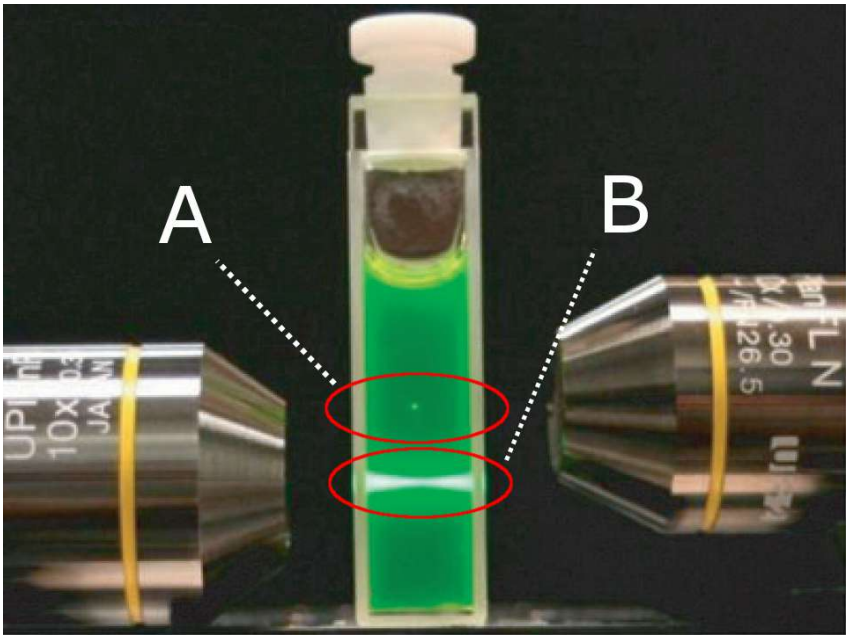

Figure 6.4: Difference between two-photon excitation and confocal excitation. Localized excitation is demonstrated by excitation and emission of light only at the focal volume (A) in two-photon excitation, when the intensity becomes very high. No out-of-focus excitation takes place. In contrast, fluorescence or single-photon excitation occurs throughout the whole light cone in confocal imaging (B). Out-of-focus light has to be eliminated by use of a pinhole aperture. Modified from [222].

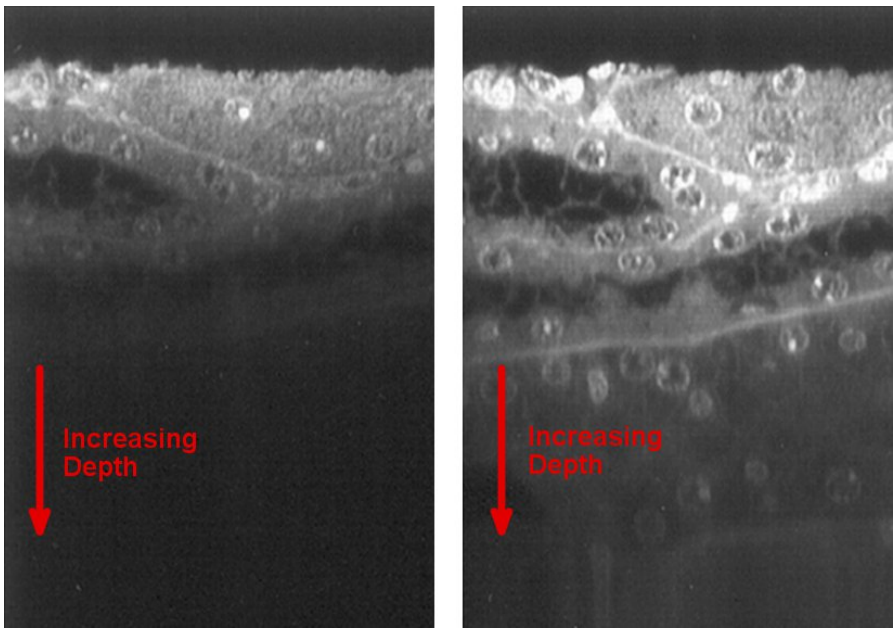

(A) (B)

Figure 6.5: Depth penetration in between confocal and two-photon microscopy. In a confocal microscopy image (A), depth penetration is as large as 100 µm, which is a factor of 10 smaller than in multiphoton microscopy (B). Modified from [225].

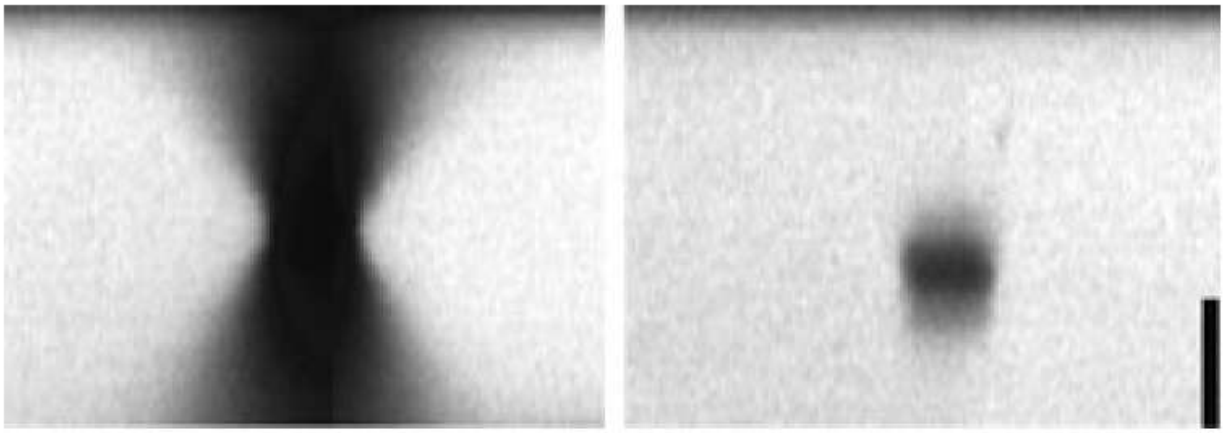

(A) (B)

Figure 6.6: Reduced photobleaching in two-photon microscopy. The photobleaching effect seen in confocal microscopy (A) is significantly reduced to only a small focal volume in two-photon microscopy (B). Modified from [222].

Laser scanning microscopy is one of the image scanning techniques used in confocal microscopy, and the only scanning technique used in multiphoton microscopy. In this method, two computer controlled galvanometer mirrors are used to position the focused laser beam onto the specimen [224]. The oscillating mirrors scan the beam across the specimen in a raster pattern along an *x-y* plane, and return the light from the illuminated spot to the photodetector. The signal from the photodetector is sampled over the scanning time and correlated with position of the focused beam to construct the *xy* image of the specimen being scanned [224]. By adjusting the oscillation of the mirrors, the path of the beam can be controlled over time and produce low or high resolution images of the specimen. A schematic of a two-photon microscope is shown in Fig. 6.7.

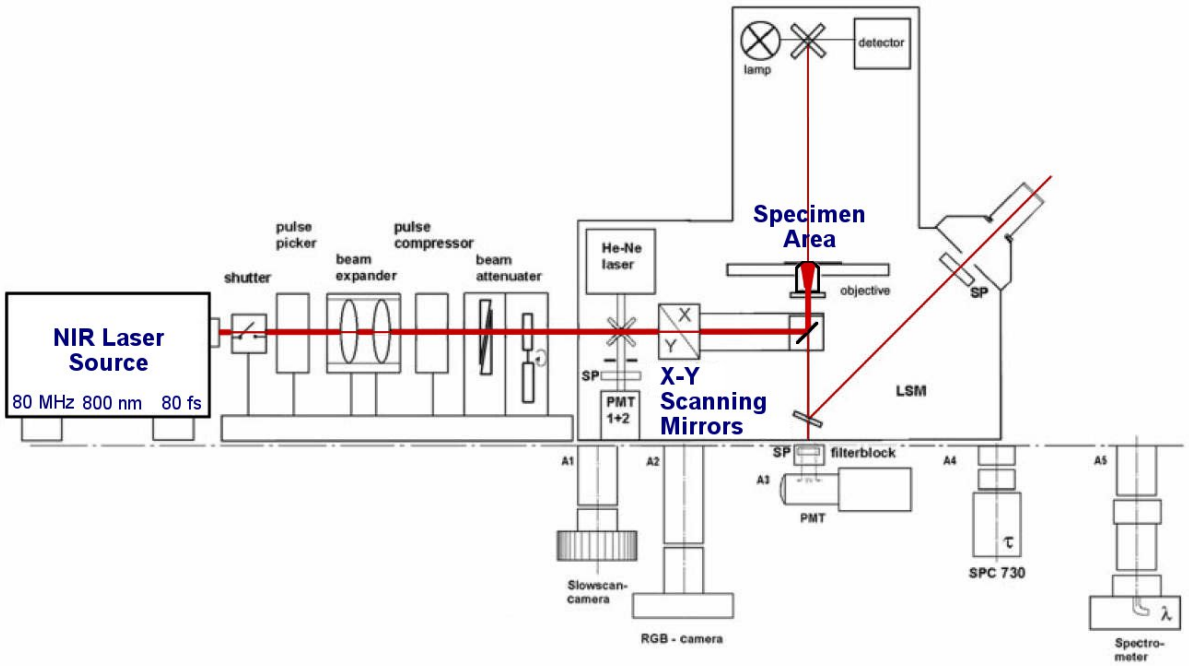

Figure 6.7: Schematic of a laser scanning microscope.
The X-Y scanning unit consists of a pair of oscillating mirrors that scan the light beam across the sample in a raster pattern along the x-y plane. The right is returned through the objective and directed to the photomultiplier tube (PMT) via a dichroic mirror. Modified from [227].

Three- and higher-photon excitation work in the same way as two-photon excitation, except 3 or more photons simultaneously excite the fluorophore. Three photon microscopy has been used in some studies, but three and higher photon excitation are unlikely to see wider application because it would require the use of wavelengths higher than 1100 nm, and water has high absorption for wavelengths above 1100 nm, while water absorption is much lower at 790-900 nm (the spectrum commonly used for two-photon microscopy) [229].

6.3 Methods

All animal handling and surgical techniques were approved by the Institute of Animal Care and Use Committees (IACUC) of Stony Brook University and Albert Einstein College of Medicine. All experimental procedures were carried out in accordance with the NIH Guide for Care and Use of Laboratory Animals. All efforts were taken to minimize any suffering of the animals and the number of animals used in experiments.

6.3.1 Experimental Design, Timeline & Animal grouping.

All animals used in this study were adult female Sprague-Dawley rats of weight 200-250g. After the surgical, experimental and data acquisition techniques were optimized, capillary velocity data was collected in a group of 5 control rats. Data analysis techniques were designed and optimized using this control set (§6.3.6), after which experiments were conducted on CH rats. A second group of 5 control animals

were also included afterwards, giving a total of about 250 vessels in the control dataset. One surgical control animal (§3) was also included.

CH was induced in 16 rats by the basal cistern kaolin injection technique (§3). Capillary flow and pulsatility was measured in 8 animals at the acute stage of CH, 5-7 days post induction (acute group), and in the remaining 8 animals at the chronic stage of CH, 3-5 weeks post induction (chronic group). Ventricular dilation and aqueductal CSF pulsatile flow was characterized in the CH animals a few days prior to microscopy by MRI using the techniques described in §4, and the ventricular volume (VV) and aqueductal CSF stroke volume (SV) were quantified. All animals were euthanized at the end of the imaging session in this study.

6.3.2 Rat Head-holder

For these experiments, a custom stereotaxic head-holder with ear bars, an incisor bar and a nose restraint was designed by our lab and constructed by the Physics Machine Shop at SBU. The head-holder, with an animal in place, is shown in Fig. 6.8. A standard stereotaxic head-holder could not be used because it was too large to fit under the two-photon microscope. Animals were secured on the head-holder for both the duration of surgery and microscopy. During microscopy, the head-holder was screwed down to the specimen base of the microscope.

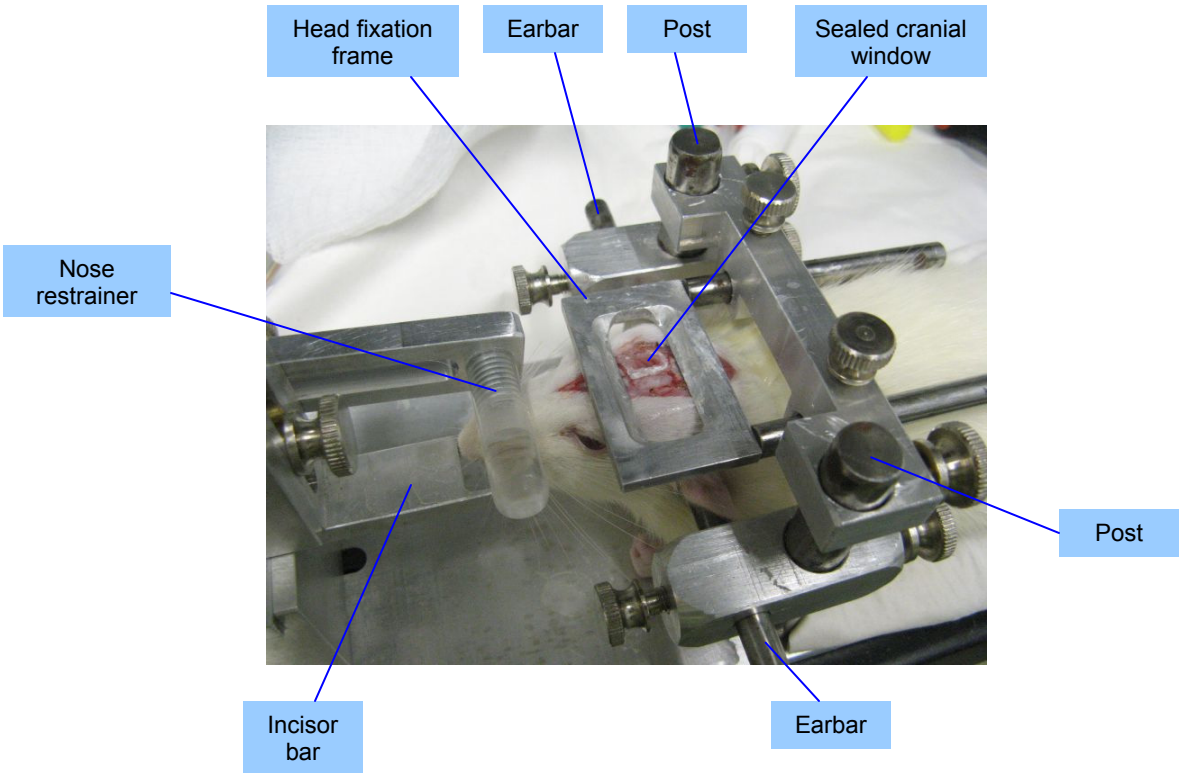

Figure 6.8: Stereotaxic head holder used in the microscopy experiments. The stereotaxic head-holder was used to stabilize the animal's head for the cranial window surgery. The head-holder shown here has an animal with a sealed cranial window and the head fixation frame affixed.

6.3.3 Choice of Anesthesia

Ketamine-xylazine (70/7 mg/kg) was the anesthetic used in these experiments, delivered by bolus IP injections. An initial full dosage was used to induce anesthesia, which was subsequently maintained by 50% supplements at approximately 45 minute intervals or as needed. Xylazine was administered in every other supplement, as it has a longer half-life than ketamine. Pentobarbital was initially used as the anesthetic; however, it severely depressed the cardiovascular system, and requires operation close to the lethal dose; on a few occasions, the animal died in the middle of the experiment (~2-3 hours after start). The ideal anesthetic was isoflurane, because of its ease of use

and stability induced in the animal [230], but was not available at the SBU multiphoton microscope facility.

6.3.4 Surgical Techniques & Cranial Window

An optically transparent cranial window was opened in the right parietal bone to provide access to neocortical capillaries for multiphoton microscopy. The animal was anesthetized and secured on the head-holder. The head was shaved, a 2” midline incision was made, running from between the eyes to the back of the head, and the underlying tissue was removed to expose the skull. Bleeding was controlled by cauterization and applying pressure. A 5 x 3 mm craniectomy was made using a hand-held drill equipped with a 0.7 mm drill bit. The craniectomy was positioned over the right parietal bone, centered approximately 5 mm posterior and 2.5 mm lateral to Bregma. The craniectomy was made by thinning the bone along the periphery and then carefully removing the bone flap with forceps. The drilling area was irrigated frequently with cold saline to prevent heating of the underlying tissue; the dura was left intact in all animals. Bleeding often occurred from the dura, on account of blood vessels that passed from the dura into the periosteum. This was controlled by rinsing and applying pieces of a styptic pad.

The cranial window was completed by filling the craniectomy with warm (~45 °C) 1% agarose and covering it with a custom-cut (6 x 4 mm) No. 1½ glass coverslip, which was then sealed to the skull with cyanoacrylate gel, ensuring no air bubbles were introduced. The sealed cranial window served to maintain normal intracranial pressure and flow dynamics. In some animals, after removal of the bone flap, the brain surface

would be exceedingly cloudy due to bleeding under the dura. This usually happened due to excess heating of the brain (when the drilling was done too rapidly) or if the drill broke through the bone and damaged the dura. These animals were euthanized and removed from the study.

After the cranial window was sealed, a 4.5 x 2.5 cm metal frame with a 3.2 x 1.2 cm opening was attached to the skull with cyanoacrylate (with the cranial window at the center of the opening) and fixed to the earbar posts of the head-holder (Fig. 6.8). This "head-fixation" frame was used to further minimize head motion caused by respiration. Because the capillaries being imaged are 5-8 μm in width, motion as small as 3-4 μm was enough to prevent successful acquisition of capillary images. Initial experiments, in which we did not use the head-fixation frame, produced images with severe motion artifacts and did not yield useful data.

6.3.5 Fluorophore Choice and Delivery

Fluorescein isothiocyanate (FITC), conjugated to dextran of molecular weight 70 kDa, was the fluorophore of choice (Sigma, St. Louis, MO). FITC-dextran was dissolved in 1M PBS at a concentration of 40 mg/ml, in accordance with product manuals. The dextran solution distributes evenly in the animal's circulation, and is not taken up by RBCs, effectively labeling blood plasma. Dextran conjugated fluorophores are frequently used in multiphoton studies of capillary flow [221, 231]. The excitation/emission wavelengths of fluorescein are 494/521 nm. Optimal two-photon excitation of FITC-dextran in blood was 800 nm; this was the wavelength used for the two-photon laser.

In an effort to increase the maximum depth attained, we attempted to use rhodamine B isothiocyanate dextran (70 kDa). Rhodamine B has higher excitation/emission wavelengths of 540/621 nm, as well as a larger two-photon absorption cross-section, and thus has a higher quantum yield. Because of its higher excitation/emission wavelengths, we expected it would give greater depth penetration into brain, since higher wavelength light scatters less in tissue. However, resulting images were far poorer and noisier because the microscope filter sets were not optimized for rhodamine B, and rhodamine B was discarded as a possible fluorophore.

The FITC-dextran solution was delivered intravenously through a tail vein. In all animals, one of the lateral tail veins was cannulated with a 0.75”, 24G catheter, capped by an injection plug. After cannulation, the catheter was flushed with about 0.3 ml heparinized saline (5-10 units of heparin per ml). The main advantage of tail vein cannulation is that it requires no surgery and is rapid, requiring only minutes to insert, as opposed to femoral vein cannulation. However, it is also much more difficult to ascertain patency of the tail vein catheter since the vein is narrow and difficult to visualize.

6.3.6 Microscopy and Data Acquisition

Multiphoton microscopy was carried out at the Central Microscopy Imaging Center at Stony Brook University (SBU). This center was equipped with an upright Olympus BX60WI microscope (Olympus America Inc., Center Valley, PA), powered by a 1.7 W Chameleon laser (a Ti:Sapphire femtosecond laser) (Coherent Inc., Santa Clara, CA), and equipped with 10x and 60x water immersion objectives (NA = 0.3 and 0.9). Imaging was controlled by the software FluoView FV300 running on a PC.

After the cranial window surgery was completed, the animal was positioned in the microscope and 0.5 cc of the fluorophore was injected through the tail vein. The fluorophore labels blood serum but is not taken up by red blood cells (RBCs), causing them to appear as dark moving objects against the bright, labeled serum.

Capillaries were imaged at 2-4 non-overlapping sites within the cranial window with a total of 20-40 capillaries in each animal, at depths of 40-500 μm. All depths were measured from the pial surface. They exclude the thickness of the dura and cover cortical layers 1-3; the dorsal edge of layer 4 is approximately 500 μm from the pial surface in control rats. Capillaries were visualized by 2D planar scans (Fig. 6.9), which were later used for vessel diameter determination. Capillaries selected for imaging had a straight in-plane length of at least 20 μm. Individual line scans were approximately 16 seconds long with temporal resolution of 1.6 ± 0.3 ms per line and spatial extent of 26 ± 4 μm at the SBU facility.

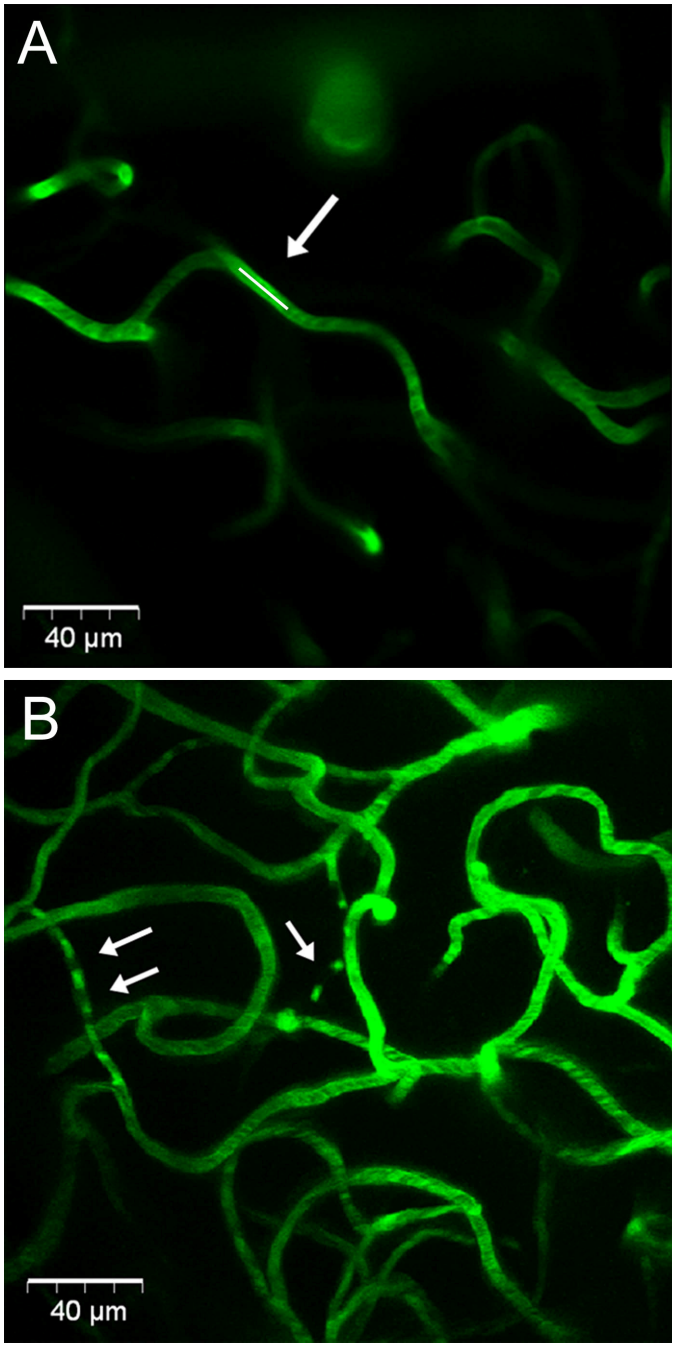

Figure 6.9: A 2D planar image and a MIP of a capillary network.
Capillaries were located from 2D planar images such as the one shown here (A) at a depth of 160 µm, in a control animal. The white line indicates the scan-line, over which the capillary was scanned (A). A maximum intensity projection (MIP) is produced by stacking a number of 2D planar images, such as the one shown here (B) in a chronic CH animal, in the depth range of 185-250 µm. The bright signal in the capillaries are produced by two-photon excitation of FITC-dextran, which labels the blood plasma, but is not taken up red blood cells. White arrows indicate vessels with flowing red blood cells, which appear as dark voids against the bright labeled plasma (B).

Capillary velocity measurements were made by acquiring “line-scan” images. A line-scan is an image consisting of diagonal bands, which are formed by flowing RBCs. The formation of a line-scan is described pictorially in Fig. 6.10. In a line scan, a line (the scan-line) along the central axis of the capillary is imaged rapidly, repeatedly over time (Fig. 6.10). The lines are stacked vertically to form the line-scan image, in which the vertical axis is the time dimension, and the horizontal axis is the spatial dimension along the capillary’s central axis. Therefore, each moving RBC forms a diagonal dark band, or streak, in the line scan image. The vertical “height” of each band represents the time taken by the RBC to move along the scan line, while the horizontal “width” of the band, i.e. the length traversed by the RBC, is the length of the scan-line. Therefore, the inverse slope of each band is the velocity of the RBC (Fig. 6.11).

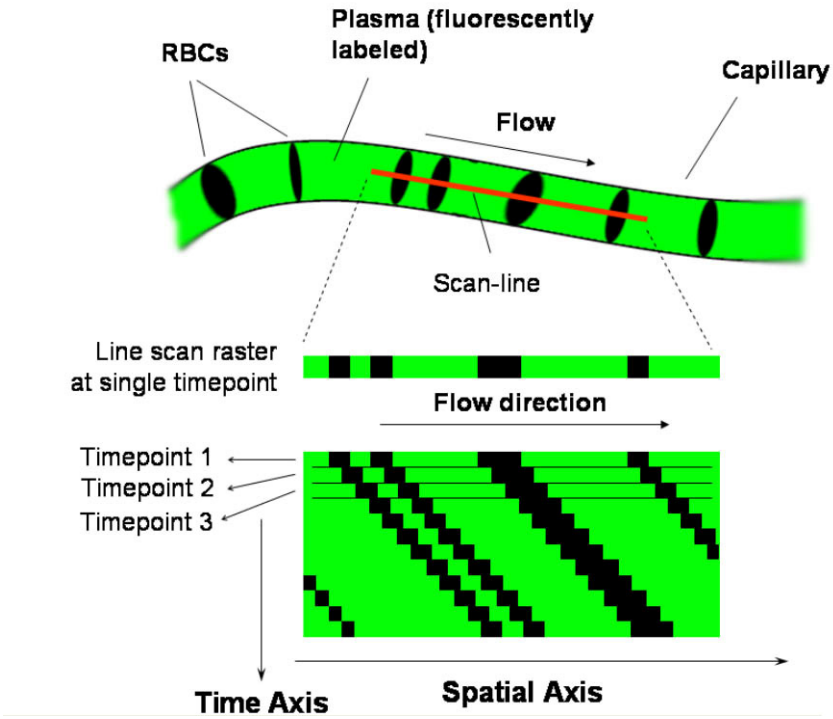

Figure 6.10: Formation of a line-scan.
A line-scan image is formed from multiple, repeat acquisitions over time of the same line (the scan-line) along the central axis of a capillary, as depicted in this cartoon. In a line scan, the horizontal axis represents the spatial length of the scan line, while time increases along the vertical axis. In any single scan-line, each non-fluorescent-labeled RBC appears as a dark band against a bright backdrop of fluorescence-labeled serum. Each successive line is stacked beneath the previous acquired line in the image. As a result, moving RBCs form diagonal dark bands. The horizontal extent of each band represents the distance traversed by the RBC, while the vertical extent represents the time taken to traverse that distance. Thus, velocity of each RBC is given by the inverse of the slope of the RBC band (*i.e.*, rapid-moving RBCs have shallow slopes and slow-moving RBCs have steep slopes), as shown in Fig. 6.11.

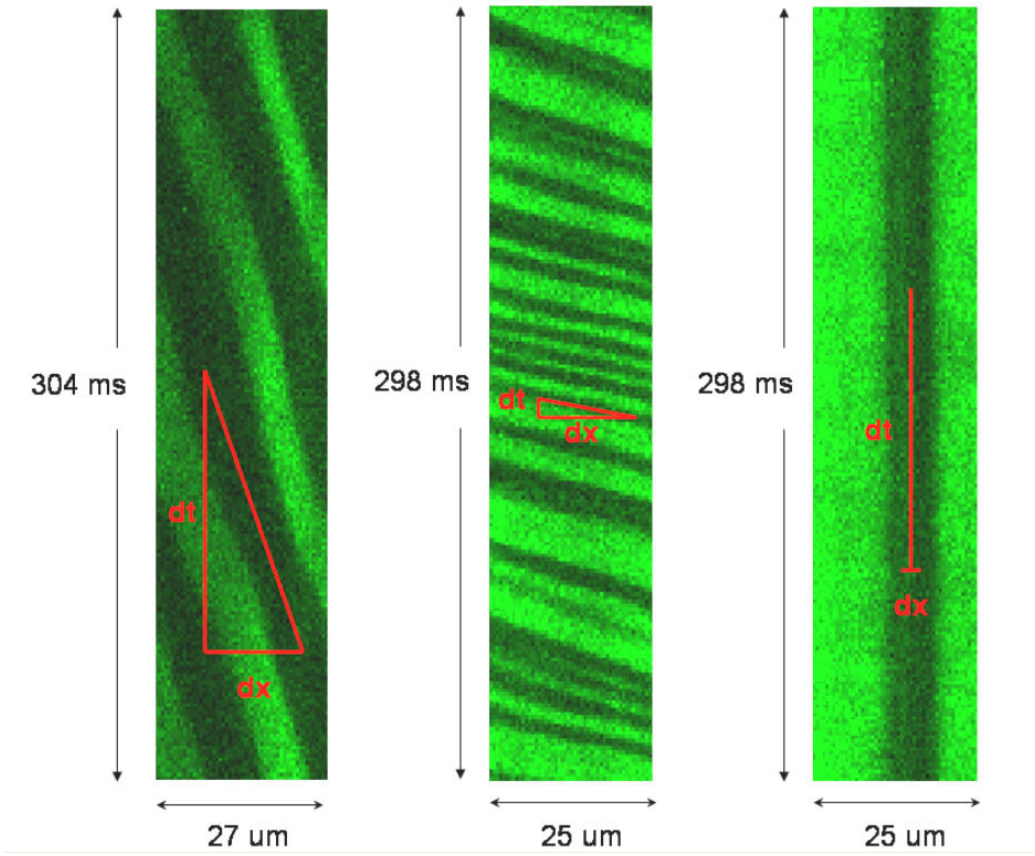

Figure 6.11: Examples of line-scan images.
Flowing RBCs form diagonal dark bands. These line-scans have RBCs with slow flow (left), rapid flow (middle) and no flow (right, *i.e.* position of the RBC in the capillary does not change with time). Velocity is measured by dx/dt, *i.e.* inverse of the slope of the RBC bands.

ECG was acquired during experiments for anesthesia monitoring and heart rate determination for the data processing. ECG was acquired using a clinical ECG monitor (Propaq Encore 204EL, Protocol Systems Inc., Beaverton, OR), using a 3 electrode system, with the electrodes connected to the animal's paws with electrode gel and tape. The analog output signal was captured from the monitor using a 4-channel NIDAQ data acquisition module (NI 6008, National Instruments). ECG data was acquired using a program written with Matlab's Data Acquisition Toolbox, allowing both real-time monitoring and recording of the ECG signal.

6.3.7 Data Analysis

All image processing and data analysis was carried out using programs written on Matlab (The Mathworks, Natick, MA). Statistical analysis was carried out using SAS, as described later. The data analysis techniques described below were designed and optimized after the control dataset was acquired.

In order to measure pulsatility of blood flow from the line-scan, a method was needed to measure velocity as a function of time along the line-scan. Because this implied a large number of measurements for each line-scan, an automatic program to measure the slopes of the RBCs in the line-scans was developed. In the literature, all applications of line-scans measured an average velocity of blood flow, which required a single measurement of the RBC slope in a line-scan [221, 231, 232]. The challenge in this study was to quantify the velocity as a function of time, in order to discern the *changes* in velocity as a function of time, which would allow measurement of pulsatility.

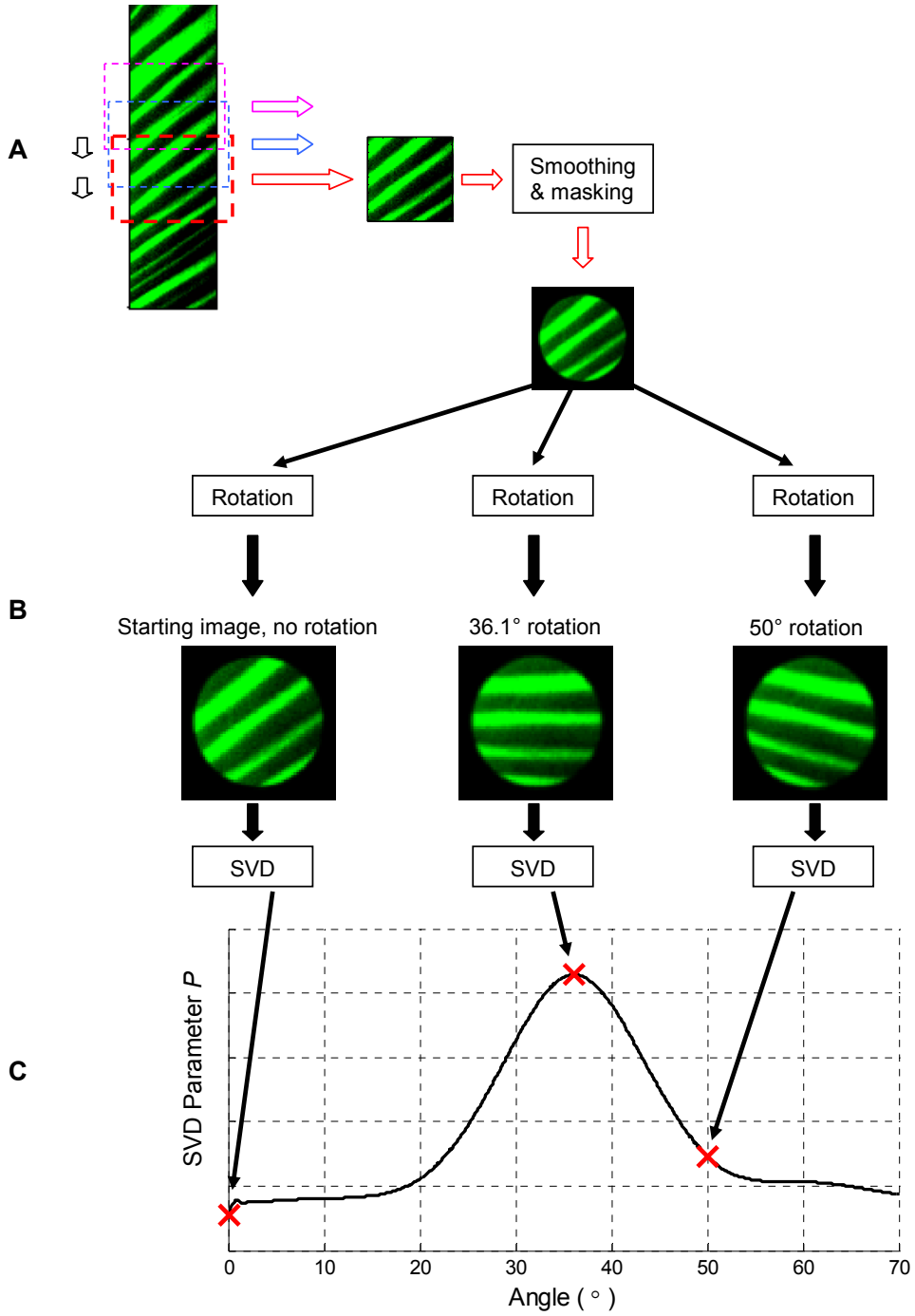

Figure 6.12: Demonstration of the SVD algorithm.
Each line-scan is split into overlapping segments (A), and each segment is smoothed and masked. The segment is rotated incrementally through a range of angles (B), and for each angle, the SVD parameter *P* (which equals the first singular value squared divided by the sum of all singular values squared). *P* produces a maximum at the angle at which the RBC bands in the segment become horizontal. In this example, the angle is 36.1°, which corresponds to a velocity of 1.51 mm/s.

6.3.7.1 The SVD Algorithm

The analysis algorithm for velocity measurement from line-scans was based on an SVD technique, first described by Kleinfeld et al. [221], which can detect the angle or slope of the RBC bands in a line-scan image. The algorithm scheme is shown in Fig. 6.12. Each line-scan image is divided into overlapping segments. The algorithm computes the average slope of the RBC bands in each segment. Each segment is resized so that it is square (if needed), smoothed, and masked with a circular mask, to remove the corners of the square, as these sometimes interfere with the SVD computation. Each segment is rotated incrementally through a range of angles, and at each increment, an SVD parameter, *P*, is calculated for the segment:

$$P(\alpha) = \frac{(s_1(\alpha))^2}{\sum_{n=1}^{m} (s_n(\alpha))^2} \qquad (1)$$

where s is a m x 1 array of the singular values from the SVD computation of the image segment of size m x m, rotated by the angle *α*. The SVD parameter *P* has a maximum at the rotation angle where the bands in the rotated image segment become horizontal or vertical. By identifying this peak and the corresponding rotation angle, the slope of the RBC bands in the segment is determined. Velocity is calculated from the inverse of the slope. The algorithm is then repeated for all segments to produce a velocity waveform for the entire line-scan image.

Since each line-scan segment produces a single data point for the velocity waveform, the temporal spacing between adjacent segments, or segment stepsize, determines the resolution of the waveform. The segment size (i.e. number of scan-lines in the segment) determines the magnitude of the averaging effect. The segment size

was 30 scan-lines (~45 ms), and adjacent segments were separated by 10 lines (~15 ms). Segment size and stepsize were chosen by taking into consideration velocity accuracy, desired temporal resolution in velocity waveform and computational speed. Calculations were initially performed at a lower temporal resolution, with a stepsize of 30 lines (~45 ms), but this produced a statistically significant drop in PI for all animals of 6-10% compared to the higher temporal resolution analyses (the discrepancy was discovered during statistical analyses, where we found that results with higher heart rate were being underestimated; the underestimation occurred because at a temporal resolution of 45 ms, velocity waveforms at a heart rate of 6-7 Hz would be undersampled, containing only 3-4 datapoints per cardiac cycle, causing pulse amplitudes to be artifactually lower). To identify the optimal segment size and stepsize, a group of line-scan images were reanalyzed at several different segment sizes and stepsizes, from which the high-resolution segment size and stepsize of 30 and 10 lines were selected. While the higher temporal resolution also led to more vessel measurements being excluded due to spike artifacts (at higher resolution, periods with no RBC's become more frequent), we felt this was the better choice to ensure accurate PI measurements.

Rotation of the line-scan segments was carried out using the *imtransform* command from Matlab's Image Processing Toolbox, using the affine transformation matrix S:

$$S = \begin{pmatrix} \cos(\alpha) & \sin(\alpha) & 0 \\ -\sin(\alpha) & \cos(\alpha) & 0 \\ 0 & 0 & 1 \end{pmatrix} \qquad (2)$$

where α is the counter-clockwise rotation angle. The *imtransform* command was used instead of the simpler *imrotate* command, because for “loose” transformations (where the resulting image is large enough to contain the entire rotated image, and is generally larger than the original image), the *imtransform* command can fill the background (region outside the original rotated image) with any predefined value, whereas the *imrotate* command fills the background only with zeros.

Preprocessing

Before the SVD algorithm could be used, several preprocessing steps had to be applied to all line-scan images. All files had to be checked visually to determine the orientation of the bands, i.e. whether the slopes of the bands were positive or negative. Images with negative slopes were flipped along the left-right dimension. Because the SVD parameter produces a peak when RBC bands are either horizontal or vertical, it was necessary to ensure that the RBC bands had a positive slope, and restrict the rotation range between 0 and 90°. Also, several line-scan images had “dark” edges, where the scan-line extended outside the vessel. These edges had to be “trimmed”, otherwise they can produce artifacts in the algorithm. Trimming was done automatically for good quality images and manually by mouse-clicks for poorer images, and was verified visually.

Iteration Scheme

The SVD algorithm was a very time consuming computation process, since querying angles in the range 2-85°, at increments of 0.5°, requires over 160 rotation transformations and SVD computations for each of the 1000 segments in each line-scan image. On the lab PC (1.86 GHz Intel Pentium M processor, Intel Corp., Santa Clara, CA) each line-scan image required 15 minutes of computation time to be analyzed. To speed up the process, an iteration scheme was devised where angles were queried at 7° intervals in the first iteration (typical SVD peaks spanned 15°). The highest value would be presumed to lie at the SVD peak, and angles would be queried over a smaller range centered at the highest value in the next iteration. Four iterations were required to locate the peak with an accuracy of 0.3°. This iterative scheme reduced number of computation steps by a factor of over 4 and provided greater accuracy. An accuracy of at least 0.5° was necessary, because at a mean velocity of 2 mm/s, an angle difference of 1° corresponds to a velocity difference of 0.25 mm/s.

6.3.7.2 Pulsatility Index Calculation

Pulsatility was calculated from the Fourier transform of the velocity waveform, using the method employed by Czosnyka et al. [233]. Pulsatility was quantified from the velocity waveforms with the Gosling pulsatility index (PI), which is typically calculated in the time domain from the ratio of the mean peak-to-peak amplitude of the waveform to its mean velocity [234]. However, in order to limit pulsatility calculations to cardiac-induced pulsations, PI was computed in the frequency domain from the Fourier

transform of the velocity waveform by integrating over the cardiac frequency peak and its second harmonic, which were identified using the animal's heart rate extracted from the ECG waveform. This integral was then divided by the first bin of the Fourier transform, which corresponds to the mean velocity, to produce the PI. The pulsatility was computed in quadrature, i.e. the Fourier transform was squared before computation of the integral over the cardiac peaks, and the square root of the integral sum was calculated. A baseline, computed from the average of the spectral points immediately adjacent to the peaks, was subtracted from the Fourier transform prior to PI calculation, to remove the effects of background noise at the cardiac frequency.

To evaluate whether the quadrature integration was appropriate or needed, a group of files with clean, noise-free velocity waveforms were selected, and their PI in the time domain was calculated by detecting peaks and troughs and computing amplitudes from the mean. The PI was also calculated in the Fourier domain in quadrature and with a linear integration (non-quadrature). It was found that the temporal pulsatility (which was the true, gold-standard pulsatility) did not match the linear integration, but matched the quadrature integration, although the quadrature values were slightly lower than the temporal values in all cases. This can be explained because the quadrature method captures the pulsatility due to only the cardiac frequency components, while the temporal method cannot avoid influence of other frequencies that might be present (such as low frequency oscillations, e.g. respiration). On the other hand, the linear integration overestimates the pulse amplitude because it includes spectral leakage at the edges of the cardiac peaks. Spectral leakage is eliminated in the quadrature technique, and so this is the most suitable method.

6.3.7.3 Noise and Error Handling

In several waveforms, spikes were produced by the SVD algorithm due to noise artifacts caused by respiratory motion or abnormal flow (low RBC flux). Spikes are produced in image segments with no RBCs, which have no recognizable features for the velocity calculation. The SVD algorithm was adjusted to correct the more severe spikes. Less severe spikes were removed with a median filter. Averaging filters were applied to the input image before SVD, which helped reduce noise. There were a number of good images with segments of noise, where either the vessel momentarily moved out of the scan line (due to respiratory motion), or the flow stopped momentarily or reversed. In extremely poor images (the RBC bands in such images were barely visible by eye), SVD analysis produced waveforms with too much noise. Because of these issues, after SVD was done, all waveforms were visually inspected. Waveforms that contained too many spikes or too much noise were discarded. In images with an unusable segment (due to motion or stopped flow), only the usable portion was selected out and used to compute pulsatility. These procedures were carried out using Matlab scripts.

6.3.7.4 Vessel Width Calculation

Capillary diameters were measured from 2D planar scans by selecting a profile perpendicular to the axis of the capillary, averaged over the segment through which flow was measured. A flat topped function with Gaussian edges was fit to this profile, and diameter was measured as the full-width at half-maximum of the function.

6.3.8 Modifications in Techniques for Experiments at AECOM

After the microscopy studies at SBU were completed, we repeated the experiments on a group of animals at Albert Einstein College of Medicine (AECOM). AECOM was equipped with a two-photon microscope in which the optical system was optimized for *in vivo* animal studies, as opposed to the SBU facility which was originally designed for *in vitro* studies. In addition, isoflurane was available as an anesthetic at the AECOM microscopy facility.

6.3.8.1 Experimental Design

All animals studied at AECOM were adult female Sprague-Dawley rats of weight 200-250 g. Capillary flow and pulsatility data were acquired in 8 animals at the acute stage of CH, which was 5-7 days after induction (acute group). Ventricular dilation and aqueductal CSF flow was measured in these 1-2 days prior to microscopy. Stroke volume (SV) of aqueductal CSF and ventricular volume (VV) were quantified using the techniques described in §4. Capillary flow and pulsatility was also measured in 12 intact controls and 2 saline controls (control group).

6.3.8.2 Choice of Anesthesia Delivery

Isoflurane anesthesia was used in these experiments. Anesthesia was induced initially by placing the animal in a plastic induction chamber and using 5% isoflurane mixed with O_2 (1 L/min flow). Anesthesia was subsequently maintained with 1.5-2.5% isoflurane delivered through a nose cone during surgery. For microscopy, the animal

was placed in a clear plastic chamber (the Iso-Chamber) (Fig. 6.13). Isoflurane was delivered into the chamber, providing a stable anesthetic plane throughout the imaging session.

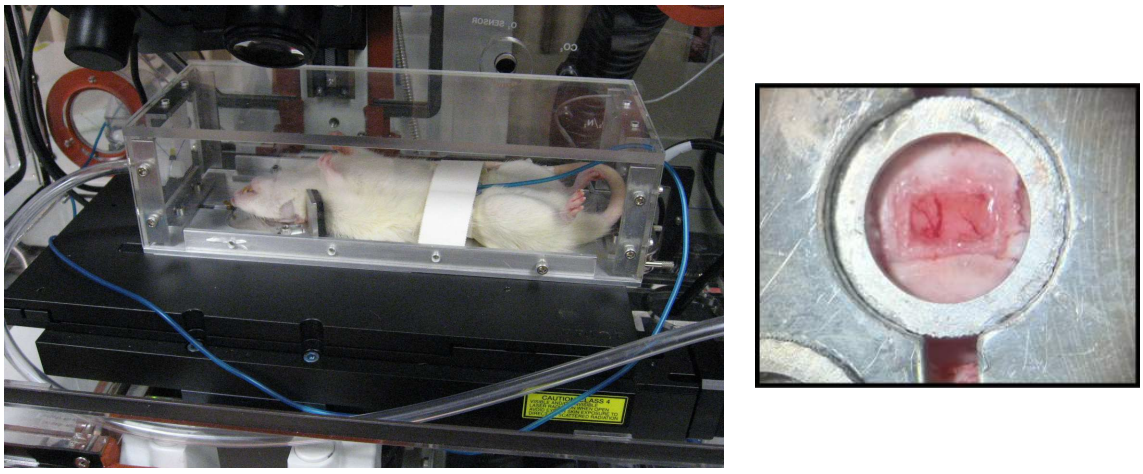

(A) (B)

Figure 6.13: Iso-Chamber used to deliver isoflurane in AECOM experiments. The Iso-Chamber (A) was a clear plastic box into which isoflurane was delivered, producing a stable anesthetic plane throughout the imaging plane. The animal's head was affixed to the base of the Iso-Chamber by means of a ring (B), which was attached to the skull with cyanoacrylate; the ring was then fit into a groove in the base of the Iso-Chamber using cyanoacrylate.

6.3.8.3 Surgical and Head Restraint Techniques

In experiments at the AECOM facility, all surgical procedures were identical to those used at SBU. The primary change in experimental procedure was animal head restraint and placement in the microscope. Craniectomy and cranial window attachment were done with the animal positioned in the head-holder used previously. After the glass coverslip was sealed, an aluminum ring (inner diameter = 10 mm, outer diameter = 14 mm) was attached to the skull with cyanoacrylate gel with the coverslip in the center of

the ring. The animal was removed from the head holder and placed supine in the Iso-Chamber. The ring fit into an opening on the base of the Iso-Chamber, where it was attached with cyanoacrylate gel; this ensured stability of the head and minimized motion. The Iso-Chamber was designed to fit precisely into the inverted microscope above the objective (Fig. 6.13).

6.3.8.4 Microscopy and Data Acquisition

Two-photon microscopy at AECOM was carried out in the Gruss Lipper Biophotonics Center. This facility was equipped with an Olympus IX81 inverted two photon microscope (Olympus America Inc., Center Valley, PA), powered by a MaiTai DeepSee Ti:Sapphire femtosecond laser (Spectra Physics, Newport Corp., Irvine, CA) and equipped with a 25X water immersion objective (NA = 1.05).

Individual line scans were approximately 5 seconds long with temporal resolution of 1.8 ± 0.1 ms per line at the AECOM facility. ECG was captured using a commercial acquisition hardware (Biotrig, Bruker Biospin Corp., Billerica, MA), which allowed real-time monitoring and recording of the animal's respiration and heart rate.

6.3.9 Statistical Analysis

The SBU and AECOM data were analyzed separately. Differences in vessel diameter, vessel depth and heart rate between the experimental groups in each dataset were compared using one-way repeated measures ANOVA. PI for the SBU data were compared among the three experimental groups (acute, chronic and control) using two

linear mixed models, treating repeated measures in each animal as a random effect and controlling for vessel diameter, vessel depth and heart rate (HR), all of which varied randomly within the datasets. In one model, fixed effects of experimental group, diameter, depth and HR on PI were tested. In a second model, three interaction terms group by depth, group by diameter and group by HR were added to the model to test for differences within the groups based on linear variations in PI with these varying experimental parameters. PI for the AECOM data were also compared among the three experimental groups (acute, intact control and saline control) using two linear mixed models, which were identical to those used for the SBU data except that vessel diameters were not available.

Based on the results of these initial models, showing significant group by depth and group by HR interactions, post-hoc analysis was carried out to identify specific subgroups of depth and HR ranges contributing to differences between the groups. PI data of the SBU animals were split into six subgroups: three depth ranges (<200 μm, 200-300 μm and >300 μm) and each with two HR ranges (low and high HR, separated by the median HR of 240 beats per minute (BPM)). Within each subgroup, PI was then compared between experimental groups using repeated measures ANOVA. PI data for the AECOM animals were split into four subgroups: two depth ranges (low and high depth, separated by mean depth of 336 μm) and two HR ranges (low and high HR, separated by mean HR of 346 BPM). Within each subgroup, PI was compared between acute and control animals using one-way ANOVA.

Pearson correlations were used to examine the association between capillary PI (calculated for each animal, averaged over all vessels) and aqueductal stroke volume.

Similarly, Pearson correlations between PI and ventricular volume were also used to determine the relationship between capillary pulsatility and ventricular dilation.

All data are reported as mean ± standard deviation. Normal distribution of data was verified using histograms. Statistical computations were carried out in SAS (SAS Institute Inc., Cary, NC), and results were considered significant at $p < 0.05$.

6.4 Results: SBU Animals

6.4.1 CH Induction Results

Three chronic animals did not develop hydrocephalus and were excluded from analysis. Fig. 6.14 illustrates the marked difference in ventricular size between hydrocephalic and control animals. Mean VV was 132 ± 31 and 77 ± 31 µl for the acute and chronic groups respectively; the difference between these groups was significant ($p < 0.01$). Mean CSF stroke volume (SV) was 256 ± 96 nl and 30 ± 19 nl for the acute and chronic animals respectively; this difference was also significant ($p < 0.01$). While MRIs were not performed on intact control animals, previous studies have shown that these values for both VV and SV are significantly elevated compared to normal control values (VV: 15.5 ± 2.0 µl, SV: 0.72 ± 0.13 nl [152]).

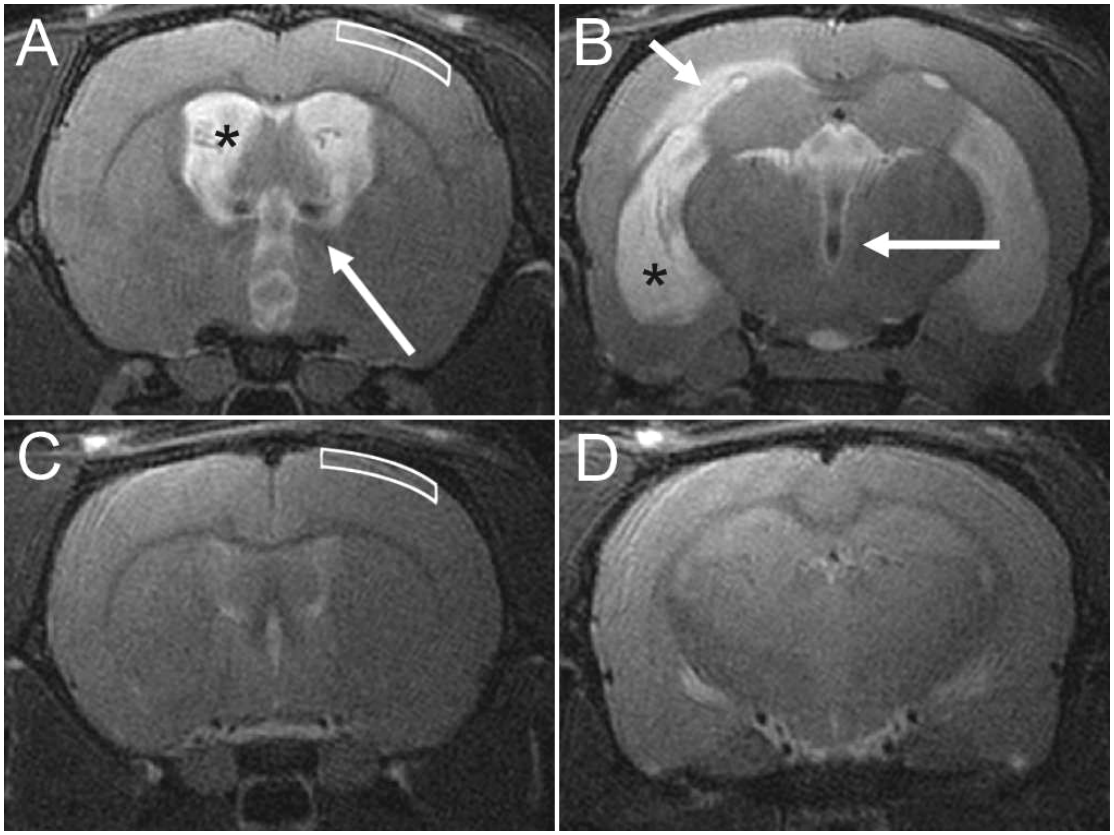

Figure 6.14: Coronal MRI images of a CH and a control animal.
Representative T2-weighted coronal magnetic resonance images at the level of the foramen of Monro (A & C) and the temporal horn of the lateral ventricles (B & D). In the acute CH rat (A & B), the lateral ventricles (asterisks) and third ventricle were markedly dilated. In some animals, the periventricular white matter was edematous (short arrow), and flow voids due to elevated CSF pulsatility were usually noticeable (long arrows). This pattern was also observed in chronic CH animals (not shown). In a control rat (C & D) the lateral ventricles were slit-like and no edema was found in the periventricular white matter. The white boxes (A & C) show the region of the cortex imaged by microscopy, to a depth of about 500 μm from the pial surface, primarily covering cortical layers 2 and 3 (the dorsal edge of layer 4 lies at approximately 500 μm in a control animal).

6.4.2 Image Quality

The maximum depths achieved by microscopy were in the range of 500 μm, which is near the dorsal edge of cortical layer IV. Nineteen percent of line scan images were discarded due to the presence of artifacts, poor quality or abnormal flow. In some

images, cardiac- or respiratory-induced pulsations caused excessive vessel motion and periodic motion artifacts in the line scan images. Images with very low RBC-density resulted in large data segments with no RBCs, and thus no recognizable features for the velocity calculation. This was the primary cause of spikes in the extracted velocity waveform, and as noted above, datasets with less than 4 seconds of continuous RBC motion were excluded. In some vessels, blood flow in a capillary slowed or stopped, and then resumed after a few seconds or even minutes. In rare cases, flow would reverse direction. In images with such artifacts or aberrant flow, the portion of the image containing the artifact(s) or arrested flow was discarded, and only the portion of the image with good contrast was used for velocity waveform analysis.

6.4.3 Depth, Width and Heart Rate

Valid RBC velocity waveforms were collected in 765 capillaries (323 acute CH, 184 chronic CH and 258 intact controls). Average depth of capillaries for all animals was 254 ± 90 μm beneath the pial surface; all capillaries were deeper than 40 μm, with one-third deeper than 300 μm, and the deepest capillary was imaged at 549 μm. The maximum depth achieved in each animal depended mainly on the quality of the cranial window. Because the dura was left intact, capillaries could not be visualized in most animals beneath 450 μm. Mean capillary depths for the acute, chronic and control groups were 276 ± 78, 259 ± 98, and 242 ± 99 μm, respectively; the depth for the control group was significantly smaller than that of the acute group ($p < 0.02$). Mean capillary diameters were 4.4 ± 0.7, 4.5 ± 0.8 and 4.7 ± 1.0 μm for the acute, chronic and control animals, respectively. Diameters for the control animals were significantly larger

than that of both acute and chronic animals ($p < 0.001$ and $p < 0.05$, respectively). Mean heart rates were 276 ± 72, 224 ± 45, and 240 ± 58 BPM for the acute, chronic and control animals, respectively; these differences were not statistically significant. While mean blood flow was not the focus of our work, flow rates extracted from our mean flow velocities and capillary diameter data were 0.6 ± 0.6, 0.8 ± 0.7, and 0.8 ± 0.9 nl/min for the acute, chronic and control animals respectively; blood flow in the acute group was significantly lower than in the control group ($p < 0.001$).

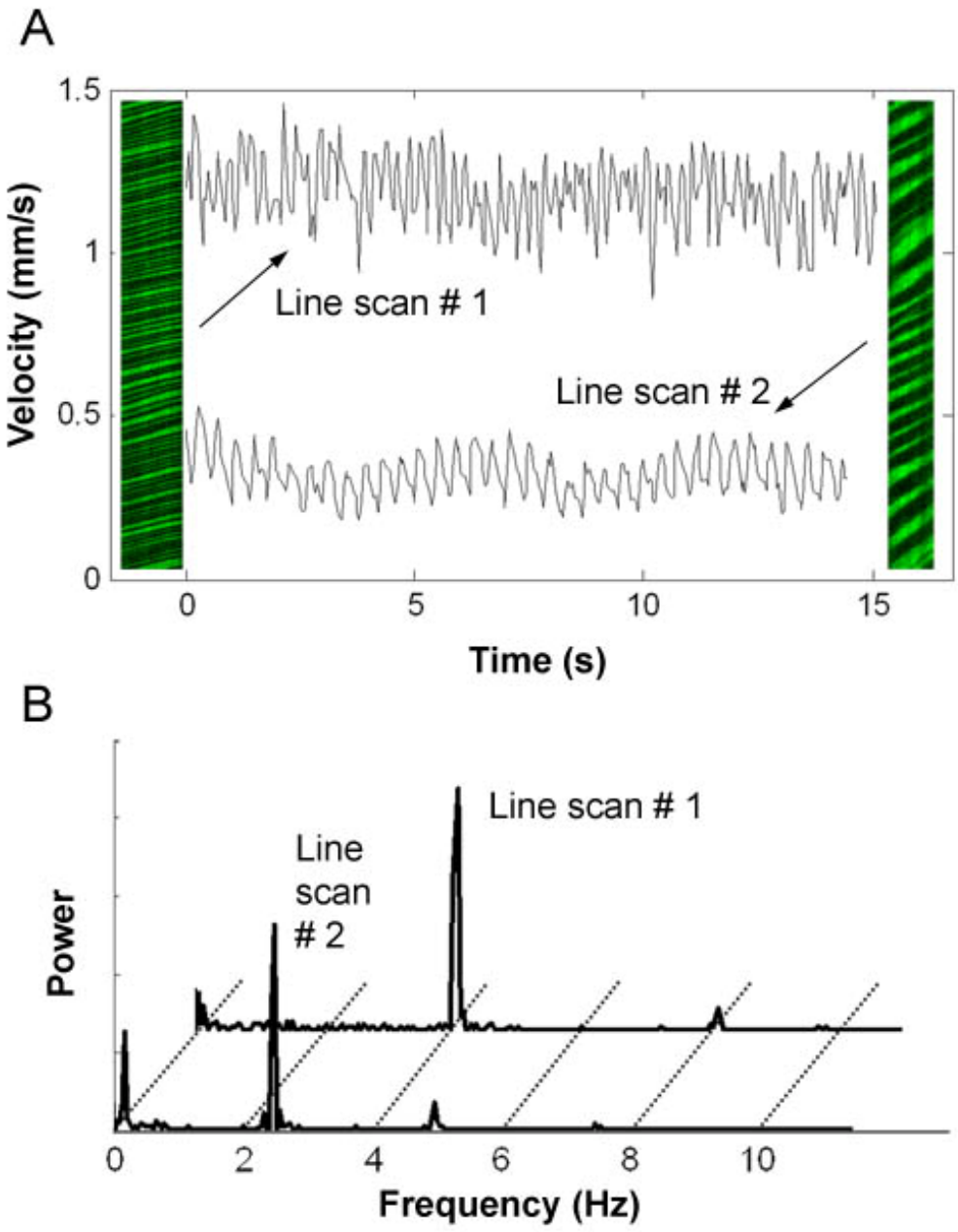

Figure 6.15: Examples of line-scans with velocity waveforms and power spectra. Two representative line scans, with their corresponding velocity waveforms (A). The line scan on the left (Line scan # 1) has rapid flow (mean velocity = 1.18 mm/s), while the one on the right (Line scan # 2) has slower flow (mean velocity = 0.32 mm/s). Pulsatility can be clearly seen in the waveforms; pulsatility indices were 0.41 and 0.14, respectively. As discussed in the Methods section, PI for each line scan was calculated in the frequency domain by integrating over these peaks in order to extract a cardiac-induced pulsatility measure only. Indeed, the corresponding power spectra (B) verify that the pulsatility is primarily cardiac in nature, as is evident from the prominent frequency components at the heart rate frequencies (4.0 Hz and 2.5 Hz for these two vessels respectively).

6.4.4 Capillary Pulsatility

Most waveforms were clearly pulsatile, with a distinct frequency peak at the ECG-derived heart rate. Two representative examples of line scan images, and their associated velocity waveforms and frequency spectra, are shown in Fig. 6.15.

The highly significant, linear relationship between absolute pulse amplitude and mean flow velocity for all measurements in the study, illustrated in Fig. 6.15, provides good justification of the choice of pulsatility index, the ratio of pulse amplitude to mean velocity, as a measure of flow pulsatility which is minimally influenced by variations in vessel caliber and mean flow velocity.

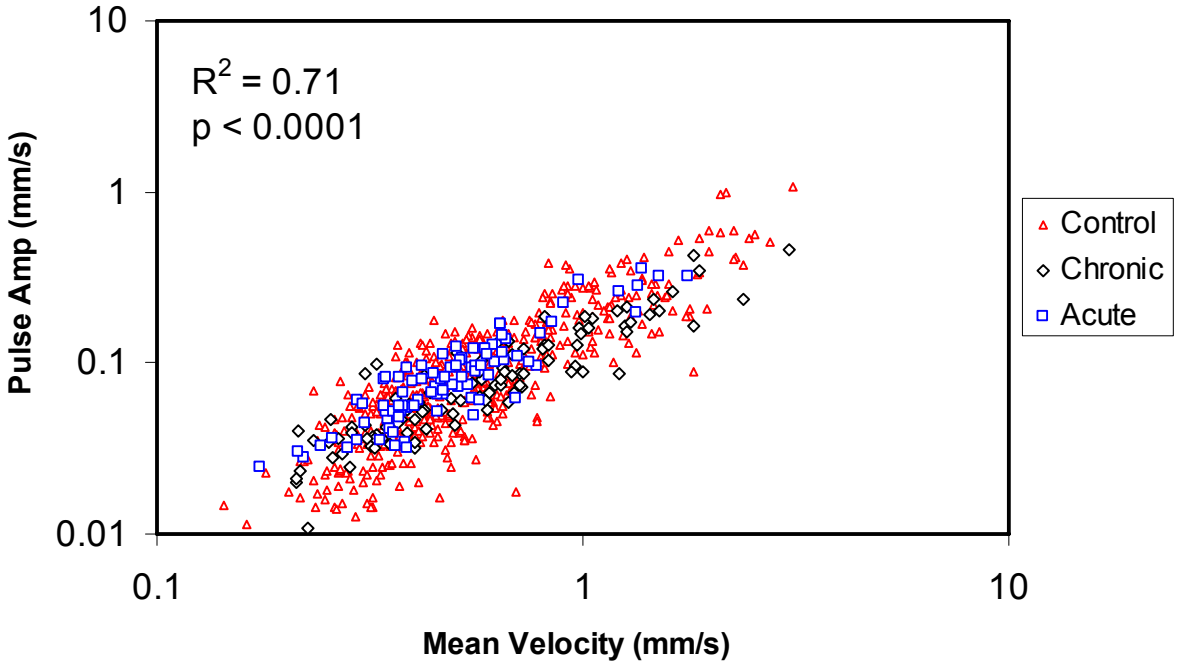

Figure 6.16: Pulse amplitude and mean velocity in the SBU animals.
Linear relationship between absolute pulse amplitude and mean velocity, plotted for all vessels and all experimental groups in the study (plotted on log-log scales). The highly significant, linear relationship provides the justification for using the ratio between pulse amplitude and mean velocity, the pulsatility index, as the experimental measure of choice. The use of PI minimizes the variability of pulsatility measurements due to changes in absolute blood flow, which is well-known to be lowered in hydrocephalus and was in fact found to be lower in the acute group.

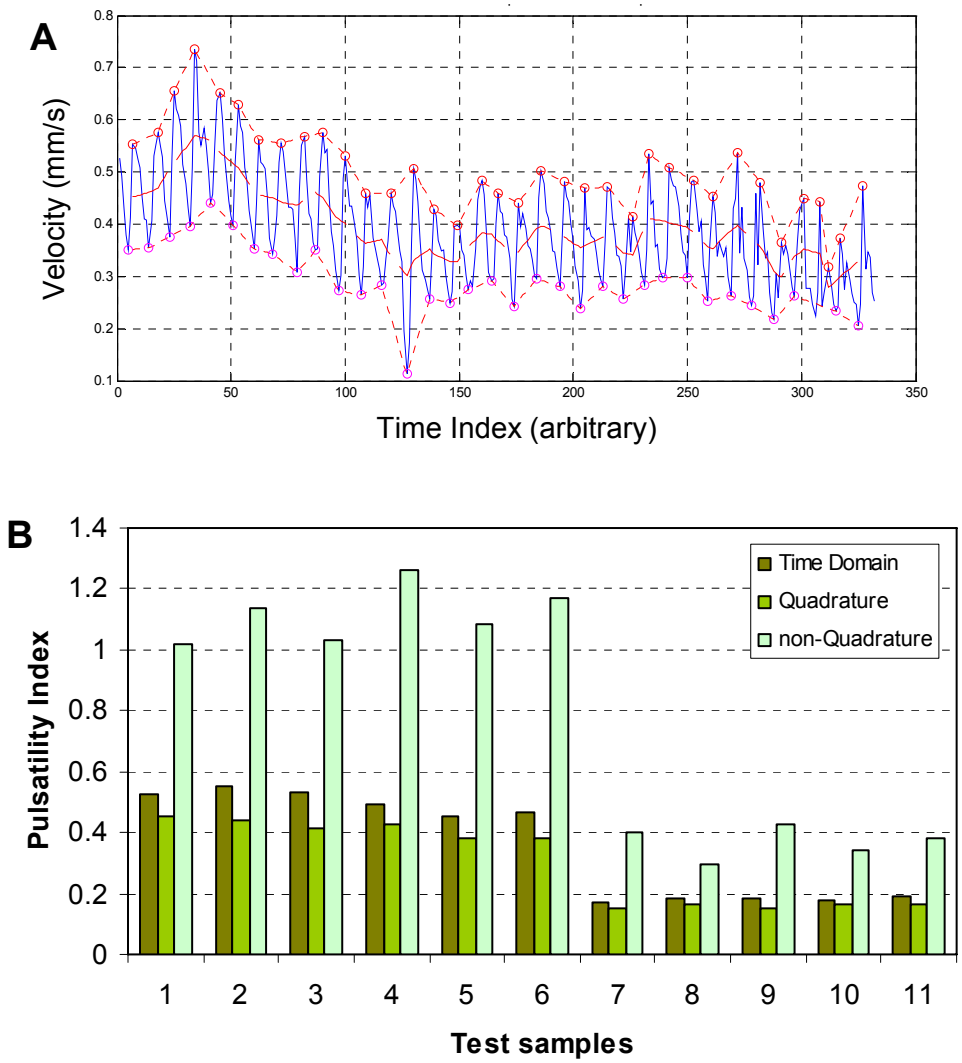

Figure 6.17: PI in the time domain and differences in PI calculation methods. PI can be calculated in the time domain by detecting the upper and lower envelopes of the velocity waveform, and computing the difference to generate the pulse amplitude (A). The quadrature-PI matched the time-domain-PI closely (although always lower due to the presence non-cardiac variation accounted for in the time domain), while the non-quadrature-PI was significantly larger than the time-domain PI, on account of spectral leakage (B)

6.4.4.1 Quadrature vs. Non-quadrature calculation and Background Subtraction

As described before, pulsatility index was initially calculated in quadrature, where the pulse amplitude is calculated by taking the square root of the integral of the square

of the peak. A question arose as to whether the quadrature calculation was appropriate as opposed to a straight integration. Pulsatility indices for a group of vessels were calculated in quadrature, non-quadrature and also in time domain. These results are shown in Fig. 6.17. It was found that the quadrature technique was the most appropriate, and matched the most closely with the time domain technique. The non-quadrature technique fails, because it severely overestimates the pulsatility index. This is presumed to be due to “spectral leakage”, i.e. the presence of frequency sidelobes and peak broadening in the FFT of a discrete waveform. The non-quadrature technique includes spectral leakage, and is overestimated. However, the quadrature technique minimizes spectral leakage, and is thus a more accurate representation of the pulse amplitude.

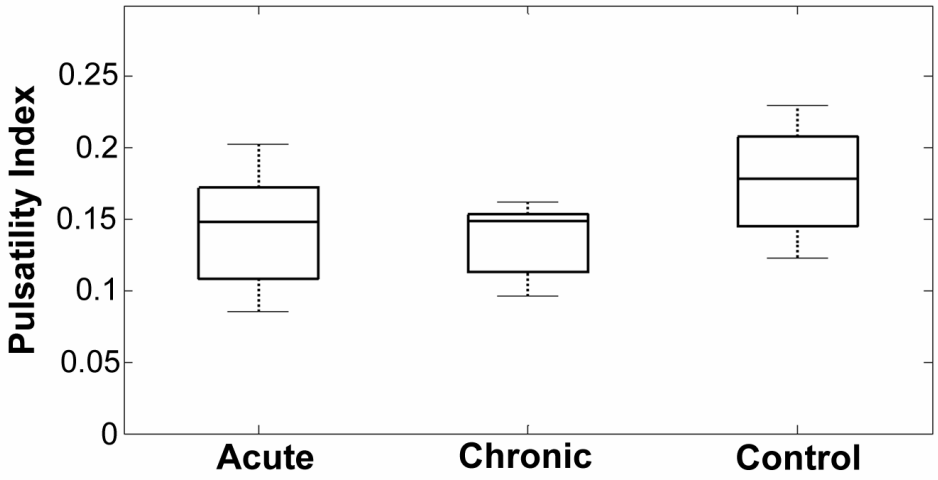

Figure 6.18: PI for the acute, chronic and control animals in the SBU group. Without accounting for variations in vessel diameter, depth or heart rate, there was no significant difference between the groups, other than a trend toward higher pulsatility in controls ($p = 0.07$).

6.4.4.2 Relationship of Capillary Pulsatility with Depth, Width and Heart Rate

Pulsatility indices for the acute, chronic and control groups, as analyzed in the first linear mixed model without controlling for HR, depth or vessel size, are shown in Fig. 6.18. PIs were 0.15 ± 0.06 (acute), 0.14 ± 0.05 (chronic) and 0.18 ± 0.07 (control); although there was a trend toward lower PIs for the hydrocephalic animals, this was not statistically significant ($p = 0.07$). However, PI varied significantly over vessel depth ($p < 0.0005$), HR ($p < 0.0001$) and diameter ($p = 0.02$). The second linear mixed model, which did control for these experimental parameters, showed that PI was significantly larger in controls compared to both acute and chronic animals ($p < 0.0001$ and $p < 0.005$), when accounting for varying depth, diameter and HR. The association between PI and depth differed significantly across the groups: in controls, PI increased with increasing depth (0.02 for every 100 μm), while there was no increase in PI with depth for either CH groups (control vs. acute: $p < 0.05$, control vs. chronic: $p < 0.0005$) (Fig. 6.19). The association between PI and HR also differed significantly across the groups ($p < 0.0001$). PI increased in the control group with HR (0.08 for every 100 BPM), but not in the acute and chronic CH groups (control vs. acute: $p < 0.0001$, control vs. chronic: $p < 0.005$). The association between PI and vessel diameter did not differ significantly across the groups ($p = 0.24$). In summary, PI increased significantly with depth and heart rate in the controls, but not in the acute or chronic animals.

Post-hoc analysis showed that PI differences between control and hydrocephalic animals were most prominent in the high HR-largest depth subgroup (Fig. 6.20B). Although this difference was not statistically significant because of the small number of vessels in this subgroup, there was a trend toward higher PI in the control group ($p =$

0.08). In addition, PI was significantly increased in controls compared to chronic CH animals, in the low HR-largest depth subgroup ($p = 0.03$) (Fig. 6.20A). Thus, while the subgrouping weakened the statistical significance, the post-hoc analyses in general showed that the PI differences between the control and hydrocephalic groups were primarily driven by increased PI in the control group in the largest depth vessels.

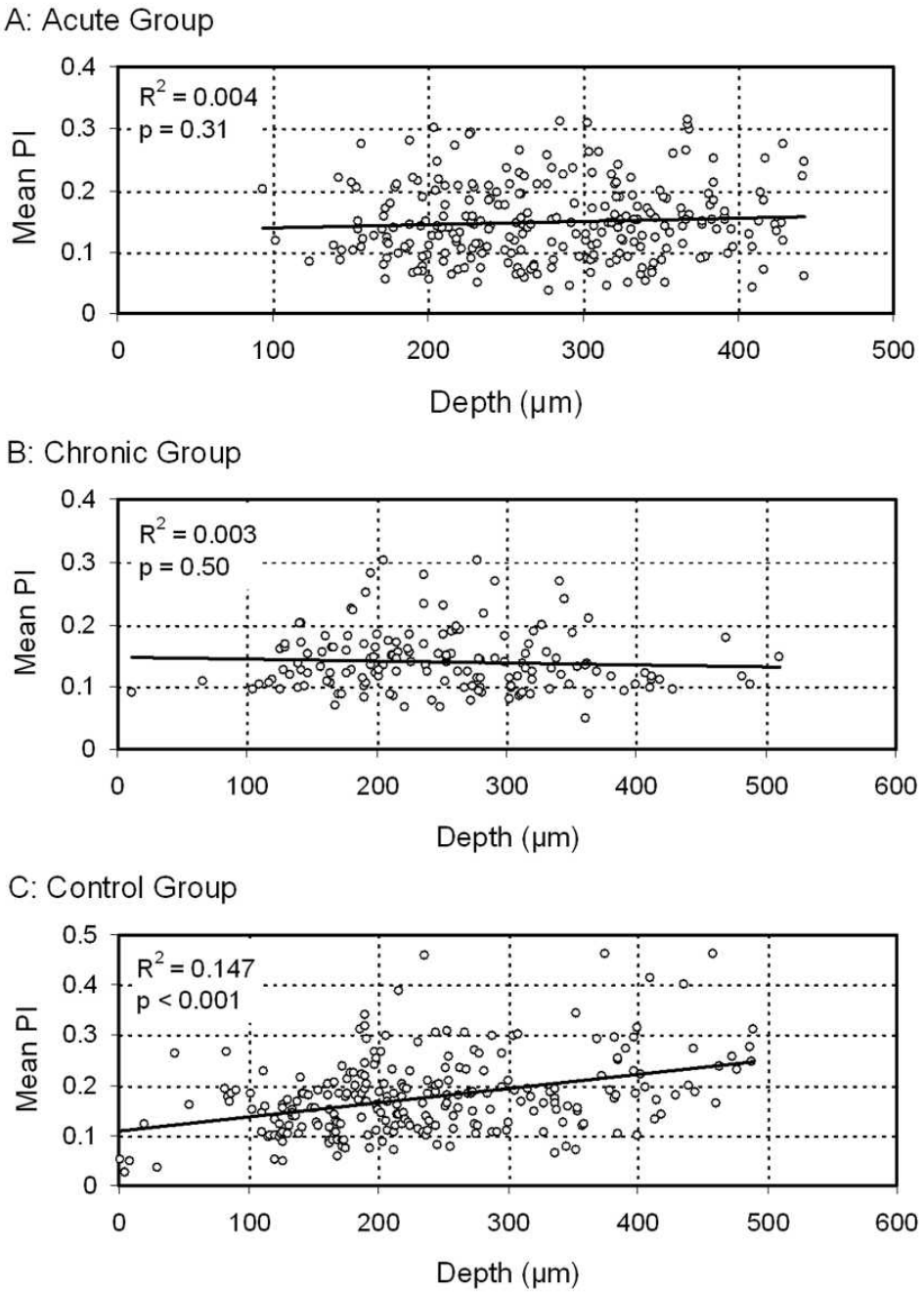

Figure 6.19: Effect of vessel depth on PI in SBU animals.
Effect of vessel depth on PI in the acute (A), chronic (B) and control (C) groups in the SBU animals. Linear mixed model analyses revealed a significant depth association in the controls, with pulsatility increasing with increasing depth from the pial surface, but no such relationship in either of the hydrocephalic groups. There was also a significant association between PI and heart rate in the control group, again with PI increasing with the higher heart rates (not shown).

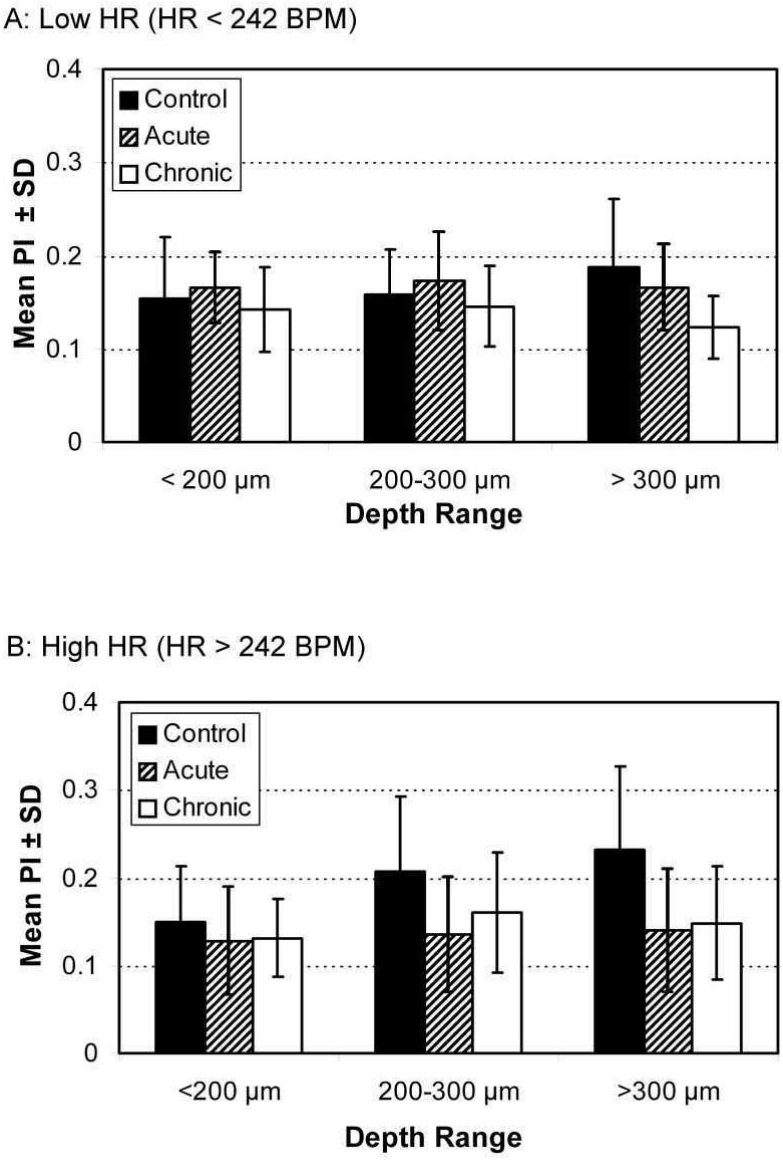

Figure 6.20: Post-hoc subgroup analysis of PI in the SBU animals.
Post-hoc analysis, where PI data were split into six subgroups, 3 depth ranges, each with two heart rate ranges, low heart rate (A) and high heart rate (B), to confirm that the differences between the groups were primarily being driven by increased pulsatility in the deeper vessels of control animals compared to the pulsatility in similar depth vessels. The statistical significance of these tests was dramatically impacted due to the smaller number of vessels in each individual subgroup. Nonetheless, the increase in pulsatility for control animals with depth can be clearly seen in both graphs, and the increase in pulsatility for deeper vessel in controls compared to hydrocephalics is now starkly evident.

6.4.4.3 Relationship of Capillary Pulsatility with CSF SV and VV

PI results for the acute and chronic CH animals, averaged over all vessels in each animal, were compared with their CSF stroke volumes and ventricular volumes (Fig. 6.21). No correlation was found between either ventricular volume or aqueductal CSF stroke volume and PI, for either acute or chronic CH animals. Based on prior measurements of CSF stroke volume in intact control animals [152], we can conclude that there is no change in microvascular flow pulsatility, even in the presence of a 10 to 500-fold increase in ventricular CSF pulsatility as measured at the cerebral aqueduct.

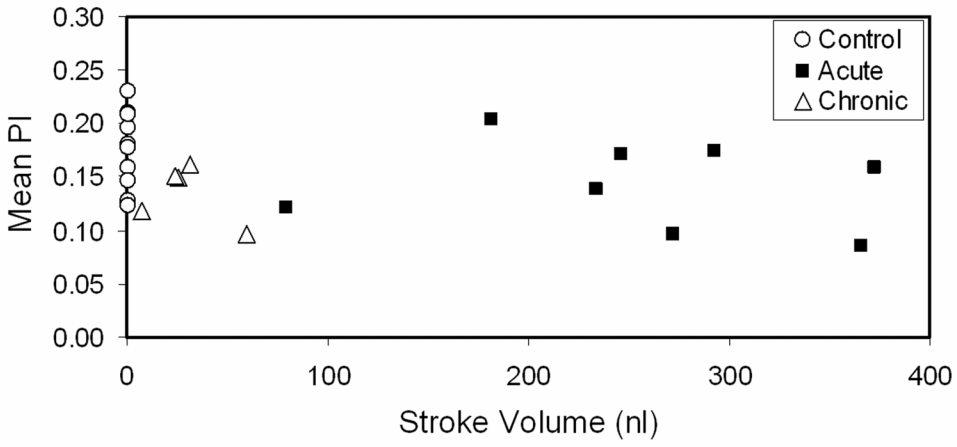

Figure 6.21: Relationship between PI and SV in the SBU animals.
Mean pulsatility index, averaged by animals, for both acute and chronic hydrocephalic animals against CSF stroke volume in the cerebral aqueduct. There was no correlation in either group. For comparison, PI is plotted for all control animals, with stroke volumes taken from the mean control stroke volume from §4. The plot clearly indicates that even in cases where the ventricular CSF pulsatility is markedly elevated (with a 10-500 fold increase compared to normal) there is no increase in cortical microvascular pulsatility.

6.5 Results: AECOM Animals

6.5.1 Microscopy and Data Acquisition

In the AECOM animals, capillaries were imaged in the cortex of the right parietal lobe, as in the SBU animals. The maximal depths achieved were between 500-650 μm; several vessels were deeper than 600 μm in a few of the acute animals. Quality of the images were superior compared to the SBU data; 9% of the vessels had to discarded due to poor quality (as compared to 19% in the SBU data).

6.5.2 CH Induction Results

Mean VV for the 8 acute CH animals was 144.9 ± 79.0 μl while their mean SV was 148.0 ± 112.3 nl.

6.5.3 Image Quality

Valid RBC velocity waveforms were collected in 626 capillaries (293 acute and 333 control). Mean depths for the acute and control groups were 354.43 ± 129.88 μm and 320.88 ± 95.90 μm, respectively. Average depth for all capillaries was 336.56 ± 114.22 μm beneath the pial surface (range: 131.89 – 658.26 μm); two-thirds of all vessels were deeper than 277 μm; a quarter was beneath 400 μm. The maximal depths achieved were between 500-650 μm; several vessels were deeper than 600 μm in a few of the acute animals.

Mean heart rates for the acute and control animals were 362.14 ± 58.61 and 331.62 ± 70.10 BPM ($p = 0.2$). The higher heart rates in these animals compared to the SBU animals are likely due to the use of isoflurane as the anesthetic medium.

6.5.4 Capillary Pulsatility

Velocity waveforms in the AECOM dataset were clearly pulsatile, as in the SBU data, with a distinct frequency peak at the ECG-derived heart rate. The highly significant, linear relationship between absolute pulse amplitude and mean flow velocity for all flow measurements that had been observed in the SBU group was also found in the AECOM animals, as shown in Fig. 6.22. This result provided further justification for the choice of using pulsatility index as the measure of flow pulsatility which is minimally influenced by variations in vessel caliber and mean velocity, since this was in a different group of animals under a different anesthetic regime as compared to the SBU cohort.

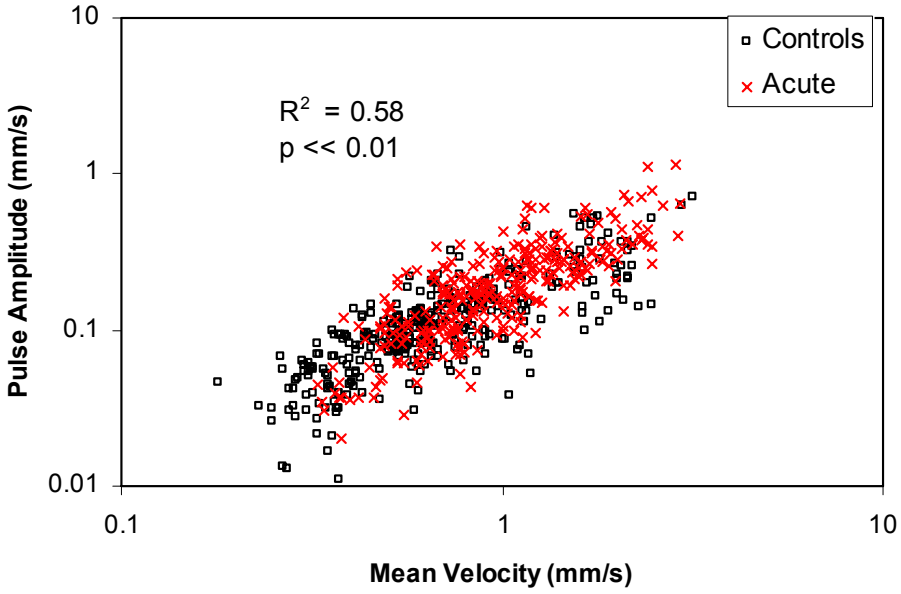

Figure 6.22: Pulse amplitude and mean velocity in AECOM animals.
Linear relationship between absolute pulse amplitude and mean velocity, plotted for all vessels in both acute and control animals in the AECOM set (plotted on log-log scales). As in the SBU animals, the significant linear relationship justifies the use of the ratio between absolute pulse amplitude and average velocity, i.e. the pulsatility index, as the experimental outcome. This reduces the variability of pulsatility measurements due to changes in cortical blood flow, which is well-known to be decreased in hydrocephalus.

6.5.5 Relationship of Capillary Pulsatility with Depth and Heart Rate

PI for the acute and control animals were 0.20 ± 0.09 and 0.17 ± 0.07 respectively (Fig. 6.23). PI for acute animals was significantly higher than that of the intact controls ($p < 0.02$), while there was no significant difference in PI between intact controls and saline controls ($p = 0.5$), according to the analysis in the first linear mixed model, which did not control for HR or depth. Additionally, PI did not vary significantly over HR ($p = 0.2$) or depth ($p = 0.2$) across all groups.

The second linear mixed model, which controlled for HR and depth, also showed that PI was significantly higher in acute animals compared to intact controls ($p = 0.03$),

while there was no difference in PI between intact controls and saline controls ($p = 0.5$). The association between PI and HR varied significantly between the acute animals and intact controls ($p < 0.006$). PI increased significantly in the acute group (0.04 for every 100 BPM). PI did not change significantly with HR in the saline controls ($p = 0.6$) or the intact controls ($p = 0.1$). The association between PI and depth did not differ significantly across the groups ($p = 0.7$).

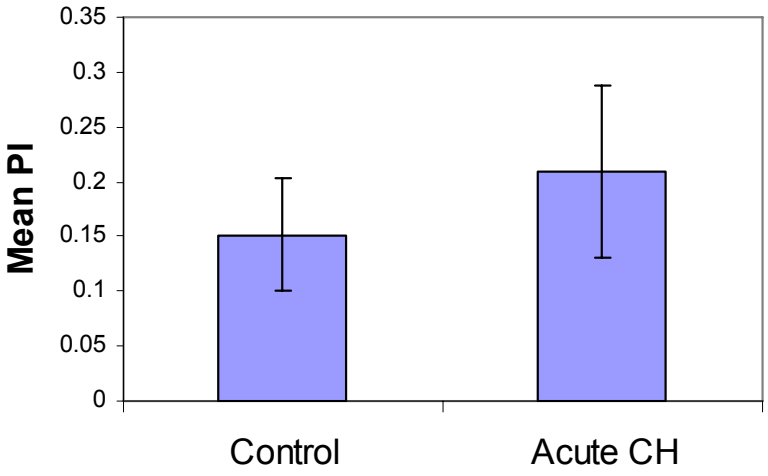

Figure 6.23: Pulsatility indices of acute and control animals in the AECOM group. In contrast to the SBU data, pulsatility index of the acute animals in the AECOM group was significantly higher than that of controls.

PI and depth were not correlated in the control animals when all vessels were included in the regression. However, when the vessels were divided into two groups based on the mean heart rate of 346 BPM, significant correlations were found between PI and depth in the control animals (intact and saline) (Fig. 6.24). PI increased significantly with depth ($R^2 = 0.026$, $p = 0.02$) in vessels with low HR (HR < 346 BPM). On the other hand, PI *decreased* significantly with depth ($R^2 = 0.105$, $p < 0.01$) in

vessels with high HR (HR > 346 BPM). No correlations were found between depth and PI in the acute animals, neither when all vessels were considered together nor when vessels were grouped by median HR ($p > 0.10$ in all cases) (Fig. 6.25).

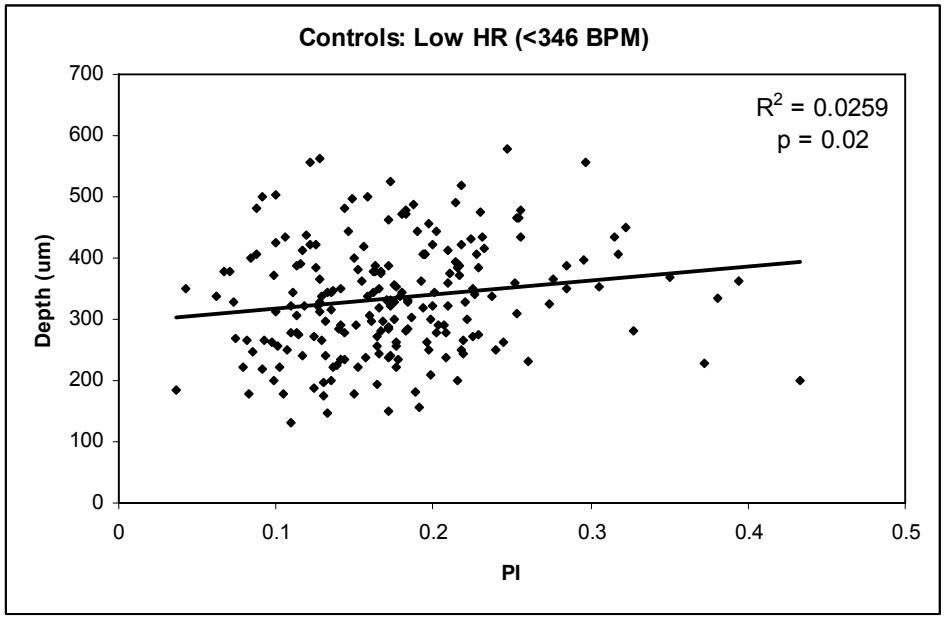

(A)

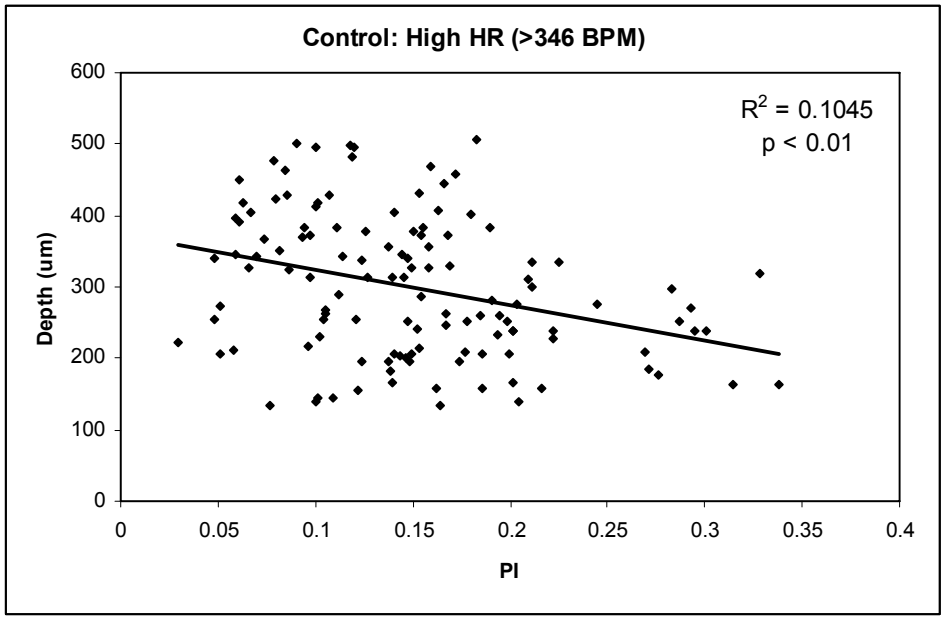

(B)

Figure 6.24: Effect of vessel depth on PI in the AECOM control animals.
PI was significantly correlated to depth in the AECOM control animals when the PI data was divided into two groups by mean heart rate (346 BPM). At the lower heart rates, PI increases with depth significantly (R^2 = 0.0259, p = 0.02) (A). This relationship is similar to that seen in the SBU control animals. On the other hand, at the higher heart rates, the relationship in the AECOM data is reversed and PI decreases with depth (R^2 = 0.1045, p < 0.01) (B). PI was not correlated to depth when values at all heart rates are considered together.

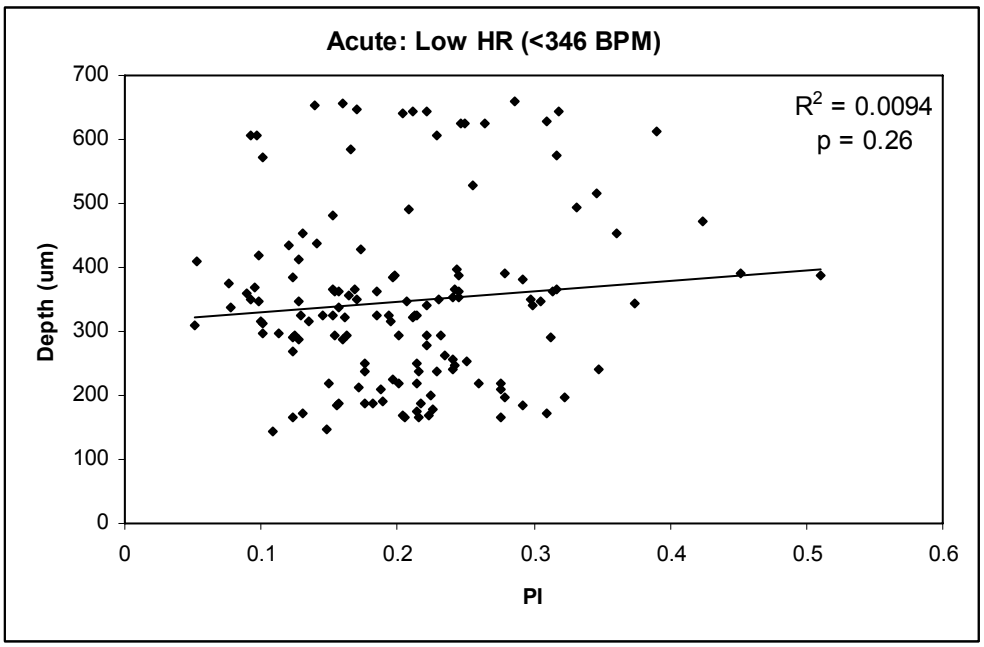

(A)

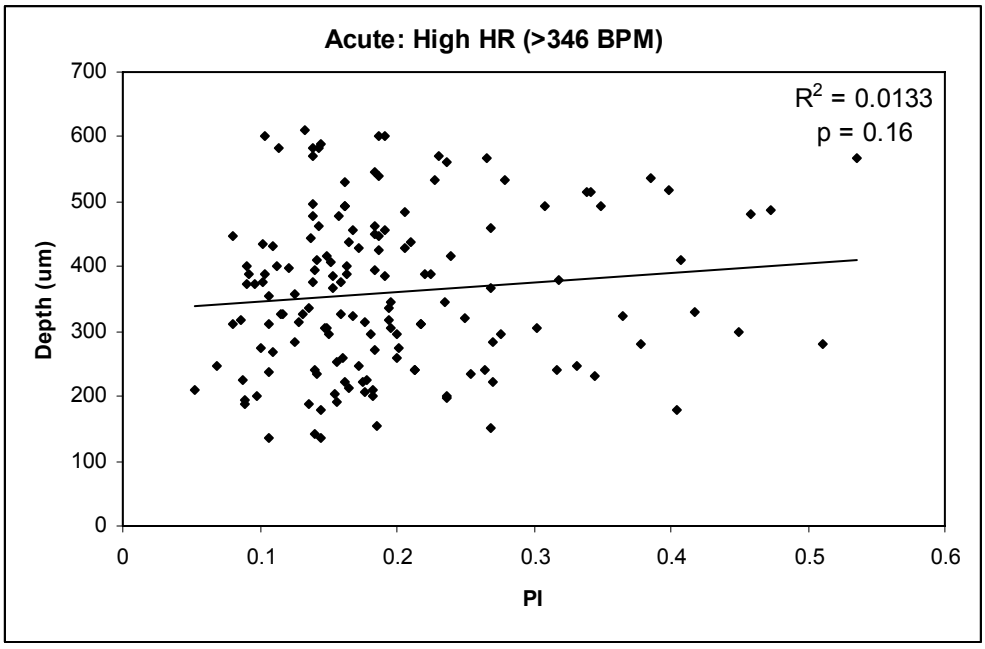

(B)

Figure 6.25: Effect of vessel depth on PI in the AECOM acute animals.
No correlation was found between PI and depth in the AECOM acute animals, neither when the PI data was grouped by mean heart rate (346 BPM) (A: low HR, B: high HR), nor when values at all heart rates were considered at once.

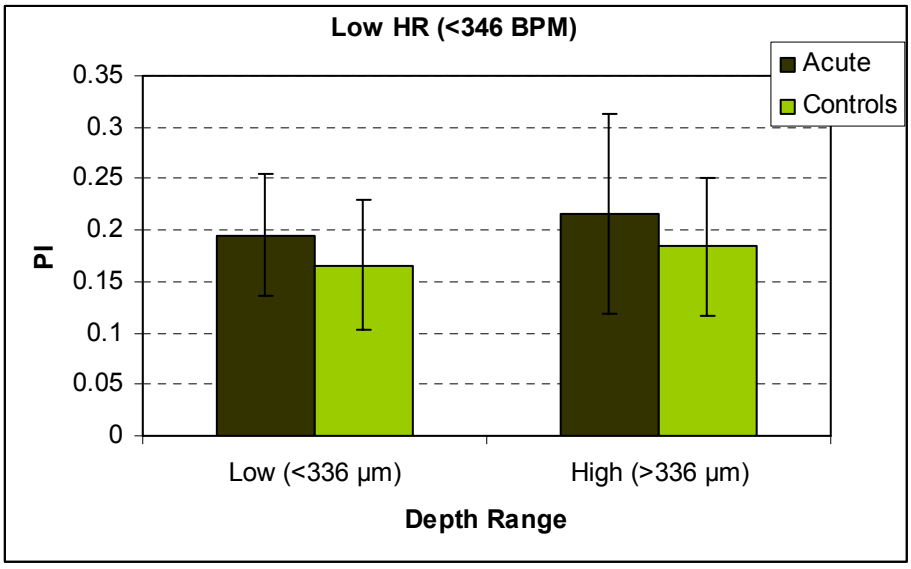

(A)

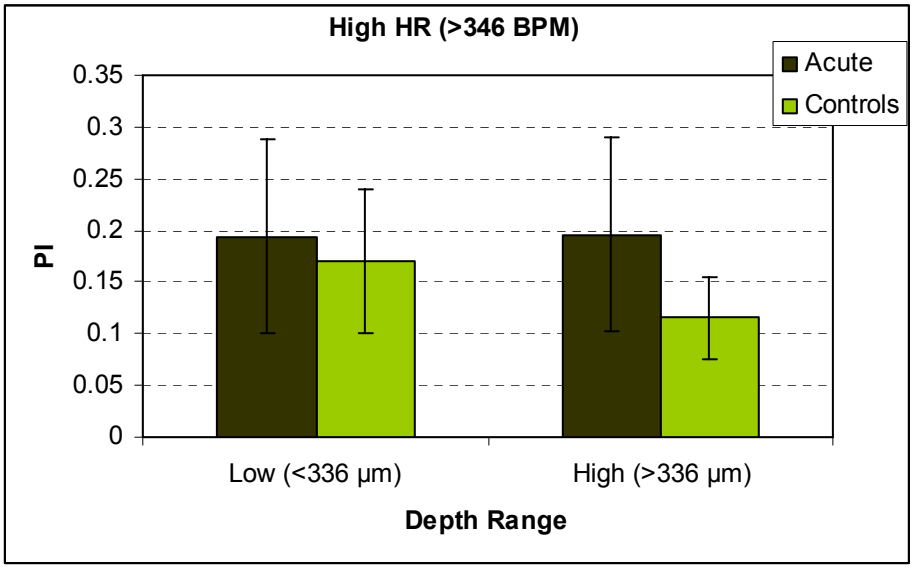

(B)

Figure 6.26: Post-hoc analysis of PI comparison between acute and controls.
PI data were split into four subgroups, two depth ranges, each with two heart rate ranges (A: HR < 346 BPM, B: HR > 346 BPM), to determine whether the differences between the groups were primarily being driven by pulsatility variation with depth and heart rate. The increase in pulsatility for acute animals is most prominent in the highest depth and highest heart rate subgroup (B).

Post-hoc analyses showed that the PI difference between the acute and control groups was most prominent in the highest HR-highest depth subgroup, where the control PI was 41% lower than acute PI ($p < 0.001$) (Fig. 6.26 B, right). PI differences between acute and control animals were also significant in the low HR-low depth and low HR-high depth subgroups ($p = 0.003$ and 0.01), but the differences were smaller in these cases (15% for both).

6.5.5 Relationship of Capillary Pulsatility with CSF SV and VV

PI results for the acute CH animals, averaged over all vessels in each animal, were compared with their CSF stroke volumes (Fig. 6.27) and ventricular volumes. No correlation was found between PI and either aqueductal CSF stroke volume ($R^2 = 0.05$, $p > 0.6$) or ventricular volume ($R^2 = 0.02$, $p > 0.7$).

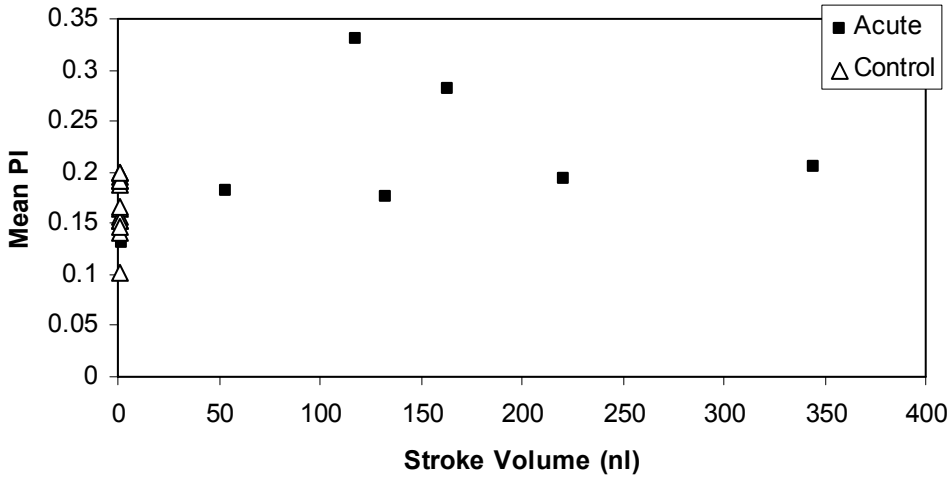

Figure 6.27: Relationship between PI and SV in the AECOM animals.
Mean pulsatility index, averaged by animals, for acute CH animals against CSF stroke volume in the cerebral aqueduct. No correlation was found ($R^2 = 0.05$, $p > 0.6$). For comparison, PI is plotted for all control animals, with stroke volumes taken from the mean control stroke volume from §4.

6.6 Discussion

Our results from the AECOM data indicate that pulsatility of capillary blood flow in the rat neocortex is elevated in CH, which supports the pulsatility redistribution theory of communicating hydrocephalus. Our initial findings from the SBU animals had shown that pulsatility in the rat neocortex was *not* elevated in CH. The SBU experiments were conducted using ketamine-xylazine anesthesia, whereas the AECOM experiments were conducted using isoflurane anesthesia. This suggests that capillary pulsatility is highly influenced by the mode of anesthesia, and that pathophysiological changes in capillary pulsatility may be evident under isoflurane anesthesia and not ketamine-xylazine. Statistical analyses accounting for multiple experimental factors were able to demonstrate a new finding, that there are normally significant changes in capillary pulsatility with depth from the pial surface, that this effect depends on heart rate, but that this effect disappears in hydrocephalus.

6.6.1 Differences due Anesthesia Regimen

As mentioned earlier, the ideal anesthetic for use in these experiments is isoflurane, because of its ease of use and stability induced in the animal [230]. Isoflurane was not available for use at the SBU facility, and ketamine-xylazine was chosen as the alternative, as it has been used in other rodent blood-flow studies [235, 236]. However, ketamine-xylazine has been shown to cause a decrease in mean cerebral blood flow as compared to isoflurane (this effect is thought to be primarily due to xylazine) [237, 238], as well as respiratory depression [239] and hypotension [240, 241]. Its effect on flow pulsatility is unknown. We had anticipated that since all animals

received the same anesthetic regime, effect of the anesthesia on pulsatility would be the same in all experimental groups, and the differences that existed in awake animals would be preserved under anesthesia. Clearly, this is not the case, since the results are different under isoflurane anesthesia. One possible explanation for this difference is that brain metabolism of ketamine-xylazine is altered in hydrocephalus, and this anesthetic has a more potent effect on CH rats than normal animals, as a result of which flow pulsations were depressed more in the CH rats than in controls. Brain metabolism is known to be altered in hydrocephalus [242, 243], but changes in anesthesia metabolism in hydrocephalus has not been studied.

An additional factor that may also explain the differences between the two anesthetic regimes is intracranial pressure (ICP). Anecdotal evidence from our experiments indicate that ICP is elevated in CH rats at the acute stage of CH (since brain herniation in these animals is greater than in controls). Ketamine-xylazine is depresses the cardiovascular system far more severely than isoflurane [239], and a greater drop in ICP may be produced in the acute animals under the influence of ketamine-xylazine than isoflurane. In contrast, the corresponding drop in ICP in control animals may not be so large. As discussed earlier (§5), due to compliance changes, pulsatility is decreased at lower mean ICP. Therefore, increased pulsatility in the acute animals may not be apparent under the influence of ketamine-xylazine, as opposed to isoflurane.

6.6.2 Relationship of Pulsatility with Vessel Depth, Diameter, and Heart Rate

Three parameters, depth of the vessels from the pial surface, vessel diameter, and heart rate, were examined in the SBU animals in order to assess their effect on pulsatility. In the SBU control animals, our results show a complex dependence of pulsatility on all three parameters. Vessel diameter is expected to affect mean flow velocity and therefore absolute pulse amplitude. Studies documenting changes in capillary morphology also show that cortical capillary density is altered in hydrocephalus, with an initial decrease in the acute phase followed by a compensatory increase [147, 244]. Such effects may give rise to changes in mean blood flow and absolute pulse amplitude in capillaries, but should not affect their ratio. Thus, in order to mitigate the effect of vessel diameter and density on our results, pulsatility index was chosen as the outcome measure. The SBU results do show a very small increase in pulsatility with vessel diameter, which may be related to changes in effective vessel compliance with size. However, there was no difference in this dependence between experimental groups, indicating that any differences in intracranial compliance between the groups which might lead to changes in pulsatility are driven by factors unrelated to vessel morphology but more likely driven by extra-vascular factors.

Pulsatility index in the SBU data showed a much stronger dependence on depth and, in contrast to vessel diameter, this dependence differed significantly between control and hydrocephalic animals. In controls, pulsatility increased significantly with depth, while there was no change in pulsatility with depth for either of the hydrocephalic groups. Similarly, there was a relationship between pulsatility and heart rate in control animals, with pulsatility rising with increasing heart rate, which was not significant in the

hydrocephalic animals. Heart rate varied over time and from animal to animal in an uncontrolled manner, either due to physiological variation or due to changes in depth of anesthesia. Based on these depth-by-group and heart rate-by-group associations, we conducted a post-hoc test to identify subgroups of pulsatility measurements responsible for these differences. This analysis revealed that the subgroups with the deepest vessels were primarily responsible for the significant differences between the groups, with a significantly higher pulsatility in controls compared to hydrocephalic animals.

Our findings in the AECOM animals, in terms of pulsatility relationship to vessel depth and heart rate, were similar to the SBU results. Pulsatility in the AECOM control animals increased with depth when heart rate was 346 BPM or less. This is similar to the result obtained in the SBU control animals, in which the highest heart rates were near 400 BPM. Because data at higher heart rates were not obtained in the SBU animals, we did not see the effect of pulsatility decreasing with depth at hearts greater than 346 BPM, which we observed in the AECOM animals. As in the SBU data, there was no association between PI and depth in the hydrocephalic animals, in either heart rate range. Based on these depth-by-group and heart rate-by-group relationships, we conducted a post-hoc analysis in the AECOM data to identify subgroups of pulsatility measurements for differences in pulsatility between the acute and control animals. As in the SBU data, this test showed that the AECOM subgroup with the deepest vessels and highest heart rates were primarily responsible for the significant difference between the groups.

Our results in both the SBU and AECOM data can be explained in terms of changes in brain compliance with the development of hydrocephalus, and the effect

compliance changes may have on the distribution of pulsations throughout the brain. As discussed earlier in §6, the relationship between intracranial compliance and pulsatility is based on the pressure-volume relationship [201]. Marmarou showed that the exponential pressure-volume relationship in the brain leads to a larger pressure pulsatility with either an increase in intracranial pressure or a decrease in intracranial compliance (see Fig. 5.1 & 5.2). Thus, the increase in pulsatility with depth demonstrated in the SBU and AECOM control data can be explained by a change in relative compliance for vessels deeper within the cortex. The primary sources of intracranial compliance are the veins and CSF filled subarachnoid spaces, because of their direct communication with the compliant extracranial compartment. With this in mind, we can understand why deep vs. shallow capillaries might experience varying compliance effects: shallow capillaries are in closer proximity to the CSF-filled cortical subarachnoid spaces, as well as the dural sinuses, resulting in an effective higher compliance (Fig. 6.28A). This would explain the increase in pulsatility for vessels further from the cortical surface, as seen in the SBU control data and the AECOM control data at low heart rates.

This situation can change in hydrocephalus, providing a new compliance mechanism not present in the healthy brain: a new effective pathway to the compliant extracranial spaces has opened up through the dilated aqueduct and the enlarged ventricles provide enhanced coupling of brain tissue to this pressure outlet (not a flow pathway, but rather a compliance pathway which allows for redirection of pulsations via the mechanical coupling between the ventricles and brain parenchyma) (Fig. 6.28B). Thus, while the foramen magnum normally provides the primary exit pathway for

pulsations, the enlarged ventricles in hydrocephalus can provide an alternate exit pathway for pulsations. The enlarged ventricles in hydrocephalus may thus create an effective increase in deep brain compliance, leading to a drop in flow pulsatility compared to the normal brain, explaining the decrease in deep vessel flow pulsatility in hydrocephalic animals compared to controls.

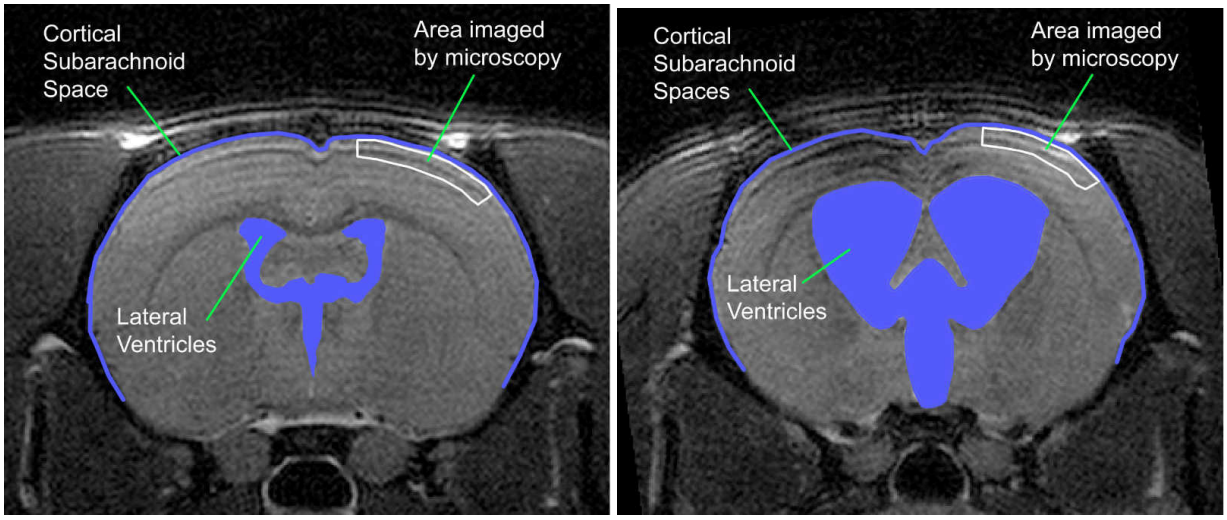

(A) (B)

Figure 6.28: Proximity of ventricles to SAS in CH and control animals.
Coronal slice images of a typical control rat (left) and a severely hydrocephalic rat (right), with the ventricles and the CSF-filled cortical subarachnoid space (SAS) highlighted. The approximate region of the cortex where capillaries are imaged by microscopy are indicated (white boxes). In control animals, the cortical SAS may dominate compliance effects, giving rise to decreasing pulsatility with decreasing depths. The small ventricles are far away and may have no effect. The situation is reversed in CH, where the enlarged ventricles are in closer proximity to deeper capillaries; additionally, the dilated aqueduct (not shown) may be providing an alternate compliance pathway for redirection of pulsations, which may be the reason decreased pulsations with depth.

In support of this understanding of compliance effects in hydrocephalus, a recent study showed that brain parenchymal compliance is in fact *increased* in normal pressure hydrocephalus [206]. Using magnetic resonance elastography (MRE),

increased brain compliance was demonstrated in the periventricular tissue, as well as in deep white and cortical grey matter. Since pulsations are expected to be reduced under conditions of increased compliance, this study supports our findings of reduced capillary pulsatility in CH. It should be noted, however, that these results are in sharp contrast with findings from several other studies: compliance measured by Marmarou's CSF infusion technique [201] and vascular compliance measured by MRI at the sagittal sinus were both reduced in hydrocephalus [189, 190, 198]. These disparities might be explained by considering that the MRE is a measure of "local" tissue compliance, while CSF infusion measures the "global" compliance of the entire cranial CSF system, and thus may reflect different aspects of compliance changes in the brain. As explained above, our capillary pulsatility data are likely a reflection of local tissue compliance, and so may better match the MRE compliance results.

6.6.2 Significance of Pulsatility in CH

The primary motivation for studying capillary pulsatility in hydrocephalus was to elucidate a possible role of microvascular pulsations in the pathogenesis of hydrocephalus. While ventriculomegaly is a well-explained phenomenon in cases with a clear obstruction to ventricular outflow, in communicating hydrocephalus clear-cut explanations for the mechanisms of ventricular dilation are lacking [6, 8]. As discussed in §2, a number of early studies suggested that ventricular dilation in CH may be a result of elevated ventricular pulsations, and that reduction of the CSF pulse wave can inhibit ventricular dilation [74, 76]. The most striking evidence came from a study demonstrating that ventricular dilation could be induced in the absence of any CSF

obstruction by artificially elevating the CSF pulse wave with a pulsating, intraventricular balloon [79]. Finally, elevated pulsations have also been extensively reported in clinical studies [91, 198, 245, 246].

The present study was thus designed to detect increased flow pulsations in neocortical capillaries with the induction of CH as a test of a pulsatility redistribution theory. Our results from the AECOM animals support this theory: neocortical capillaries do exhibit increased pulsatility with hydrocephalus induction. However, our results from the SBU animals, which were studied under a different anesthetic regime, indicate that differences in anesthesia may have a significant effect on capillary pulsatility. Our explanation for decreased pulsatility is that the hydrocephalic brain metabolizes ketamine-xylazine differently than the normal rat brain, resulting in a more significant depressive effect on pulsatility in CH. Changes in anesthesia metabolism with hydrocephalus has not been investigated and requires study.

6.6.3 Limitations

One potential limitation of the study with respect to the SBU data is related to the anesthesia delivery. Since an injectable anesthetic was used with supplemental boluses as needed rather than a continuous infusion, the level of anesthesia varied over time, and may have been responsible for some of the variability in pulsatility. In particular, studies of the effect of hypercapnia on pressure pulsatility show that the systemic arterial and CSF pulse amplitudes are elevated with hypercapnia, with the latter attributed to capillary dilation [212, 247]. However, there is a clear correlation between anesthesia depth (and thus potentially hypercapnia, due to depressed respiratory rate)

and heart rate. If anything, our data show increased pulsatility in controls with increased heart rate, not the reverse, and no change in hydrocephalic animals. A further possible concern is the effect of anesthesia on cerebral blood flow. As discussed above, ketamine-xylazine has been shown to cause a decrease in cerebral flow as compared to isoflurane [237, 238]. However, this is an effect on mean blood flow and the effects of ketamine-xylazine on flow pulsatility are not known. Moreover, because all animals received the same anesthetic regime, we did not expect the particulars of the anesthesia to have affected our final results.

We have explained the differences in results between the SBU data and the AECOM data by suggesting that the metabolism of ketamine-xylazine is altered in hydrocephalus, giving rise to a decrease in flow pulsations as compared to controls, but the reverse may also be true in case of isoflurane: if isoflurane metabolism is altered in the hydrocephalic brain, giving rise to *increased* flow pulsations as compared to the normal brain, then this effect may be masking our new results. Moreover, isoflurane is thought to produce spontaneous fluctuations in blood flow [230]. To verify our results, it may be useful to repeat these experiments under urethane anesthesia, which is thought to produce a highly stable basal blood flow [248]. Urethane had not been used in our experiments because it is toxic and carcinogenic, presents potential danger to personnel and is unsuitable for survival studies.

Our findings indicate that there is an average of about 20% increase in capillary pulsatility in the rat neocortex in CH. While this is an important finding with respect to the redistribution theory, this does not provide any information on capillary pulsatility changes deep within the periventricular region, where pulsatility may be elevated to a

higher degree. Our maximum imaging depth was 0.5 mm, while the depth of the periventricular white matter is about 1.5 mm in our most severely hydrocephalic rats. The theoretical maximum imaging depth for multiphoton microscopy is approximately one millimeter without resorting to much more invasive surgical procedures. Optical coherence tomography allows deeper imaging but does not provide the resolution required for capillary imaging. Use of a smaller animal model, such as a mouse model, may allow us to elucidate capillary pulsatility changes in the periventricular white matter, but a mouse model of communicating hydrocephalus does not yet exist.

In the SBU animals, ventriculomegaly was less pronounced in the chronic CH group in the compared to the acute CH group. The ventricular volumes of these animals clearly fit our criteria for hydrocephalus, with enlarged ventricles as well as elevated CSF stroke volume compared to controls. Ventricular dilation in this hydrocephalus model, as in many other hydrocephalus models, generally varies over a wide range, and we have to consider it an unfortunate, unexplained coincidence that all animals in the chronic CH group were only mildly hydrocephalic. We have shown in §4 that chronic animals can experience the entire range of mild to severe ventricular dilation [152]. Nonetheless, even with the limited ventriculomegaly in this group, we were able to show that hydrocephalus leads to reduced capillary pulsatility compared to controls at the deeper cortical levels.

It should be noted that the difference between the SBU and AECOM data may be due to the differences in animal posture. SBU animals were imaged in a prone position, but AECOM animals were imaged in a supine position. There are two possible effects that may manifest in the supine position: 1) weight of the brain may cause increased

pressure in the neocortex, giving rise to decreased compliance, and 2) weight of the tongue may obstruct the airway and upset the acid-base balance of blood, causing the animal to become more hypercapnic. Both of these effects can potentially cause an increase in capillary pulsatility.

6.6.4 Conclusion

This study is the first attempt to measure capillary pulsatility deep in the rat neocortex. We have shown that capillary pulsatility is elevated in communicating hydrocephalus, and normally increases with increasing depth from the pial surface. Furthermore, we found that the normal increase in pulsatility with depth disappears with hydrocephalus induction, and explanations of this effect based on local intracranial compliance changes have been suggested. Future studies will investigate capillary pulsatility at earlier time-points, potentially within hours of induction, when the kaolin blockage may cause changes in pulsation distribution but ventricular enlargement has not yet occurred.

Chapter 7

---

7. Characterization of Behavioral Deficits in Communicating Hydrocephalus

7.1 Introduction

In the preceding sections of this dissertation, we have presented strong evidence that aqueductal pulsatility may be an important marker of outcome in our animal model of communicating hydrocephalus. We have established that aqueductal pulsatility and ventricular dilation may be influenced by other factors, such as variations in intracranial compliance with the development of CH, and we have explored cerebral microvascular pulsatility as a potential source of elevated aqueductal pulsatility in CH. Next, in order to establish the relevance of aqueductal pulsatility to the clinical presentations of CH, it is

important to determine the relationship of aqueductal pulsatility to the clinical standards of the management of CH.

While we inherently used ventricular size as the gauge of severity of CH in the preceding studies of this dissertation, clinically, ventricular dilation by itself is a poor marker of the severity of hydrocephalus. While ventriculomegaly has traditionally been the hallmark characteristic of all forms of hydrocephalus, it also occurs in other disorders in young adults and the elderly, such as Alzheimer's disease [249-251], spina bifida [154, 252], multiple sclerosis [253, 254] and asymptomatic ventricular dilation [199, 255]. There is great variability in the size of the ventricles among patients, and no functional relationship has been shown between ventricular dilation and other symptoms [99, 194]. These problems make it difficult for neurosurgeons to gauge the severity of hydrocephalus, which in turn makes it difficult to determine which patients might benefit from shunting, and how to best treat patients suffering from shunt failure [256, 257]. Thus, the diagnosis and management of CH is a difficult problem that continues to be challenging to clinicians [1, 178, 256, 258].

The gold standard for the assessment of CH severity is the characterization of behavioral deficits. These are useful in both clinical practice and experimental research, because they yield data that can be used to correlate functional impairment to severity in a disease process affecting the central nervous system, such as hydrocephalus [99]. Behavioral outcome measures, such as gait, incontinence and cognitive impairment or dementia are routinely used in the diagnosis and grading of normal pressure hydrocephalus [1]. In experimental hydrocephalus, behavioral studies are equally important in that they provide a measure of functional impairment [99], as well as a

means to gauge the severity of hydrocephalus and compare it to clinical correlates. However, a number of critical gaps remain. Behavioral studies conducted in experimental hydrocephalus to date are limited in number, and most have been conducted in young rats [99, 192, 193, 196, 259-264]. Moreover, all such studies were investigated in obstructive forms of hydrocephalus, either using H-Tx rats, which have hydrocephalus caused by aqueductal stenosis, or rats in which hydrocephalus was induced by cisternal kaolin injections obstructing the fourth ventricle outlets. No behavioral studies have yet been conducted in experimental communicating hydrocephalus, mainly due to a lack of appropriate communicating models, but this is now possible with our rat model of CH.

Clearly, the pathophysiology of CH is best gauged by behavioral deficits, so it would be very informative to correlate aqueductal pulsatility with results from behavioral studies in our animal model, as they may indicate to what degree aqueductal pulsatility is associated with severity of hydrocephalus. This would also help establish a link between aqueductal pulsatility and the clinically relevant features of CH. Numerous studies have been conducted to explore the importance of aqueductal pulsatility and intracranial pressure pulse amplitude in human CH [70, 91, 93, 94, 181, 210, 265-268] , but these were conducted in the context of shunt responsiveness or physiological parameters. One study examined aqueductal pulsatility with severity of symptoms, but did not provide any data on the relationship between pulsatility and severity [188]. Thus, the question of whether any relationship exists between aqueductal pulsatility and severity is still unanswered.

The objective of this study was thus to measure behavioral characteristics in cognitive memory and motor coordination in control and kaolin induced hydrocephalic animals. In particular, it was hypothesized that CH rats will exhibit behavioral deficits in memory, cognitive ability and motor coordination, compared to normal rats and that behavioral deficit scores of CH rats will be correlated with aqueductal pulsatility, and not to volume of the ventricles.

7.2 Methods

All animal handling and surgical techniques were approved by the Institute of Animal Care and Use Committees (IACUC) of Stony Brook University and Albert Einstein College of Medicine. All experimental procedures were carried out in accordance with the NIH Guide for Care and Use of Laboratory Animals. All efforts were taken to minimize any suffering of the animals and the number of animals used in experiments.

7.2.1 Behavioral Study Techniques

Behavioral studies were conducted at the Behavioral Core of Albert Einstein College of Medicine. Five behavioral tests were conducted: open field (OF), object placement (OP), object recognition (OR), balance beam (BB) and social preference (SP). General descriptions of the tests given below, and the specific parameters used in this study are given later.

The open field, object placement and object recognition tests were carried out in an arena, a 27” x 27” x 12” (high) box made of wooden floors and walls without a top

cover. Dark blue or black plastic sheets on the floor provided maximum contrast to differentiate the animals on video. The walls were left bare and were light gray. Each wall was labeled with a different symbol near the eye level of the rat, to give the animals spatial references. Since rats are blind to red light, illumination was provided with ambient red lighting using floor/table lamps directed at the wall next to the arena. For the social preference test, a Y-maze was used, which consisted of three arms, 25” x 8” x 16” (high) each. The floor was covered with dark blue plastic sheets, and the walls were left bare and were light grey in color.

The open field, object placement, object recognition and social preference tests were video recorded using a monochrome digital video camera (Sony exwaveHAD, Sony, Tokyo, Japan), which was positioned about 6 feet above the arena. Videos were recorded by the behavioral analysis software Viewer2 (BIOBSERVE Gmbh, Bonn, Germany). Before experiments, the software was set up to trace and record the animal’s movements over the arena or the Y-maze.

7.2.2.1 Open Field

The open field test [269, 270] was carried out to allow animals to become acclimated to the arena for the object placement and object recognition tests, and to provide a measure of the level of activity. Open field tests lasted 9 minutes, broken into three 3-minute continuous intervals. The number of times the animal reared up on its hindpaws was recorded manually. The tracklength, or total length of ambulation, was calculated by the Viewer2 program from the recorded video.

7.2.2.2 Object Placement

The object placement test was designed to obtain a measure of spatial memory in animals [271-273]. This test consisted of a training phase and a testing phase. In the training phase, two identical visually-rich objects (defined as inanimate objects with textured surfaces), objects A and B, were placed at two spatially asymmetric positions in the arena (with respect to the walls), not near the center and not near the walls. The animal was introduced into the arena and allowed to explore the arena and the objects freely for a period of 5 minutes, and then returned to its cage for a retention period (retention periods of 5,7, 10 and 20 minutes were tested in these experiments).

In the test phase, object B is moved to a new position, ensuring that the positions of the two objects are still spatially asymmetric with respect to the walls of the arena and the orientation is distinguishable from that in the train phase. After the retention period has elapsed, the animal is returned to the arena for the test phase and allowed to explore the arena and the objects for 3 minutes. The amount of time the animal spent exploring each object in each phase was recorded. Animals that explored the objects in the test phase for less than three seconds were excluded (no-explore).

A spatial memory score was calculated for each animal from the ratio of the period of time spent exploring object B to the total time spent exploring both objects in the test phase. Object placement tests were typically carried out once per animal per retention period. When the test was repeated (either using a new retention period or to repeat a no-explore test), a new spatially unique position and a new pair of objects were used.

7.2.2.3 Object Recognition

The object recognition test was to measure visual memory, also consisting of training and testing phases [271-273]. Test conditions were identical to the object placement test, with a few exceptions. Two identical visually-neutral objects (defined as objects with plain and smooth sides), objects A and B, were used in the training phase, which consisted of 3 minutes. Retention periods of 20, 25, 30 and 60 minutes were used. In the test phase, object B is replaced with object C, a different visually neutral object. A visual memory score is computed from the ratio of the time spent by the animal exploring object C to the total time exploring both object A and C in the test phase. Object recognition tests were also carried out once per animal per retention period; for repeated tests a new set of visually-neutral objects (A, B and C) were used.

7.2.2.4 Balance Beam

The balance beam test was designed to estimate motor deficits in animals [274, 275]. In this test, animals walk across a wooden beam 5 feet long with 1.5” diameter circular cross section. Animals with normal motor coordination are generally able to cross the beam from end to end without any slips or falls. Slips are defined as instances where the animal loses its footing and the axis of its spine stops being parallel to the beam.

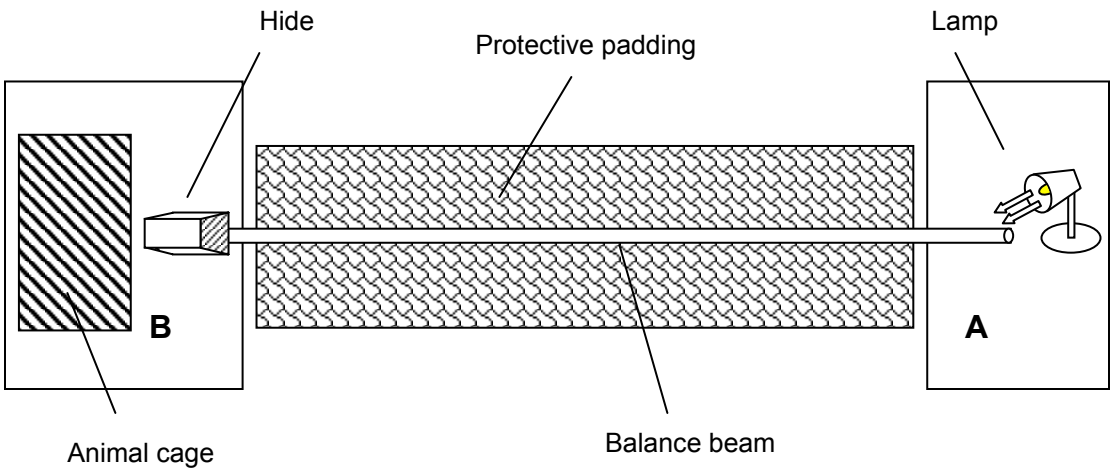

Figure 7.1: Top-view schematic of the balance beam setup.
The balance beam suspended between two tabletops/carts. A bright light source was placed at the starting end (A) to encourage the animal to start walking across the beam. A dark "hide" and the animal's home cage was placed at the finishing end (B), to encourage the animal to cross the beam.

A schematic of the experimental setup is shown in Fig. 7.1. The balance beam is positioned about 3-4 feet above the floor and kept horizontal, suspended between two tabletops/carts. Animals are initially placed on the beam ~6 inches from one end (A) and allowed to walk across to the other end (B). To encourage animals to readily cross to B, a darkened "hide" is placed at B, since rats prefer dark places. Additional encouragement is provided by placing food stimulus in the hide, and by placing the animal's home cage near B. To discourage animals from returning to A, an incandescent white light-lamp is placed at A, since rats do not prefer bright lights. Motor deficits are scored by counting the number of times animals slip while crossing the length of the beam. To ensure that animals cross the balance beam readily during the test, animals are pre-trained using a 3.5 inch wide plank of the same length as the balance beam, set up in the same fashion as the beam. Animals are placed on the

plank and encouraged to walk across, with gentle prodding at first if needed. Animals are pre-trained 2-4 times, after which they generally cross the plank readily.

7.2.2.5 Social Preference

The social preference test was designed to measure deficits in social preference in rats [276]. Rats are normally highly social animals, and when given a preference between an inanimate neutral object and another rat, rats should have a preference for other rats. The social preference test was conducted using the Y-maze. The arms of the Y-maze are labeled A, B and C. An 8” long section at the ends of arms B and C was closed off from the rest of the maze using perforated plastic screens. A neutral inanimate object was placed in the partitioned section of C, and a stimulus animal was placed in the partitioned section of B. Ovarectomized female rats of weight 250-300g were used as stimulus animals. During the test, the test animal was placed in arm A and allowed to explore the maze freely for a period of 5 minutes. The time spent by the test animal exploring the inanimate object and the stimulus animal was recorded. A social preference score was measured as the ratio of the total time spent by the animal exploring the stimulus animal to the total time spent exploring both the stimulus animal and the inanimate object.

7.2.2 Experimental Design

Forty female Sprague-Dawley rats (250-300g) were used for behavioral analysis. These included kaolin induced CH animals (n = 13), surgical CH control animals (n =

16) and intact controls (n = 11). All surgical procedures for the kaolin CH and surgical CH control animals are described in Chapter 3. Animals were divided into 3 cohorts (details in Table 7.1).

	# of kaolin CH	# surgical CH controls	# intact controls
Cohort 1	0	5	5
Cohort 2	5	5	0
Cohort 3	8	6	6

Table 7.1: Number of animals used in each cohort

		Cohort 1	Cohort 2	Cohort 3
Open Field (OF)		x	x	x
Balance Beam (BB)		x	x	x
Social Preference (SP)		x	x	
Object Placement:				
Retention Interval	5		x	
	7	x	x	
	10		x	
	20	x		
Object Recognition:				
Retention Interval	20		x	
	25	x		
	30			x
	60	x	x	

Table 7.2: Parameters of the different tests performed in the animals.

The tests carried out in each cohort are shown in Table 7.2. Open field, balance beam and object recognition tests were carried out in all cohorts. Object placement and social preference tests were carried out only in cohorts 1 and 2, as these tests were not able to demonstrate any difference between the groups and was thus abandoned in cohort 3. Behavioral studies were carried out 1-2 weeks post induction for cohort 1 animals, 2-3 weeks post induction for cohort 2 animals and 3-4 weeks post induction for cohort 3 animals. All tests were completed in the span of 1-2 weeks.

During the behavioral studies, the experimenter was blinded to animal surgical status. All animals within each cohort were randomly numbered and identified using tail color markings. To ensure that intact control animals had the same external appearance as surgical controls, intact controls in cohort 1 were anesthetized with isoflurane, their necks were shaved, and a neck incision was made under aseptic conditions, similar to the neck incision made during surgeries of saline control and kaolin CH animals, and immediately closed.

7.2.3 Data Analysis and Statistics

Statistical comparison between two groups was done using a two-tailed t-test and a one-way ANOVA followed by an LSD post-hoc test. Differences were considered significant for $p < 0.05$.

7.3 Results

7.3.1 CH Induction Results

All animals tolerated surgery well. In Cohort 2, 4 animals developed CH (VV > 30 µl), with VV of 433.1 ± 142.2 µl and SV of 189.2 ± 57.7 nl. In Cohort 3, 8 out of 11 animals developed CH (VV > 30 µl), with VV of 135.8 ± 77.0 µl and SV of 110.8 ± 81.0 nl.

7.3.2 Open Field Results

Overview

All animals completed the open field test. The tracklength for all animals was 2715 ± 1150 cm (range: 24 – 4630 cm). The largest tracklengths were recorded for 2 intact control animals, with values over 4400 cm. The animals with very low tracklengths tended to remain in a corner of the arena for most of the test (the lowest values were from two surgical controls and two kaolin animals). During exploration of the arena, it is typical for rats to rear up on their hindlegs; this is another means of exploration of the arena for rats. The number of rears for all animals was 42 ± 22 (range: 4-81). The lowest number of rears was recorded for the surgical control that also had the lowest tracklength. A strong correlation was found between number rears and tracklength for all animals across all cohorts (Fig. 7.2). This is not unusual, since both these values are expressions of animal activity and level of exploration.

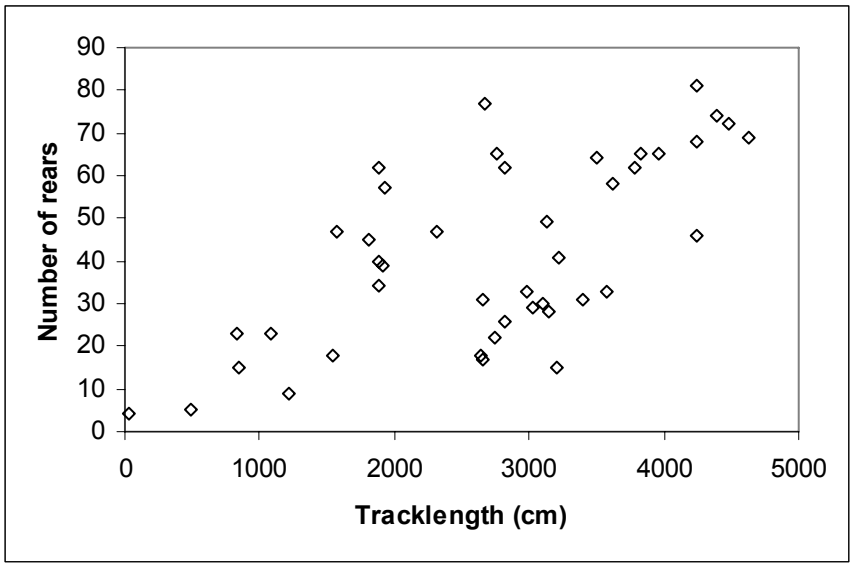

Figure 7.2: Tracklengths and number of rears for all animals.
A significant correlation was observed between tracklengths and the number of rears across all cohorts ($R = 0.66$, $R^2 = 0.43$, $p < 0.0001$).

Animal Grouping

In cohort 1, a significant difference was found in the number of rears between surgical controls and intact controls (29 ± 21 and 58 ± 13, $p = 0.03$) (Fig. 7.3A). Surgical controls in cohort 1 also had a trend towards a lower tracklength than intact controls in cohort 1, although this difference was not significant (1147 ± 1058 cm vs. 2648 ± 665 cm, $p = 0.07$) (Fig. 7.3B). The kaolin induced animals had a significantly lower number of rears than the saline controls in cohort 2 (17 ± 14 vs. 46 ± 16, $p = 0.02$) (Fig. 7.3C). However, there was no significant difference between tracklengths for these animals (Fig. 7.3D). In cohort 3 animals, significant differences were found between tracklengths of intact controls vs. saline controls (4190 ± 377 cm vs. 3476 ± 472 cm, $p = 0.02$) and intact vs. kaolin animals (4190 ± 377 cm vs. 3171 ± 543 cm, $p = 0.001$), while no significant difference was found between tracklengths of saline controls vs. kaolin

animals (3476 ± 472 vs. 3171 ± 543, p = 0.22) (Fig. 7.3E). On the other hand, differences in number of rears was not significant for any of the groups in cohort 3 (61 ± 18 (intact), 47 ± 17 (saline), 36 ± 20 (kaolin)) (Fig. 7.3F).

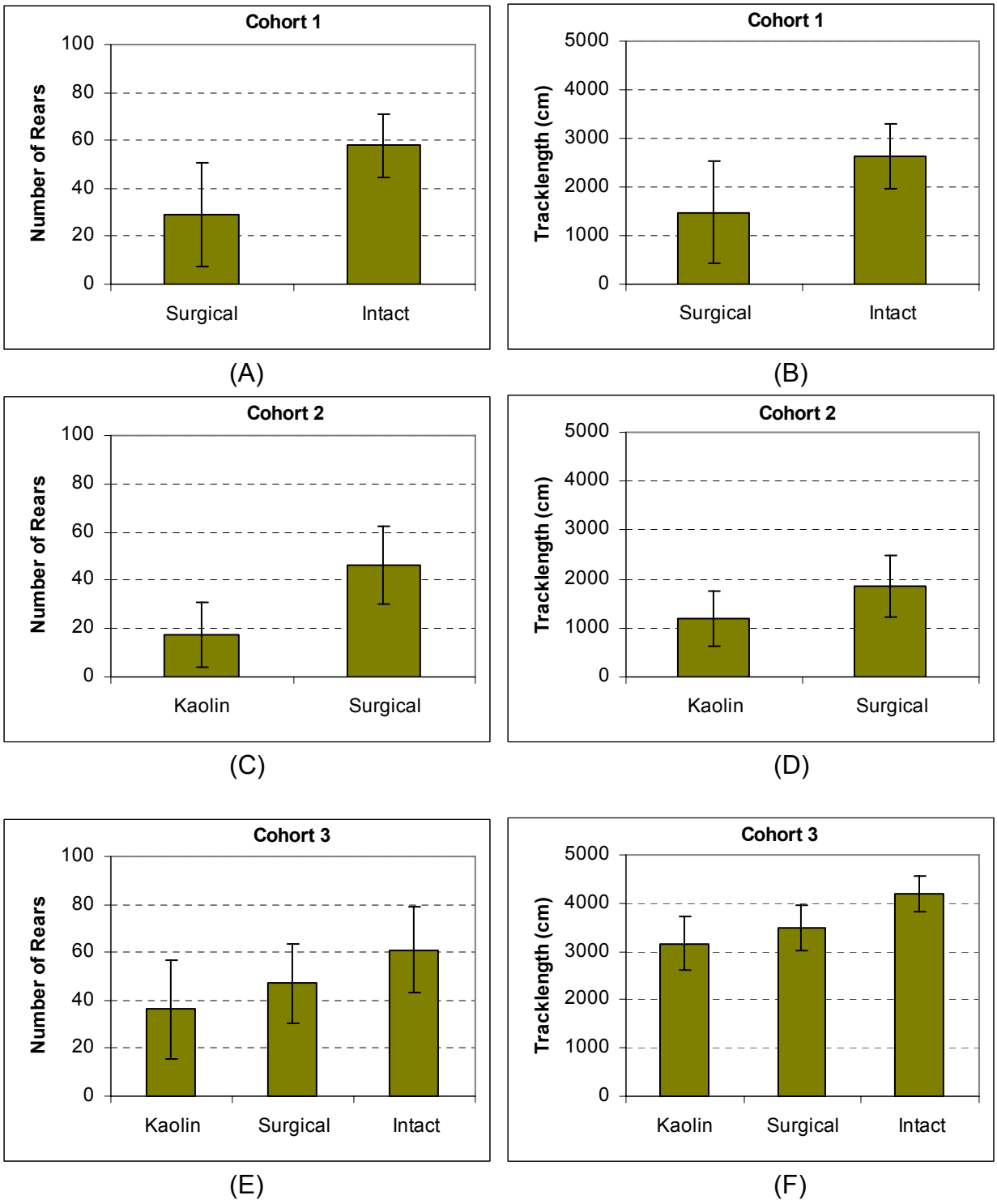

Figure 7.3: Tracklengths and number of rears for the different cohorts.
This figure shows the number of rears (left column) and the tracklengths (right column) for cohort 1 (A & B), cohort 2 (C & D) and cohort 3 (E & F).

7.3.3 Object Recognition Results

In cohort 1, two animals, one intact and one surgical control, were excluded from both OR tests. The intact control did not explore the arena or objects, and the surgical control had less than 3 seconds of exploration in the training phase. In the 60 minute retention interval test, 3 of 4 intact controls and 2 of 4 surgical controls had a preference for the novel object; preference scores were not significantly different (75.9 ± 23.6 vs. 55.2 ± 16.8, $p = 0.20$). In the 25 minute retention interval test, all animals had a preference for the novel object; preference scores were also not significantly different (64.6 ± 11.3 vs. 79.5 ± 17.4, $p = 0.20$).

In cohort 2, in the 60-minute retention interval OR test, two kaolin and one surgical control animals did not explore the objects and were excluded. All three kaolin animals and three of four surgical controls had a preference for the novel object (scores: 79.2 ± 9.5 (kaolin) and 58.8 ± 10.2 (control)). Preference scores for the kaolin animals was significantly higher ($p = 0.043$). In the first 20 minute retention interval test, 7 animals (4 kaolin and 3 control) did not explore the arena. The test at this retention period was repeated, and 2 kaolin animals did not explore the arena and were excluded. Two of three kaolin animals and four of five surgical controls had a preference for the novel object (scores: 69.6 ± 22.4 (kaolin) and 65.7 ± 22.7 (control)). There was no significant difference between these scores ($p = 0.82$).

In cohort 3, 5 kaolin animals, 1 surgical control and 1 intact control did not explore the objects and were excluded. All of the remaining 6 kaolin animals had a preference for the novel object (score: 80.6 ± 11.4). Four of five surgical controls had a preference for the novel object (score: 77.3 ± 17.6). Three of five intact controls had a

preference for the novel object (score of 54.6 ± 27.1). The preference scores of the 3 groups were not significantly different from each other (p = 0.095).

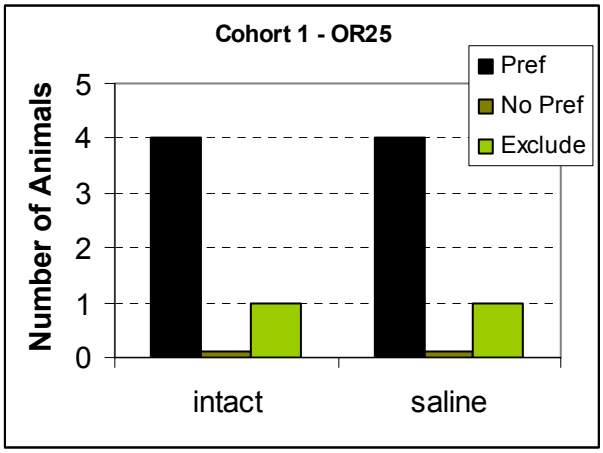

(A)

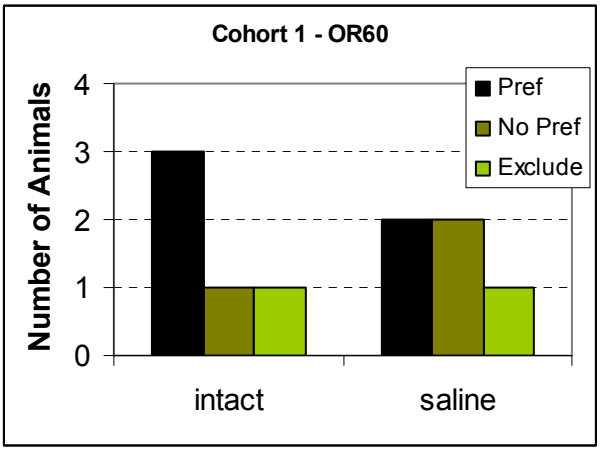

(B)

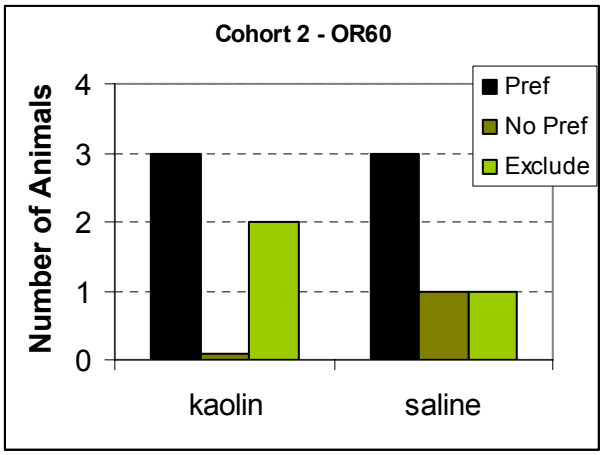

(C)

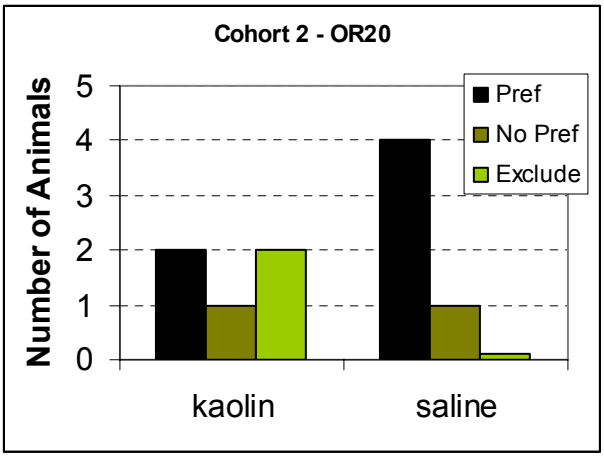

(D)

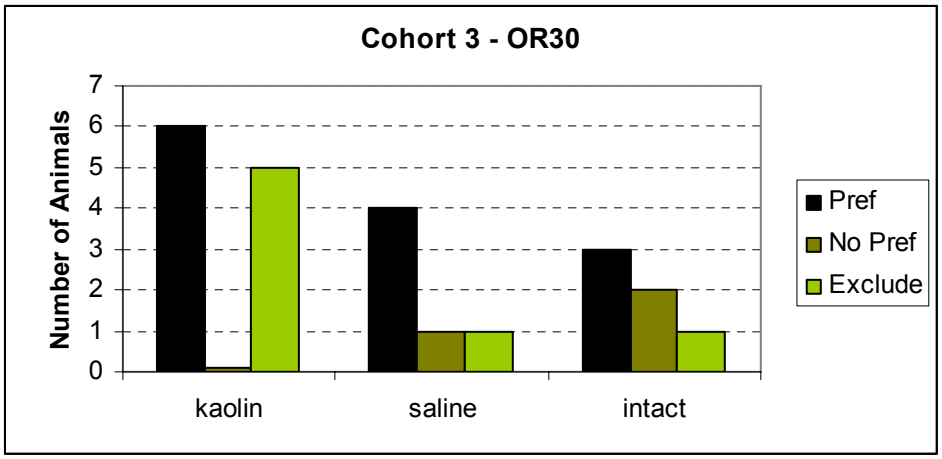

(E)

Figure 7.4: Animal outcome for object recognition tests (visual memory).
This figure shows the number of animals that had a preference for the novel object, the number of animals that did not, and the number of animals that were excluded due to lack of exploration.

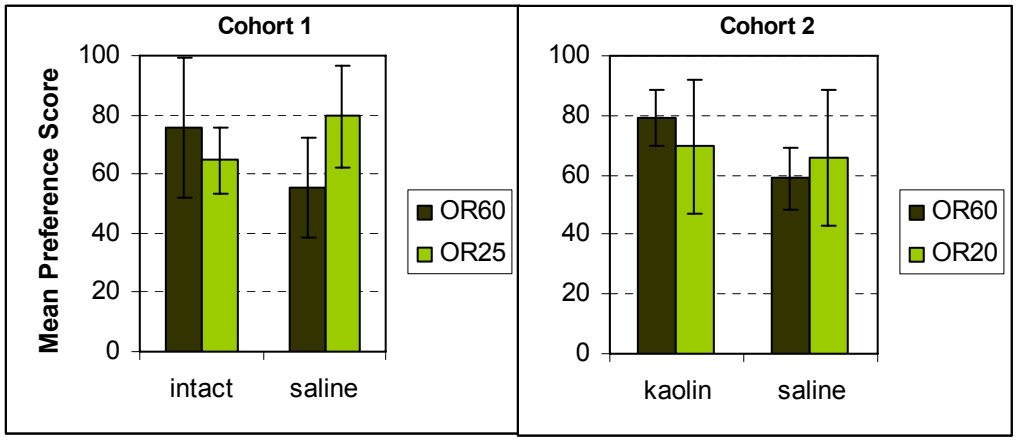

Figure 7.5: Preference scores for the object recognition tests.

In summary, the object recognition test results were inconclusive since the kaolin animals had similar or better preference for the novel object than the control animals.

7.3.4 Object Placement Results

Several animals completed the object placement test successfully, but a number of them did not explore the arena and the objects adequately and had to be excluded. A few animals were excluded because they climbed over the objects, producing a bias. In cohort 1, in the 20 minute retention test, 1 intact control and 3 saline controls were excluded. Among the remaining, 2 of 4 intact controls had a preference for the novel object, while 1 of 2 saline controls had a preference for the novel object. The preference score for the intact controls was 43.7 ± 25.2, and the preference score for the surgical controls was 47.4 ± 26.6. In the 7 minute retention test, 2 surgical control and 1 intact control were excluded; of the rest, only 1 intact control had a preference for the novel object while 4 did not. Two intact controls had a preference for the novel object, and 1 saline control did not.

In cohort 3, 7 minute retention, 1 kaolin animal and 2 saline controls were excluded. Two of 4 kaolin animals had a preference for the novel object, while only 1 of 3 of the remaining saline controls had a preference for the new object. Preference scores were 57.0 ± 12.3 and 50.7 ± 37.9 for the kaolin and saline controls respectively. In the 10 minute retention test, 2 kaolin animals were excluded. One of the remaining 2 kaolin animals had a preference for the new object while 3 of the 5 saline controls had a preference for the new object. Preference scores were 47.7 ± 24.7 and 58.8 ± 18.3 for the kaolin and saline controls respectively. In the 5 minute retention test, 1 kaolin and 1 saline control animals were excluded. Three of the remaining 4 kaolin animals had a preference for the new object, while all4 remaining saline animals had a preference for

the novel object. Preference scores were 50.6 ± 20.5 and 72.4 ± 16.2 for the kaolin and saline controls respectively.

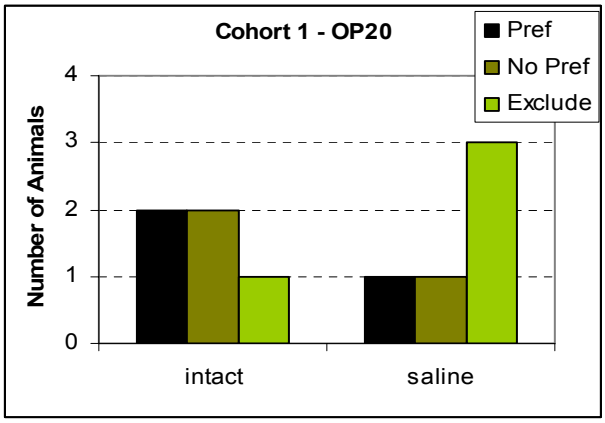

(A)

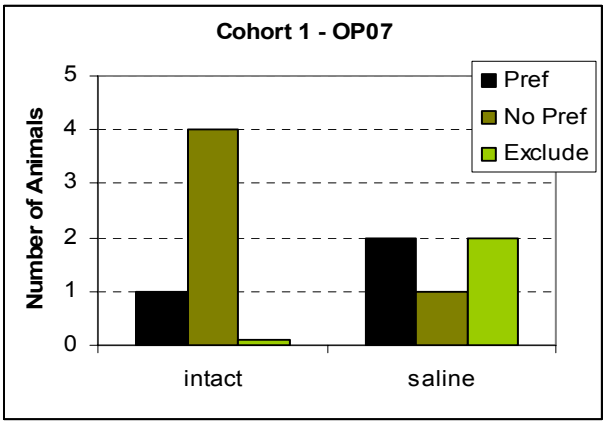

(B)

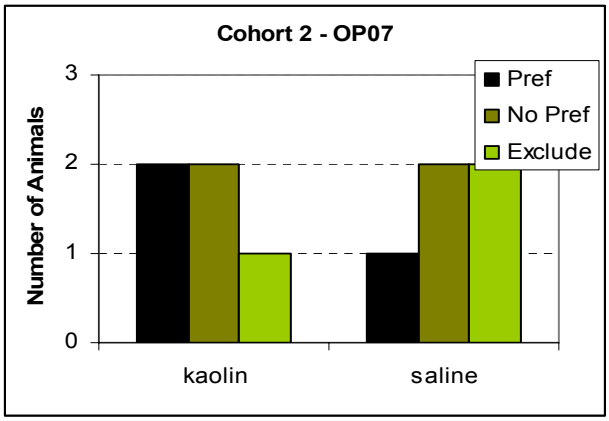

(C)

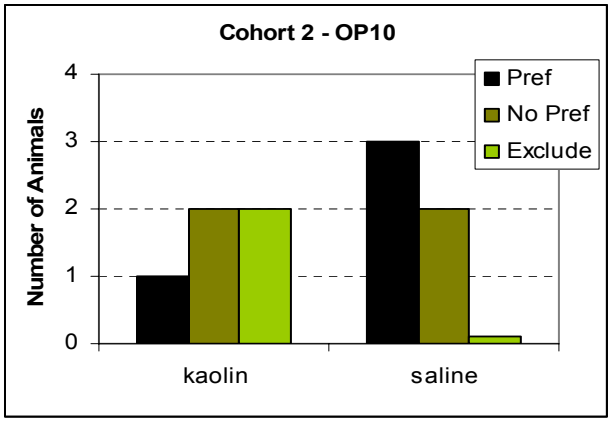

(D)

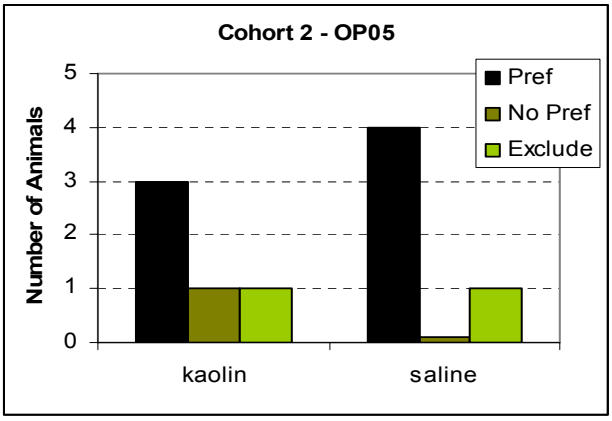

(E)

Figure 7.6: Animal outcome for object placement tests (spatial memory).
This figure shows the number of animals that had a preference for the novel object, the number of animals that did not, and the number of animals that were excluded due to lack of exploration.

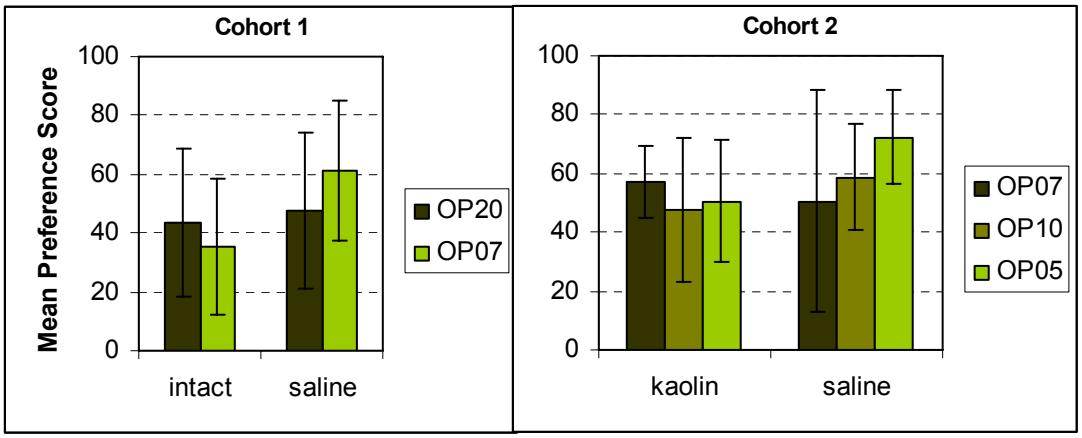

(A)

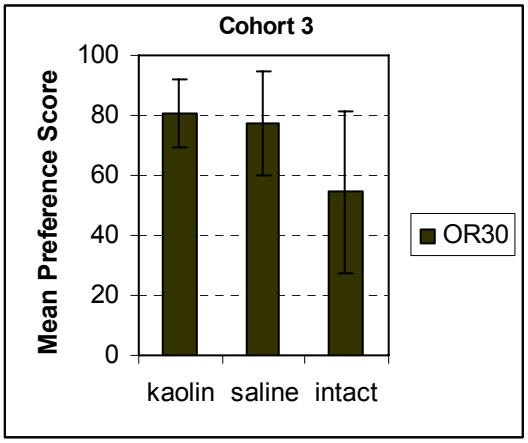

(B)

Figure 7.7: Preference scores for all cohorts for all object placement tests.

7.3.5 Balance Beam Results

All animals except one were able to complete the balance beam test successfully. One animal, which was found to be severely hydrocephalic, had over 20 slips before completing the balance beam and was removed. In cohort 1, the intact

controls had 4.8 ± 1.8 slips while the saline controls had 3.5 ± 1.3 slips ($p = 0.26$). Three of the intact controls registered 6 slips each, while two of the saline controls registered 4 and 5 slips.

In cohort 2, the surgical control animals had 0.4 ± 0.6 slips, while the kaolin animals 10.8 ± 8.0 slips ($p = 0.02$). The high variability in the cohort 2 kaolin animals was due to the fact that one of the animals did not develop hydrocephalus and had only 3 slips, while one hydrocephalic animal, with a high ventricular volume of 540 µl, also registered 3 slips. The number of slips for the hydrocephalic animals alone was 12.8 ± 7.8, which was also significantly larger than that of the saline controls ($p = 0.009$).

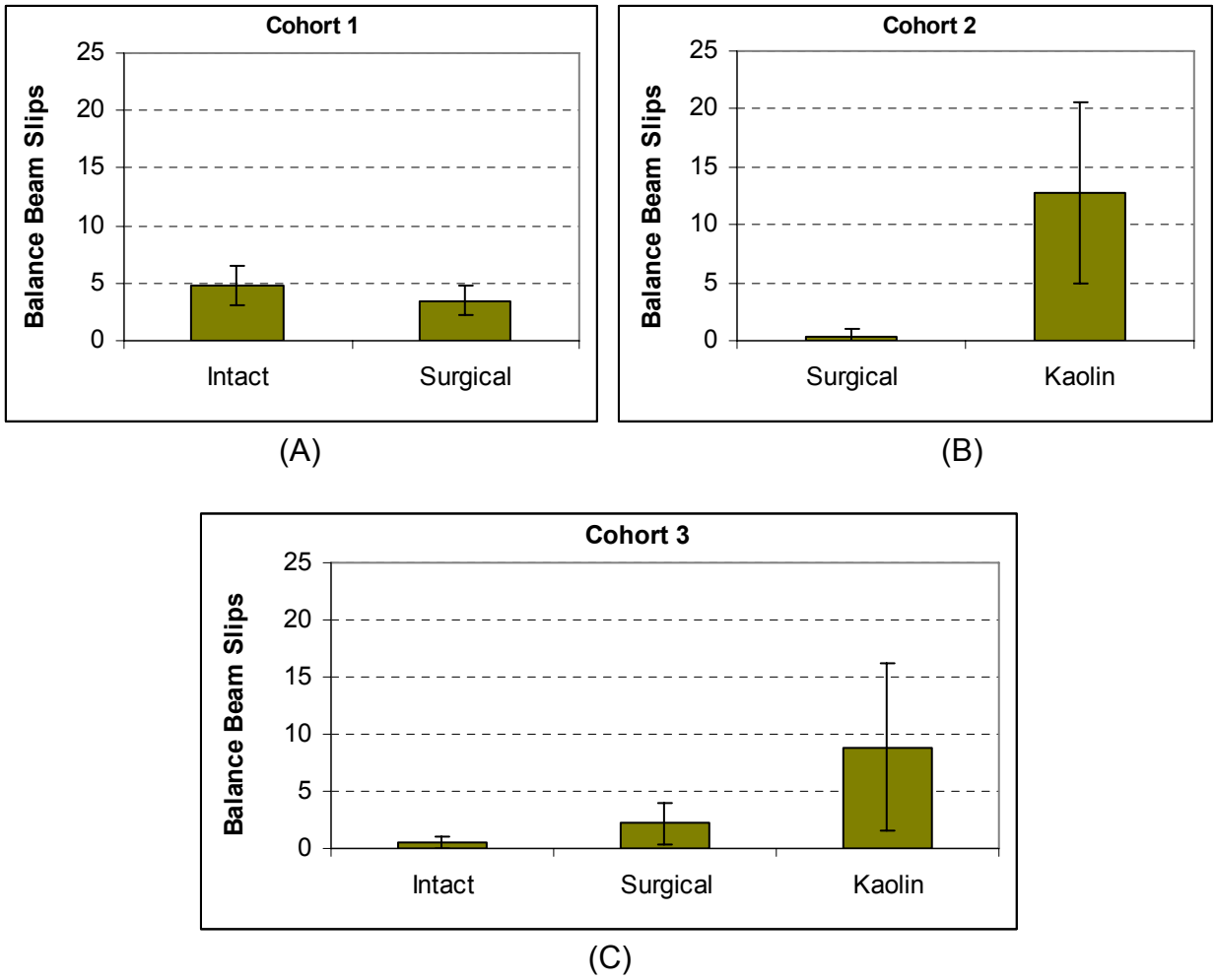

Figure 7.8: Balance beam slips for the different groups in each cohort.
Hydrocephalic animals had significantly higher number of balance beam slips than controls in each group.

In cohort 3, the intact control animals had 0.5 ± 0.55 slips, while the saline controls had 2.2 ± 1.8 slips. One of the saline controls registered 5 slips. The kaolin animals in cohort 3 had 6.7 ± 7.2 slips; 3 of these animals did not develop hydrocephalus and registered 2 or fewer slips each, while one animal, which had a ventricular volume of 26 µl (lower than the threshold for hydrocephalus) registered a high number of 17 slips. The difference in the number of slips among the 3 groups was not statistically significant when all kaolin animals were included, although the kaolin

animals did have a trend toward higher number of slips ($p = 0.059$). However, when the 3 kaolin animals with normal ventricles and low number of slips were excluded, then the difference becomes statistically significant ($p = 0.005$ for kaolin vs. intact controls, and $p = 0.02$ for kaolin vs. saline controls).

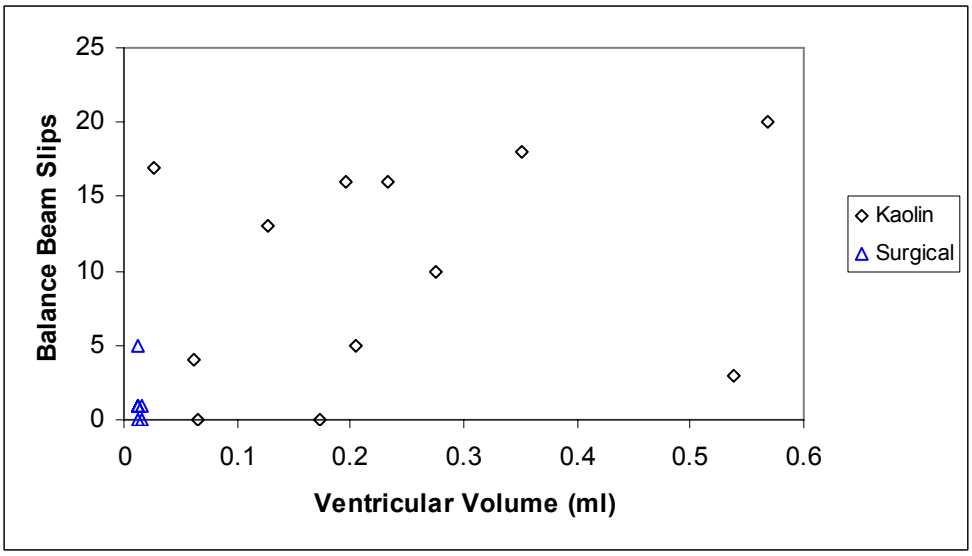

(A)

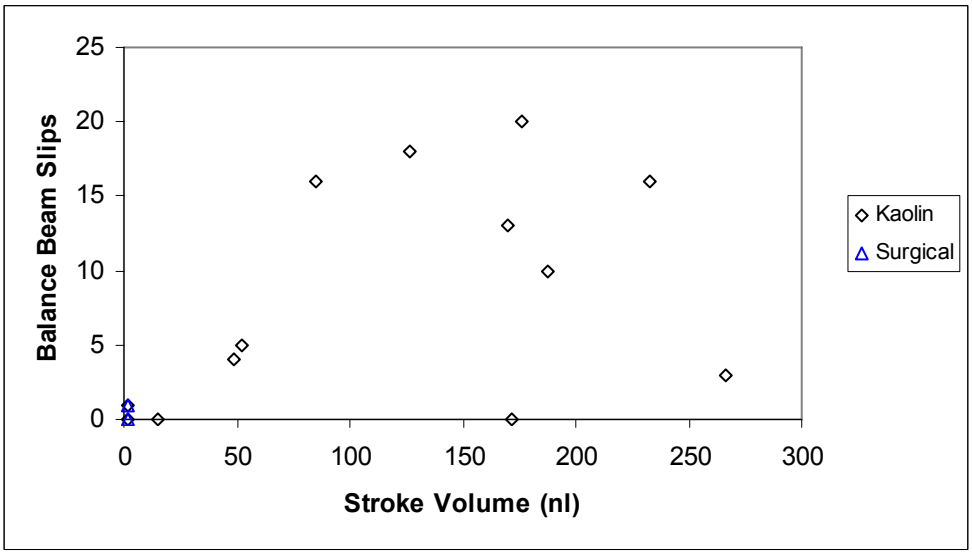

(B)

Figure 7.9: Regression analysis of motor deficits with stroke volume and ventricular volume.
A weak correlation (including all animals, saline and kaolin) was found between ventricular volume and balance beam slips (R^2 = 0.26, p = 0.03), but this may have been driven by the surgical control animals clustered near the origin of the graph. No correlation was found between stroke volume and balance beam slips.

Regression analysis between balance beam slips and ventricular volumes revealed a weak but statistically significant correlation (R = 0.51, R^2 = 0.26, p = 0.03)

(Fig 7.9A). However, this correlation was probably being driven mainly by the surgical control animals, clustered near the origin. No significant correlation was found between balance beam slips and aqueductal pulsatility (measured as CSF stroke volume) (Fig. 7.9B)

7.3.6 Social Preference Results

One CH animal from cohort 2 failed the social preference test, because it remained sitting in Arm C and did not move throughout the test and was excluded. This resulted in a net sample size of 4 kaolin animals in cohort 2. All remaining animals completed the social preference test. Overall, all animals had a preference for the social stimulus (ovarectomized rat) as opposed to the neutral object. Average social preference score for all animals in all cohorts was 84.4 ± 8.2%. There was no significant difference in social preference scores of intact and surgical controls in cohort 1 (78.2 ± 7.4% vs. 86.9 ± 8.8%, $p = 0.13$), nor between surgical controls and kaolin animals in cohort 2 (88.7 ± 7.8% vs. 83.4 ± 6.6%, $p = 0.32$).

7.4 Discussion

Deficits in behavioral characteristics, such as cognitive and motor deficits, are one of the most uselful methodologies for determining clinical outcome in communicating hydrocephalus (CH). We therefore characterized behavioral traits in normal rats and surgical controls in order to determine deficits in behavior in our CH rat model. Two of the tests used, open field (OF) and balance beam (BB), which

characterize animal activity and motor coordination respectively, showed promise in being able to discern between control and hydrocephalic animals.

In the OF test, the two measures used, total tracklength and total number of rears, are both measurements of animal activity. A statistically significant difference was found between the tracklengths but not the number of rears of control and hydrocephalic animals in one cohort, while a significant difference in the number of rears but not tracklength was found in another cohort. The differences being seen between these groups may be due to the small number of animals used. One confounding factor is that significant differences were found between the results of intact controls and surgical controls. Surgical controls do not develop any symptoms of hydrocephalus, so the differences found between the two control groups may be due to the fact that all these tests was done within a few weeks after surgery, especially cohorts 1 and 2, which were tested only 2 weeks after surgery. A longer delay after surgery may mitigate these differences.

The BB test showed a major difference between control and hydrocephalic animals, with the latter having significantly greater gait abnormalities based on the number of slips on the balance beam. This is an important finding: gait disturbances are usually one of the first symptoms that present in human hydrocephalus. The fact that our animal model also exhibits prominent gait abnormalities support the clinical relevance of our animal model. A weak correlation was found between the number of balance beam slips and ventricular size; however, no correlation was found between the number of balance beam slips and aqueductal pulsatility. This is likely due to the fact that a few animals with high aqueductal pulsatility registered only a few slips when

crossing the balance beam. This may be an indication that the BB test is not highly sensitive unless a larger group of test animals are included.

The behavioral tests used in this study are all voluntary tests, in the sense that animals are not deprived of food or water or subjected to noxious stimuli to force them to perform the tests. A drawback of this feature is the possibility that some animals may choose not to perform the test. Previous studies by other investigators have shown that this voluntary factor is usually not a serious problem, and that the results from these tests are similar to those obtained from coercive behavioral tests (such as those utilizing electric shocks) [271-273]. In the present study, though, a number of animals refused to complete some of the tests, mainly the spatial and visual memory tests. Of course, issue can be addressed simply by using a larger number of animals. Another limitation is the use of Sprague-Dawley rats as the animal model. Sprague-Dawley rats have poor vision, the same as other albino rat strains [277-279], but have excellent olfactory ability; it is very likely that these rats carry out most of their exploration and other behavioral activities using olfactory cues, rather than visual cues. The behavioral tests used here were designed to be visual based rather than olfactory, and care was taken to remove olfactory cues, by cleaning the arena with alcohol and wiping down the test objects with alcohol. On the other hand, if visual or spatial memory was tested using some form of olfactory cues, the results might be entirely different and may in fact be more sensitive to behavioral changes in our animal model.

One possible explanation for the lack of visual and spatial memory deficits is the fact that these animals were tested within a few weeks after induction of CH. It is possible that deficits in memory may not become evident until a longer period of time

after induction. Behavioral tests conducted on young rats in an obstructive model of hydrocephalus showed motor deficits after about 9 months post induction, and not at earlier time-points [193].

A significant drawback in the design of the balance beam test is the fact that these tests are not recorded in any way. The test scoring has to be done visually while the test is conducted, and since the test is not video recorded, it is not possible to verify the scores. Video recording is difficult, because ambient lighting has to be kept to a minimum to make the test environment conducive to animals, and video recording with the available equipment would have been very difficult under such conditions of low lighting. As a result, there is no way to eliminate or reduce possible human error in the scoring process. Moreover, the test is single shot, and was not repeated for animals, so there was no possibility of averaging the scores from multiple trials. The problem with repeating the test on the same animal is that rats can adapt to the balance beam quite rapidly, and a second or third trial might not have adequately reflected the animal's motor coordination as compared to the initial trial.

Chapter 8

---

8. General Discussion

8.1 Summary of Results

In this dissertation, our main conclusions are:

- Aqueductal pulsatility is clearly elevated in our rat model of communicating hydrocephalus (CH)
- Aqueductal pulsatility has a relationship with ventricular size, but this relationship varies over time and may be modulated by other factors such as intracranial compliance
- Capillary pulsatility is elevated in CH, but not correlated with aqueductal pulsatility.

8.2 Implications of Our Studies

Our results represent a significant series of steps forward in the understanding of the complex mechanisms of communicating hydrocephalus. Elevated aqueductal pulsatility is a phenomenon that has been observed in human communicating hydrocephalus for some time, but the mechanism of pulsatility increase is unknown.

Elevated pulsatility has not been studied in a rodent model before, primarily because the vast majority of pre-existing rodent models mimic various forms of obstructive hydrocephalus, with at least partial obstruction of fourth ventricle outflow. Our rat model is the first model of communicating hydrocephalus 1) which produces moderate to severe levels of ventricular dilation, 2) is reproducible and 3) closely mimics the pathophysiology of acquired human communicating hydrocephalus without other co-morbidities [9]. The results of our CSF flow studies clearly demonstrate elevated aqueductal pulsatility in our CH rats, which is by itself an important breakthrough, as it paves the way for many future studies to investigate the role that pulsatility plays in the pathophysiology of CH.

Secondly, we found that aqueductal pulsatility is significantly correlated with ventricular size in CH, but that this relationship changes over the course of hydrocephalus development. This suggests that there is no strict one-to-one relationship between pulsatility and ventricular size. Instead, this implies that changes in other parameters, such as compliance, may affect both aqueductal pulsatility and ventricular size. Intracranial compliance is the primary factor underlying changes in intracranial pressure pulsations: a decreased compliance causes increased arterial-driven pressure pulsations in the brain [201, 203], and compliance is known to be decreased in CH [189-191]. Compliance, measured invasively in terms of intracranial pressure pulsations, has been shown to be a good prognostic marker of shunt outcome as compared to other tests such as CSF outflow resistance or lumbar tap [179, 265, 267, 280]. However, the effect of compliance on aqueductal pulsatility has not been studied. If the relationship between intracranial compliance and aqueductal pulsatility

can be characterized, then this would suggest that aqueductal pulsatility is a viable non-invasive prognostic marker of shunt outcome. Clinical application of such a non-invasive measurement would be a significant benefit to patients suffering from CH.

Following up on these observations, our craniectomy and shunting experiments were an attempt to model the effects of altering compliance on aqueductal pulsatility. We concluded that aqueductal pulsatility has a strong relationship with compliance, and that an increased compliance caused either by removal of the rigid calvarium or diversion of accumulated CSF by shunting causes aqueductal pulsatility to decrease. This provides strong support for our hypothesis on a relationship between aqueductal pulsatility and compliance. The next logical step is to elucidate a mathematical relationship between aqueductal pulsatility and compliance. For such studies, measurements of intracranial pressure (ICP) are required. ICP levels would need to be measured at different stages of CH in our rat model, and in the craniectomy studies. A precise mathematical relationship between compliance and aqueductal pulsatility would be important in demonstrating whether or not aqueductal pulsatility is a good prognostic marker for shunting, as described earlier.

Moreover, the shunting experiments represent another significant advance in experimental hydrocephalus. As our CH rat model was intended to be used for the study of CSF flow dynamics in CH, the success of shunting these animals further validates the viability and importance of this model. Success of the shunting experiments opens up avenues to study shunt failures and malfunctions in the context of a small animal model. In addition, our results indicate that aqueductal pulsatility is decreased with shunting, which is similar to results in shunted hydrocephalic patients

[210]. Our success with shunting provides us the opportunity to investigate why and how CSF flow patterns change with shunting.

To provide further understanding of the mechanism of intracranial pulsatility and a potential relationship to vascular pathology, we quantified capillary pulsatility in our rat model of CH. Our results of elevated capillary pulsatility represent another enormous breakthrough in our understanding of the mechanism of CH development by providing support for the pulsatility redistribution theory of CH development. Elevated pulsatility in cerebral capillary beds has been implicated in the mechanism of CH for some time by many prominent neurosurgeons [6, 8], but prior to our results, there had been no experimental evidence to support or refute this vital component of the theory of pulsatility redistribution. Our results suggest that capillary pulsatility is indeed elevated in CH, and consequently, it may indeed be involved in the mechanism and pathophysiology of CH. Increased levels of microvascular pulsatility may be a key factor in the neuropathology of CH, because increased capillary pulsations are known to affect normal hemodynamics [281, 282]. With this conclusion, we are now uniquely positioned to address several important questions regarding increased microvascular pulsatility: what is the role of increased microvascular pulsatility in the neuropathology of hydrocephalus? Does microvascular pulsatility affect neuroinflammatory reactions such as microglia proliferation? Is increased microvascular pulsatility a factor in decreased capillary density in hydrocephalus? Is increased microvascular pulsatility the key driving force behind elevated aqueductal pulsatility and ventricular dilation? Is glucose transport across the capillary endothelium altered by increased capillary pulsatility?

One of our conclusions from the capillary pulsatility studies is that anesthesia has a strong impact on capillary pulsatility changes, and in some cases may mask capillary pulsatility increase. We were able to demonstrate elevated capillary pulsatility in our CH rats under the influence of isoflurane anesthesia, but our studies with ketamine-xylazine produced dissimilar results, that capillary pulsatility is not elevated in CH. This is an important finding, because it suggests that different anesthetics can have varying effects on ICP and local brain parenchymal compliance, which can mask changes in pulsatility. Ketamine-xylazine is known to produce a greater decrease in cerebral blood flow, compared to isoflurane [237]. The effect of anesthetics requires further study of capillary pulsatility using other anesthetics such as urethane and α-chloralose.

In order to evaluate the relationship between aqueductal pulsatility, severity in CH and cognitive and motor coordination deficits in our rat model of CH, behavioral studies were conducted. These results are significant in that they show that the presentation of CH in our rats is similar to clinical symptoms in terms of gait disturbances. This by itself provides further validity with regards to the viability of our model being representative of human communicating hydrocephalus. We found that our CH rats had motor deficits, but we could not demonstrate any cognitive impairments in our rats. However, behavioral deficits remain the key method for evaluating improvement of symptoms following shunting and other possible interventions.

8.3 Technical Achievements

In order to attain our results, a number of important technical achievements were made in the course of this dissertation:

- We refined the surgical technique of induction of communicating hydrocephalus to achieve a 66% success rate
- We designed the techniques for measuring and calculating aqueductal pulsatility in a rodent model of CH using phase contrast MRI
- We perfected the techniques for measuring capillary pulsatility in the rat neocortex, and we designed a suite of algorithms to automatically and efficiently analyze large volumes of data to quantify capillary pulsatility

8.4 Addressing Overall Hypotheses

Our results have supported most of our initial hypotheses. One of the hypotheses in this dissertation was that we would be able to measure aqueductal pulsatility in rats with phase contrast MRI. We found, however, that normal rat aqueductal pulsatility is very small and below the threshold of noise in our scans. While this gave us an upper limit for normal aqueductal pulsatility in rats, it would be helpful to determine the actual value of normal aqueductal pulsatility. This may require the use of a stronger magnet or a more sensitive flow sequence, such as a phase contrast balanced SSFP.

We had also hypothesized that aqueductal stroke volume will *not* be correlated with ventricular size. While we found that there are strong correlations between these two parameters, the relationship also varies over time, as discussed above. This

variation indicates that there may not be a one-to-one relationship between the aqueductal pulsatility and ventricular size, but that other factors, such as intracranial compliance, may be involved in the changes in aqueductal pulsatility and ventricular size.

Two of hypotheses regarding aqueductal pulsatility were that that aqueductal pulsatility would be correlated with elevated capillary pulsatility and with behavioral deficits in motor coordination, but we were not able to establish these postulates. This may be due to the fact that aqueductal pulsatility depends significantly on physiological parameters such as respiration and blood gas levels, factors for which we have not accounted. Preliminary results of the effects of varying respiration under different levels of anesthesia show that aqueductal pulsatility can vary significantly under different physiological conditions. These physiological variations may weaken any correlation between aqueductal pulsatility and other parameters such as capillary pulsatility and motor deficit scores. This aspect of aqueductal pulsatility requires further study before we can comment on the significance of the lack of correlation.

Finally, we had also hypothesized that CH rats would exhibit cognitive deficits in memory, but we were not able to establish this relationship. As mentioned above, this may be due to the fact that we studied only a very small number of animals, and larger animal groups are needed to see differences between normal and diseased rats in the studies that we used. Another possibility is that cognitive deficits may take much longer to take effect. A study of cognitive deficits in kaolin induced hydrocephalic rats showed that cognitive deficits may take several months to manifest [193], whereas we studied

our animals within a month of induction. Further study is required to assess cognitive impairment in our rat model.

8.5 Future Directions

Our results pave the way for further exploration of the pathophysiology of CH in the context of elevated aqueductal pulsations. Important future work includes:

- **Characterization of intracranial compliance in CH and its relationship to aqueductal CSF pulsatility.** As discussed above, experiments have to be conducted in which intracranial compliance will be measured by characterizing the pressure-volume curve from CSF infusion tests, and the relationship of compliance with aqueductal pulsatility should be explored at different stages in the development of hydrocephalus in our rat model of CH. In addition, histopathological studies should also be conducted in these studies to quantify the extent of gliosis in grey matter and white matter of the brain, to explore the relationship between compliance and gliosis.
- **Characterization of intracranial pressure pulsatility in CH and its relationship to aqueductal CSF pulsatility.** Changes in intracranial pressure pulsatility should be characterized, together with aqueductal pulsatility.
- **Shunting studies.** Shunting studies should be conducted to determine whether CH in these animals is similar to clinical CH in terms of shunt responsiveness (i.e. do symptoms in CH animals improve with shunting?). These studies will also allow exploration of how good a prognostic marker aqueductal stroke volume is to shunt responsiveness.

- **Investigation of the role of physiological parameters on aqueductal pulsatility.** Our preliminary results showed that aqueductal pulsatility is strongly impacted by different rates of respiration, produced by different levels of anesthesia. This likely is a consequence of changes in blood gas levels with depth of anesthesia and respiration. These effects on aqueductal pulsatility need to be fully investigated, by measuring changes in aqueductal pulsatility with blood gas measurements. These results may impact many future studies utilizing aqueductal pulsatility, and could have important consequences in the clinical use of aqueductal pulsatility in hydrocephalus.
- **Investigation of the effect of anesthesia on capillary pulsatility**. Capillary pulsatility studies should also be conducted using other anesthetics such as urethane and chloralose to further evaluate the extent of anesthesia effect on capillary pulsatility changes.
- **Changes in capillary pulsatility in other components of the microvasculature, such as arterioles.** While we have shown elevated pulsations in capillaries, one component of the microvasculature that we have not investigated is the arteriolar network. Arterioles are larger than capillaries and may be an even greater source of microvascular pulsatility changes in CH.
- **Changes in microvascular pulsatility in periventricular white matter.** We have studied capillary pulsatility changes in the neocortex. However, studies have shown that significant changes in the microvasculature take place deeper within the hydrocephalic brain, primarily in the periventricular white matter, and so microvascular pulsatility changes in these regions need to be quantified. The

main limitation with our experiments is that we only achieved depths of 650 μm; removal of the dura may provide an additional 100-150 μm depth penetration (although this may have detrimental effects on intracranial dynamics), but the theoretical maximum depth of two-photon microscopy is about 1 mm, whereas the periventricular white matter was nearly 1.5 mm deep in our most severely hydrocephalic animals. So, to study changes in the periventricular white matter, a new technique may be required, such as endoscopy or optical coherence tomography, or a mouse model of CH needs to be developed. The cortical mantle of the mouse, especially in hydrocephalus, is much thinner and the periventricular white matter is easily accessible with our technique.

- **Super-acute changes in capillary pulsatility.** One hypothesis that we did not address in this dissertation is whether capillary pulsatility is elevated immediately after induction, before changes in aqueductal pulsatility and ventricular size are manifested. Such a study would provide very interesting results and further support the pulsatility redistribution theory, because it may show that capillary pulsatility is a consequence of CSF obstruction in the subarachnoid spaces, and as such may clearly be involved in the elevation of aqueductal pulsatility.
- **Temporal changes in capillary pulsatility.** It will be extremely interesting to measure a time-course of capillary pulsatility changes in mildly CH animals, such as the group 2 animals described in §4. Aqueductal pulsatility in these animals is significantly elevated one week after induction, but returns to normal after 2-3 post induction. It would be very informative to determine if corresponding

changes exist in capillary pulsatility. This may further prove a link between increased capillary pulsatility and aqueductal CSF pulsatility.

- **Behavioral studies.** Further characterization of behavioral deficits, especially with regards to cognitive impairments, is required in our animal model. As stated previously, behavioral deficits are the most important method for gauging severity of hydrocephalus, and behavioral results may be important in determining improvement after shunting or other interventions.

8.6 Conclusion

Communicating hydrocephalus is a complex and multifactorial disorder whose pathophysiology has received less attention from the scientific community than other diseases with similar prevalence in human society. This is due to the fact that hydrocephalus is traditionally viewed as a “plumbing problem” of the CSF system, with excess CSF accumulation due to an obstruction in the CSF flow pathway or malabsorption of CSF at the arachnoid granulations. Closer study, however, has revealed that this view is in fact a gross oversimplification of a far more complex disorder [283], and many of the issues surrounding hydrocephalus that require further study are outlined in a recent position paper aptly titled “What we don’t know (but should) about Hydrocephalus” [57]. This report, however, did not address one phenomenon that has generated considerable interest in clinical communicating hydrocephalus and may yet prove to an important marker for severity and prognosis: elevated aqueductal pulsatility. In this dissertation, we studied elevated aqueductal pulsatility in our rat model of CH, and have uncovered a number of important new

findings which have significant implications for hydrocephalus research. We anticipate that, in the short term, these will help pave the way towards a more complete understanding of the mechanisms of this dynamic and complex disorder, and in the long term, these may lead to better treatment options for hydrocephalic patients.

Bibliography

[1] N.C. Keong, M. Czosnyka, Z. Czosnyka, and J.D. Pickard, “Clinical Evaluation of Adult Hydrocephalus,” in Youmans Neurological Surgery, vol. 1, H. R. Winn and J. R. Youmans eds., Philadelphia, Pa.: W.B. Saunders, 2011.

[2] O.o.C.a.P. Liaison., “Hydrocephalus Fact Sheet,” in *NIH Publications*, [Internet article], Bethesda:National Institutes of Health (www.nih.gov), 2008, [updated 2008; cited August 2009] Accession no. Accession Number| Available rom Database Provider|.

[3] J.M. Drake, J.R. Kestle, R. Milner, G. Cinalli, F. Boop, J. Piatt, Jr., S. Haines, S.J. Schiff, D.D. Cochrane, P. Steinbok, and N. MacNeil, “Randomized trial of cerebrospinal fluid shunt valve design in pediatric hydrocephalus,” *Neurosurgery*, vol. 43, (no. 2), pp. 294-303; discussion 303-5, Aug 1998.

[4] J.R. Kestle, H.J. Garton, W.E. Whitehead, J.M. Drake, A.V. Kulkarni, D.D. Cochrane, C. Muszynski, and M.L. Walker, “Management of shunt infections: a multicenter pilot study,” *J Neurosurg*, vol. 105, (no. 3 Suppl), pp. 177-81, Sep 2006.

[5] M.J. McGirt, J.C. Leveque, J.C. Wellons, 3rd, A.T. Villavicencio, J.S. Hopkins, H.E. Fuchs, and T.M. George, “Cerebrospinal fluid shunt survival and etiology of failures: a seven-year institutional experience,” *Pediatr Neurosurg*, vol. 36, (no. 5), pp. 248-55, May 2002.

[6] M. Egnor, L. Zheng, A. Rosiello, F. Gutman, and R. Davis, “A model of pulsations in communicating hydrocephalus,” *Pediatr Neurosurg*, vol. 36, (no. 6), pp. 281-303, Jun 2002.

[7] D. Greitz, “Cerebrospinal fluid circulation and associated intracranial dynamics. A radiologic investigation using MR imaging and radionuclide cisternography,” *Acta Radiol Suppl*, vol. 386, pp. 1-23, 1993.

[8] D. Greitz, “Radiological assessment of hydrocephalus: new theories and implications for therapy,” *Neurosurg Rev*, vol. 27, (no. 3), pp. 145-65; discussion 166-7, Jul 2004.

[9] J. Li, J.P. McAllister, 2nd, Y. Shen, M.E. Wagshul, J.M. Miller, M.R. Egnor, M.G. Johnston, E.M. Haacke, and M.L. Walker, “Communicating hydrocephalus in adult rats with kaolin obstruction of the basal cisterns or the cortical subarachnoid space,” *Exp Neurol*, vol. 211, (no. 2), pp. 351-61, Jun 2008.

[10] E.N. Marieb, *Human anatomy & physiology*, San Francisco: Benjamin Cummings, 2001.

[11] M. Rubin, J.E. Safdieh, and F.H. Netter, *Netter's concise neuroanatomy*, Philadelphia: Saunders Elsevier, 2007.

[12] W.F. Boron and E.L. Boulpaep, *Medical physiology : a cellular and molecular approach*, Philadelphia, PA: W.B. Saunders, 2003.

[13] A.C. Guyton and J.E. Hall, *Textbook of medical physiology*, Philadelphia: Elsevier Saunders, 2006.

[14] C.E. Johanson, J.A. Duncan, 3rd, P.M. Klinge, T. Brinker, E.G. Stopa, and G.D. Silverberg, “Multiplicity of cerebrospinal fluid functions: New challenges in health and disease,” *Cerebrospinal Fluid Res*, vol. 5, pp. 10, 2008.
[15] E.R. Kandel, J.H. Schwartz, and T.M. Jessell, *Principles of neural science*, New York: McGraw-Hill, Health Professions Division, 2000.
[16] E. Rubenstein, “Relationship of senescence of cerebrospinal fluid circulatory system to dementias of the aged,” *Lancet*, vol. 351, (no. 9098), pp. 283-5, Jan 24 1998.
[17] A. Marmarou and A. Beaumont, “Physiology of the Cerebrospinal Fluid and Intracranial Pressure,” in Youmans Neurological Surgery, vol. 1, H. R. Winn and J. R. Youmans eds., Philadelphia, Pa.: W.B. Saunders, 2011.
[18] N.K. Tanna, M.I. Kohn, D.N. Horwich, P.R. Jolles, R.A. Zimmerman, W.M. Alves, and A. Alavi, “Analysis of brain and cerebrospinal fluid volumes with MR imaging: impact on PET data correction for atrophy. Part II. Aging and Alzheimer dementia,” *Radiology*, vol. 178, (no. 1), pp. 123-30, Jan 1991.
[19] E.J. McCormack, “Quantitative Measurements of Intracranial Cerebrospinal Fluid Dynamics: Methods to Evaluate Changes in the Biomechanics of the Brain,” in Book Quantitative Measurements of Intracranial Cerebrospinal Fluid Dynamics: Methods to Evaluate Changes in the Biomechanics of the Brain, vol. PhD, *Series Quantitative Measurements of Intracranial Cerebrospinal Fluid Dynamics: Methods to Evaluate Changes in the Biomechanics of the Brain*, Editor ed.^eds., City: Stony Brook University, 2006.
[20] R.W. Cutler, L. Page, J. Galicich, and G.V. Watters, “Formation and absorption of cerebrospinal fluid in man,” *Brain*, vol. 91, (no. 4), pp. 707-20, 1968.
[21] R.C. Rubin, E.S. Henderson, A.K. Ommaya, M.D. Walker, and D.P. Rall, “The production of cerebrospinal fluid in man and its modification by acetazolamide,” *J Neurosurg*, vol. 25, (no. 4), pp. 430-6, Oct 1966.
[22] C. Nilsson, F. Stahlberg, C. Thomsen, O. Henriksen, M. Herning, and C. Owman, “Circadian variation in human cerebrospinal fluid production measured by magnetic resonance imaging,” *Am J Physiol*, vol. 262, (no. 1 Pt 2), pp. R20-4, Jan 1992.
[23] M.R. Del Bigio, “Cellular damage and prevention in childhood hydrocephalus,” *Brain Pathol*, vol. 14, (no. 3), pp. 317-24, Jul 2004.
[24] M. Pollay and F. Curl, “Secretion of cerebrospinal fluid by the ventricular ependyma of the rabbit,” *Am J Physiol*, vol. 213, (no. 4), pp. 1031-8, Oct 1967.
[25] C.E. Johanson, “Production and Flow of Cerebrospinal Fluid,” in Youmans Neurological Surgery, H. R. Winn and J. R. Youmans eds., Philadelphia, Pa.: W.B. Saunders, 2011, pp. 2002-2008.
[26] H. Davson and M.B. Segal, *Physiology of the CSF and blood-brain barriers*, Boca Raton: CRC Press, 1996.
[27] M. Johnston and C. Papaiconomou, “Cerebrospinal fluid transport: a lymphatic perspective,” *News Physiol Sci*, vol. 17, pp. 227-30, Dec 2002.
[28] C. Johanson, “Ventricles and Cerebrospinal Fluid,” in Neuroscience in medicine, P. M. Conn ed., Philadelphia: Lippincott, 1995, pp. 171-196.
[29] M. Bradbudy and H. Cserr, “Drainage of cerebral interstitial fluid and of cerebrospinal fluid into lymphatics.,” in Experimental biology of the lymphatic

circulation, M. G. Johnston ed., Amsterdam ; New York: Elsevier, 1985, pp. 355-394.
[30] T. Brinker, W. Ludemann, D. Berens von Rautenfeld, and M. Samii, “Dynamic properties of lymphatic pathways for the absorption of cerebrospinal fluid,” *Acta Neuropathol*, vol. 94, (no. 5), pp. 493-8, Nov 1997.
[31] S. Kida, A. Pantazis, and R.O. Weller, “CSF drains directly from the subarachnoid space into nasal lymphatics in the rat. Anatomy, histology and immunological significance,” *Neuropathol Appl Neurobiol*, vol. 19, (no. 6), pp. 480-8, Dec 1993.
[32] G. Nagra, J. Li, J.P. McAllister, 2nd, J. Miller, M. Wagshul, and M. Johnston, “Impaired lymphatic cerebrospinal fluid absorption in a rat model of kaolin-induced communicating hydrocephalus,” *Am J Physiol Regul Integr Comp Physiol*, vol. 294, (no. 5), pp. R1752-9, May 2008.
[33] I. Silver, C. Kim, R. Mollanji, and M. Johnston, “Cerebrospinal fluid outflow resistance in sheep: impact of blocking cerebrospinal fluid transport through the cribriform plate,” *Neuropathol Appl Neurobiol*, vol. 28, (no. 1), pp. 67-74, Feb 2002.
[34] M. Boulton, M. Flessner, D. Armstrong, J. Hay, and M. Johnston, “Determination of volumetric cerebrospinal fluid absorption into extracranial lymphatics in sheep,” *Am J Physiol*, vol. 274, (no. 1 Pt 2), pp. R88-96, Jan 1998.
[35] M. Johnston, A. Zakharov, L. Koh, and D. Armstrong, “Subarachnoid injection of Microfil reveals connections between cerebrospinal fluid and nasal lymphatics in the non-human primate,” *Neuropathol Appl Neurobiol*, vol. 31, (no. 6), pp. 632-40, Dec 2005.
[36] M. Johnston, A. Zakharov, C. Papaiconomou, G. Salmasi, and D. Armstrong, “Evidence of connections between cerebrospinal fluid and nasal lymphatic vessels in humans, non-human primates and other mammalian species,” *Cerebrospinal Fluid Res*, vol. 1, (no. 1), pp. 2, Dec 10 2004.
[37] W. Luedemann, D. Kondziella, K. Tienken, P. Klinge, T. Brinker, and D. Berens von Rautenfeld, “Spinal cerebrospinal fluid pathways and their significance for the compensation of kaolin-hydrocephalus,” *Acta Neurochir Suppl*, vol. 81, pp. 271-3, 2002.
[38] M.C. Staff., “Hydrocephalus,” in *Diseases and Conditions*, [Internet article], Rochester:www.mayoclinic.com, 2007, [updated 2007; cited September 2009] Accession no. Accession Number| Available rom Database Provider|.
[39] N.H. Foundation, “Hydrocephalus Facts,” in *Info on Hydrocephalus*, [Webpage], Lakewood, CA:National Hydrocephalus Foundation, [cited September 2009] Accession no. Accession Number| Available rom Database Provider|.
[40] T.D. Simon, J. Riva-Cambrin, R. Srivastava, S.L. Bratton, J.M. Dean, and J.R. Kestle, “Hospital care for children with hydrocephalus in the United States: utilization, charges, comorbidities, and deaths,” *J Neurosurg Pediatr*, vol. 1, (no. 2), pp. 131-7, Feb 2008.
[41] T. Hattori, T. Yuasa, S. Aoki, R. Sato, H. Sawaura, T. Mori, and H. Mizusawa, “Altered microstructure in corticospinal tract in idiopathic normal pressure hydrocephalus: comparison with Alzheimer disease and Parkinson disease with dementia,” *AJNR Am J Neuroradiol*, vol. 32, (no. 9), pp. 1681-7, Oct 2011.

[42] M.J. Kim, S.W. Seo, K.M. Lee, S.T. Kim, J.I. Lee, D.H. Nam, and D.L. Na, “Differential diagnosis of idiopathic normal pressure hydrocephalus from other dementias using diffusion tensor imaging,” *AJNR Am J Neuroradiol*, vol. 32, (no. 8), pp. 1496-503, Sep 2011.
[43] S. Savolainen, H. Hurskainen, L. Paljarvi, I. Alafuzoff, and M. Vapalahti, “Five-year outcome of normal pressure hydrocephalus with or without a shunt: predictive value of the clinical signs, neuropsychological evaluation and infusion test,” *Acta Neurochir (Wien)*, vol. 144, (no. 6), pp. 515-23; discussion 523, Jun 2002.
[44] A. Miodrag, T.K. Das, and R.J. Shepherd, “Normal pressure hydrocephalus presenting as Parkinson's syndrome,” *Postgrad Med J*, vol. 63, (no. 736), pp. 113-5, Feb 1987.
[45] R.V. Patwardhan and A. Nanda, “Implanted ventricular shunts in the United States: the billion-dollar-a-year cost of hydrocephalus treatment,” *Neurosurgery*, vol. 56, (no. 1), pp. 139-44; discussion 144-5, 2005.
[46] M.R. Del Bigio, “Epidemiology and direct economic impact of hydrocephalus: a community based study,” *Can J Neurol Sci*, vol. 25, (no. 2), pp. 123-6, May 1998.
[47] D. Greitz, T. Greitz, and T. Hindmarsh, “A new view on the CSF-circulation with the potential for pharmacological treatment of childhood hydrocephalus,” *Acta Paediatr*, vol. 86, (no. 2), pp. 125-32, Feb 1997.
[48] E. Faivre, “ ” *Compt. rend. de l'Acad. des Sciences*, vol. 34, 1854 1854.
[49] A. Key and G. Retzius, *Studien in der anatomie des nerven systems und des bindegewebes*, Stockholm, 1875.
[50] W.E. Dandy and K.D. Blackfan, “Internal hydrocephalus. An experimental, clinical and pathological study,” *American Journal of Diseases of Children*, vol. 8, (no. 6), pp. 406-482, December 1914 1914.
[51] K. Welch and V. Friedman, “The cerebrospinal fluid valves,” *Brain*, vol. 83, pp. 454-69, Sep 1960.
[52] G. Di Chiro, “Observations on the circulation of the cerebrospinal fluid,” *Acta Radiol Diagn (Stockh)*, vol. 5, pp. 988-1002, 1966.
[53] R.C. Heros, “Acute hydrocephalus after subarachnoid hemorrhage,” *Stroke*, vol. 20, (no. 6), pp. 715-7, Jun 1989.
[54] O. Suarez-Rivera, “Acute hydrocephalus after subarachnoid hemorrhage,” *Surg Neurol*, vol. 49, (no. 5), pp. 563-5, May 1998.
[55] M. Bergsneider, “Management of hydrocephalus with programmable valves after traumatic brain injury and subarachnoid hemorrhage,” *Curr Opin Neurol*, vol. 13, (no. 6), pp. 661-4, Dec 2000.
[56] L.A. Alvarez, J. Maytal, and S. Shinnar, “Idiopathic external hydrocephalus: natural history and relationship to benign familial macrocephaly,” *Pediatrics*, vol. 77, (no. 6), pp. 901-7, Jun 1986.
[57] M. Bergsneider, M.R. Egnor, M. Johnston, D. Kranz, J.R. Madsen, J.P. McAllister, 2nd, C. Stewart, M.L. Walker, and M.A. Williams, “What we don't (but should) know about hydrocephalus,” *J Neurosurg*, vol. 104, (no. 3 Suppl), pp. 157-9, Mar 2006.
[58] J.G. McComb, “Recent research into the nature of cerebrospinal fluid formation and absorption,” *J Neurosurg*, vol. 59, (no. 3), pp. 369-83, Sep 1983.

[59] D. Greitz, “Paradigm shift in hydrocephalus research in legacy of Dandy's pioneering work: rationale for third ventriculostomy in communicating hydrocephalus,” *Childs Nerv Syst*, vol. 23, (no. 5), pp. 487-9, May 2007.
[60] E.S. Conner, L. Foley, and P.M. Black, “Experimental normal-pressure hydrocephalus is accompanied by increased transmantle pressure,” *J Neurosurg*, vol. 61, (no. 2), pp. 322-7, Aug 1984.
[61] R.D. Penn, M.C. Lee, A.A. Linninger, K. Miesel, S.N. Lu, and L. Stylos, “Pressure gradients in the brain in an experimental model of hydrocephalus,” *J Neurosurg*, vol. 102, (no. 6), pp. 1069-75, Jun 2005.
[62] K. Shapiro, I.J. Kohn, F. Takei, and C. Zee, “Progressive ventricular enlargement in cats in the absence of transmantle pressure gradients,” *J Neurosurg*, vol. 67, (no. 1), pp. 88-92, Jul 1987.
[63] H. Stephensen, M. Tisell, and C. Wikkelso, “There is no transmantle pressure gradient in communicating or noncommunicating hydrocephalus,” *Neurosurgery*, vol. 50, (no. 4), pp. 763-71; discussion 771-3, Apr 2002.
[64] L. Koh, G. Nagra, and M. Johnston, “Properties of the lymphatic cerebrospinal fluid transport system in the rat: impact of elevated intracranial pressure,” *J Vasc Res*, vol. 44, (no. 5), pp. 423-32, 2007.
[65] A. Zakharov, C. Papaiconomou, L. Koh, J. Djenic, R. Bozanovic-Sosic, and M. Johnston, “Integrating the roles of extracranial lymphatics and intracranial veins in cerebrospinal fluid absorption in sheep,” *Microvasc Res*, vol. 67, (no. 1), pp. 96-104, Jan 2004.
[66] K.G. Kapoor, S.E. Katz, D.M. Grzybowski, and M. Lubow, “Cerebrospinal fluid outflow: an evolving perspective,” *Brain Res Bull*, vol. 77, (no. 6), pp. 327-34, Dec 16 2008.
[67] S.A. Glimcher, D.W. Holman, M. Lubow, and D.M. Grzybowski, “Ex vivo model of cerebrospinal fluid outflow across human arachnoid granulations,” *Invest Ophthalmol Vis Sci*, vol. 49, (no. 11), pp. 4721-8, Nov 2008.
[68] D.M. Grzybowski, D.W. Holman, S.E. Katz, and M. Lubow, “In vitro model of cerebrospinal fluid outflow through human arachnoid granulations,” *Invest Ophthalmol Vis Sci*, vol. 47, (no. 8), pp. 3664-72, Aug 2006.
[69] F. Magendie, “Mémoire sur un liquide que se trouve dans le crâne et le canal vertébral de l'homme et des animaux mammifères,” *Journal de physiologie expérimentale et de pathologie*, vol. 5, pp. 27-37, 1825.
[70] O. Baledent, C. Gondry-Jouet, M.E. Meyer, G. De Marco, D. Le Gars, M.C. Henry-Feugeas, and I. Idy-Peretti, “Relationship between cerebrospinal fluid and blood dynamics in healthy volunteers and patients with communicating hydrocephalus,” *Invest Radiol*, vol. 39, (no. 1), pp. 45-55, Jan 2004.
[71] J.E.A. O'Connell, “The vascular factor in intracranial pressure and the maintenance of the cerebrospinal fluid circulation.,” *Brain*, vol. 66, pp. 204-228, 1943.
[72] N. Antoni, “Pressure curves from the cerebrospinal fluid,” *Acta Medica Scandinavica*, vol. 123, (no. S170), pp. 439-462, 1946.
[73] E.A. Bering, Jr., “Choroid plexus and arterial pulsation of cerebrospinal fluid; demonstration of the choroid plexuses as a cerebrospinal fluid pump,” *AMA Arch Neurol Psychiatry*, vol. 73, (no. 2), pp. 165-72, Feb 1955.

[74] E.A. Bering, Jr., “Circulation of the cerebrospinal fluid. Demonstration of the choroid plexuses as the generator of the force for flow of fluid and ventricular enlargement,” *J Neurosurg*, vol. 19, pp. 405-13, May 1962.
[75] H.S. Dunbar, T.C. Guthrie, and B. Karpell, “A study of the cerebrospinal fluid pulse wave,” *Arch Neurol*, vol. 14, (no. 6), pp. 624-30, Jun 1966.
[76] C.B. Wilson and V. Bertan, “Interruption of the anterior choroidal artery in experimental hydrocephalus,” *Arch Neurol*, vol. 17, (no. 6), pp. 614-9, Dec 1967.
[77] C. Di Rocco, G. Di Trapani, V.E. Pettorossi, and M. Caldarelli, “On the pathology of experimental hydrocephalus induced by artificial increase in endoventricular CSF pulse pressure,” *Childs Brain*, vol. 5, (no. 2), pp. 81-95, 1979.
[78] C. Di Rocco, V.E. Pettorossi, M. Caldarelli, R. Mancinelli, and F. Velardi, “Communicating hydrocephalus induced by mechanically increased amplitude of the intraventricular cerebrospinal fluid pressure: experimental studies,” *Exp Neurol*, vol. 59, (no. 1), pp. 40-52, Mar 1978.
[79] V.E. Pettorossi, C. Di Rocco, R. Mancinelli, M. Caldarelli, and F. Velardi, “Communicating hydrocephalus induced by mechanically increased amplitude of the intraventricular cerebrospinal fluid pulse pressure: rationale and method,” *Exp Neurol*, vol. 59, (no. 1), pp. 30-9, Mar 1978.
[80] G.H. Du Boulay, “Pulsatile movements in the CSF pathways,” *Br J Radiol*, vol. 39, (no. 460), pp. 255-62, Apr 1966.
[81] G. Bergstrand, M. Bergstrom, B. Nordell, F. Stahlberg, A. Ericsson, A. Hemmingsson, G. Sperber, K.A. Thuomas, and B. Jung, “Cardiac gated MR imaging of cerebrospinal fluid flow,” *J Comput Assist Tomogr*, vol. 9, (no. 6), pp. 1003-6, Nov-Dec 1985.
[82] J.L. Sherman and C.M. Citrin, “Magnetic resonance demonstration of normal CSF flow,” *AJNR Am J Neuroradiol*, vol. 7, (no. 1), pp. 3-6, Jan-Feb 1986.
[83] W.G. Bradley, Jr., K.E. Kortman, and B. Burgoyne, “Flowing cerebrospinal fluid in normal and hydrocephalic states: appearance on MR images,” *Radiology*, vol. 159, (no. 3), pp. 611-6, Jun 1986.
[84] W.G. Bradley, Jr., A.R. Whittemore, K.E. Kortman, A.S. Watanabe, M. Homyak, L.M. Teresi, and S.J. Davis, “Marked cerebrospinal fluid void: indicator of successful shunt in patients with suspected normal-pressure hydrocephalus,” *Radiology*, vol. 178, (no. 2), pp. 459-66, Feb 1991.
[85] J. Vanneste, P. Augustijn, C. Dirven, W.F. Tan, and Z.D. Goedhart, “Shunting normal-pressure hydrocephalus: do the benefits outweigh the risks? A multicenter study and literature review,” *Neurology*, vol. 42, (no. 1), pp. 54-9, Jan 1992.
[86] L. Jacobs, D. Conti, W.R. Kinkel, and E.J. Manning, “"Normal-pressure" hydrocephalus. Relationship of clinical and radiographic findings to improvement following shunt surgery,” *JAMA*, vol. 235, (no. 5), pp. 510-2, Feb 2 1976.
[87] N.R. Graff-Radford and J.C. Godersky, “Normal-pressure hydrocephalus. Onset of gait abnormality before dementia predicts good surgical outcome,” *Arch Neurol*, vol. 43, (no. 9), pp. 940-2, Sep 1986.
[88] C.M. Fisher, “Hydrocephalus as a cause of disturbances of gait in the elderly,” *Neurology*, vol. 32, (no. 12), pp. 1358-63, Dec 1982.

[89] E. Knutsson and U. Lying-Tunell, “Gait apraxia in normal-pressure hydrocephalus: patterns of movement and muscle activation,” *Neurology*, vol. 35, (no. 2), pp. 155-60, Feb 1985.
[90] D.A. Feinberg and A.S. Mark, “Human brain motion and cerebrospinal fluid circulation demonstrated with MR velocity imaging,” *Radiology*, vol. 163, (no. 3), pp. 793-9, Jun 1987.
[91] W.G. Bradley, Jr., D. Scalzo, J. Queralt, W.N. Nitz, D.J. Atkinson, and P. Wong, “Normal-pressure hydrocephalus: evaluation with cerebrospinal fluid flow measurements at MR imaging,” *Radiology*, vol. 198, (no. 2), pp. 523-9, Feb 1996.
[92] M.E. Wagshul, J.J. Chen, M.R. Egnor, E.J. McCormack, and P.E. Roche, “Amplitude and phase of cerebrospinal fluid pulsations: experimental studies and review of the literature,” *J Neurosurg*, vol. 104, (no. 5), pp. 810-9, May 2006.
[93] G.R. Dixon, J.A. Friedman, P.H. Luetmer, L.M. Quast, R.L. McClelland, R.C. Petersen, C.O. Maher, and M.J. Ebersold, “Use of cerebrospinal fluid flow rates measured by phase-contrast MR to predict outcome of ventriculoperitoneal shunting for idiopathic normal-pressure hydrocephalus,” *Mayo Clin Proc*, vol. 77, (no. 6), pp. 509-14, Jun 2002.
[94] B. Kahlon, M. Annertz, F. Stahlberg, and S. Rehncrona, “Is aqueductal stroke volume, measured with cine phase-contrast magnetic resonance imaging scans useful in predicting outcome of shunt surgery in suspected normal pressure hydrocephalus?,” *Neurosurgery*, vol. 60, (no. 1), pp. 124-9; discussion 129-30, Jan 2007.
[95] W.W. Chiang, C.G. Takoudis, S.H. Lee, A. Weis-McNulty, R. Glick, and N. Alperin, “Relationship between ventricular morphology and aqueductal cerebrospinal fluid flow in healthy and communicating hydrocephalus,” *Invest Radiol*, vol. 44, (no. 4), pp. 192-9, Apr 2009.
[96] E.A. Bering, Jr., “Studies on the role of the choroid plexus in tracer exchanges between blood and cerebrospinal fluid,” *J Neurosurg*, vol. 12, (no. 4), pp. 385-92, Jul 1955.
[97] T.E. Cosan, D. Gucuyener, E. Dundar, A. Arslantas, M. Vural, K. Uzuner, and E. Tel, “Cerebral blood flow alterations in progressive communicating hydrocephalus: transcranial Doppler ultrasonography assessment in an experimental model,” *J Neurosurg*, vol. 94, (no. 2), pp. 265-9, Feb 2001.
[98] T.E. Cosan, A.I. Guner, N. Akcar, K. Uzuner, and E. Tel, “Progressive ventricular enlargement in the absence of high ventricular pressure in an experimental neonatal rat model,” *Childs Nerv Syst*, vol. 18, (no. 1-2), pp. 10-4, Feb 2002.
[99] M.R. Del Bigio, C.R. Crook, and R. Buist, “Magnetic resonance imaging and behavioral analysis of immature rats with kaolin-induced hydrocephalus: pre- and postshunting observations,” *Exp Neurol*, vol. 148, (no. 1), pp. 256-64, Nov 1997.
[100] G.M. Hochwald, S. Nakamura, and M.B. Camins, “The rat in experimental obstructive hydrocephalus,” *Z Kinderchir*, vol. 34, (no. 4), pp. 403-10, Dec 1981.
[101] G.M. Hochwald, F. Epstein, C. Malhan, and J. Ransohoff, “The role of the skull and dura in experimental feline hydrocephalus,” *Dev Med Child Neurol Suppl*, vol. 27, pp. 65-9, 1972.

[102] L.H. Weed, “Meninges and Cerebrospinal Fluid,” *J Anat*, vol. 72, (no. Pt 2), pp. 181-215, Jan 1938.
[103] G.B. Wislocki and T.J. Putnam, “Absorption from the ventricles in experimentally produced internal hydrocephalus,” *American Journal of Anatomy*, vol. 29, (no. 3), pp. 313-320, 1921.
[104] H. Wisniewski, R.O. Weller, and R.D. Terry, “Experimental hydrocephalus produced by the subarachnoid infusion of silicone oil,” *J Neurosurg*, vol. 31, (no. 1), pp. 10-4, Jul 1969.
[105] M.R. Del Bigio and J.E. Bruni, “Changes in periventricular vasculature of rabbit brain following induction of hydrocephalus and after shunting,” *J Neurosurg*, vol. 69, (no. 1), pp. 115-20, Jul 1988.
[106] M.R. Del Bigio and J.E. Bruni, “Cerebral water content in silicone oil-induced hydrocephalic rabbits,” *Pediatr Neurosci*, vol. 13, (no. 2), pp. 72-7, 1987.
[107] D.L. Price, A.E. James, Jr., E. Sperber, and E.P. Strecker, “Communicating hydrocephalus. Cisternographic and neuropathologic studies,” *Arch Neurol*, vol. 33, (no. 1), pp. 15-20, Jan 1976.
[108] A. Bachs and A.E. Walker, “Experimental hydrocephalus,” *J Neuropathol Exp Neurol*, vol. 12, (no. 3), pp. 283-92, Jul 1953.
[109] K.R. Lodhia, P. Shakui, and R.F. Keep, “Hydrocephalus in a rat model of intraventricular hemorrhage,” *Acta Neurochir Suppl*, vol. 96, pp. 207-11, 2006.
[110] S. Matsumoto, A. Hirayama, S. Yamasaki, K. Shirataki, and K. Fujiwara, “Comparative study of various models of experimental hydrocephalus,” *Childs Brain*, vol. 1, (no. 4), pp. 236-42, 1975.
[111] A. Adeloye and J. Warkany, “Experimental congenital hydrocephalus. A review with special consideration of hydrocephalus produced by zinc deficiency,” *Childs Brain*, vol. 2, (no. 6), pp. 325-60, 1976.
[112] J.G. Chamberlain, “Early neurovascular abnormalities underlying 6-aminonicotinamide (6-AN)-induced congenital hydrocephalus in rats,” *Teratology*, vol. 3, (no. 4), pp. 377-88, Nov 1970.
[113] K.S. Khera and L. Tryphonas, “Ethylenethiourea-induced hydrocephalus: pre- and postnatal pathogenesis in offspring from rats given a single oral dose during pregnancy,” *Toxicol Appl Pharmacol*, vol. 42, (no. 1), pp. 85-97, Oct 1977.
[114] P.H. Schurr, R.L. McLaurin, and F.D. Ingraham, “Experimental studies on the circulation of the cerebrospinal fluid and methods of producing communicating hydrocephalus in the dog,” *J Neurosurg*, vol. 10, (no. 5), pp. 515-25, Sep 1953.
[115] W.E. Dandy, “Experimental Hydrocephalus,” *Ann Surg*, vol. 70, (no. 2), pp. 129-42, Aug 1919.
[116] T.H. Milhorat, “Choroid plexus and cerebrospinal fluid production,” *Science*, vol. 166, (no. 3912), pp. 1514-6, Dec 19 1969.
[117] R.G. Clark and T.H. Milhorat, “Experimental hydrocephalus. 3. Light microscopic findings in acute and subacute obstructive hydrocephalus in the monkey,” *J Neurosurg*, vol. 32, (no. 4), pp. 400-13, Apr 1970.
[118] V.A. Levin, T.H. Milhorat, J.D. Fenstermacher, M.K. Hammock, and D.D. Rall, “The pathophysiology of obstructive hydrocephalus in the monkey,” *Trans Am Neurol Assoc*, vol. 95, pp. 274-6, 1970.

[119] T.H. Milhorat, “Experimental hydrocephalus. 1. A technique for producing obstructive hydrocephalus in the monkey,” *J Neurosurg*, vol. 32, (no. 4), pp. 385-9, Apr 1970.
[120] T.H. Milhorat, R.G. Clark, and M.K. Hammock, “Experimental hydrocephalus. 2. Gross pathological findings in acute and subacute obstructive hydrocephalus in the dog and monkey,” *J Neurosurg*, vol. 32, (no. 4), pp. 390-9, Apr 1970.
[121] D.S. Kim, S. Oi, M. Hidaka, O. Sato, and J.U. Choi, “A new experimental model of obstructive hydrocephalus in the rat: the micro-balloon technique,” *Childs Nerv Syst*, vol. 15, (no. 5), pp. 250-5, May 1999.
[122] A.R. Cohen, D.W. Leifer, M. Zechel, D.P. Flaningan, J.S. Lewin, and W.D. Lust, “Characterization of a model of hydrocephalus in transgenic mice,” *J Neurosurg*, vol. 91, (no. 6), pp. 978-88, Dec 1999.
[123] E.J. Sweger, K.B. Casper, K. Scearce-Levie, B.R. Conklin, and K.D. McCarthy, “Development of hydrocephalus in mice expressing the G(i)-coupled GPCR Ro1 RASSL receptor in astrocytes,” *J Neurosci*, vol. 27, (no. 9), pp. 2309-17, Feb 28 2007.
[124] M.L. Robinson, C.E. Allen, B.E. Davy, W.J. Durfee, F.F. Elder, C.S. Elliott, and W.R. Harrison, “Genetic mapping of an insertional hydrocephalus-inducing mutation allelic to hy3,” *Mamm Genome*, vol. 13, (no. 11), pp. 625-32, Nov 2002.
[125] L.F. Batiz, P. Paez, A.J. Jimenez, S. Rodriguez, C. Wagner, J.M. Perez-Figares, and E.M. Rodriguez, “Heterogeneous expression of hydrocephalic phenotype in the hyh mice carrying a point mutation in alpha-SNAP,” *Neurobiol Dis*, vol. 23, (no. 1), pp. 152-68, Jul 2006.
[126] M. Wozniak, D.G. McLone, and A.J. Raimondi, “Micro- and macrovascular changes as the direct cause of parenchymal destruction in congenital murine hydrocephalus,” *J Neurosurg*, vol. 43, (no. 5), pp. 535-45, Nov 1975.
[127] H.C. Jones, S. Dack, and C. Ellis, “Morphological aspects of the development of hydrocephalus in a mouse mutant (SUMS/NP),” *Acta Neuropathol*, vol. 72, (no. 3), pp. 268-76, 1987.
[128] J.E. Bruni, M.R. del Bigio, E.R. Cardoso, and T.V. Persaud, “Neuropathology of congenital hydrocephalus in the SUMS/NP mouse,” *Acta Neurochir (Wien)*, vol. 92, (no. 1-4), pp. 118-22, 1988.
[129] E. Galbreath, S.J. Kim, K. Park, M. Brenner, and A. Messing, “Overexpression of TGF-beta 1 in the central nervous system of transgenic mice results in hydrocephalus,” *J Neuropathol Exp Neurol*, vol. 54, (no. 3), pp. 339-49, May 1995.
[130] M. Wiesmann, U. Koedel, H. Bruckmann, and H.W. Pfister, “Experimental bacterial meningitis in rats: demonstration of hydrocephalus and meningeal enhancement by magnetic resonance imaging,” *Neurol Res*, vol. 24, (no. 3), pp. 307-10, Apr 2002.
[131] L.E. Davis, “Communicating hydrocephalus in newborn hamsters and cats following vaccinia virus infection,” *J Neurosurg*, vol. 54, (no. 6), pp. 767-72, Jun 1981.
[132] R.T. Johnson, “Hydrocephalus and viral infections,” *Dev Med Child Neurol*, vol. 17, (no. 6), pp. 807-16, Dec 1975.

[133] H. Ogata, K. Oka, and A. Mitsudome, “Hydrocephalus due to acute aqueductal stenosis following mumps infection: report of a case and review of the literature,” *Brain Dev*, vol. 14, (no. 6), pp. 417-9, Nov 1992.
[134] R. Nyberg-Hansen, A. Torvik, and R. Bhatia, “On the pathology of experimental hydrocephalus,” *Brain Res*, vol. 95, (no. 2-3), pp. 343-50, Sep 23 1975.
[135] G.M. Hochwald, F. Epstein, C. Malhan, and J. Ransohoff, “The relationship of compensated to decompensated hydrocephalus in the cat,” *J Neurosurg*, vol. 39, (no. 6), pp. 694-7, Dec 1973.
[136] G.M. Hochwald, “Animal models of hydrocephalus: recent developments,” *Proc Soc Exp Biol Med*, vol. 178, (no. 1), pp. 1-11, Jan 1985.
[137] R.C. Rubin, G.M. Hochwald, M. Tiell, F. Epstein, N. Ghatak, and H. Wisniewski, “Hydrocephalus: III. Reconstitution of the cerebral cortical mantle following ventricular shunting,” *Surg Neurol*, vol. 5, (no. 3), pp. 179-83, Mar 1976.
[138] R. Eskandari, J.P. McAllister, 2nd, J.M. Miller, Y. Ding, S.D. Ham, D.M. Shearer, and J.S. Way, “Effects of hydrocephalus and ventriculoperitoneal shunt therapy on afferent and efferent connections in the feline sensorimotor cortex,” *J Neurosurg*, vol. 101, (no. 2 Suppl), pp. 196-210, Nov 2004.
[139] R.C. Rubin, G.M. Hochwald, M. Tiell, and B.H. Liwnicz, “Hydrocephalus: II. Cell number and size, and myelin content of the pre-shunted cerebral cortical mantle,” *Surg Neurol*, vol. 5, (no. 2), pp. 115-8, Feb 1976.
[140] R.C. Rubin, G.M. Hochwald, M. Tiell, H. Mizutani, and N. Ghatak, “Hydrocephalus: I. Histological and ultrastructural changes in the pre-shunted cortical mantle,” *Surg Neurol*, vol. 5, (no. 2), pp. 109-14, Feb 1976.
[141] F. Epstein, R.C. Rubin, and G.M. Hochwald, “Restoration of the cortical mantle in severe feline hydrocephalus: a new laboratory model,” *Dev Med Child Neurol*, vol. 16, (no. 6 Suppl 32), pp. 49-53, Dec 1974.
[142] R.C. Rubin, G. Hochwald, M. Tiell, B. Liwnicz, and F. Epstein, “Reconstitution of the cerebral cortical mantle in shunt-corrected hydrocephalus,” *Dev Med Child Neurol Suppl*, (no. 35), pp. 151-6, 1975.
[143] P. Collins, “Experimental obstructive hydrocephalus in the rat: a scanning electron microscopic study,” *Neuropathol Appl Neurobiol*, vol. 5, (no. 6), pp. 457-68, Nov-Dec 1979.
[144] M.R. Del Bigio, J.N. Kanfer, and Y.W. Zhang, “Myelination delay in the cerebral white matter of immature rats with kaolin-induced hydrocephalus is reversible,” *J Neuropathol Exp Neurol*, vol. 56, (no. 9), pp. 1053-66, Sep 1997.
[145] T. Yamaki, G. Odake, S. Naruse, Y. Ibata, and Y. Nojo, “Experimental hydrocephalus of the rat, produced by cisternal injection of kaolin-solution (author's transl),” *No Shinkei Geka*, vol. 5, (no. 6), pp. 537-40, Jun 1977.
[146] H.C. Jones and R.M. Bucknall, “Changes in cerebrospinal fluid pressure and outflow from the lateral ventricles during development of congenital hydrocephalus in the H-Tx rat,” *Exp Neurol*, vol. 98, (no. 3), pp. 573-83, Dec 1987.
[147] H.C. Jones, R.M. Bucknall, and N.G. Harris, “The cerebral cortex in congenital hydrocephalus in the H-Tx rat: a quantitative light microscopy study,” *Acta Neuropathol*, vol. 82, (no. 3), pp. 217-24, 1991.

[148] H.C. Jones and B.A. Lopman, “The relation between CSF pressure and ventricular dilatation in hydrocephalic HTx rats,” *Eur J Pediatr Surg*, vol. 8 Suppl 1, pp. 55-8, Dec 1998.
[149] A.E. James, Jr., B. Burns, W.F. Flor, E.P. Strecker, T. Merz, M. Bush, and D.L. Price, “Pathophysiology of chronic communicating hydrocephalus in dogs (Canis familiaris). Experimental studies,” *J Neurol Sci*, vol. 24, (no. 2), pp. 151-78, Feb 1975.
[150] E.P. Strecker, A.E. James, Jr., B. Konigsmark, and T. Merz, “Autoradiographic observations in experimental communicating hydrocephalus,” *Neurology*, vol. 24, (no. 2), pp. 192-7, Feb 1974.
[151] D. Sillman, “Review of Rat Muscles,” in *http://www.personal.psu.edu/dys100/anatomy/rat/Show/headneck.htm*, 2007, [2011] Accession no. Accession Number| Available rom Database Provider|.
[152] M.E. Wagshul, J.P. McAllister, S. Rashid, J. Li, M.R. Egnor, M.L. Walker, M. Yu, S.D. Smith, G. Zhang, J.J. Chen, and H. Benveniste, “Ventricular dilation and elevated aqueductal pulsations in a new experimental model of communicating hydrocephalus,” *Exp Neurol*, vol. 218, (no. 1), pp. 33-40, Jul 2009.
[153] I. Slobodian, D. Krassioukov-Enns, and M.R. Del Bigio, “Protein and synthetic polymer injection for induction of obstructive hydrocephalus in rats,” *Cerebrospinal Fluid Res*, vol. 4, pp. 9, 2007.
[154] M.R. Del Bigio and Y.W. Zhang, “Cell death, axonal damage, and cell birth in the immature rat brain following induction of hydrocephalus,” *Exp Neurol*, vol. 154, (no. 1), pp. 157-69, Nov 1998.
[155] O.H. Khan, T.L. Enno, and M.R. Del Bigio, “Brain damage in neonatal rats following kaolin induction of hydrocephalus,” *Exp Neurol*, vol. 200, (no. 2), pp. 311-20, Aug 2006.
[156] D.K. Nakayama, M.R. Harrison, M.S. Berger, D.H. Chinn, M. Halks-Miller, and M.S. Edwards, “Correction of congenital hydrocephalus in utero I. The model: intracisternal kaolin produces hydrocephalus in fetal lambs and rhesus monkeys,” *J Pediatr Surg*, vol. 18, (no. 4), pp. 331-8, Aug 1983.
[157] M. Shinoda and L. Olson, “Immunological aspects of kaolin-induced hydrocephalus,” *Int J Neurosci*, vol. 92, (no. 1-2), pp. 9-28, Nov 1997.
[158] C. Irigoin, E.M. Rodriguez, M. Heinrichs, K. Frese, S. Herzog, A. Oksche, and R. Rott, “Immunocytochemical study of the subcommissural organ of rats with induced postnatal hydrocephalus,” *Exp Brain Res*, vol. 82, (no. 2), pp. 384-92, 1990.
[159] M.R. Del Bigio, “Neuropathological changes caused by hydrocephalus,” *Acta Neuropathol*, vol. 85, (no. 6), pp. 573-85, 1993.
[160] M.R. Del Bigio, J.E. Bruni, and H.D. Fewer, “Human neonatal hydrocephalus. An electron microscopic study of the periventricular tissue,” *J Neurosurg*, vol. 63, (no. 1), pp. 56-63, Jul 1985.
[161] P. Glees and M. Hasan, “Ultrastructure of human cerebral macroglia and microglia: maturing and hydrocephalic frontal cortex,” *Neurosurg Rev*, vol. 13, (no. 3), pp. 231-42, 1990.

[162] P. Glees and D. Voth, “Clinical and ultrastructural observations of maturing human frontal cortex. Part I (Biopsy material of hydrocephalic infants),” *Neurosurg Rev*, vol. 11, (no. 3-4), pp. 273-8, 1988.
[163] M. Hasan and P. Glees, “The fine structure of human cerebral perivascular pericytes and juxtavascular phagocytes: their possible role in hydrocephalic edema resolution,” *J Hirnforsch*, vol. 31, (no. 2), pp. 237-49, 1990.
[164] M.R. Del Bigio, M.C. da Silva, J.M. Drake, and U.I. Tuor, “Acute and chronic cerebral white matter damage in neonatal hydrocephalus,” *Can J Neurol Sci*, vol. 21, (no. 4), pp. 299-305, Nov 1994.
[165] P.M. Hale, J.P. McAllister, 2nd, S.D. Katz, L.C. Wright, T.J. Lovely, D.W. Miller, B.J. Wolfson, A.G. Salotto, and D.V. Shroff, “Improvement of cortical morphology in infantile hydrocephalic animals after ventriculoperitoneal shunt placement,” *Neurosurgery*, vol. 31, (no. 6), pp. 1085-96; discussion 1096, Dec 1992.
[166] F.T. Mangano, J.P. McAllister, 2nd, H.C. Jones, M.J. Johnson, and R.M. Kriebel, “The microglial response to progressive hydrocephalus in a model of inherited aqueductal stenosis,” *Neurol Res*, vol. 20, (no. 8), pp. 697-704, Dec 1998.
[167] J.P. McAllister, 2nd, F.T. Mangano, H.C. Jones, and R.M. Kriebel, “The microglial response in experimental infantile hydrocephalus,” *Eur J Pediatr Surg*, vol. 8 Suppl 1, pp. 62, Dec 1998.
[168] J.P. McAllister, 2nd and J.M. Miller, “Minocycline inhibits glial proliferation in the H-Tx rat model of congenital hydrocephalus,” *Cerebrospinal Fluid Res*, vol. 7, pp. 7, 2010.
[169] J.M. Miller and J.P. McAllister, 2nd, “Reduction of astrogliosis and microgliosis by cerebrospinal fluid shunting in experimental hydrocephalus,” *Cerebrospinal Fluid Res*, vol. 4, pp. 5, 2007.
[170] E.R. Laws and B. Mokri, “Occult hydrocephalus: results of shunting correlated with diagnostic tests,” *Clin Neurosurg*, vol. 24, pp. 316-33, 1977.
[171] C.M. Fisher, “The clinical picture in occult hydrocephalus,” *Clin Neurosurg*, vol. 24, pp. 270-84, 1977.
[172] S.E. Borgesen and F. Gjerris, “The predictive value of conductance to outflow of CSF in normal pressure hydrocephalus,” *Brain*, vol. 105, (no. Pt 1), pp. 65-86, Mar 1982.
[173] J.R. Nelson and S.J. Goodman, “An evaluation of the cerebrospinal fluid infusion test for hydrocephalus,” *Neurology*, vol. 21, (no. 10), pp. 1037-53, Oct 1971.
[174] C. Wikkelso, H. Andersson, C. Blomstrand, and G. Lindqvist, “The clinical effect of lumbar puncture in normal pressure hydrocephalus,” *J Neurol Neurosurg Psychiatry*, vol. 45, (no. 1), pp. 64-9, Jan 1982.
[175] L. Jacobs and W. Kinkel, “Computerized axial transverse tomography in normal pressure hydrocephalus,” *Neurology*, vol. 26, (no. 6 PT 1), pp. 501-7, Jun 1976.
[176] T.V. Greitz, A.O. Grepe, M.S. Kalmer, and J. Lopez, “Pre- and postoperative evaluation of cerebral blood flow in low-pressure hydrocephalus,” *J Neurosurg*, vol. 31, (no. 6), pp. 644-51, Dec 1969.
[177] N.T. Mathew, J.S. Meyer, A. Hartmann, and E.O. Ott, “Abnormal cerebrospinal fluid-blood flow dynamics. Implications in diagnosis, treatment, and prognosis in normal pressure hydrocephalus,” *Arch Neurol*, vol. 32, (no. 10), pp. 657-64, Oct 1975.

[178] M. Bergsneider, C. Miller, P.M. Vespa, and X. Hu, “Surgical management of adult hydrocephalus,” *Neurosurgery*, vol. 62 Suppl 2, pp. 643-59; discussion 659-60, Feb 2008.
[179] A. Marmarou, M. Bergsneider, P. Klinge, N. Relkin, and P.M. Black, “The value of supplemental prognostic tests for the preoperative assessment of idiopathic normal-pressure hydrocephalus,” *Neurosurgery*, vol. 57, (no. 3 Suppl), pp. S17-28; discussion ii-v, Sep 2005.
[180] M.C. Henry-Feugeas, I. Idy-Peretti, O. Baledent, P. Cornu, H. Lejay, J. Bittoun, and A.E. Schouman-Claeys, “Cerebrospinal fluid flow waveforms: MR analysis in chronic adult hydrocephalus,” *Invest Radiol*, vol. 36, (no. 3), pp. 146-54, Mar 2001.
[181] D.S. Kim, J.U. Choi, R. Huh, P.H. Yun, and D.I. Kim, “Quantitative assessment of cerebrospinal fluid hydrodynamics using a phase-contrast cine MR image in hydrocephalus,” *Childs Nerv Syst*, vol. 15, (no. 9), pp. 461-7, Sep 1999.
[182] M. Mascalchi, G. Arnetoli, D. Inzitari, G. Dal Pozzo, F. Lolli, D. Caramella, and C. Bartolozzi, “Cine-MR imaging of aqueductal CSF flow in normal pressure hydrocephalus syndrome before and after CSF shunt,” *Acta Radiol*, vol. 34, (no. 6), pp. 586-92, Nov 1993.
[183] O. Algin, B. Hakyemez, and M. Parlak, “The efficiency of PC-MRI in diagnosis of normal pressure hydrocephalus and prediction of shunt response,” *Acad Radiol*, vol. 17, (no. 2), pp. 181-7, Feb 2010.
[184] E.M. Haacke, *Magnetic resonance imaging : physical principles and sequence design*, New York: Wiley, 1999.
[185] E.J. McCormack, M.R. Egnor, and M.E. Wagshul, “Improved cerebrospinal fluid flow measurements using phase contrast balanced steady-state free precession,” *Magn Reson Imaging*, vol. 25, (no. 2), pp. 172-82, Feb 2007.
[186] H.G. Friden and J. Ekstedt, “Volume/pressure relationship of the cerebrospinal space in humans,” *Neurosurgery*, vol. 13, (no. 4), pp. 351-66, Oct 1983.
[187] M. Kiefer, R. Eymann, and W.I. Steudel, “The dynamic infusion test in rats,” *Childs Nerv Syst*, vol. 16, (no. 7), pp. 451-6, Jul 2000.
[188] A. Scollato, R. Tenenbaum, G. Bahl, M. Celerini, B. Salani, and N. Di Lorenzo, “Changes in aqueductal CSF stroke volume and progression of symptoms in patients with unshunted idiopathic normal pressure hydrocephalus,” *AJNR Am J Neuroradiol*, vol. 29, (no. 1), pp. 192-7, Jan 2008.
[189] G.A. Bateman, “Vascular compliance in normal pressure hydrocephalus,” *AJNR Am J Neuroradiol*, vol. 21, (no. 9), pp. 1574-85, Oct 2000.
[190] J.M. Gonzalez-Darder and J.L. Barcia-Salorio, “Pulse amplitude and volume-pressure relationships in experimental hydrocephalus,” *Acta Neurochir (Wien)*, vol. 97, (no. 3-4), pp. 166-70, 1989.
[191] K. Shapiro, F. Takei, A. Fried, and I. Kohn, “Experimental feline hydrocephalus. The role of biomechanical changes in ventricular enlargement in cats,” *J Neurosurg*, vol. 63, (no. 1), pp. 82-7, Jul 1985.
[192] M.R. Del Bigio and E.M. Massicotte, “Protective effect of nimodipine on behavior and white matter of rats with hydrocephalus,” *J Neurosurg*, vol. 94, (no. 5), pp. 788-94, May 2001.

[193] M.R. Del Bigio, M.J. Wilson, and T. Enno, “Chronic hydrocephalus in rats and humans: white matter loss and behavior changes,” *Ann Neurol*, vol. 53, (no. 3), pp. 337-46, Mar 2003.
[194] W.C. Hanigan, A. Morgan, A. Shaaban, and P. Bradle, “Surgical treatment and long-term neurodevelopmental outcome for infants with idiopathic aqueductal stenosis,” *Childs Nerv Syst*, vol. 7, (no. 7), pp. 386-90, Nov 1991.
[195] G. Nagra, M.E. Wagshul, S. Rashid, J. Li, J.P. McAllister, 2nd, and M. Johnston, “Elevated CSF outflow resistance associated with impaired lymphatic CSF absorption in a rat model of kaolin-induced communicating hydrocephalus,” *Cerebrospinal Fluid Res*, vol. 7, (no. 1), pp. 4.
[196] H.C. Jones, K.M. Rivera, and N.G. Harris, “Learning deficits in congenitally hydrocephalic rats and prevention by early shunt treatment,” *Childs Nerv Syst*, vol. 11, (no. 11), pp. 655-60, Nov 1995.
[197] G.A. Bateman, “The reversibility of reduced cortical vein compliance in normal-pressure hydrocephalus following shunt insertion,” *Neuroradiology*, vol. 45, (no. 2), pp. 65-70, Feb 2003.
[198] T. Miyati, M. Mase, T. Banno, T. Kasuga, K. Yamada, H. Fujita, K. Koshida, S. Sanada, and M. Onoguchi, “Frequency analyses of CSF flow on cine MRI in normal pressure hydrocephalus,” *Eur Radiol*, vol. 13, (no. 5), pp. 1019-24, May 2003.
[199] T. Miyati, M. Mase, H. Kasai, M. Hara, K. Yamada, Y. Shibamoto, M. Soellinger, C. Baltes, and R. Luechinger, “Noninvasive MRI assessment of intracranial compliance in idiopathic normal pressure hydrocephalus,” *J Magn Reson Imaging*, vol. 26, (no. 2), pp. 274-8, Aug 2007.
[200] J.P. McAllister, “Experimental Hydrocephalus,” in Youmans Neurological Surgery, H. R. Winn and J. R. Youmans eds., Philadelphia, Pa.: W.B. Saunders, 2011, pp. 2002-2008.
[201] A. Marmarou, K. Shulman, and J. LaMorgese, “Compartmental analysis of compliance and outflow resistance of the cerebrospinal fluid system,” *J Neurosurg*, vol. 43, (no. 5), pp. 523-34, Nov 1975.
[202] H.W. Ryder, F.F. Espey, F.D. Kimbell, E.J. Penka, A. Rosenauer, B. Podolsky, and J.P. Evans, “The mechanism of the change in cerebrospinal fluid pressure following an induced change in the volume of the fluid space,” *J Lab Clin Med*, vol. 41, (no. 3), pp. 428-35, Mar 1953.
[203] A. Marmarou, K. Shulman, and R.M. Rosende, “A nonlinear analysis of the cerebrospinal fluid system and intracranial pressure dynamics,” *J Neurosurg*, vol. 48, (no. 3), pp. 332-44, Mar 1978.
[204] K. Shulman and A. Marmarou, “Pressure-Volume Considerations in Infantile Hydrocephalus,” *Developmental Medicine & Child Neurology*, vol. 13, (no. s25), pp. 90-95, December 1971 1971.
[205] C.J. Avezaat, J.H. van Eijndhoven, and D.J. Wyper, “Cerebrospinal fluid pulse pressure and intracranial volume-pressure relationships,” *J Neurol Neurosurg Psychiatry*, vol. 42, (no. 8), pp. 687-700, Aug 1979.
[206] K.J. Streitberger, E. Wiener, J. Hoffmann, F.B. Freimann, D. Klatt, J. Braun, K. Lin, J. McLaughlin, C. Sprung, R. Klingebiel, and I. Sack, “In vivo viscoelastic

properties of the brain in normal pressure hydrocephalus," *NMR Biomed*, Oct 7 2010.
[207] K. Shapiro, A. Fried, F. Takei, and I. Kohn, "Effect of the skull and dura on neural axis pressure-volume relationships and CSF hydrodynamics," *J Neurosurg*, vol. 63, (no. 1), pp. 76-81, Jul 1985.
[208] W.G. Bradley, "Cerebrospinal fluid dynamics and shunt responsiveness in patients with normal-pressure hydrocephalus," *Mayo Clin Proc*, vol. 77, (no. 6), pp. 507-8, Jun 2002.
[209] M.R. Del Bigio and J.P. McAllister, "Hydrocephalus - pathology," in Pediatric Neurosurgery, M. Choux, R. DiRocco, A. D. Hockley and M. L. Walker eds. 4 ed., Philadelphia: Churchill Livingstone, 1999, pp. 217-236.
[210] A. Scollato, P. Gallina, B. Gautam, G. Pellicano, C. Cavallini, R. Tenenbaum, and N. Di Lorenzo, "Changes in aqueductal CSF stroke volume in shunted patients with idiopathic normal-pressure hydrocephalus," *AJNR Am J Neuroradiol*, vol. 30, (no. 8), pp. 1580-6, Sep 2009.
[211] C. Botel and T. Brinker, "Measurement of the dynamics of the cerebrospinal fluid system in the rat," *J Exp Anim Sci*, vol. 36, (no. 2-3), pp. 78-83, Mar 1994.
[212] H.D. Portnoy and M. Chopp, "Cerebrospinal fluid pulse wave form analysis during hypercapnia and hypoxia," *Neurosurgery*, vol. 9, (no. 1), pp. 14-27, Jul 1981.
[213] H.D. Portnoy and M. Chopp, "Intracranial fluid dynamics. Interrelationship of CSF and vascular phenomena. 1983," *Pediatr Neurosurg*, vol. 20, (no. 1), pp. 92-7; discussion 98, 1994.
[214] M.E. Wagshul, P.K. Eide, and J.R. Madsen, "The pulsating brain: A review of experimental and clinical studies of intracranial pulsatility," *Fluids Barriers CNS*, vol. 8, (no. 1), pp. 5, 2011.
[215] M. Egnor, A. Rosiello, and L. Zheng, "A model of intracranial pulsations," *Pediatr Neurosurg*, vol. 35, (no. 6), pp. 284-98, Dec 2001.
[216] N.J. Alperin, S.H. Lee, F. Loth, P.B. Raksin, and T. Lichtor, "MR-Intracranial pressure (ICP): a method to measure intracranial elastance and pressure noninvasively by means of MR imaging: baboon and human study," *Radiology*, vol. 217, (no. 3), pp. 877-85, Dec 2000.
[217] M.F. Quigley, B. Iskandar, M.E. Quigley, M. Nicosia, and V. Haughton, "Cerebrospinal fluid flow in foramen magnum: temporal and spatial patterns at MR imaging in volunteers and in patients with Chiari I malformation," *Radiology*, vol. 232, (no. 1), pp. 229-36, Jul 2004.
[218] Y.C. Fung, *Biomechanics : circulation*, New York: Springer, 1997.
[219] G.A. Bateman and A.M. Loiselle, "Can MR measurement of intracranial hydrodynamics and compliance differentiate which patient with idiopathic normal pressure hydrocephalus will improve following shunt insertion?," *Acta Neurochir (Wien)*, vol. 149, (no. 5), pp. 455-62; discussion 462, 2007.
[220] W. Denk, J.H. Strickler, and W.W. Webb, "Two-photon laser scanning fluorescence microscopy," *Science*, vol. 248, (no. 4951), pp. 73-6, Apr 6 1990.
[221] D. Kleinfeld, P.P. Mitra, F. Helmchen, and W. Denk, "Fluctuations and stimulus-induced changes in blood flow observed in individual capillaries in layers 2

through 4 of rat neocortex," *Proc Natl Acad Sci U S A*, vol. 95, (no. 26), pp. 15741-6, Dec 22 1998.
[222] A. Ustione and D.W. Piston, "A simple introduction to multiphoton microscopy," *J Microsc*, vol. 243, (no. 3), pp. 221-6, Sep.
[223] M. Göppert-Mayer, "Über Elementarakte mit zwei Quantensprüngen," *Annalen der Physik*, vol. 401, (no. 3), pp. 273-294, 1931.
[224] A. Fine, "Confocal Microscopy: Principles and Practice," in Imaging neurons, R. Yuste, F. Lanni and A. Konnerth eds., Cold Spring Harbor, N.Y.: Cold Spring Harbor Laboratory Press, 1999, pp. 1 v. (various pagings).
[225] D. Entenberg, "Intro to Multi-Photon. Quantitative Imaging of Cells.," Albert Einstein College of Medicine, Bronx2009.
[226] W. Denk, "Principles of Multiphoton-excitation Fluorescence Microscopy," in Imaging neurons, R. Yuste, F. Lanni and A. Konnerth eds., Cold Spring Harbor, N.Y.: Cold Spring Harbor Laboratory Press, 1999, pp. 1 v. (various pagings).
[227] K. Konig, "Multiphoton microscopy in life sciences," *J Microsc*, vol. 200, (no. Pt 2), pp. 83-104, Nov 2000.
[228] D. Kobat, M.E. Durst, N. Nishimura, A.W. Wong, C.B. Schaffer, and C. Xu, "Deep tissue multiphoton microscopy using longer wavelength excitation," *Opt Express*, vol. 17, (no. 16), pp. 13354-64, Aug 3 2009.
[229] C. Xu, "Two-photon Cross Sections of Indicators," in Imaging neurons, R. Yuste, F. Lanni and A. Konnerth eds., Cold Spring Harbor, N.Y.: Cold Spring Harbor Laboratory Press, 1999, pp. 1 v. (various pagings).
[230] E.V. Golanov, S. Yamamoto, and D.J. Reis, "Spontaneous waves of cerebral blood flow associated with a pattern of electrocortical activity," *Am J Physiol*, vol. 266, (no. 1 Pt 2), pp. R204-14, Jan 1994.
[231] E. Chaigneau, M. Oheim, E. Audinat, and S. Charpak, "Two-photon imaging of capillary blood flow in olfactory bulb glomeruli," *Proc Natl Acad Sci U S A*, vol. 100, (no. 22), pp. 13081-6, Oct 28 2003.
[232] E.B. Hutchinson, B. Stefanovic, A.P. Koretsky, and A.C. Silva, "Spatial flow-volume dissociation of the cerebral microcirculatory response to mild hypercapnia," *Neuroimage*, vol. 32, (no. 2), pp. 520-30, Aug 15 2006.
[233] M. Czosnyka, H.K. Richards, H.E. Whitehouse, and J.D. Pickard, "Relationship between transcranial Doppler-determined pulsatility index and cerebrovascular resistance: an experimental study," *J Neurosurg*, vol. 84, (no. 1), pp. 79-84, Jan 1996.
[234] R.G. Gosling and D.H. King, "Arterial assessment by Doppler-shift ultrasound," *Proc R Soc Med*, vol. 67, (no. 6 Pt 1), pp. 447-9, Jun 1974.
[235] D. Kleinfeld and W. Denk, "Two-photon Imaging of Neocortical Microcirculation," in Imaging neurons, R. Yuste, F. Lanni and A. Konnerth eds., Cold Spring Harbor, N.Y.: Cold Spring Harbor Laboratory Press, 1999, pp. 1 v. (various pagings).
[236] L. Wei, C.M. Rovainen, and T.A. Woolsey, "Ministrokes in rat barrel cortex," *Stroke*, vol. 26, (no. 8), pp. 1459-62, Aug 1995.
[237] H. Lei, O. Grinberg, C.I. Nwaigwe, H.G. Hou, H. Williams, H.M. Swartz, and J.F. Dunn, "The effects of ketamine-xylazine anesthesia on cerebral blood flow and oxygenation observed using nuclear magnetic resonance perfusion imaging and

electron paramagnetic resonance oximetry," *Brain Res*, vol. 913, (no. 2), pp. 174-9, Sep 21 2001.
[238] K. Masamoto, T. Obata, and I. Kanno, "Intracortical microcirculatory change induced by anesthesia in rat somatosensory cortex," *Adv Exp Med Biol*, vol. 662, pp. 57-61, 2010.
[239] P.A. Flecknell, "Chapter 2 - Anaesthesia," in Laboratory Animal Anaesthesia (Third Edition), San Diego: Academic Press, 2009, pp. 19-78.
[240] D.G. Allen, D.H. Dyson, P.J. Pascoe, and M.R. O'Grady, "Evaluation of a xylazine-ketamine hydrochloride combination in the cat," *Can J Vet Res*, vol. 50, (no. 1), pp. 23-6, Jan 1986.
[241] D.J. Middleton, J.E. Ilkiw, and A.D. Watson, "Physiological effects of thiopentone, ketamine and CT 1341 in cats," *Res Vet Sci*, vol. 32, (no. 2), pp. 157-62, Mar 1982.
[242] D. Kondziella, W. Ludemann, T. Brinker, O. Sletvold, and U. Sonnewald, "Alterations in brain metabolism, CNS morphology and CSF dynamics in adult rats with kaolin-induced hydrocephalus," *Brain Res*, vol. 927, (no. 1), pp. 35-41, Feb 8 2002.
[243] D. Kondziella, U. Sonnewald, M. Tullberg, and C. Wikkelso, "Brain metabolism in adult chronic hydrocephalus," *J Neurochem*, vol. 106, (no. 4), pp. 1515-24, Aug 2008.
[244] M.G. Luciano, D.J. Skarupa, A.M. Booth, A.S. Wood, C.L. Brant, and M.J. Gdowski, "Cerebrovascular adaptation in chronic hydrocephalus," *J Cereb Blood Flow Metab*, vol. 21, (no. 3), pp. 285-94, Mar 2001.
[245] D. Greitz, J. Hannerz, T. Rahn, H. Bolander, and A. Ericsson, "MR imaging of cerebrospinal fluid dynamics in health and disease. On the vascular pathogenesis of communicating hydrocephalus and benign intracranial hypertension," *Acta Radiol*, vol. 35, (no. 3), pp. 204-11, May 1994.
[246] P.H. Luetmer, J. Huston, J.A. Friedman, G.R. Dixon, R.C. Petersen, C.R. Jack, R.L. McClelland, and M.J. Ebersold, "Measurement of cerebrospinal fluid flow at the cerebral aqueduct by use of phase-contrast magnetic resonance imaging: technique validation and utility in diagnosing idiopathic normal pressure hydrocephalus," *Neurosurgery*, vol. 50, (no. 3), pp. 534-43; discussion 543-4, Mar 2002.
[247] C.J. Avezaat, J.H. van Eijndhoven, and D.J. Wyper, "Effects of hypercapnia and arterial hypotension and hypertension on cerebrospinal fluid pulse pressure and intracranial volume-pressure relationships," *J Neurol Neurosurg Psychiatry*, vol. 43, (no. 3), pp. 222-34, Mar 1980.
[248] U. Lindauer, A. Villringer, and U. Dirnagl, "Characterization of CBF response to somatosensory stimulation: model and influence of anesthetics," *Am J Physiol*, vol. 264, (no. 4 Pt 2), pp. H1223-8, Apr 1993.
[249] K.M. Bradley, G.M. Bydder, M.M. Budge, J.V. Hajnal, S.J. White, B.D. Ripley, and A.D. Smith, "Serial brain MRI at 3-6 month intervals as a surrogate marker for Alzheimer's disease," *Br J Radiol*, vol. 75, (no. 894), pp. 506-13, Jun 2002.
[250] S.M. Nestor, R. Rupsingh, M. Borrie, M. Smith, V. Accomazzi, J.L. Wells, J. Fogarty, and R. Bartha, "Ventricular enlargement as a possible measure of Alzheimer's disease progression validated using the Alzheimer's disease

neuroimaging initiative database," *Brain*, vol. 131, (no. Pt 9), pp. 2443-54, Sep 2008.
[251] G.A. Bateman, C.R. Levi, P. Schofield, Y. Wang, and E.C. Lovett, "The pathophysiology of the aqueduct stroke volume in normal pressure hydrocephalus: can co-morbidity with other forms of dementia be excluded?," *Neuroradiology*, vol. 47, (no. 10), pp. 741-8, Oct 2005.
[252] M.R. Del Bigio, "Neuropathology and structural changes in hydrocephalus," *Dev Disabil Res Rev*, vol. 16, (no. 1), pp. 16-22, 2010.
[253] A.W. de Weerd, "Computerized tomography in patients with multiple sclerosis," *Clin Neurol Neurosurg*, vol. 80, (no. 4), pp. 258-63, 1977.
[254] L.A. Hershey, M.H. Gado, and J.L. Trotter, "Computerized tomography in the diagnostic evaluation of multiple sclerosis," *Ann Neurol*, vol. 5, (no. 1), pp. 32-9, Jan 1979.
[255] M. Mase, T. Miyati, H. Kasai, K. Demura, T. Osawa, M. Hara, Y. Shibamoto, and K. Yamada, "Noninvasive estimation of intracranial compliance in idiopathic NPH using MRI," *Acta Neurochir Suppl*, vol. 102, pp. 115-8, 2008.
[256] M. Bergsneider, P.M. Black, P. Klinge, A. Marmarou, and N. Relkin, "Surgical management of idiopathic normal-pressure hydrocephalus," *Neurosurgery*, vol. 57, (no. 3 Suppl), pp. S29-39; discussion ii-v, Sep 2005.
[257] A. Marmarou, P. Black, M. Bergsneider, P. Klinge, and N. Relkin, "Guidelines for management of idiopathic normal pressure hydrocephalus: progress to date," *Acta Neurochir Suppl*, vol. 95, pp. 237-40, 2005.
[258] A. Marmarou, M. Bergsneider, N. Relkin, P. Klinge, and P.M. Black, "Development of guidelines for idiopathic normal-pressure hydrocephalus: introduction," *Neurosurgery*, vol. 57, (no. 3 Suppl), pp. S1-3; discussion ii-v, Sep 2005.
[259] H.C. Jones, K.M. Rivera, and J.E. Coleman, "Spatial learning and visual discrimination tests in hydrocephalic rat pups performed using the Morris water maze," *Eur J Pediatr Surg*, vol. 6 Suppl 1, pp. 37, Dec 1996.
[260] D. Hawkins, T.M. Bowers, C.M. Bannister, and J.A. Miyan, "The functional outcome of shunting H-Tx rat pups at different ages," *Eur J Pediatr Surg*, vol. 7 Suppl 1, pp. 31-4, Dec 1997.
[261] Y.S. Hwang, I. Shim, and J.W. Chang, "The behavioral change of locomotor activity in a kaolin-induced hydrocephalus rat model: evaluation of the effect on the dopaminergic system with progressive ventricle dilatation," *Neurosci Lett*, vol. 462, (no. 3), pp. 198-202, Oct 25 2009.
[262] O.H. Khan, T. Enno, and M.R. Del Bigio, "Tacrolimus and cyclosporine A are of no benefit to young rats with kaolin-induced hydrocephalus," *Pediatr Neurosurg*, vol. 39, (no. 6), pp. 309-13, Dec 2003.
[263] H. Kuchiwaki, M. Nagasaka, S. Inao, and K. Sugita, "Progression of kaolin-induced hydrocephalus and changes in performance of operant tasks by rats," *J Neurol Sci*, vol. 121, (no. 1), pp. 32-8, Jan 1994.
[264] T. Miyazawa, K. Sato, Y. Ikeda, N. Nakamura, and K. Matsumoto, "A rat model of spontaneously arrested hydrocephalus. A behavioural study," *Childs Nerv Syst*, vol. 13, (no. 4), pp. 189-93, Apr 1997.

[265] P.K. Eide and W. Sorteberg, “Diagnostic intracranial pressure monitoring and surgical management in idiopathic normal pressure hydrocephalus: a 6-year review of 214 patients,” *Neurosurgery*, vol. 66, (no. 1), pp. 80-91, Jan.
[266] P.K. Eide and W. Sorteberg, “Changes in intracranial pulse pressure amplitudes after shunt implantation and adjustment of shunt valve opening pressure in normal pressure hydrocephalus,” *Acta Neurochir (Wien)*, vol. 150, (no. 11), pp. 1141-7; discussion 1147, Nov 2008.
[267] P.K. Eide and A. Brean, “Cerebrospinal fluid pulse pressure amplitude during lumbar infusion in idiopathic normal pressure hydrocephalus can predict response to shunting,” *Cerebrospinal Fluid Res*, vol. 7, pp. 5.
[268] P.K. Eide, A. Egge, B.J. Due-Tonnessen, and E. Helseth, “Is intracranial pressure waveform analysis useful in the management of pediatric neurosurgical patients?,” *Pediatr Neurosurg*, vol. 43, (no. 6), pp. 472-81, 2007.
[269] T. Horvath, H.W. Kirby, and A.A. Smith, “Rats' heart rate and grooming activity in the open field,” *J Comp Physiol Psychol*, vol. 76, (no. 3), pp. 449-53, Sep 1971.
[270] D.M. Quadagno, J. Shryne, C. Anderson, and R.A. Gorski, “Influence of gonadal hormones on social, sexual, emergence, and open field behaviour in the rat (Rattus norvegicus),” *Anim Behav*, vol. 20, (no. 4), pp. 732-40, Nov 1972.
[271] A. Ennaceur and J.P. Aggleton, “Spontaneous recognition of object configurations in rats: effects of fornix lesions,” *Exp Brain Res*, vol. 100, (no. 1), pp. 85-92, 1994.
[272] A. Ennaceur and K. Meliani, “A new one-trial test for neurobiological studies of memory in rats. III. Spatial vs. non-spatial working memory,” *Behav Brain Res*, vol. 51, (no. 1), pp. 83-92, Oct 31 1992.
[273] A. Ennaceur, N. Neave, and J.P. Aggleton, “Spontaneous object recognition and object location memory in rats: the effects of lesions in the cingulate cortices, the medial prefrontal cortex, the cingulum bundle and the fornix,” *Exp Brain Res*, vol. 113, (no. 3), pp. 509-19, Mar 1997.
[274] L.B. Goldstein and J.N. Davis, “Influence of lesion size and location on amphetamine-facilitated recovery of beam-walking in rats,” *Behav Neurosci*, vol. 104, (no. 2), pp. 320-7, Apr 1990.
[275] L.B. Goldstein and J.N. Davis, “Beam-walking in rats: studies towards developing an animal model of functional recovery after brain injury,” *J Neurosci Methods*, vol. 31, (no. 2), pp. 101-7, Feb 1990.
[276] R. Dantzer, R.M. Bluthe, G.F. Koob, and M. Le Moal, “Modulation of social memory in male rats by neurohypophyseal peptides,” *Psychopharmacology (Berl)*, vol. 91, (no. 3), pp. 363-8, 1987.
[277] P. Heiduschka and U. Schraermeyer, “Comparison of visual function in pigmented and albino rats by electroretinography and visual evoked potentials,” *Graefes Arch Clin Exp Ophthalmol*, vol. 246, (no. 11), pp. 1559-73, Nov 2008.
[278] P. Herreros de Tejada, D.G. Green, and C. Munoz Tedo, “Visual thresholds in albino and pigmented rats,” *Vis Neurosci*, vol. 9, (no. 3-4), pp. 409-14, Sep-Oct 1992.
[279] G.T. Prusky, K.T. Harker, R.M. Douglas, and I.Q. Whishaw, “Variation in visual acuity within pigmented, and between pigmented and albino rat strains,” *Behav Brain Res*, vol. 136, (no. 2), pp. 339-48, Nov 15 2002.

[280] P.K. Eide, “Demonstration of uneven distribution of intracranial pulsatility in hydrocephalus patients,” *J Neurosurg*, vol. 109, (no. 5), pp. 912-7, Nov 2008.
[281] P. Silacci, A. Desgeorges, L. Mazzolai, C. Chambaz, and D. Hayoz, “Flow pulsatility is a critical determinant of oxidative stress in endothelial cells,” *Hypertension*, vol. 38, (no. 5), pp. 1162-6, Nov 2001.
[282] T. Ziegler, K. Bouzourene, V.J. Harrison, H.R. Brunner, and D. Hayoz, “Influence of oscillatory and unidirectional flow environments on the expression of endothelin and nitric oxide synthase in cultured endothelial cells,” *Arterioscler Thromb Vasc Biol*, vol. 18, (no. 5), pp. 686-92, May 1998.
[283] J.R. Madsen, M. Egnor, and R. Zou, “Cerebrospinal fluid pulsatility and hydrocephalus: the fourth circulation,” *Clin Neurosurg*, vol. 53, pp. 48-52, 2006.